Department of Earth, Ocean and Ecological Sciences

School of Environmental Sciences

University of Liverpool

UNIVERSITY OF LIVERPOOL

Investigating the earthquake cycle of normal faults

Thesis submitted in accordance with the requirements of

the University of Liverpool for the degree of Doctor in Philosophy

by

Lidong Bie

August 2015

Supervised by Dr Isabelle Ryder and Prof. Andreas Rietbrock

To my grandparents, for their love and wisdom

Investigating the earthquake cycle of normal faults

Lidong Bie

Geodetic observations of crustal deformation through the earthquake cycle provide unique opportunities to gain essential knowledge of faulting mechanisms, lithospheric rheology, and fault interaction. Normal faults, an integral geologic unit responsible for crustal deformation, are specifically investigated in this thesis, via three case studies in two significantly different tectonic environments: the 2008 M_w 6.3 Damxung and M_w 7.1 Yutian earthquakes on the Tibetan Plateau, and the 2005 M_w 7.8 Tarapaca earthquake in the northern Chile subduction zone.

To move toward realistic slip models, I consider crustal layering for the Damxung earthquake, and non-planar rupture for the Yutian earthquake. The Damxung study shows that assuming a homogeneous crust underestimates the depth of slip and overestimates the magnitude, in comparison to a crustal model with a weak sedimentary lid. A curved fault model composed of triangular dislocation elements (TDEs) for the Yutian earthquake recovers the geodetic observation better than rectangular fault segments. Normal faulting earthquakes are characterized by shallow slip deficit, which is partially compensated by patchy afterslip around, but no deeper than, the coseismic rupture. The complementary and partially-overlapping relationship between coseismic slip and afterslip implies complexity of frictional properties in both down-dip and along-strike directions.

Postseismic deformation induced by viscoelastic relaxation (VER) following normal faulting earthquakes is fundamentally different in pattern from that produced by afterslip. This difference enables identification of afterslip as the major postseismic mechanism for the Damxung and Yutian earthquakes, and VER for the Tarapaca earthquake. In addition to understanding the faulting mechanism, I also place constraints on local rheological structure. In central Tibet, where the Damxung earthquake occurred, lack of noticeable VER-related signal allows a lower bound of 1×10^{18} Pa s for the viscosity of the lower crust/upper mantle. In northern Chile, geodetic observations following the Tarapaca earthquake indicate a weak layer with viscosity of $4 - 8 \times 10^{18}$ Pa s beneath a higher-viscosity lower crust and mantle lithosphere, and a strong continental forearc.

Based on the co- and post-seismic models, I investigate fault interaction from a perspective of static stress change. Stress computation suggests that the 2014 M_w 6.9 strike-slip event close to the Altyn Tagh fault occurred on a fault that was positively stressed by the Yutian earthquake, and the Altyn Tagh fault to the east of the 2014 rupture is a potential locus for future failure. Although the Coulomb stress change on the 2014 Iquique earthquake rupture is negative due to the Tarapaca earthquake and its postseismic VER process, positive loading on the shallow-dipping nodal plane of its M 6.7 preshock suggests that the Tarapaca earthquake may have acted as an indirect trigger of the 2014 Iquique earthquake. Both studies reveal the role played by normal faults in interacting with other types of faults and have implications for seismic hazard assessment.

Declaration

I, Lidong Bie, declare that the contents of this thesis are all my own work, except where otherwise stated. The views and opinions expressed herein are mine and not necessarily those of any other person or body unless so attributed.

Acknowledgements

After nearly four years in Liverpool, my seemingly-endless education is getting closer to the finishing line. When I am finalizing the thesis, I deeply realize that there are so many people behind me making it possible. I firstly thank the University of Liverpool and China Scholarship Council for the PhD studentship.

I am grateful to my supervisors, Dr. Isabelle Ryder and Prof. Andreas Rietbrock, for their tremendous support and guidance throughout my PhD. Thanks to Isabelle, for being a source of ideas, constructive suggestions and encouragement. I thank Andreas, for greatly broadening my knowledge of seismology. I would like to thank you both for supporting me in attending conferences home and abroad, which allows me to reach out to the larger scientific community.

I would also like to thank coauthors of my publications, Stuart Nippress, Roland Bürgmann and Marianne Metois, for their practical advice, helpful discussions, and technical assistance. Thanks also go to Rongjiang Wang and Sylvain Barbot, who offered kind help with their numerical codes.

I am glad to be a student member of the Centre for the Observation and Modelling of Earthquakes and Tectonics (COMET) in the UK. The annual student meeting offers a great chance to meet old friends and make new ones, and to visit geology departments in different universities. The latter is always one of my hobbies.

Thanks go to fellow PhD students and postdocs in the seismology and geodesy group, for making life easy and happy. Tea breaks are always great with us sharing jokes, fun and other things, although quite often we end up with a casual discussion of science. Tom, Christina, Steve, Amaya, Minxuan, Ludo and Xiao, you are wonderful friends to me. I also thank fellow Chinese PhD students I met here in Liverpool,

Qiang Ren, Jing Du, Lei Jiang and Yu Wang, for those happy chats and dinners together.

Finally, I thank my parents for their love, support and encouragement all the time through everything. Thanks also go to my parents-in-law for their support. My love and thanks go to my wife, Beichuan, for taking good care of the family while managing her own research well, and for her constant patience and unconditional love that sustains me through these years. I own you all too much.

Contents

List of Figures

List of Tables

Chapter 1

Introduction

1.1 Motivation and aims

How the continents deform has been a long-pursued scientific question, as it is closely linked to topography growth and climate change (e.g. Molnar et al., 1993). In tectonically active regions, understanding the kinematics and dynamics of continental deformation fundamentally helps future earthquake hazard assessment. At present, there exist two end-member models that explain the kinematic behavior of continental deformation, namely, the microplate and continuum models. Micro-plate models treat plate-like but small-scale blocks as being rigid and bounded by major deforming faults (Thatcher, 2009). Continuum models regard continental deformation as a widely-distributed, long-wavelength phenomenon due to viscous flow of weak, ductile materials in the lithosphere (England & Molnar, 1997). One critical aspect regarding the two models is where in the continental lithosphere the long-term strength resides – the seismogenic crust or the upper mantle?

Improved knowledge of how mechanical properties vary with depth for the continental lithosphere is important in potentially resolving the above question. From a more practical viewpoint of earthquake hazard assessment, improvements in understanding of the material rheology at depth can help characterize earthquake cycle deformation across active faults in the brittle upper crust (Bürgmann & Dresen, 2008), and assess the stress evolution caused by viscous flow. With the advancement of space geodetic techniques, accurate measurement of surface deformation allows not only rigorous testing of various physical mechanisms in fitting observations, but also allows constraints to be placed on the rheological structure of lithosphere. Previous studies mostly focus on how major strike-slip faults deform through the

earthquake cycle (e.g. Fialko, 2006; Elliott et al., 2008; Yamasaki et al., 2014). For dip-slip earthquakes, megathrust faults in subduction zones have been increasingly investigated (e.g. Lin et al., 2013; Sun et al., 2014), given the fact that they host a great percentage of the largest and most damaging earthquakes. Improved understanding of normal fault-related earthquake cycle deformation is crucially required, as normal faulting is an integral part of continental deformation.

The aims of this thesis can be categorized into three distinct but strongly inter-related groups. The first aim is to improve the inversion strategy for a more realistic retrieval of extensional earthquake source parameters from geodetic observations. I consider a layered elastic medium and curved fault geometry in deriving source parameters for extensional earthquakes on the Tibetan Plateau. Secondly, this work aims to explore different postseismic mechanisms that explain aseismic deformation following normal fault earthquakes. Kinematic and dynamic models are tested to reveal the temporal and spatial characteristics of postseismic slip, and to constrain the rheological structure of the lithosphere, respectively. Models are applied to geodetic observations both on the Tibetan Plateau and in the Chile subduction zone. Finally, the above two strands serve together for one ultimate purpose, that is, a better estimation of seismic potential. I put individual earthquakes in a regional tectonic context, to evaluate the stress loading on nearby faults due to previous co- and post-seismic activities.

1.2 Normal faulting Earthquakes

Normal faults are inclined dip-slip faults that occur in locally extensional environments. When a normal faulting earthquake occurs, the hanging wall block moves down relative to the footwall block, with part of the fault plane being ruptured. Normal faulting earthquakes are broadly distributed around the world (Fig. 1.1), in different tectonic environments, from continental interiors (e.g. the Tibetan Plateau)

to plate boundaries (e.g. mid-ocean ridges), and at various depths, from shallow upper crust to intermediate depth.

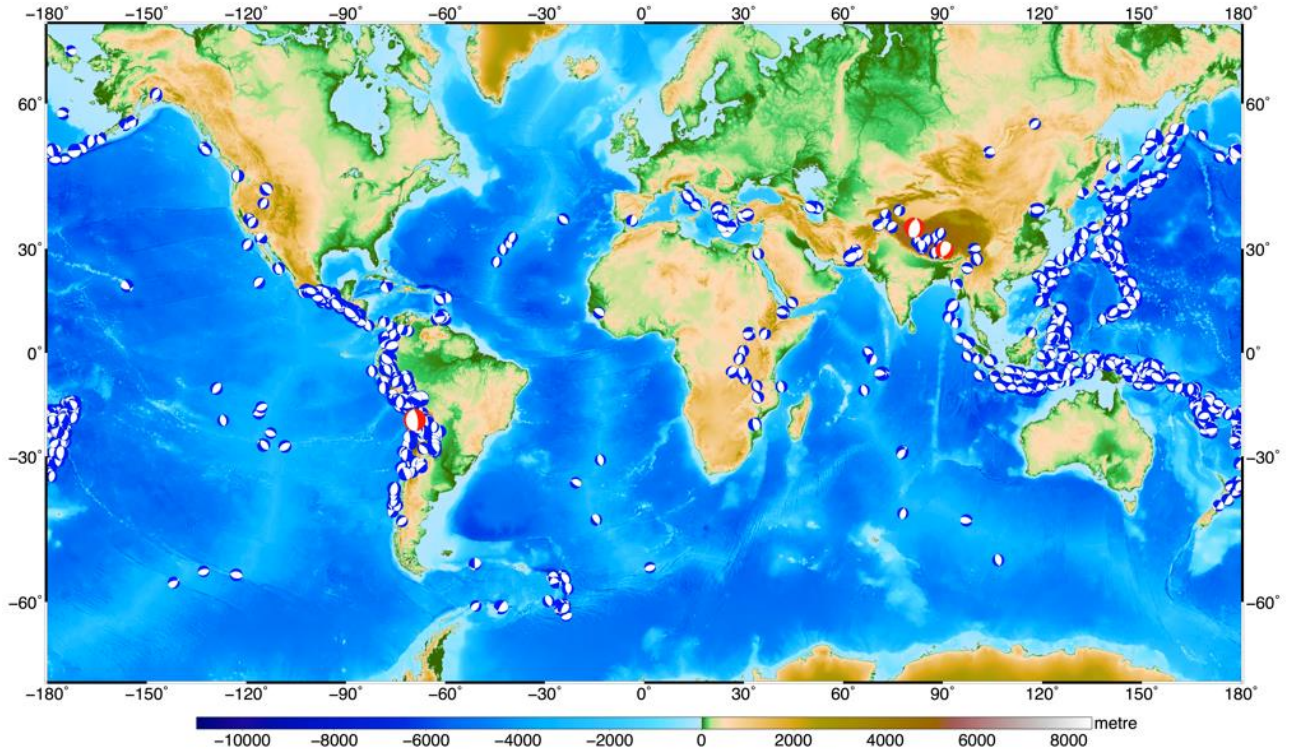

Figure 1. 1. Global distribution of M_w > 6 (1976-2015) normal fault earthquakes from the Global Centroid Moment Tensor (GCMT) catalogue. Earthquakes with at least one nodal plane with rake between -45° and -135° are marked in blue. Focal mechanisms for earthquakes studied in this thesis are emphasised in red color.

The work presented in this thesis focuses on three normal faulting earthquakes in two significantly different tectonic settings. Firstly, the Tibetan Plateau, where the India plate collides with the Eurasia plate, hosts various scales of normal faults distributed across the whole plateau. In 2008, several moderate to large normal faulting earthquakes occurred, not only in southern Tibet, where extensional rifting systems are evident, but also near the northern margin of the plateau, where recent normal faulting earthquakes are rare. I investigate the M_w 6.3 Damxung earthquake in the south, and M_w 7.1 Yutian earthquake in the north. The second type of tectonic setting in this work is the Chilean subduction zone, where the Nazca plate subducts beneath

the South American plate. The 2005 Tarapaca earthquake ruptured the downgoing slab with a magnitude 7.8.

1.2.1 Normal faulting in Tibet

E-W extension in southern Tibet is evident in the form of N-S rifting, as revealed by geologic mapping, remote sensing data interpretation and earthquake focal mechanisms (e.g. Molnar & Tapponier, 1978; Armijo et al., 1986; Molnar & Lyon-Caen, 1989). A recent modelling study by Copley et al. (2011) emphasised a contrast in tectonic regime between northern and southern Tibet, with normal fault dominating in the south and strike-slip faults in the north. However, as well as seismicity patterns, geologic investigations conducted by Yin et al. (1999) and Taylor et al. (2003) reveal that normal faults are also significant in central and northern Tibet, despite the relative sparsity of recent normal faulting earthquakes there in comparison to the south.

Although the number of normal faulting earthquakes (M_w > 4.8 earthquakes from the GCMT catalogue) in northern Tibet is less than that in the south for the last 40 years (Fig. 1.2a), the total moment release (~ 5.5×10^{19} Nm) in the Yutian rupture and its major aftershocks is even larger than the total energy released by normal faults to its south (~ 3.5×10^{19} Nm) (Fig. 1.2b-d). In general, Fig. 1.2b highlights the similarity in extensional moment release between northern and southern Tibet, at least over the last 40 years.

Multiple mechanisms have been proposed in order to explain the E-W extension in Tibet. These explanations include gravitational collapse (e.g. Molnar & Tapponnier, 1978; Molnar & Lyon-Caen, 1989), convective removal of the lower mantle lithosphere (England & Houseman, 1989), basal shear due to Indian Plate indentation (McCaffrey & Nabelek, 1998; Ratschbacher et al., 2011; Copley et al., 2011), and

simple shear induced by lower crustal flow (Zhang et al., 2013). In the study of the Yutian earthquake, Elliott et al. (2010) preferred the gravitational spreading model to explain its occurrence, in consideration of the extraordinarily high elevation (> 5000 m) of the epicentral area. Furuya & Yasuda (2011) attributed the Yutian rupture to extensional stress release in a stepover zone controlled by a large sinistral strike slip fault system.

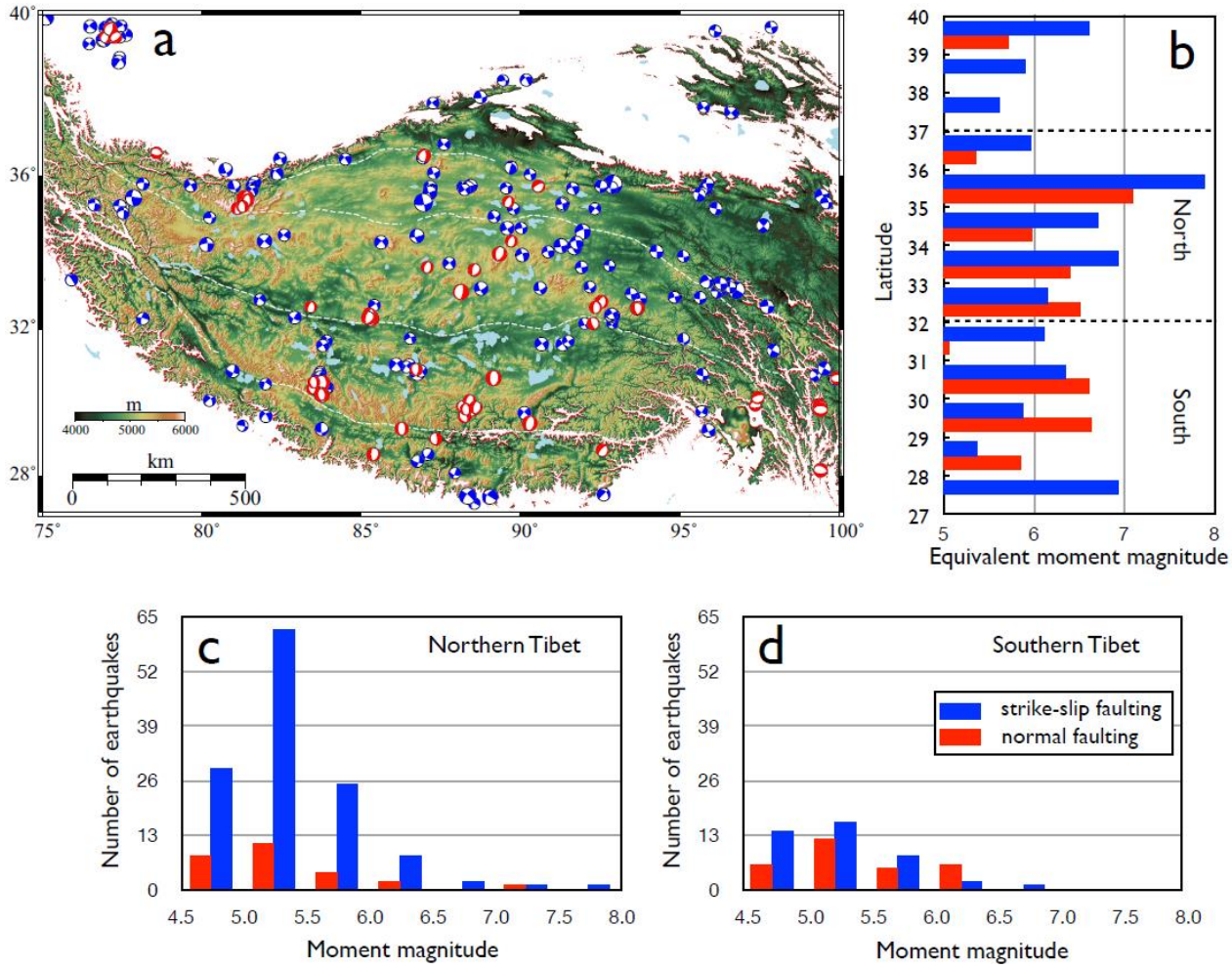

Figure 1. 2. (a) Distribution of focal mechanisms (M_w > 4.7) across the Tibetan Plateau since 1976 from the GCMT catalogue, overlain on GTOPO30 topography. Earthquakes included are restricted to those with solutions near pure-normal and pure strike-slip (that is, rake is within 20° of the pure sense of slip). Red are extensional solutions and blue are strike-slip solutions. Elevations below 4000 m and above 6000 m are set to white, to sharpen the relief in the plateau interior. (b) Equivalent moment magnitude converted from moment release of the events grouped by degree of latitude. N32° is taken as the approximate dividing line between northern and southern Tibet. (c) Frequency-magnitude plots for strike-slip faulting events (blue bars) and normal faulting events (red bars) in northern Tibet. (d) Frequency-magnitude plots for strike-slip faulting events (blue bars) and normal faulting events (red bars) in southern Tibet.

In addition to large normal faulting earthquakes that release strain accumulated across the rift system, such as the 1411 AD M 8.0 earthquake in the Yadong-Gulu rift, active extensional faulting occurs over a width-scale larger than the graben as defined by the geomorphology. As demonstrated in Chapter 3, the fault that ruptured in the 2008 Damxung earthquake was not mapped before and is a secondary normal fault on the hanging wall of the major Nyainqentanglha fault. Similar to the 2008 Damxung earthquake, the 1992 M_w 6.2 Nyemu earthquake (Elliott et al., 2010) and the normal faulting sequence in the 1990s near the Pumqu-Xianza rift (Wang et al., 2014) are all located away from mapped major faults. The 'off-rift' spatial characteristic of these small-to-moderate normal faulting events indicates a distributed rather than localized upper crustal deformation. More importantly, the distributed deformation urges a spatially-expanded monitoring of strain accumulation in extensional tectonic regimes for better seismic hazard assessment.

1.2.2 Intraslab normal faulting in subduction zones

Subduction zones are where the world's largest devastating earthquakes occur. The earthquake mechanism usually involved is thrust faulting, with the plate interface between the overriding and underthrusting plates rupturing suddenly. As well as megathrust earthquakes, subduction zones also host other types of earthquakes, including normal faulting earthquakes in the subducted oceanic slab. The earthquake that I study in this thesis (Chapter 5) is an example of this type of event: an intermediate depth event located within the subducted Nazca plate in northern Chile, with a magnitude of 7.8.

Several explanations exist to explain the genesis of intraslab normal faulting earthquakes. The first relates brittle behavior at intermediate depth to dehydration embrittlement in the subducted slab (e.g. Kirby et al., 1996; Jung et al., 2004). Dehydration of hydrous minerals, principally serpentine, could generate and/or

reactivate fractures. Secondly, intraslab seismicity could occur as a result of the slab-pull stress due to the negative buoyancy caused by sinking heavy oceanic slab and tensile coherence of lithosphere (Lay et al., 1989). Given the relatively young slab age beneath northern Chile and the large convergence rate of ~ 8 cm/yr, Lemoine et al. (2002) exclude the predominance of the slab-pull effect in this part of the Nazca plate.

Another explanation places intraslab earthquakes within the context of the subduction zone earthquake cycle, which involves the state of stress in the subducted slab being modulated by megathrust earthquakes. In a subduction zone with strong seismic coupling, such as the north Chilean subduction zone presented in Chapter 5, extensional stresses develop on the downdip edge of the locked zone (Astiz et al., 1988; Lay et al., 1989), causing normal faulting earthquakes prior to the rupture of shallow megathrust faults. However, the intraslab normal faulting earthquakes do not always occur before the megathust ones. The temporal order can be reversed by the complex geometry of the subducted slab, which influences the state of stress. For example, Cocco et al. (1997) speculate that the occurrence of the 1994 M_w 6.6 Zihuatanejo, Mexico earthquake in the subducted Cocos plate was due to increased buckling of the sub-horizontal slab following several large shallow up-dip thrust earthquakes in 1979 and 1985.

It is clear that the state of stress across a subduction zone plate interface could be altered by intraslab normal faulting earthquakes at intermediate depth. Understanding the interaction between intraslab normal faulting earthquakes and interplate coupling is of particular importance for seismic hazard estimation in subduction zones that have been characterized as seismic gaps. The northern segment of the Chilean subduction zone has been well-known as a seismic gap, with an absence of large earthquakes since 1877 (e.g. Ruiz et al., 2014; Schurr et al., 2014; Bürgmann, 2014). The occurrence of a M_w 8.1 megathrust earthquake (hereafter named as the Iquique

earthquake) in 2014 following the 2005 Tarapaca earthquake shows agreement with the above-mentioned temporal character that normal faulting earthquakes occur prior to the rupture of shallow megathrust faults. The sequence of events encourages us to investigate in detail how the 2005 Tarapaca earthquake influenced the state of stress on the ruptured plate interface, in order to further decipher the interaction between these two types of events in subduction zones.

1.3 The earthquake cycle

The concept of the earthquake cycle stems from the elastic rebound theory proposed by Reid (1910) in explaining the displacement fields measured by triangulation surveys before and after the 1906 San Francisco earthquake. Comparison of surveys carried out in the 1880s and 1860s showed that the SW side of the San Andreas Fault was moving towards the northwest, and the amount of displacement increased away from the fault. Another comparison of displacement fields surveyed in the 1880s and after the 1906 earthquake showed an opposite pattern, that is, the displacement decreased away from the fault.

Through comparison of the kinematic behavior of the San Andreas Fault before and after the 1906 San Francisco earthquake, Reid (1910) formulated the theory of elastic rebound, which stated that earthquakes occurred as a result of abrupt release of strain accumulated during the long interseismic period. In the interseismic period, strain slowly builds up, due to steady plate motion either side of the fault, until the stress overcomes the frictional resistance to produce an earthquake. The kinematic expression of an earthquake cycle is a step-like net deformation across the fault, and both plates either side of the fault return to their original shape.

In reality, the earthquake process is far more complicated than just the two phases mentioned in elastic rebound theory. Geodetic measurements following coseismic

rupture have consistently demonstrated the existence of a rapid transient deforming phase, which eventually decays back to the steady long-term loading rate (e.g. Thatcher & Rundle, 1984; Reilinger et al., 2000; Scholz, 2002). The postseismic deformation is due to a time-dependent relaxation of the stresses induced by coseismic rupture. The postseismic motion may last from days to tens of years, depending on the relaxation mechanism(s).

At present, three mechanisms are proposed to explain postseismic motion: poroelastic rebound, due to changes in drainage conditions in the upper crust (e.g. Peltzer et al., 1998; Jónsson et al., 2003; Fialko, 2004a); afterslip on coseismic and/or subsidiary faults (e.g. Bürgmann et al., 2002; Hearn et al., 2002); and viscoelastic relaxation in weak layers of the lithosphere (e.g. Pollitz et al., 2002; Ryder et al., 2014). These mechanisms differ in both temporal and spatial scale. However, due to the complexity of physical processes and the limitations of geodetic observations, it can be difficult to isolate unequivocally the contribution of the various mechanisms.

Depending on the effective permeability of shallow rocks, poroelastic rebound can last for months (e.g. Jónsson et al., 2003; Árnadóttir et al., 2005) to years (e.g. Fialko, 2004a). In the study of postseismic deformation within 5 months following the M_w 7.2 El Mayor-Cucapah earthquake, Gonzalez-Ortega et al. (2014) found that only a small fraction, if any, of early postseismic deformation could be accounted for by poroelastic rebound. In general, poroelastic rebound produces a small-wavelength signal within only a few kilometers of the coseismic rupture, and over a short time period (Freed et al., 2006). Since the studies presented in this thesis cover a much larger area and several years after the earthquakes, poroelastic rebound is unlikely to be a dominant effect.

Afterslip is a type of aseismic slip producing transient postseismic deformation. It is inferred to be a major mechanism in a number of postseismic studies (e.g. Segall et

al., 2000; Bürgmann et al., 2002; Hsu et al., 2002). The temporal and spatial evolution of afterslip can be obtained by kinematic or dynamic inversion of geodetic observations. An increasing number of studies show that afterslip tends to appear adjacent to the coseismic rupture, where coseismic stress loading is assumed to be largest. The spatial pattern is consistent with that revealed by rate-strengthening friction laws. According to these laws, afterslip is expected either at the down-dip edge of the coseismic rupture, where aseismic creep is favoured at mid-crustal temperatures (Tse & Rice, 1986), or at shallow depth within poorly-consolidated sediments (Marone et al., 1991). A logarithmic function can be applied to fit the temporal evolution of afterslip (e.g. Savage & Svarc, 2009). By fitting the afterslip evolution with dynamically-modelled stress-driven creep, one can estimate the fault frictional properties (e.g. Hsu et al., 2006; Barbot et al., 2009; Lin et al., 2013), which can be compared with those derived from laboratory experiments (Marone, 1998).

Viscoelastic relaxation (VER) is a process of gradual flow of weak materials in response to induced coseismic stress. Thus, viscoelastic behaviour depends on the rheology of the study area. A series of models exist to describe viscoelastic properties, depending on the configuration of elastic and viscous components (Section 1.4). Each of the models has a different strain rate – stress change relationship, causing a variation in temporal decay rate. By matching geodetic observations of postseismic deformation, one can test which rheological model best describes the temporal and spatial evolution, and thus, gain knowledge of local rheological properties and lithospheric structure (e.g. Freed et al., 2006; Rousset et al., 2012). A linear Maxwell rheology is most often employed to represent the lower crust and/or upper mantle underlying the elastic upper crustal lid (e.g. Pollitz et al., 2000; Ryder et al., 2014).

One character of postseismic deformation analysis is the non-uniqueness of driving mechanisms. For example, Ryder et al. (2007) explores the postseismic relaxation of the Tibetan lower crust in terms of both a standard linear solid rheology, and

localised afterslip. Another example of non-unique postseismic mechanisms is the widely-studied 1992 Landers earthquake, which is summarized in Bürgmann & Dresen (2008).

Postseismic deformation can be explained by different mechanisms, solely or in combination with others. This potential complexity poses a challenge in studies of the postseismic phase of the earthquake cycle. If only one mechanism is considered, contributions from other mechanisms maybe significantly underestimated. In a detailed postseismic study of the 2011 Tohohu-Oki earthquake, Sun et al. (2014) concluded that without including the viscoelastic relaxation mechanism, afterslip could be substantially overestimated down-dip of the coseismic rupture, and underestimated up-dip. Leaving out viscoelastic relaxation can consequently influence our understanding of fault frictional behavior, bias the estimation of aseismic slip that contributes to strain release, and, probably, impact inferences of earthquake cycle time scale (Avouac, 2015). Calibration of postseismic deformation also has important implications for estimation of regional deformation rates. A synthetic study by Hampel & Hetzel (2015) demonstrates by numerical tests that a biased interseismic rate or even an incorrect tectonic regime could be derived from GPS data that contains a postseismic relaxation signal.

In addition to the above-mentioned postseismic phase of the earthquake cycle, geodetic observation also suggests a preseismic phase, which deviates from the interseismic deformation. For example, Global Positioning System (GPS) time-series show a slow slip event preceding the 2014 Iquique megathrust earthquake in Northern Chile (Ruiz et al., 2014). A similar pre-shock phase has also been detected before the 2011 M_w 9.0 Tohoku-Oki earthquake (Kato et al., 2012). Together, they may have important implications for the prediction of future megathrust earthquakes, if such a precursory phase is common. The discussion of mechanisms for the

preseismic phase is beyond the scope of this thesis, given sparse observations and the unclear nature of such events (Scholz, 2002).

1.3.1 The earthquake cycle of normal faults: previous studies

Previous studies of earthquake cycle deformation for normal faults have mostly focused on the coseismic phase, in order to determine a slip model that reveals earthquake rupture patterns. Normally, a rectangular fault plane is assumed to be buried in a homogeneous elastic half-space (e.g. Walters et al., 2009; Elliott et al., 2010). To better fit the geodetic observations, multi-segment fault failure is sometimes invoked, and/or a curved fault plane is adopted. For example, Resor et al. (2005) examined in detail the coseismic deformation of the 1995 M_w 6.5 Kozani-Grevena earthquake in northern Greece by testing three slip models with different fault configurations and complexity, and the preferred (best-fitting) model has three segments. Another example is the coseismic study of the 2008 Yutian earthquake. Elliott et al. (2010) inverted for slip on three rectangular fault segments, while in the coseismic slip model presented by Furuya & Yasuda (2011), a smaller rectangular fault is added to the north of the major curved rupture.

Different from the postseismic deformation following strike-slip earthquakes, which can sometimes be explained by both VER and afterslip, postseismic deformation following normal faulting earthquake shows much less ambiguity. That is, for a buried normal fault rupture, postseismic VER produces a circular pattern of uplift across the fault (Segall, 2010). This circular feature is significantly different from the spatial pattern produced by afterslip, which normally would show a change in sign across the fault trace.

Short-term (months to years) geodetic observations following several normal faulting earthquakes tend to support the notion that afterslip is the major postseismic

deformation mechanism. Ryder et al. (2010) found from months of postseismic deformation following the 2008 Nima-Gaize earthquake that afterslip occurred on both the mainshock and aftershock rupture surfaces. Although the lack of VER-related deformation prohibits a direct estimation of rheology, Ryder et al. (2010) placed a lower bound on the mid-lower crustal viscosity of 3×10^{17} Pa s. In a study of the 2006 M_w 7.0 Mozambique earthquake, Copley et al. (2012) suggested a lower bound for ductile lithospheric viscosity of $\sim 2 \times 10^{19}$ Pa s for the southern end of the East African Rift zone. They also proposed that the observed shallow postseismic creeping (velocity-strengthening) behavior is in accordance with the presence of a thick sedimentary layer, which acts as a barrier partially arresting the propagation of coseismic slip.

Long-term (years to decades) observations, however, imply that VER plays an important role in contributing to postseismic deformation of normal faulting earthquakes. Reilinger (1986) found an exponential decay of crustal uplift rate from levelling measurements until 1983 following the 1959 M_w 7.3 Hebgen Lake earthquake in Montana. A simple model with a 30 – 40 km thick elastic lid overlying a Maxwell viscoelastic half-space can fit the measurements. A study by Nishimura & Thatcher (2003) gave a similar rheological model, with a viscosity of $4 \times 10^{18\pm0.5}$ Pa s. With GPS and trilateration surveys from 1973 to 2000, Chang et al. (2013) developed a model with lateral variation of transient rheology, and with a stronger lower crust than the upper mantle. Although rheological structures may vary in different studies, we see that the long-term postseismic observations of the Hebgen Lake earthquake do show a contribution from VER. An example of long-term observation of late postseismic deformation is presented by Ryder et al. (2014) on two major earthquakes in 1951 and 1952 in Tibet. A broad uplift shown by InSAR data in the Gulu Basin clearly demonstrates an unambiguous VER process following the 1952 earthquake that ruptured the east-dipping normal fault bounding the Gulu basin.

1.4 Rheology

At shallow depth with low temperatures and pressures, brittle failure can be well described by friction laws (Byerlee, 1978; Dieterich, 1979). When temperature increases with depth to a certain degree, atoms and dislocations in rocks become mobile, giving rise to aseismic creep and viscous flow. The transition from shallow brittle to deep ductile behavior is governed by rock rheology, which describes rock properties through constitutive equations that relate stress and strain rate (Bürgmann & Dresen, 2008).

Experimental data on rock mechanics suggest that the lower crust and upper mantle may creep in a non-Newtonian fashion, with strain rate being proportional to stress raised to a power $n > 1$ (Goetze, 1978). In this thesis, I only consider linear (Newtonian) rheology ($n = 1$), in which strain rate is linearly proportional to stress.

Creep processes in weak layers of the lithosphere can relax elastic stresses. The relaxation can be modelled as a rheological system that consists of both elastic and viscous components. A viscoelastic medium behaves both elastically (allowing transmission of shear waves at short time scales) and viscously (creeping at long times). Various combinations of elastic (spring) and linear viscous (dashpot) elements are used in modelling deformation due to postseismic viscoelastic relaxation. The most common two are the Maxwell rheology and the Burgers rheology.

The Maxwell rheology can be represented by a spring and dashpot in series. The elastic spring responds immediately to stress loading but eventually the dashpot dominates, deforming with a steady-state strain rate. If a Kelvin solid is added in series with a Maxwell fluid, a Burgers rheology is formed. This configuration has

two viscous components with different viscosity. The Kelvin solid accommodates the transient creep during early stages of postseismic deformation. A graphical representation of the different rheologies is shown in Fig. 1.3.

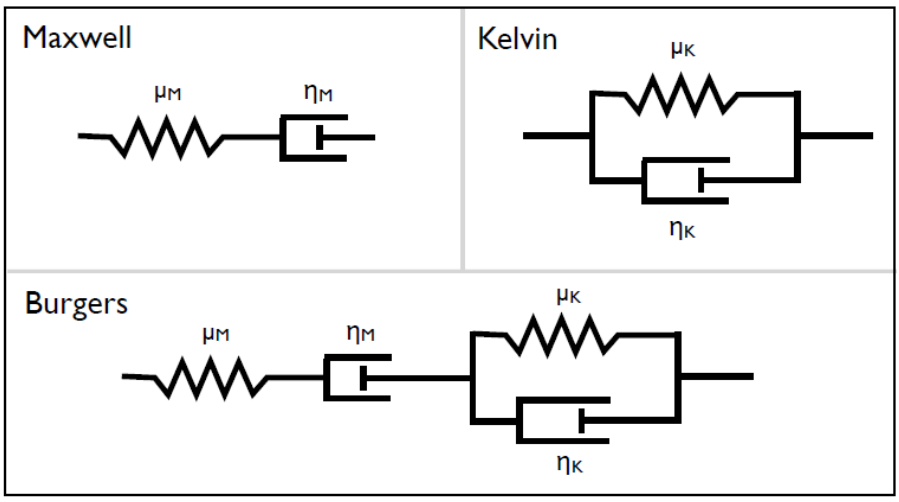

Figure 1. 3. Mechanical analogues for different rheologies, consisting of different combinations of spring and dashpot. μ and η represent the shear modulus and viscosity of the elastic and viscous elements, respectively.

Viscosity is a measure of material's ability to flow. Effective viscosity can be obtained by a scale ratio of stress to strain rate. Since in a non-Newtonian rheology, strain rate is proportional to some power of stress, effective viscosity increases when stress decreases. This character of variable viscosity can also be inferred both temporally and spatially from modelling of postseismic geodetic observations. For example, in a Burgers rheology, the steady-state viscosity is often found to be greater than the transient viscosity, showing a gradual increase of viscosity as coseismically-induced stress is relaxed with time. Also due to an immediate coseismic stress increase, viscosity right beneath a fault rupture may be much smaller than that of the bounding rocks, and over time, this would presumably lead to a zone of inherent weakness here (e.g. different grain size from the bounding rocks). Indeed, Yamasaki et al. (2014) proposed that a localised weak ductile shear zone, with lower viscosity than the bounding rocks, exists beneath the north Anatolian fault zone, based on GPS

data following the 1999 Ìzmit and Düzce earthquakes. However, whether such a rheological structure with a localised weak ductile shear zone is applicable to other major strike-slip faults and other types of faults needs to be further tested.

1.5 Fault interaction

An earthquake will alter the stress field in surrounding rocks and on neighboring faults. Depending on the previous stress condition, the fault being loaded may fail in seconds or years following the preceding earthquake, if the fault falls within one of the regions with elevated stress (e.g. King et al., 1994; Freed, 2005). The process of earthquake triggering shows that faults interact with each other through the transfer of stress.

According to the Coulomb failure criterion (Jaeger et al., 2009), when the shear stress on a fault overcomes the frictional resistance, earthquakes tend to occur. In reality, the absolute value of stress is difficult to measure. However, both shear and normal stress changes can be calculated in association with earthquake slip on the source fault. Thus, the static Coulomb stress change can be calculated according to:

$$\Delta\sigma_f = \Delta\tau + \mu'\Delta\sigma_n \tag{1.1}$$

where $\Delta\tau$ and $\Delta\sigma_n$ are shear and normal stress (unclamping positive) changes on the receiver fault, and μ' is the apparent frictional coefficient (King et al., 1994). Based on this equation, I investigate in detail how the 2008 Yutian earthquake interacts with regional fault systems (chapter 4), and shed light on the seismotectonic indication of strike-slip fault and normal fault interaction in Tibet and globally. I also present how an intraslab normal fault interacts with a megathrust in terms of stress loading from both coseismic slip and postseismic viscoelastic relaxation following the intralslab Tarapaca earthquake (chapter 5).

Different from the above-mentioned elastic (static) stress triggering, which is a local to regional scale effect, remote earthquake triggering is attributed to dynamic stress changes caused by the passage of seismic waves. Triggered earthquakes mostly occur in conjunction with or within minutes following the source rupture at greater distances than a regional fault network (Hill & Prejean, 2015), although delayed dynamic triggering long after the arrival of seismic waves is also reported (e.g. Parsons, 2005). Since the work presented in this thesis does not involve the dynamic triggering effect, no further discussion is provided.

1.6 Overview of thesis

In this thesis, I investigate the earthquake cycle deformation of three normal faulting earthquakes in Tibet and northern Chile.

Chapter 2 introduces technical aspects of the work carried out during this research. The observational technique of Interferometric Synthetic Aperture Radar (InSAR) is briefly described, and its limitations in detecting weak tectonic signals. Techniques used in this thesis to mitigate tropospheric delay are also outlined. Elastic and viscoelastic theory relevant to modelling of geodetic observations is then discussed, with a general introduction and detailed tests of the software/codes used in the following chapters.

Chapter 3 is concerned with the 2008 Damxung earthquake in Tibet. A non-linear inversion scheme is proposed to find an optimal rupture geometry and slip distribution on a fault in a layered elastic crust. A comparison between slip models derived with homogeneous and layered crust shows that the maximum slip of the latter model is smaller and deeper. The postseismic deformation mechanism is investigated based on a time-series constructed from 17 interferograms. Afterslip

patches are found to surround the coseismic rupture at shallow depth. A lower bound of 1×10^{18} Pa s is placed on the viscosity of the mid/lower crust. This work is published in Geophysical Journal International in 2014. Coauthor Isabelle Ryder supervised the work, Stuart Nippress contributed to the aftershock analysis and Roland Bürgmann participated in the discussion of the modelling results and thoroughly read an early version of the manuscript.

In **Chapter 4**, I present a coseismic slip model composed of triangular dislocation elements (TDEs) for the 2008 Yutian earthquake in northern Tibet. On the curved rupture surface, slip sense changes from extensional in the south to left-lateral in the north. This trend is in general consistent with the aftershock focal mechanisms. Similar to the Damxung earthquake, afterslip inverted from postseismic deformation time-series appears around the perimeter of the coseismic slip in a patchy way. I also investigate stress transfer from the 2008 earthquake onto nearby faults, and specifically test whether faults that ruptured in the 2012 and 2014 earthquakes were positively loaded. Collectively, these three events in 2008, 2012 and 2014 load positively on the nearby segment of the Altyn Tagh fault, which has not ruptured since early last century. This work has global implications for analogous tectonic environments, with stepover zone failure having the potential to promote failure on bounding strike-slip faults. This work is published in Geophysical Journal International in 2014. Coauthor Isabelle Ryder acted as supervisor of this study.

Chapter 5 focuses on the 2005 Tarapaca earthquake, which is an intraslab normal faulting earthquake at intermediate depth in the northern Chile subduction zone. I processed ~ 4 yrs of postseismic interferograms, with tropospheric noise corrected, to obtain a rate map. Broad uplift across the fault is attributed to VER in weak layers of continental lithosphere. I built up a 3D semi-analytic model that considers lateral heterogeneity in rheology to constrain the local rheological structure. To fit the data, a weak layer beneath the lower crust and/or upper mantle is required, with viscosity between $4 – 8 \times 10^{18}$ Pa s. The frontal forearc must be stronger than the area beneath

the volcanic arc, demonstrating a cold and stagnant medium. I also compute the stress transfer from the 2005 Tarapaca earthquake and its postseismic VER on the plate interface, to investigate the potential triggering of the 2014 Iquique earthquake. This work aims at demonstrating the feasibility of using deep normal faulting earthquakes to constrain subduction zone rheology, and investigating the interplay of different earthquake types in a subduction zone environment. This work is supervised by coauthor Isabelle Ryder. Coauthor Marianne Metois contributed to the GPS data processing and analysis, and read through the manuscript.

Chapter 6 discusses several aspects raised from the studies of three normal faulting earthquakes. First, coseismic slip models for several geodetically-studied normal fault earthquakes are compiled, in order to investigate the rupture characteristics, such as shallow slip deficit and depth dependence on magnitude. The spatial relationship between afterslip and coseismic slip is discussed, and the spatial pattern is related to earthquake mechanics. I also discuss postseismic deformation mechanisms by compiling normal faulting earthquakes with postseismic geodetic measurements. Then, estimates of lithospheric rheology for different parts of the Tibetan Plateau are compiled, with the aim of examining spatial and temporal differences in rheology estimated using various techniques. Third, I discuss the importance of subduction zone rheology in deciphering earthquake cycle deformation, and potential techniques and methods for investigation of oceanic mantle viscosity. Finally, I conclude with key findings from the thesis.

Chapter 2

Data and Modelling

This chapter is concerned with the main type of geodetic data and modelling techniques used in this thesis. I present firstly InSAR theory and error mitigation techniques. Following the introduction of data, I outline the basic elastic and viscoelastic theory based on which various codes are developed to model ground displacement data. Synthetic tests are implemented with different codes used in this thesis to compare and validate outputs.

2.1 InSAR

Interferometric Synthetic Aperture Radar (InSAR) is a radar technique that is widely used now for mapping topography and monitoring surface deformation. It essentially differentiates the phase components of two Synthetic Aperture Radar (SAR) images to form an interferogram. Technical details on SAR and interferometry can be found in reviews by Massonnet & Feigl (1998) and Bürgmann et al. (2000).

Different from optical remote sensing techniques, which passively detect radiation reflected or emitted from Earth's surface, radar remote sensing actively emits microwave signals and records backscattered electromagnetic waves. Typical wavelengths used in satellite radar remote sensing are X band (wavelength 3.1 cm), C band (5.6 cm) and L band (23.6 cm). In this work, I use the latter two, which are provided by sensors aboard the now-deceased Environmental Satellite (Envisat) and Advanced Land Observation Satellite (ALOS), respectively. Because of their long wavelength, radar waves can penetrate through clouds, offering all-weather and all-time observation of the Earth's surface.

The phase difference of two SAR images, namely the interferogram, contains contributions from several factors, including path delays due to surface deformation, topography, satellite orbit variation and atmospheric content. The topographic contribution is usually modelled using a 90-m digital elevation model (DEM) from the Shuttle Radar Topography Mission (Farr et al., 2007). The orbital contribution can be simulated based on knowledge of the satellite orbit (e.g. DORIS orbits). DORIS is an abbreviation for Doppler Orbitography and Radio-positioning Integrated by Satellite, a tracking system used to determine the precise location of the Envisat satellite. Subtraction of the topographic and orbital components leaves only the phase difference caused by surface deformation and atmospheric delay. Theoretically, displacements as small as a few millimeters can be measured. However, in real applications for measuring small-magnitude deformation, the precision is limited by atmospheric delay and, sometimes, the orbital uncertainties.

2.2 Error mitigation

Atmospheric noise in interferograms is caused by variation of water vapour, temperature and pressure in different SAR acquisitions. A brief description of atmospheric noise is presented in Chapter 3 before postseismic interferograms for the Damxung earthquake are presented. Here, I introduce mitigation techniques that are used in this thesis, with a focus on using MEdium Resolution Imaging Spectrometer (MERIS) data and the ERA-interim weather model together to mitigate the atmospheric noise.

At present, multiple techniques exist in mitigating the influence from atmospheric delay. A thorough review is given by Ding et al. (2008). The techniques fall into two general categories: those that use external data, and those that do not. In this thesis, I implement a phase-based linear correction for postseismic interferograms following the Damxung and Yutian earthquakes, and minimise atmospheric delay in the

Tarapaca earthquake postseismic study with the aid of external satellite data and weather models.

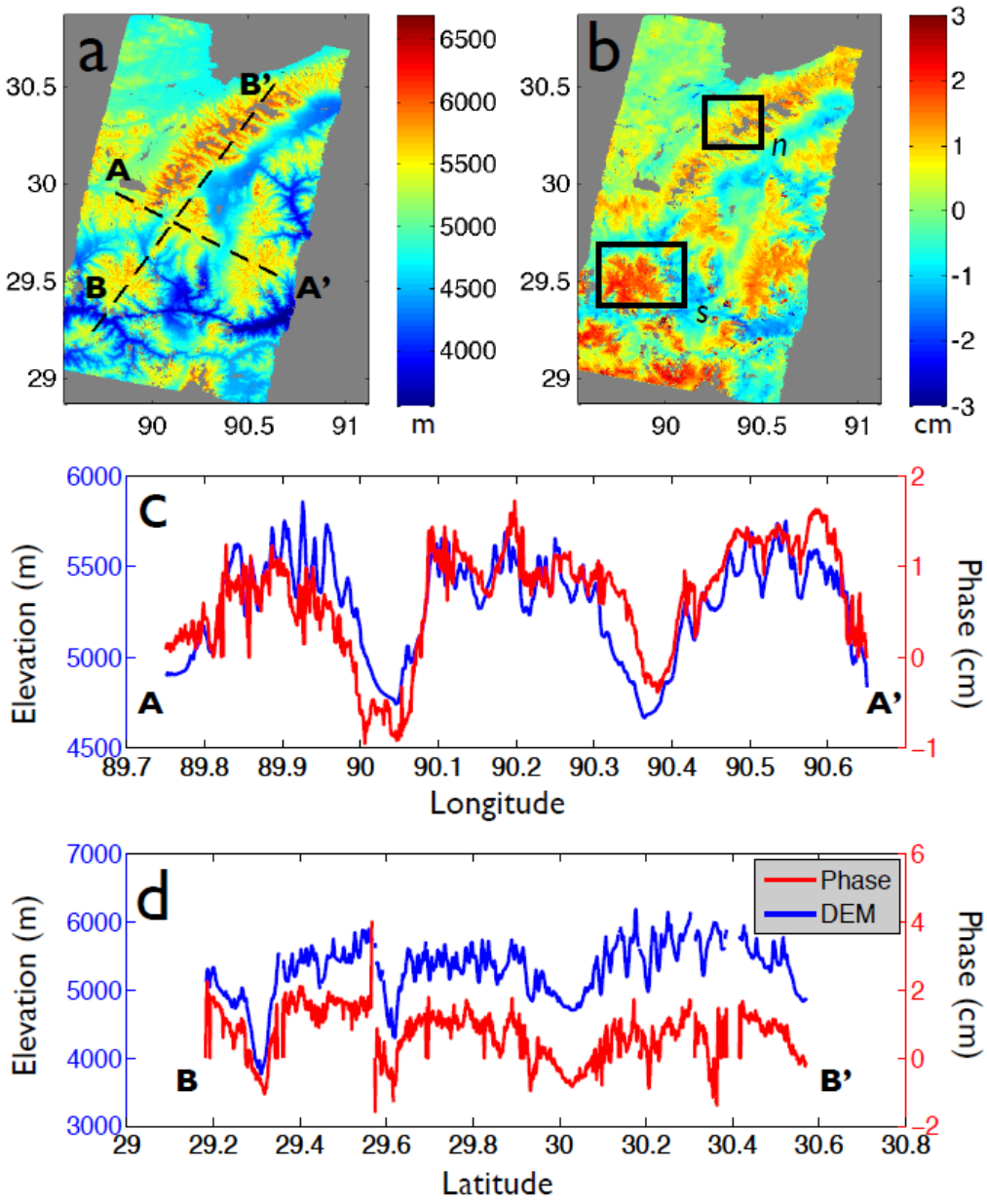

Figure 2. 1. Comparison of (a) elevation and (b) LOS phase for a postseismic interferogram of the Damxung earthquake. The example interferogram is constructed from SAR acquisitions on 2009 September 6 and 2010 January 24. (c) and (d) show the correlation of elevation and LOS phase along two profiles A-A' and B-B' as marked in (a), respectively. Black boxes in (b) marked with *n* and *s* are the regions over which the correlation coefficients are calculated and shown in Fig. 2.2.

Linear correction is based on the empirical linear relationship between interferometric phase and topography (Cavalié et al., 2007, 2008). Fig. 2.1, for

example, shows the correlation of one postseismic interferogram of the Damxung earthquake with elevation. Usually, the linear correlation factor is determined at an interferogram scale (Cavalié et al., 2007). However, the linear relationship may change across the interferogram. The variation of correlation factor is demonstrated in Fig. 2.2, where in the southern area, a larger conversion factor is required. Use of the linear correction method may also mistakenly remove deformation signal, which may correlate with topography, for example in volcanic deformation. The linear method to jointly correct topography-correlated atmospheric noise and orbital error is described in Chapter 3. Fig. 2.3 shows an example of the method being applied to a postseismic interferogram of the Damxung earthquake. After the joint correction, the remaining atmospheric noise is most profound in the southern part, at a level of ~ 1 cm, while in the area surrounding the earthquake zone (central area of the interferogram), the phase is close to zero, demonstrating the effectiveness of the joint linear correction method.

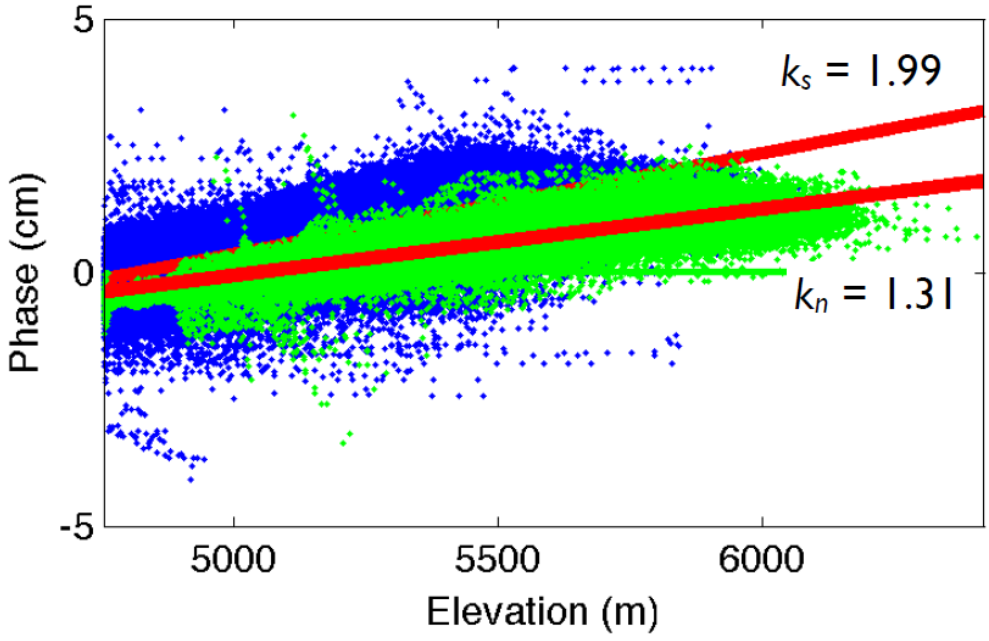

Figure 2. 2. Phase plotted against elevation for pixels boxed in two sub-regions in the south and north of the interferogram, as shown in Fig. 2.1b. The correlation coefficient for the southern sub-region (k_s) is larger than that for the northern region (k_n), demonstrating the inhomogeneity of the phase-elevation correlation across the interferogram.

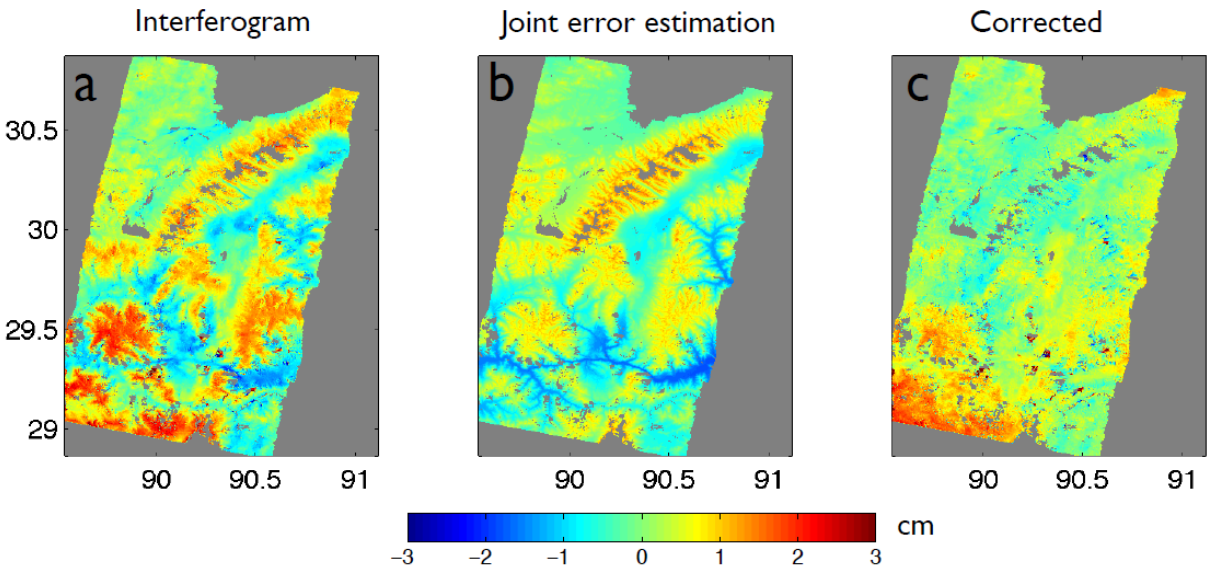

Figure 2. 3. An example demonstrating joint estimation of topography-correlated atmospheric noise and orbital error. Panels from left to right show (a) an original interferogram from the postseismic study of the Damxung earthquake (090906-100124), (b) joint estimation of topography-correlated atmospheric noise and orbital error, and (c) corrected interferogram.

MERIS was another sensor on board the Envisat satellite and measured the solar radiation reflected by Earth's surface and clouds. It was originally designed for studies of ocean biology and marine water quality by observation of ocean color. With a field of view of 68.5° around nadir, MERIS covers a swath of 1150 km and global coverage is usually within three days. Out of the 15 spectral bands, two are in the near-infrared, allowing a measurement of Precipitable Water Vapour (PWV). Two levels of water vapour products are provided with different spatial resolutions. One is known as the full resolution product (~ 300 m) and the other is with reduced resolution of ~ 1.2 km. I use the latter to simulate the atmospheric delay due to spatiotemporal variations of both water vapour and temperature, which is accordingly named as wet delay.

Weather models, such as the ERA-interim, also provide an estimation of water content. However, in comparison to MERIS data, models have shortcomings in several respects. First, MERIS data are simultaneously obtained with SAR images; thus, they share almost identical propagation paths. The ERA-interim model only

provides estimates of water vapour every six hours, which means an interpolation of two estimates encompassing the SAR acquisition is necessary. Alternatively, one can use only the closest estimation in time as an approximation. Secondly, the ERA-interim model samples every ~ 75 km. For a typical ASAR image with ~ 100 km range width, only several sample points are available to be interpolated for a simulated atmospheric delay due to water vapour. Obviously, the ERA-interim resolution is much lower than that of the MERIS data. Third, the theoretical accuracy of MERIS PWV retrieval could reach 1.7 mm (Bennartz & Fischer, 2001), corresponding to a 10.8 mm uncertainty in LOS direction (assuming a 23° incidence angle). Li et al. (2006) compared the PWV values between MERIS and GPS/Radiosonde measurements and found an agreement with root-mean-square (RMS) of ~ 1.1 mm, which corresponds to a LOS atmospheric delay of ~ 7.4 mm. The use of ERA-interim, however, has different levels of success in mitigating atmospheric noise, given the above-mentioned shortcomings (Jolivet et al., 2014).

MERIS receives radiation reflected by both Earth's surface and clouds. When clouds are present, the PWV estimated is thus applicable in the region above the clouds with highest altitude. To obtain the PWV between the land and the satellite, it is necessary for us to select MERIS data with low cloud cover. This requirement potentially limits the number of interferograms that can be corrected using the MERIS data. In Chapter 5, the PWV is converted to LOS wet delay using the equation:

$$\delta_{wet} = \frac{2 \times \Pi \times PWV}{\cos \theta_{inc}} \tag{2.1}$$

where θ_{inc} is the radar incidence angle, and Π is a conversion factor relating PWV to LOS wet delay. Π is dimensionless, with its value depending on the mean atmospheric temperature, but typically within a range of 6.0 – 6.5 (Bevis et al., 1992, 1994). I use a value of 6.2 in converting PWV to wet delay for the Tarapaca

earthquake, as Walters et al. (2013) used in the study of interseismic strain accumulation across the Ashkabad fault.

In addition to the wet component, tropospheric stratified delay also includes a hydrostatic delay that is caused by tropospheric pressure difference. An estimate of hydrostatic delay can be made as a function of ground pressure, which can be assumed as an exponential decrease with height above sea level:

$$\delta_{hyd} = \frac{2kP_0 e^{\frac{-h}{8.34}}}{\cos\theta_{inc}} \tag{2.2}$$

where *k* is the conversion factor between ground pressure and LOS hydrostatic delay, assumed to be 0.23 cm/hPa by Davis et al. (1985), P_0 is the sea level pressure and h is the altitude, which can be derived from the DEM. I use the sea level pressure provided by the ERA-Interim instead of the MERIS direct measurement, which has large error according to Ramon et al. (2003). An example of using MERIS data and ERA-interim model to correct Tarapaca postseismic interferogram is shown in Fig. 2.4.

Orbital error is modelled and removed as a linear ramp in all three studies. The linear approximation would not affect the deformation signals, because the latter are either cropped out before estimation of orbital error, or not linear in trend. In Chapter 3, I propose a joint inversion strategy for reducing atmospheric noise and orbital error, and this approach is also applied in Chapter 4.

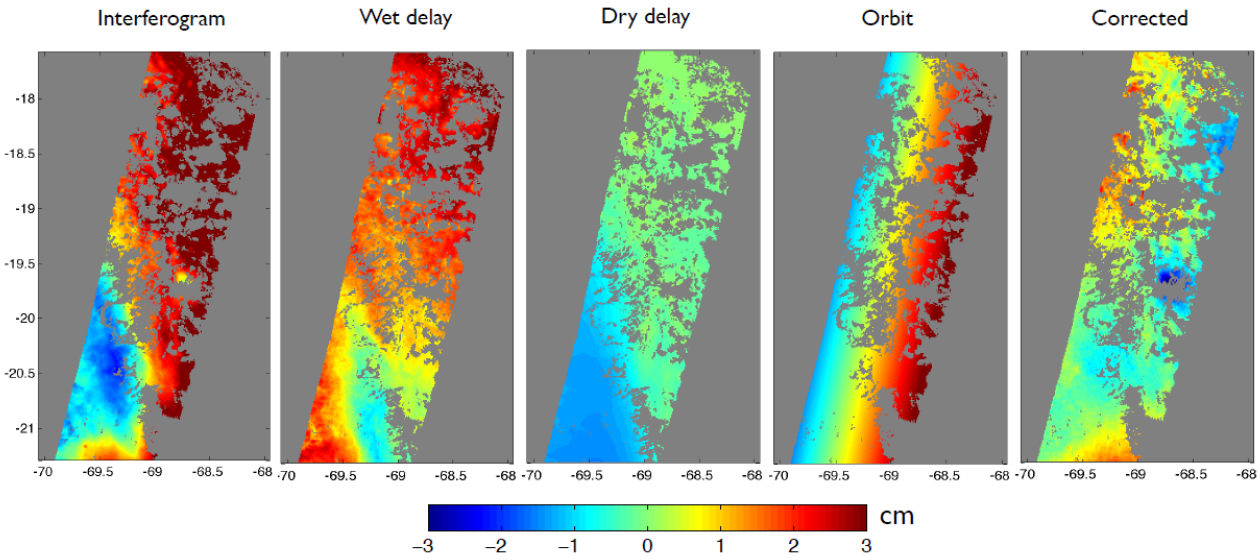

Figure 2. 4. An example demonstrating mitigation of atmospheric noise using MERIS data and the ERA-Interim weather model. Panels from left to right show an original interferogram from the postseismic study of the Tarapaca earthquake (050926-0811124), wet delay computed from MERIS data, dry delay from ERA-Interim weather model, estimated orbital error, and corrected interferogram.

2.3 Elastic and viscoelastic modelling

2.3.1 Elastic modelling

Elastic dislocation theory allows modelling deformation of an elastic medium due to slip across a dislocation. The theory is described in its simplest form by Hooke's law, which related stress and strain linearly in an elastic medium. Steketee (1958) showed the formula that derives a displacement field $u_i(x_1, x_2, x_3)$ from a dislocation $\Delta u_j(\xi_1, \xi_2, \xi_3)$ across a plane, Σ, in an isotropic medium. The formula is given as

$$u_i = \frac{1}{F} \iint_{\Sigma} \Delta u_j \left[\lambda \delta_{jk} \frac{\partial u_i^n}{\partial \xi_n} + \mu \left(\frac{\partial u_i^j}{\partial \xi_k} + \frac{\partial u_i^k}{\partial \xi_j} \right) \right] v_k \, d\Sigma \qquad (2.3)$$

where λ and μ are Lamé's elastic constants, δ_{jk} is the Kronecker delta, and v_k is the direction cosine of the normal to the surface element $d\Sigma$. u_i^j denotes the ith

component of displacement at location (x_1, x_2, x_3) due to a point force of magnitude *F* in the *j*th direction at (ξ_1, ξ_2, ξ_3).

Okada (1985) gave an analytic solution for the surface displacement due to both shear and tensile dislocation on a finite rectangular fault embedded in a uniform, isotropic elastic half-space. Equivalent analytical expressions for internal displacement are further given in Okada (1992). Current studies of earthquake source parameters from geodetically-observed displacements are largely based on the analytical form of the elastic dislocation theory as developed by Okada. To forward model the surface displacement, a set of nine parameters is required as input, including strike, dip, rake, fault's upper and lower depth, center of fault's trace, fault length and slip. For complex fault systems, a collection of rectangular fault patches can be used to obtain a more detailed slip distribution model with variable slip (e.g. Copley et al., 2012; Elliott et al., 2012).

The Okada model, as described above, is applied for the computation of displacements from a dislocation in a homogeneous elastic medium. In reality, surface displacements are affected by the crustal layering effect. Wang et al. (2003) developed numerical codes called EDGRN/EDCMP to model deformation caused by an earthquake in a multi-layered crust. Technical details of the numerical realization can be found in Wang et al. (2003). Required input parameters such as density, P-wave velocity and S-wave velocity can be obtained from crustal models (e.g. CRUST2.0) or regional seismic studies, for example, as shown in Chapter 3.

Another code used in this thesis for surface deformation calculation is developed by Meade (2007) to accommodate rupture on curved fault planes, where fault geometries may vary substantially in both strike and dip. A regular rectangular parameterization may introduce geometric gaps and/or overlaps, leading to a biased displacement and stress calculation. Instead, faults constructed using triangular dislocation elements (TDEs) can overcome the problem of geometrical complexity. Explicit algorithms to

analytically calculate the displacement associated with slip on a TDE are given in Meade (2007). Here, I test the surface displacement for triangular representation of a planar fault against a rectangular one.

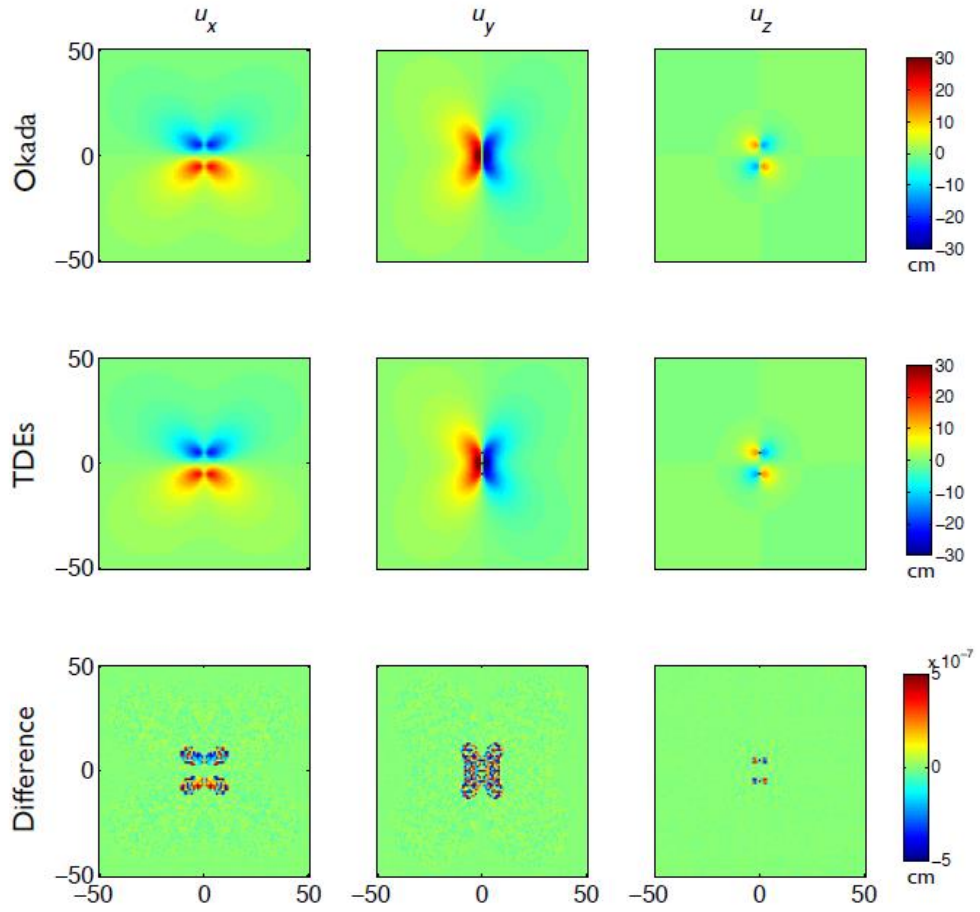

Figure 2. 5. Comparison of Okada outputs against analytic solution with TDEs. Top panels show surface displacements in three directions adopting the Okada model, middle panels are outputs from TDEs, and bottom panels show difference between outputs. X and Y axes are in units of km.

In this test, I set up a right-lateral strike-slip fault that extends from a depth of 1 km to 11 km, with a length of 10 km. The fault is aligned with the y-axis. Uniform slip of 2 m is assigned for both rectangular and triangular dislocations. In the triangular dislocation case, the rectangular fault is discretized into three triangles. Surface displacements in three directions are computed for both cases (Fig. 2.5). Values of u_y computed along a profile perpendicular to the fault and passing through its centre are also shown (Fig. 2.6). The difference between the displacement output from the

Okada model and the TDEs is negligible, being up to 7 orders of magnitude smaller than the maximum displacement.

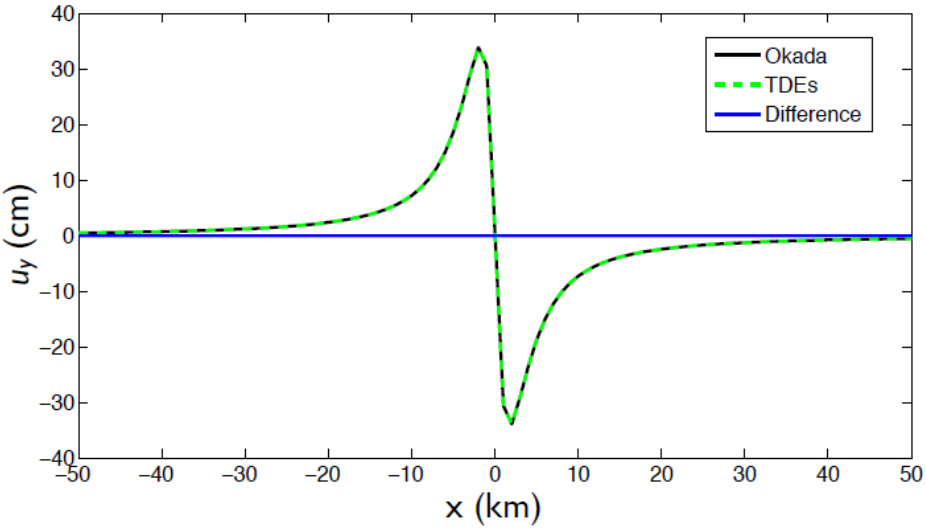

Figure 2. 6. Comparison of surface displacements u_y from the Okada model and TDEs along a profile perpendicular to the fault and passing through its centre.

2.3.1.1 Inversion for earthquake source parameters

Two steps are usually implemented to invert for a slip distribution model from coseismic geodetic observations. First, a non-linear inversion is applied to obtain a set of fault parameters that best fit the data. At this stage, slip is assumed to be uniform across a single rectangular fault. Other parameters such as fault geometry, location and slip sense are non-linearly related with the surface displacement. To solve such a non-linear problem, I adopt a Monte Carlo method incorporating a simulated annealing algorithm and downhill simplex method, as widely used in other studies (e.g. Wright et al., 1999; Funning et al., 2005). In this method, the Okada model is commonly employed to forward-model surface displacements for randomly-generated sets of parameters. The modelled displacement is then passed to an objective function that compares the modelling results with data. The set of parameters that gives a minimum misfit is taken as one solution of many. The best (or optimal) solution and error bounds are obtained based on multiple tests (usually at

least 100 re-runs with different Monte Carlo starts), with noise perturbations to a geodetic dataset. Then, a linear inversion can be applied to obtain a slip distribution model. The rectangular fault with fixed fault geometry can be subdivided into multiple patches. According to data quality and modelling needs, fault subdivision can be implemented with uniform size (e.g. Funning et al., 2005; Ryder et al., 2010), or with depth-dependent variation (e.g. Fialko, 2004b). A checkerboard test is usually required to test the sensitivity of patch size to the data. For this second stage, the Okada model is used for calculation of a Green's function matrix, which describes surface displacement at each observation point caused by unit slip on each fault patch. Slip distribution is finally derived by solving a linear least-squares equation.

The Earth model considered in the above modelling procedures is an isotropic, homogeneous elastic half-space. No crustal layering effect is considered. I improved the inversion codes by integrating the layered codes EDGRN/EDCMP into both stages. In the nonlinear inversion part, randomly-generated source parameters are automatically passed to EDGRN/EDCMP, which will forward model surface displacement for comparison with the data. In the linear inversion for slip distribution, a Green's function is automatically generated using EDGRN/EDCMP. The improved inversion strategy for earthquake source parameters is applied to the study of Damxung earthquake in Chapter 3 for retrieval of source parameters and slip distribution.

2.3.2 Viscoelastic modelling

As introduced in Chapter 1, viscoelastic relaxation is one of the major mechanisms that explain time dependent postseismic deformation. Various combinations of spring and dashpot are proposed as mechanical analogues of different rheologies. In this thesis, viscoelastic material is represented by a spring in series with a dashpot, namely, the Maxwell rheology. This is the simplest of several linear viscoelastic

rheologies. The temporal characteristic of decaying deformation is controlled by the viscosity, η, of the viscous material. The constitutive relationship between strain and stress can be written in the form:

$$\dot{\varepsilon} = \frac{1}{\eta}\sigma + \frac{1}{\mu}\dot{\sigma} \tag{2.4}$$

where η and μ are the viscosity and rigidity of the dashpot and spring respectively, and σ and ε are stress and strain respectively.

For the case of postseismic viscoelastic relaxation, in which a condition of constant strain in time and an initial stress σ_0 is applied, the stress evolves as:

$$\sigma = \sigma_0 e^{\frac{-\mu t}{\eta}} \tag{2.5}$$

Here, the stress decays exponentially with a Maxwell time $\tau = \eta/\mu$. At time t, the permanent postseismic deformation is thus expressed as:

$$\varepsilon_{\mathbf{pos}}(t) = \varepsilon_0(1 - e^{\frac{-\mu t}{\eta}}) \tag{2.6}$$

The exponential form is often employed to approximate the geodetic time-series of postseismic deformation (Savage et al., 2005).

Two codes are used in this thesis to model time-dependent postseismic viscoelastic deformation. PSGRN/PSCMP developed by Wang et al. (2006) treats the Earth as a multi-layered viscoelastic-gravitational half-space. The rheological structure and properties are defined by the user. Rheology incorporated includes the Standard Linear Solid and Maxwell rheologies. Technical details of using the correspondence principle in transferring elastic solutions to viscoelastic ones are described in Wang et al. (2006). In contrast to PSGRN/PSCMP, RELAX can model lateral rheological

heterogeneities, which is of essential importance in controlling viscous flow patterns in subduction zones.

To test and compare the two codes, postseismic displacements from strike slip and normal faulting are considered. In the model, the Earth consists of an elastic lid of thickness 20 km overlying a Maxwell viscoelastic half-space. A boundary condition of zero displacement at an infinite distance is assigned. For the strike-slip faulting case, uniform left-lateral slip of 2 m is designated. For the normal faulting test, uniform slip of 2 m is assigned on a fault plane dipping at 60° to the west. I use the same fault length (15 km) and width (20 km), and thus the same moment magnitude of 6.7 for both cases. Here, fault width means the downdip extension of the fault, measured from the upper trace of the fault to its bottom.

Output surface displacements for comparisons from the two codes are taken at one Maxwell time. One Maxwell time is chosen because the two VER studies in this thesis concern only short-term postseismic deformation. How the differences between outputs from the two codes change with longer time, say over multiple Maxwell times, is not specifically investigated here. For the normal faulting case (Fig. 2.7), although the spatial patterns of the outputs from different codes are consistent, it is obvious that the vertical component shows a large discrepancy across the fault's surface projection. For the east component of displacements, the output from PSGRN/PSCMP is larger in magnitude than that from RELAX on the hanging wall side, but smaller on the footwall side (Fig. 2.8a). The discrepancy tends to decrease closer to the fault. The maximum vertical displacement from PSGRN/PSCMP is about 20 per cent larger than that of the RELAX, and the discrepancy dies out away from the fault (Fig. 2.8b).

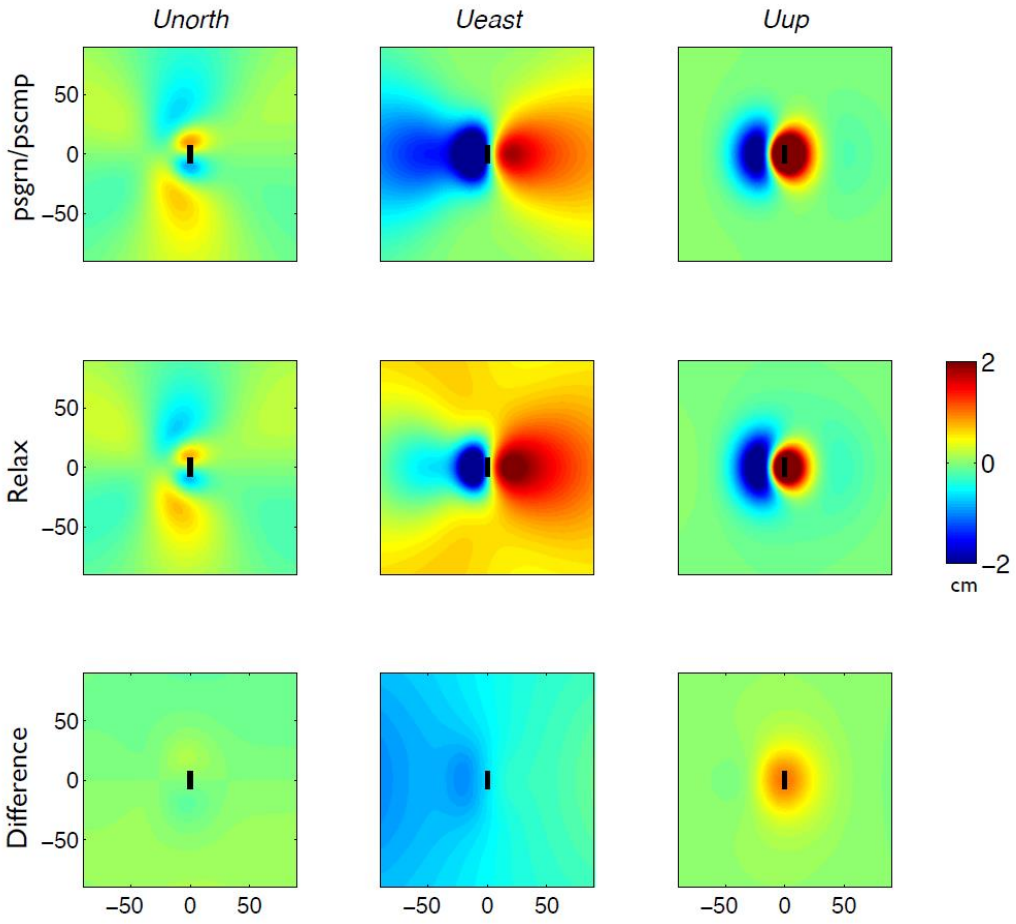

Figure 2. 7. Comparison of outputs from PSGRN/PSCMP and RELAX at one Maxwell time after a M_w 6.7 normal faulting earthquake. Top panels show surface displacements in three directions calculated by PSGRN/PSCMP, middle panels are outputs from RELAX, and bottom panels show difference between above outputs. Note that the dimension setup in RELAX is 256 km, 256 km, and 256 km in the northern, eastern and vertical directions, respectively. X and Y axes are in units of km.

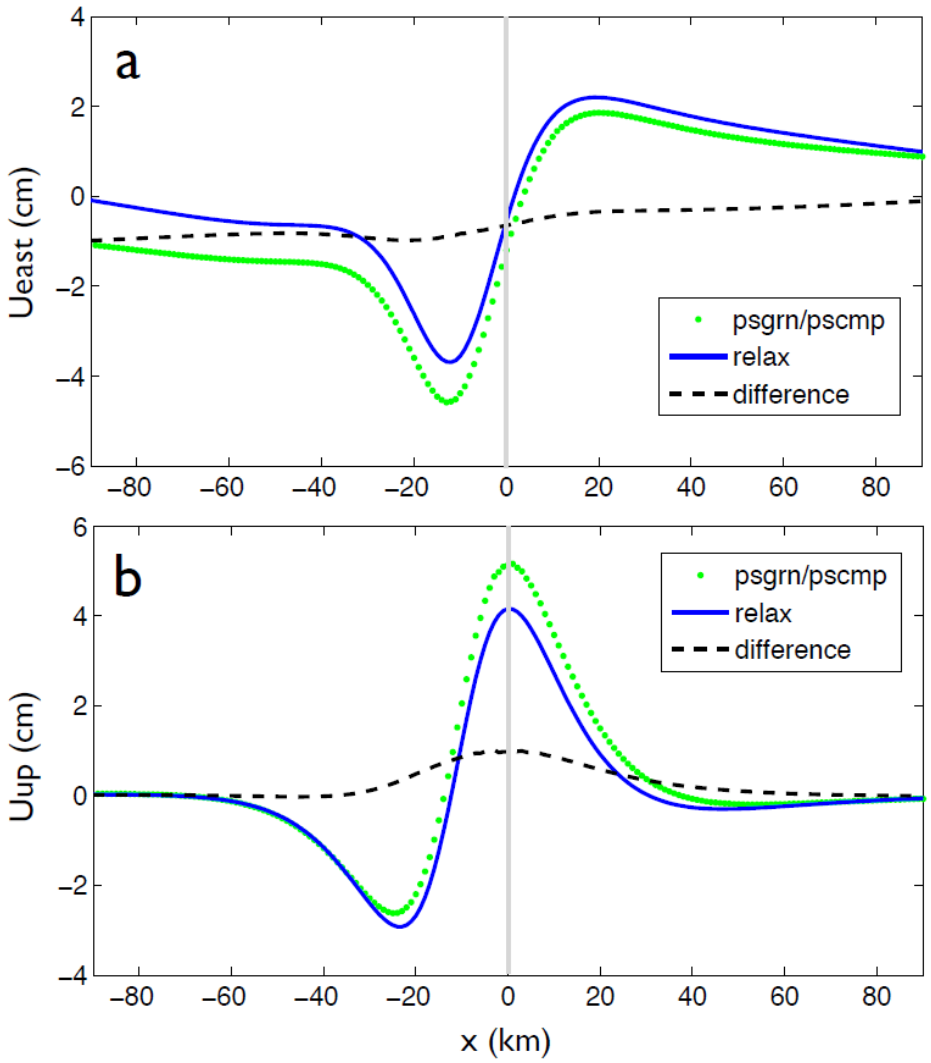

Figure 2. 8. Comparison of surface displacements in east (a) and vertical (b) directions along a profile perpendicular to the fault and passing through its centre. Grey line marks the fault surface trace. This figure corresponds to Fig. 2.7.

The discrepancy between the outputs from two codes could be due to the pre-defined calculation space. For PSGRN/PSCMP, the dimension is treated as an infinite half-space. In RELAX, a calculation space has to be set. Initially I fixed the east, north and vertical components all at 256 km. It is noted by the developer of RELAX that to ensure an accurate calculation, the extent of the model should be at least 10 times greater than the source dimension. Despite the fact that the input vertical dimension satisfies the requirement, the discrepancy with PSGRN/PSCMP still exists. I also test a model with horizontal dimensions extended to 512 km. It is clear that the horizontal discrepancy reduces accordingly (Fig. 2.9). Although an increase in the calculation

dimension can reduce the discrepancy significantly in the east component, it takes more computation time and the vertical component does not change too much (Fig. 2.10). Further increase of the vertical dimension to 512 km produces a nearly identical displacement to that from PSGRN/PSCMP (Fig. 2.11), and the relatively large discrepancies for the east and vertical components appear at ~ 20 km away the fault trace on the hanging wall side (Fig. 2.12).

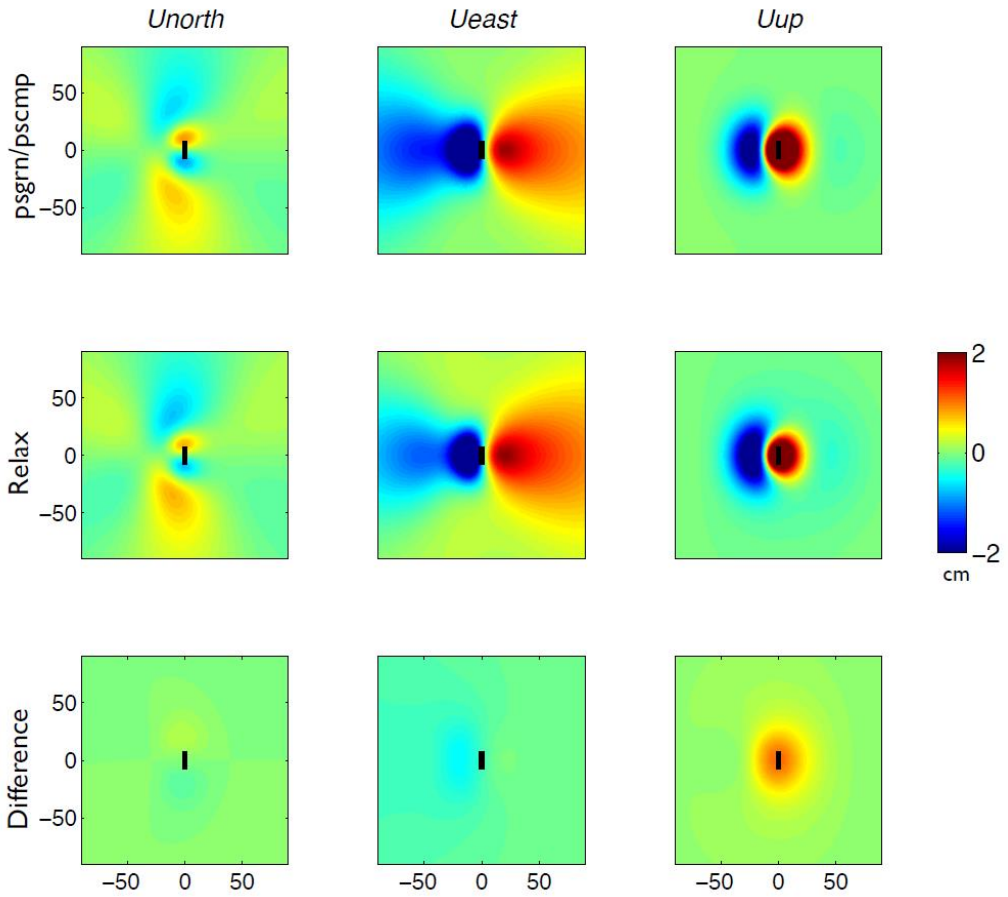

Figure 2. 9. Same as Fig. 2.7, but with horizontal dimensions increased to 512 km in the RELAX calculation. X and Y axes are in units of km.

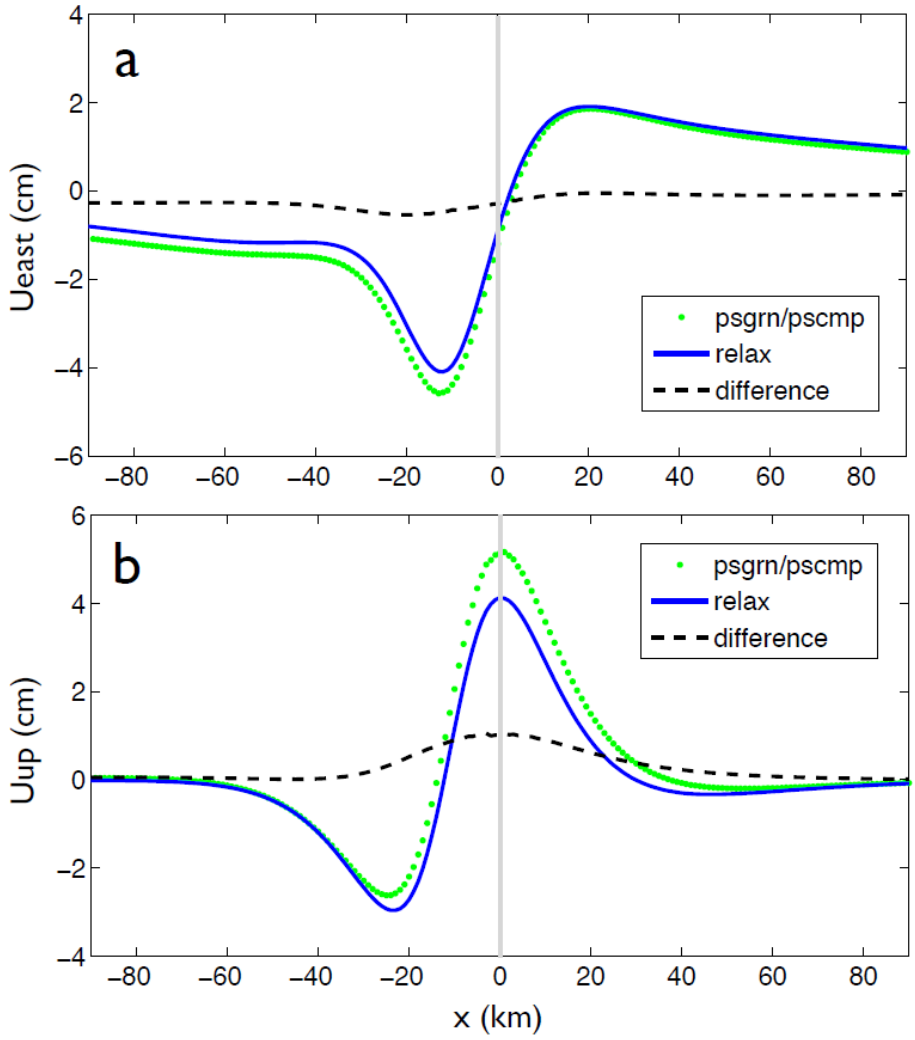

Figure 2. 10. Same as Fig. 2.8, but corresponds to surface displacements shown in Fig. 2.9.

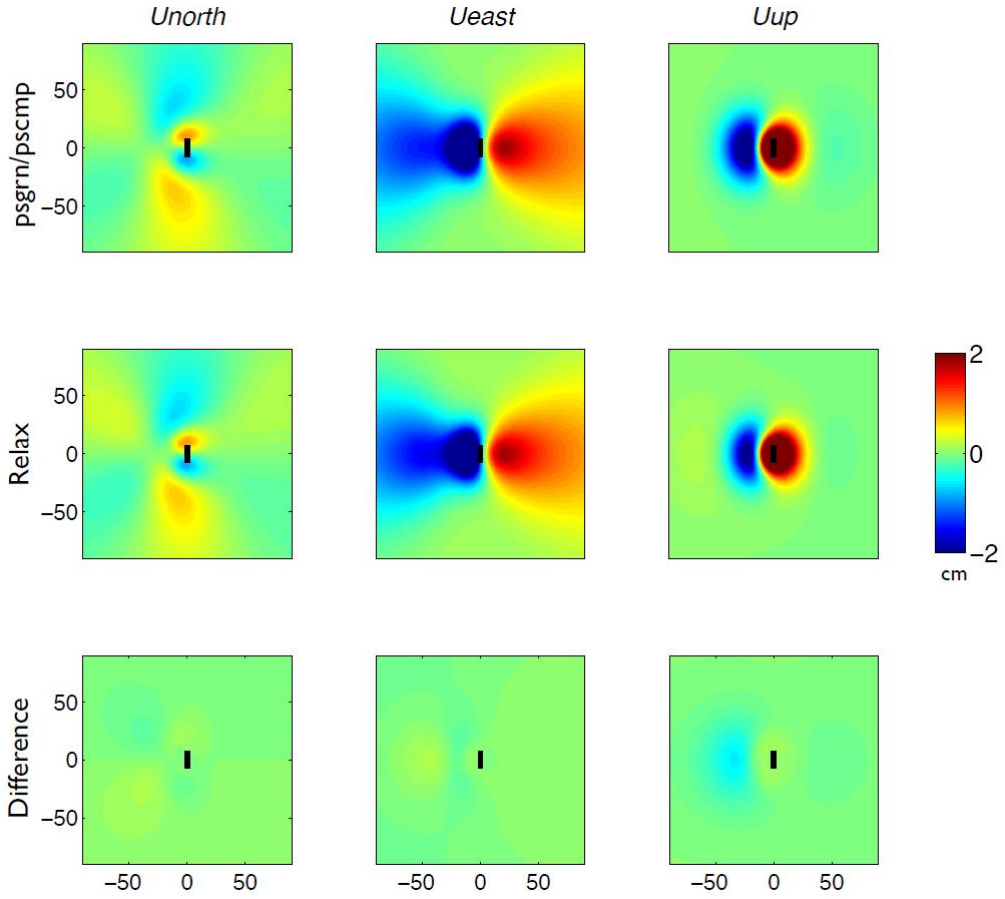

Figure 2. 11. Same as Fig. 2.7, but with all three dimensions increased to 512 km in the RELAX calculation. X and Y axes are in units of km.

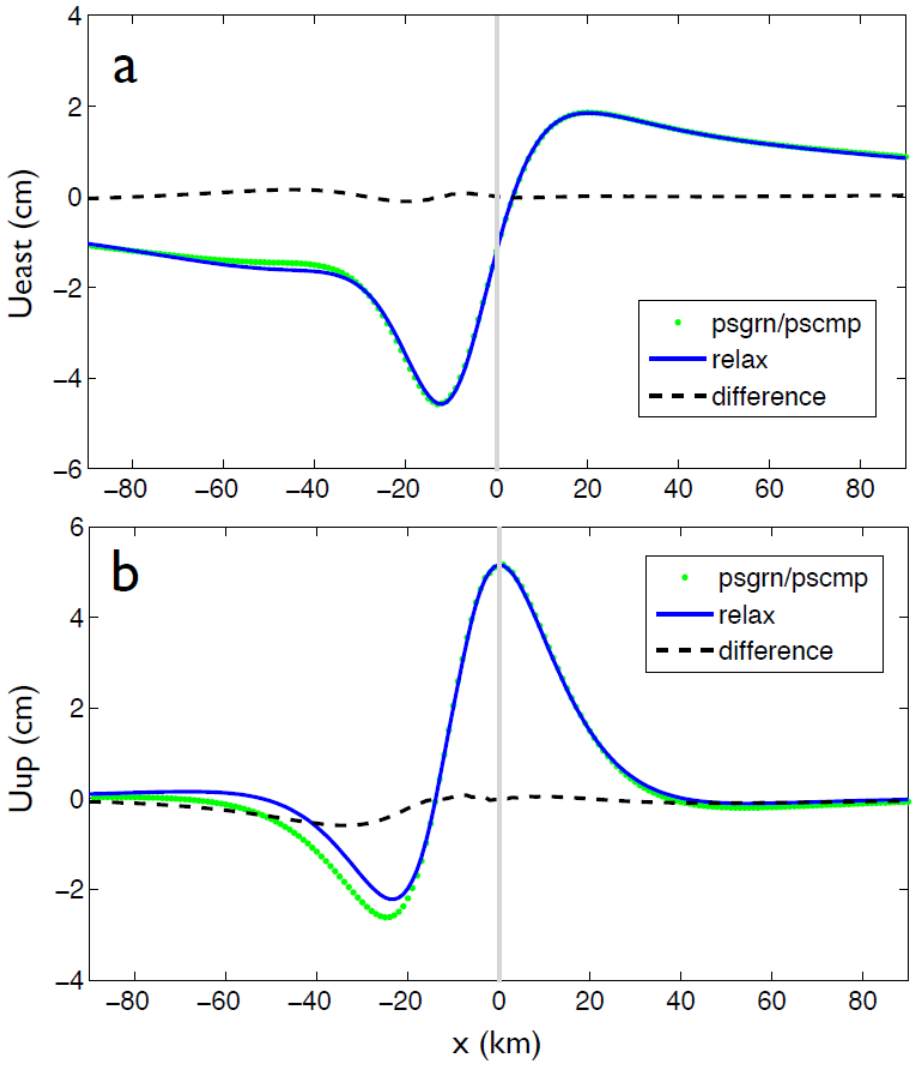

Figure 2. 12. Same as Fig. 2.8, but corresponds to surface displacements shown in Fig. 2.11.

For the strike-slip faulting test, the discrepancies between the two codes are much smaller than in the dip-slip case. The most pronounced discrepancy between the outputs of the two codes appears in the vertical component (Fig. 2.13). Generally in the near field (within 50 km) of the fault trace, PSGRN/PSCMP produces a vertical displacement larger in magnitude than RELAX. For the north component, the difference is about 6 per cent of the maximum displacement (Fig. 2.14). Extending the domain in the horizontal direction twice only slightly improves the output in the far-field, and has little effect in the near-field (Fig. 2.15-16).

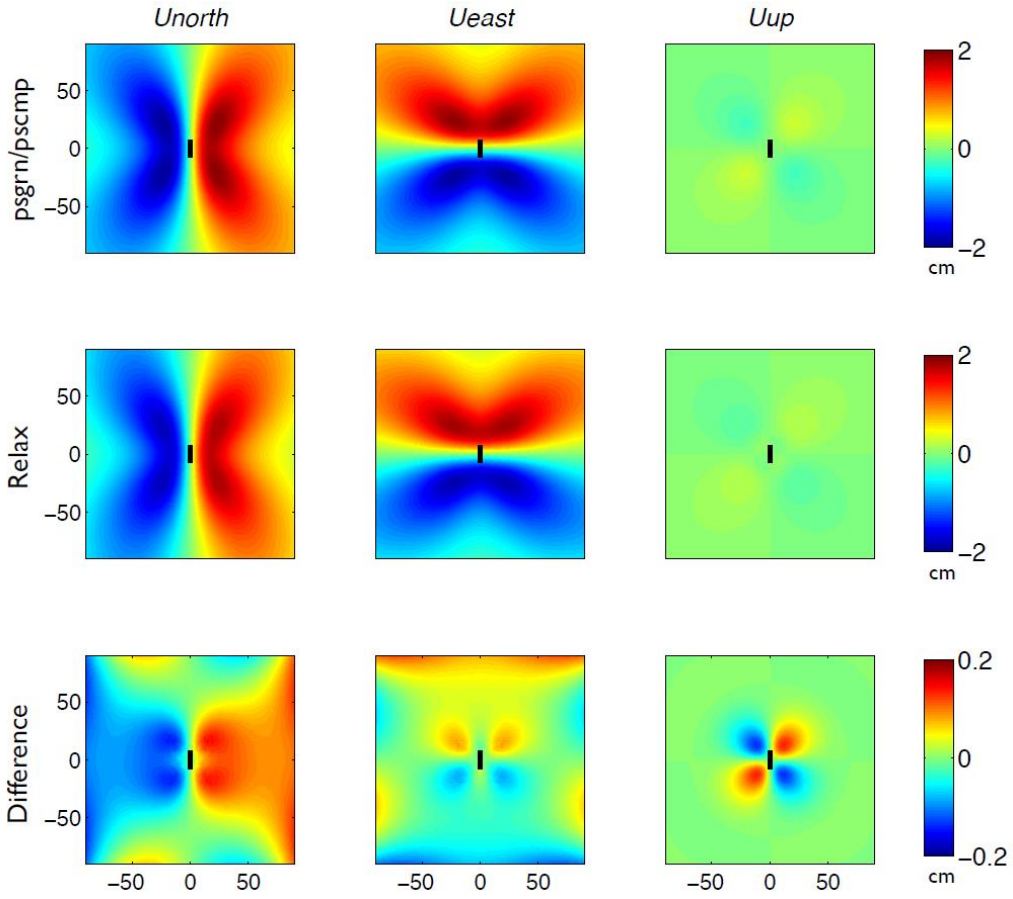

Figure 2. 13. Similar to Fig. 2.7 but for a M_w 6.7 strike-slip faulting earthquake. The dimension setup in RELAX is 256 km for three directions. X and Y axes are in units of km.

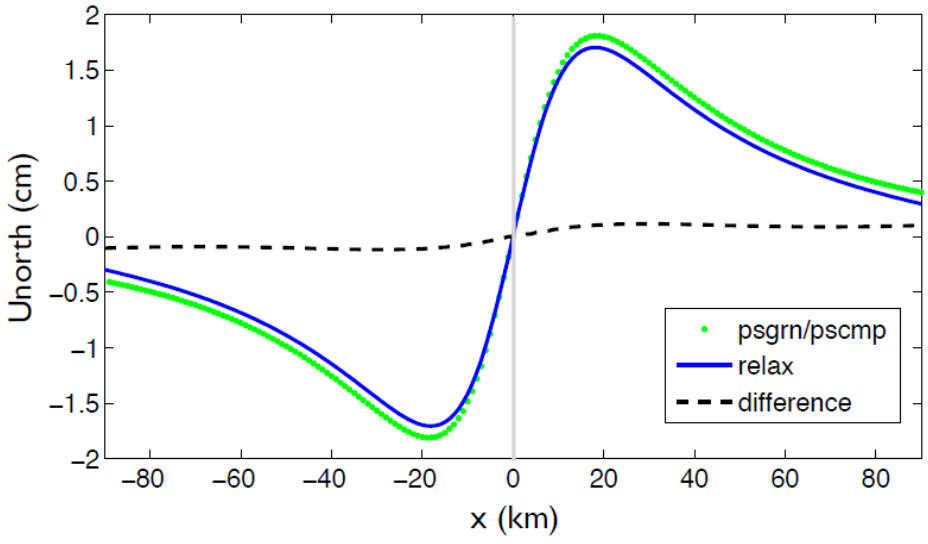

Figure 2. 14. Comparison of surface displacements in northern direction along a profile perpendicular to the fault and passing through its centre. Grey line marks the fault surface trace. This figure corresponds to Fig. 2.13.

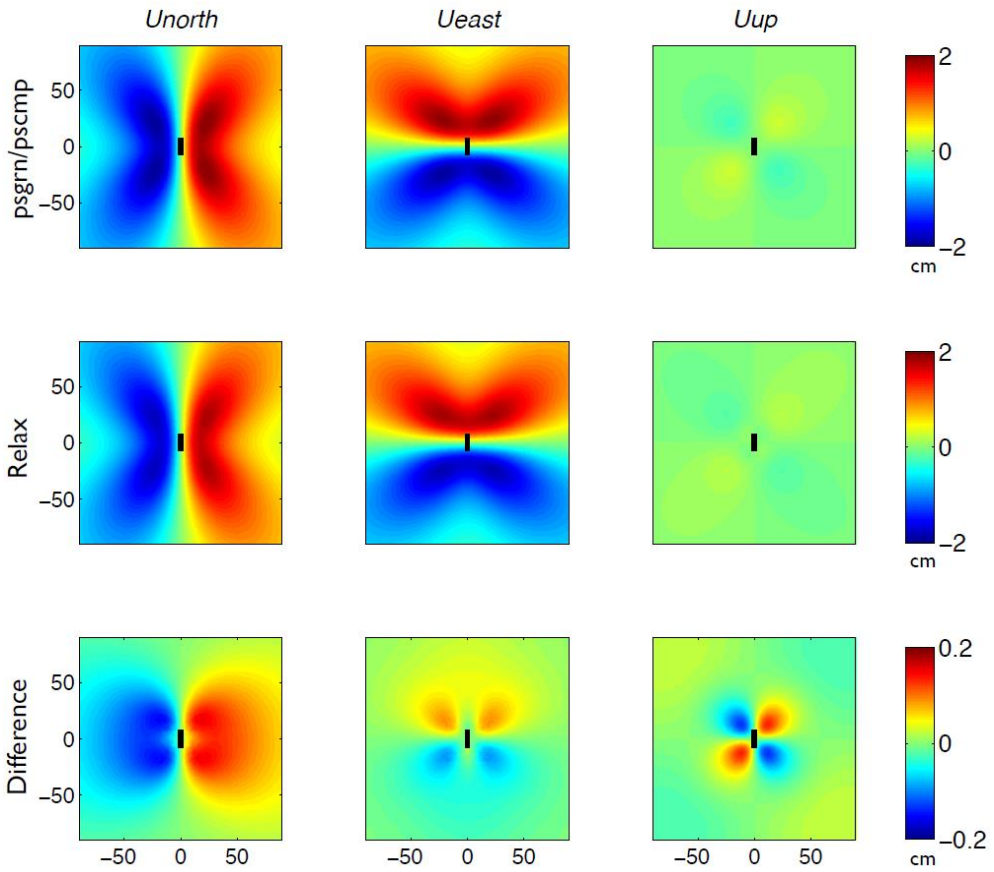

Figure 2. 15. Same as Fig. 2.13, but with horizontal dimensions increased to 512 km in the RELAX calculation. X and Y axes are in units of km.

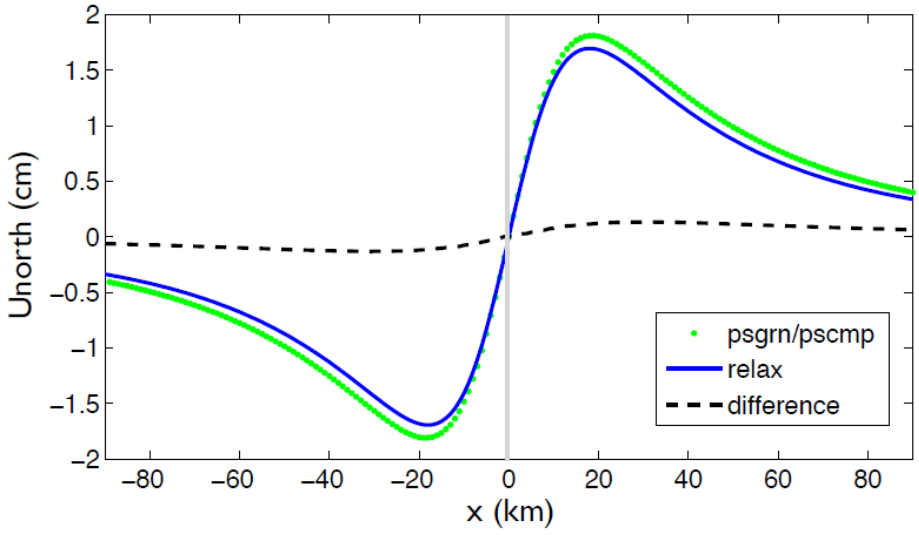

Figure 2. 16. Same as Fig. 2.14, but corresponds to surface displacements shown in Fig. 2.15.

It is noted that RELAX is a software in development. Most of the experiments and computation for the Tarapaca study were carried out when version 1.0.4 was available. The stress calculation in Chapter 5 is implemented using the newest version 1.0.7, since the stress output is ambiguous in the old version. A test of static displacement output from different versions of RELAX is shown in Fig. 2.17-20, which demonstrates a minor discrepancy for both strike-slip and normal faulting cases. For future research, it would be interesting to build a 3D finite element model for the case study in Chapter 5, and to assess its difference with outputs from RELAX.

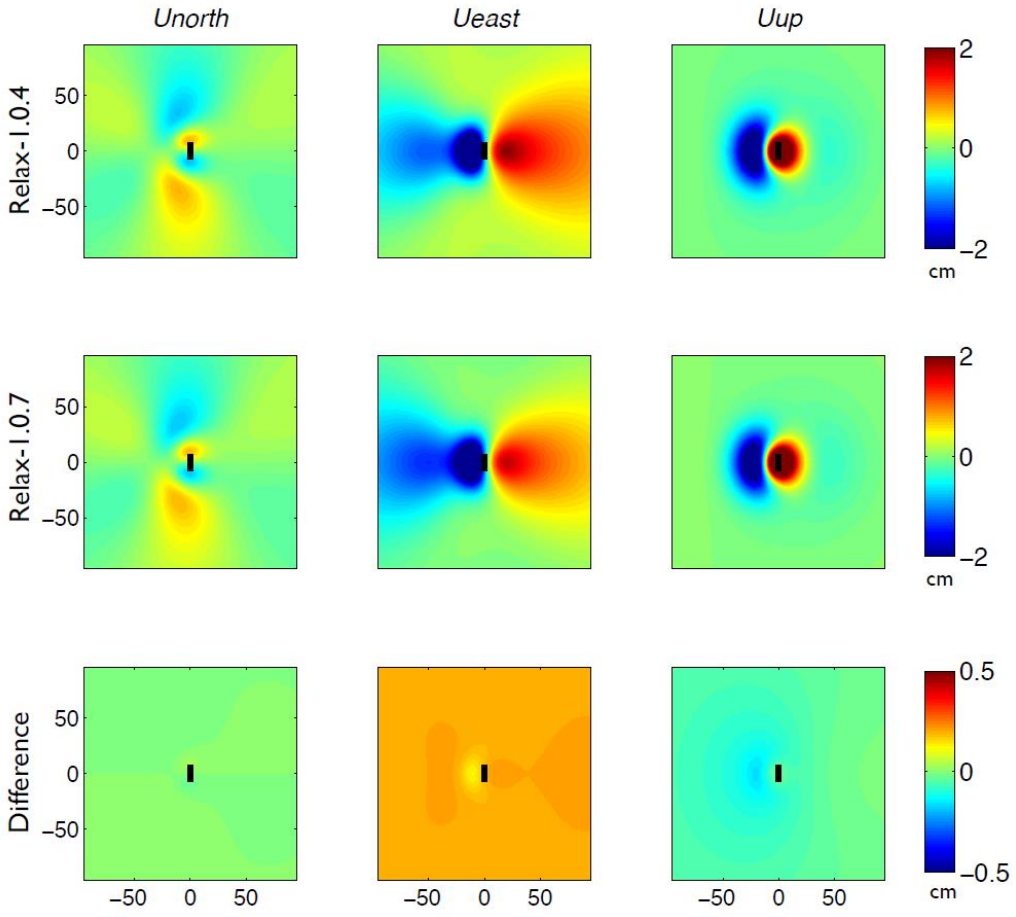

Figure 2. 17. Comparison of outputs from different versions of RELAX at one Maxwell time after a M_w 6.7 normal faulting earthquake. Top panels show displacements in three directions calculated by version 1.0.4, middle panels are outputs from the version 1.0.7, and bottom panels show difference between above outputs. Note that the dimension setup in RELAX is 512 km, 512 km, and 256 km in northern, eastern and vertical directions, respectively. X and Y axes are in units of km.

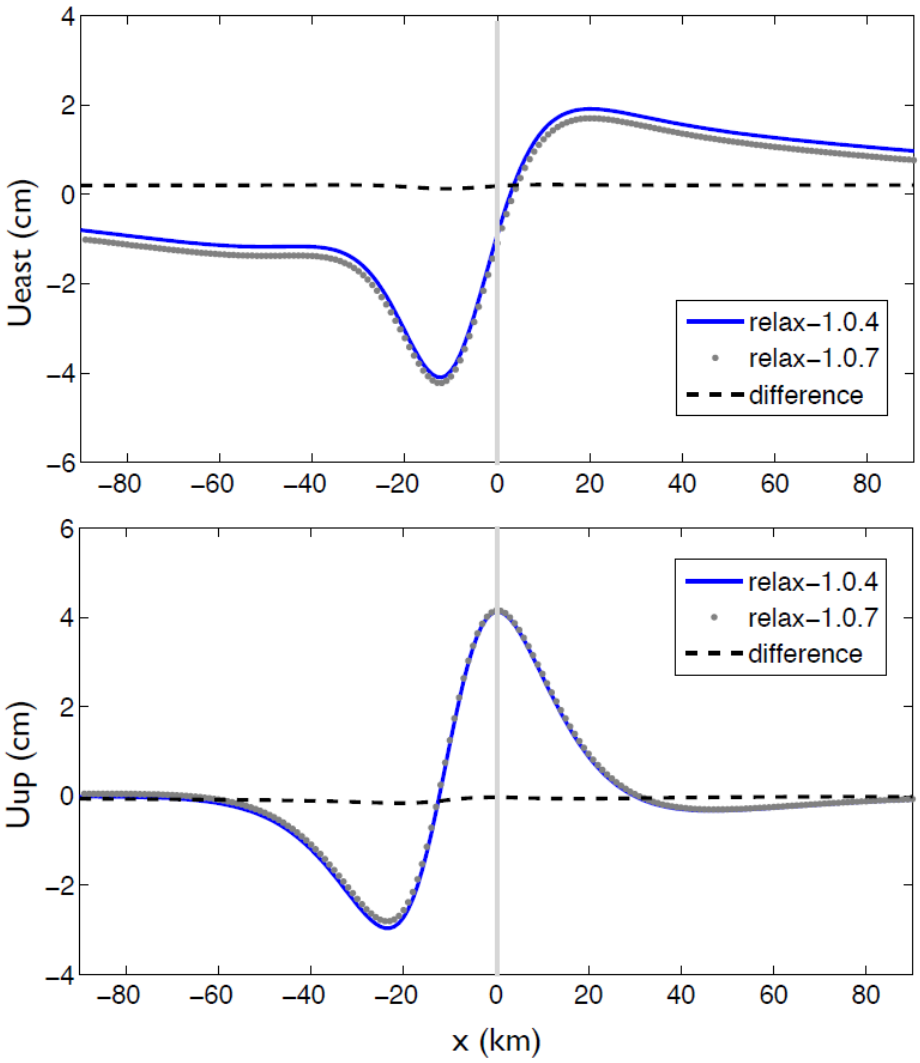

Figure 2. 18. Comparison of surface displacement outputs from different versions of RELAX in east (a) and vertical (b) directions along a profile perpendicular to the fault and passing through its centre. Grey line marks the fault surface trace. This figure corresponds to Fig. 2.17.

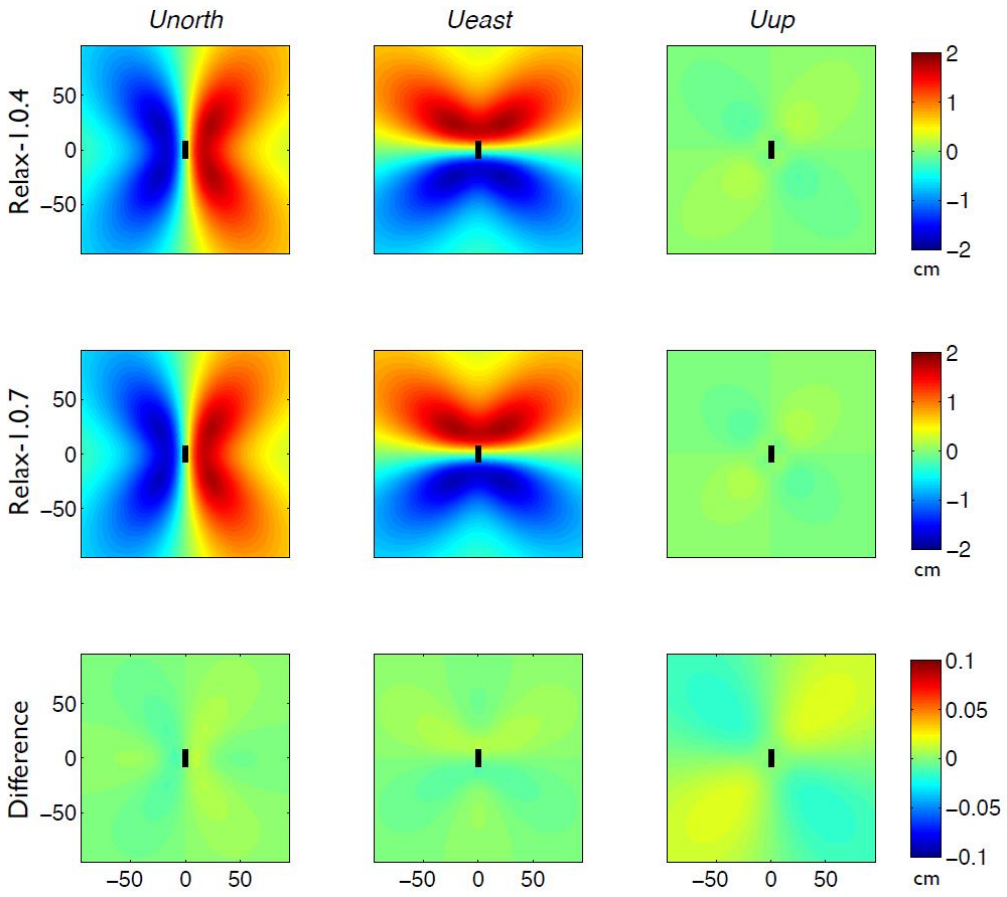

Figure 2. 19. Similar to Fig. 2.17 but for a M_w 6.7 strike-slip faulting earthquake. The dimension setup in RELAX is 512 km, 512 km, and 256 km in northern, eastern and vertical directions, respectively. X and Y axes are in units of km.

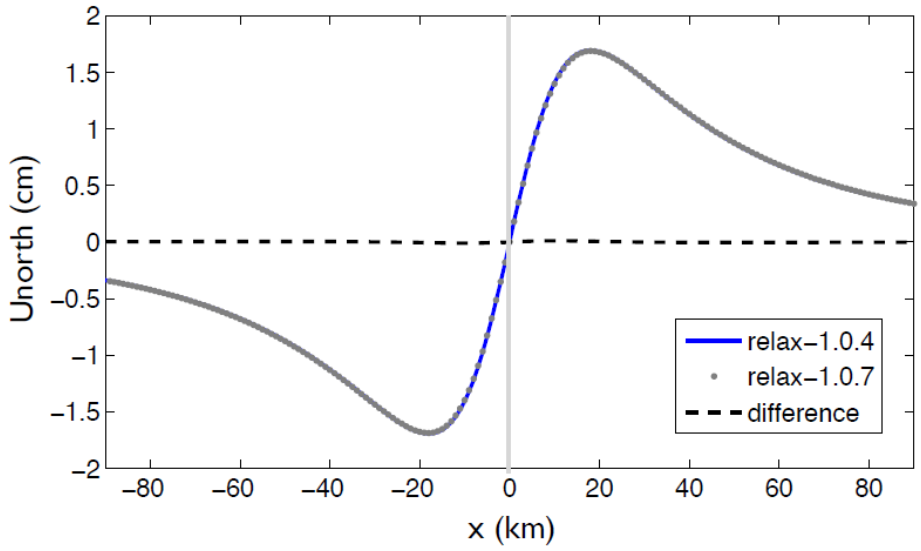

Figure 2. 20. Comparison of surface displacements in northern direction along a profile perpendicular to the fault and passing through its centre. Grey line marks the fault surface trace. This figure corresponds to Fig. 2.19.

Chapter 3

Coseismic and postseismic activity associated with the 2008 M_w 6.3 Damxung earthquake, Tibet, constrained by InSAR

Lidong Bie,[1] Isabelle Ryder,[1*] Stuart E. J. Nippress[2] and Roland Bürgmann[3]

[1]*School of Environmental Sciences, University of Liverpool, UK. E-mail i.ryder@liv.ac.uk*

[2]*AWE Blacknest, Reading, UK*

[3]*Berkeley Seismological Laboratory, University of California, Berkeley, CA, USA*

Geophysical Journal International, 2014, 196(2), 788-803, doi: 10.1093/gji/ggt444

Summary

The 2008 M_w 6.3 Damxung earthquake on the Tibetan Plateau is investigated to (i) derive a coseismic slip model in a layered elastic Earth; (ii) reveal the relationship between coseismic slip, afterslip and aftershocks; and (iii) place a lower bound on mid/lower crustal viscosity. The fault parameters and coseismic slip model were derived by inversion of Envisat InSAR data. We developed an improved nonlinear inversion scheme to find an optimal rupture geometry and slip distribution on a fault in a layered elastic crust. Although the InSAR data for this event cannot distinguish between homogeneous and layered crustal models, the maximum slip of the latter model is smaller and deeper, while the moment release calculated from both models are similar. A ~ 1.6 year postseismic deformation time-series starting 20 days after the mainshock reveals localised deformation at the southern part of the fault. Inversions for afterslip indicate three localised slip patches, and the cumulative afterslip moment after 615 days is at least ~ 11 per cent of the coseismic moment. The afterslip patches are distributed at different depths along the fault, showing no

obvious systematic depth-dependence. The deeper of the three patches, however, shows a slight tendency to migrate to greater depth over time. No linear correlation is found for the temporal evolution of afterslip and aftershocks. Finally, modelling of viscoelastic relaxation in a Maxwell half-space yields a lower bound of 1×10^{18} Pa s on the viscosity of the mid/lower crust. This is consistent with viscosity estimates in other studies of postseismic deformation across the Tibetan Plateau.

Keywords: Radar interferometry; Earthquake source observations; Seismic cycle; Time-series analysis; Rheology: Crust and lithosphere; Asia

3.1 Introduction

On 6 October, 2008, a M_w 6.3 earthquake occurred in the Damxung area of Tibet in western China. This event locates in the central part of the Yadong-Gulu rift system (Fig. 3.1), which extends about 500 km from Yadong in the Himalayan area up to the Gulu basin in central Tibet (Armijo et al., 1986). The NNE-trending, east-dipping boundary normal fault at the western side of the rift was suggested by Wu et al. (2011) as the source fault, according to analysis of isoseismal contours and aftershock distribution. However, detailed studies with various InSAR data (Elliott et al., 2010; Sun et al., 2011; Liu et al., 2012) lead to a different view that the fault causing the earthquake is a west-dipping secondary fault on the other side of the graben.

The Yadong-Gulu rift has long been characterized by moderate to large earthquakes. Last century, the 1952 M 7.5 earthquake struck the northern part of this rift at the Gulu Basin, and the 1992 M_w 6.2 earthquake hit Nyemu County immediately to the SW of the 2008 event. The 1411 A.D. M 8.0 earthquake is the largest one ever documented along this rift (Liu et al., 2012). Determination of accurate source

parameters for the 2008 Damxung event is important for understanding local seismic risk and tectonic activity.

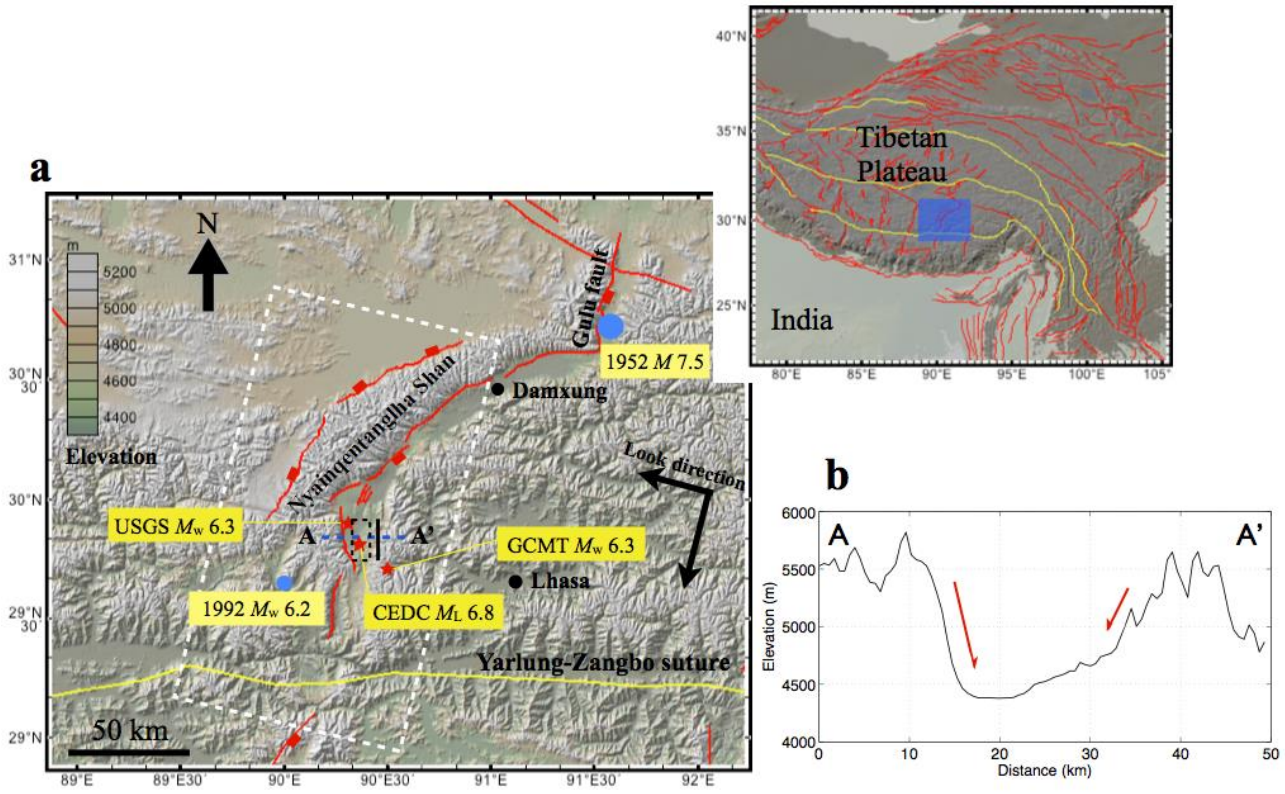

Figure 3. 1. (a) Earthquake location (red stars, marked by catalogue name and magnitude) and shaded relief topography for the Damxung area. SRTM DEM (Farr et al., 2007) at 90 m resolution is shown. Red lines mark fault traces compiled by Styron et al. (2010). The Yarlung-Zangbo suture zone is delineated by thick yellow line. Black line marks the mainshock fault surface trace and dashed black rectangle is surface-projected dislocation determined by InSAR in this study. Envisat track 176 is marked by white dashed box. Two blue circles show the locations of the 1952 *M* 7.5 and 1992 M_w 6.2 earthquakes, and magnitude is scaled to dot size. Inset shows the regional setting of the study area (blue box). (b) Topographic profile across the rift, along blue line A-A′ in (a).

Detailed analysis and modelling of seismic data from project INDEPTH II (International Deep Profiling of Tibet and the Himalaya), which extends from the Tethyan Himalaya, across the Yarlu-Zangbo suture, to the centre of the Lhasa terrane, reveals that the upper crust in this region consists of layers with different velocities and that a low-velocity mid- to lower crust exists beneath ~ 15 km (e.g. Nelson et al., 1996; Yuan et al., 1997; Kola-Ojo & Meissner, 2001; Klemperer, 2006). Klemperer (2006) also summarized the magnetotelluric (MT) studies across

the plateau and interpreted the high electrical conductivity as induced by partial melt and/or saline aqueous fluids. Rippe & Unsworth (2010) related the high conductivity of mid- to lower crust to effective viscosities of $2.5 \times 10^{18} – 3.0 \times 10^{20}$ Pa s for the southern part of the Lhasa block. It would be of interest to obtain a constraint on the mid/lower crustal viscosity at this region from modelling of the InSAR observed postseismic deformation.

A number of thrust and strike-slip events around the globe have been examined geodetically to investigate (i) the mechanism responsible for observed postseismic deformation; (ii) the relationship between afterslip and aftershocks; (iii) the rheology of the crust and/or upper mantle (e.g. Peltzer et al., 1996; Deng et al., 1998; Bürgmann et al., 2002; Pollitz, 2005; Hsu et al., 2006; Johanson et al., 2006; Ryder et al., 2007). However, only a small number of studies have focused on normal-faulting events (e.g. Nishimura & Thatcher, 2003; Gourmelen & Amelung, 2005; Riva et al., 2007; Ryder et al., 2010; D'Agostino et al., 2012; Copley et al., 2012). Previous published studies of the 2008 Damxung earthquake have examined the coseismic slip distribution (e.g. Elliott et al., 2010; Liu et al., 2012; Sun et al., 2011). The 2008 event also offers an opportunity to study the spatio-temporal evolution of afterslip, to test whether afterslip is temporally correlated with aftershocks, and to constrain the lower bound of mid/lower crustal viscosity for this part of the rift.

In this paper, we present a new inversion for coseismic slip distribution from three interferograms spanning the earthquake, exploring faults buried in both a homogeneous and a layered crust. A postseismic deformation time-series (October 2008 – June 2010) covering 12 SAR acquisitions is constructed using 17 interferograms (Table S3.1), and inverted for transient afterslip on the fault ruptured by the earthquake at each epoch. Then the temporal evolution of afterslip is compared with that of aftershocks. Finally, a lower bound on viscosity of the mid/lower crust of southern Tibet is estimated by comparing observed InSAR displacements with those computed assuming a model of viscoelastic relaxation of coseismic stress changes.

3.2 Data

3.2.1 Interferograms

SAR images used in this study are from the ESA's Envisat satellite, which operates at C-band, with wavelength ~ 5.6 cm. Scenes for both coseismic and postseismic analysis are from descending track 176. The SRTM (Shuttle Radar Topography Mission, Farr et al., 2007) DEM with 90 m resolution is used to remove the phase component contributed by the topography.

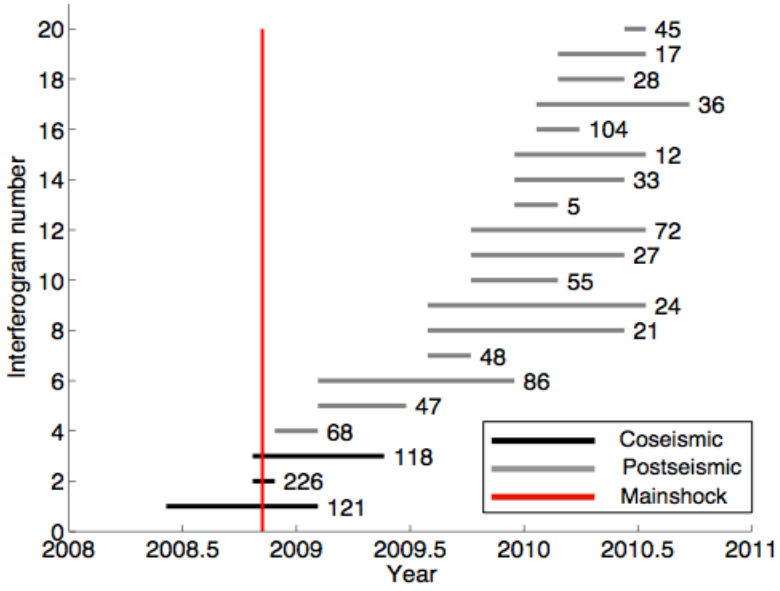

Figure 3. 2. Time intervals covered by the co- and post-seismic interferograms, with perpendicular baseline in metres marked at the end of each line. The red bar denotes the time of the mainshock.

All interferograms are produced from SAR scenes with perpendicular baseline smaller than 150 m, using the ROI_PAC software (Rosen et al., 2004). DORIS orbital information is used to remove orbital contributions to the mapped displacement. Interferograms are unwrapped using a branch-cut method (a ROI_PAC classic unwrapper) based on Goldstein et al. (1988). Out of a total of 56 interferograms, we choose three with good coherence to conduct a coseismic

inversion for distributed slip, and 17 to build up a time-series of postseismic deformation (Fig. 3.2).

3.2.1.1 Correction of tropostatic noise and orbital error

The main limitation of low-amplitude tectonic signal detection using InSAR is that orbital error and atmospheric delay projected into the line-of-sight direction can be at the same level as tectonic signals, or even larger, reaching tens of centimetres (Zebker et al., 1997). To minimize these effects, we apply a joint correction to each interferogram. Before correcting orbital error and tropostatic delay, we first reference all postseismic interferograms to the same point, and also manually fix small unwrapping errors as far as possible, in order to reduce the negative effect of unwrapping errors on estimating the correlation between phase change and topography. To minimize the effect of the residual orbital phase, we apply a first-order approximation of orbital error (Cavalié et al., 2007):

$$\varphi_{\mathrm{orb}} = ax + by + cxy + d, \tag{3.1}$$

where x and y are range and azimuth coordinates, and a, b, c and d are constants for each interferogram that best fit the phase of the non-deformed area.

Atmospheric errors consist of propagation delay through tropospheric and ionospheric layers. Here we consider only tropospheric noise, because the ionospheric propagation delay is comparatively weak for the Envisat C-band data (Gray et al., 2000). Tropospheric delay is caused by temporal and spatial variations of the stratified troposphere and consists of two major components: a turbulent mixing effect due to laterally variable tropospheric properties, and a tropostatic effect due to temporal variation of stratified water vapour and the changing ratio of temperature to pressure in the troposphere (Hanssen, 2001). To correct the tropostatic effect, a

simple linear relationship between topography and phase change was proposed by Cavalié et al. (2007, 2008).

Jointly, we can write the interferometric phase (with deformed area masked out) due to residual orbital noise and tropospheric noise as a combination of both (Doin et al., 2009):

$$\varphi_{\text{orb+tropo}} = ax + by + cxy + d + kz, \tag{3.2}$$

where a, b, c, d and k are obtained by least squares inversion, x and y are range and azimuth coordinates, and z is elevation. Although the assumption of a linear relationship between elevation and atmospheric delay does not account for the non-stationary characteristic of atmospheric noise, applying this technique reduces the apparent noise.

We iteratively run the inversion for all interferograms. Then, according to eq. (3.2), we calculate the predicted noise, and finally subtract it from the interferogram. Corrected coseismic interferograms are then inverted for fault geometry and slip distribution, while corrected postseismic interferograms are used to construct deformation time-series prior to inversion for afterslip.

As suggested by previous studies (e.g. Fialko et al., 2001; Sandwell et al., 2002; Simons et al., 2002), inversions incorporating interferograms with different look directions provide more reliable estimates of slip on the fault plane than those derived from only one look direction. However, in this study, the ascending data (Fig. S3.1) we obtained from ESA cover only part of the deformed area, and have relatively large noise (see also Figs 5a and c in Sun et al., 2011). We therefore focus on data from descending track 176. We note that the coseismic interferograms in Figs 3.3(a)-(c) cover postseismic periods (20, 90 and 215 days respectively) as well as the

earthquake itself, so there may be some postseismic deformation included. In addition, a small component of the observed phase is related to non-tectonic noise, such as uncorrected atmospheric effects, orbital error, and DEM error. Fig. 3.3(d) shows displacement profiles crossing the fault trace. The maximum line-of-sight (along the satellite's look direction) displacement in the hanging wall reaches 28 cm, while in the footwall, the negative line-of-sight displacement is only ~ 5 cm. The asymmetry of the displacement profile is expected of dip-slip earthquakes.

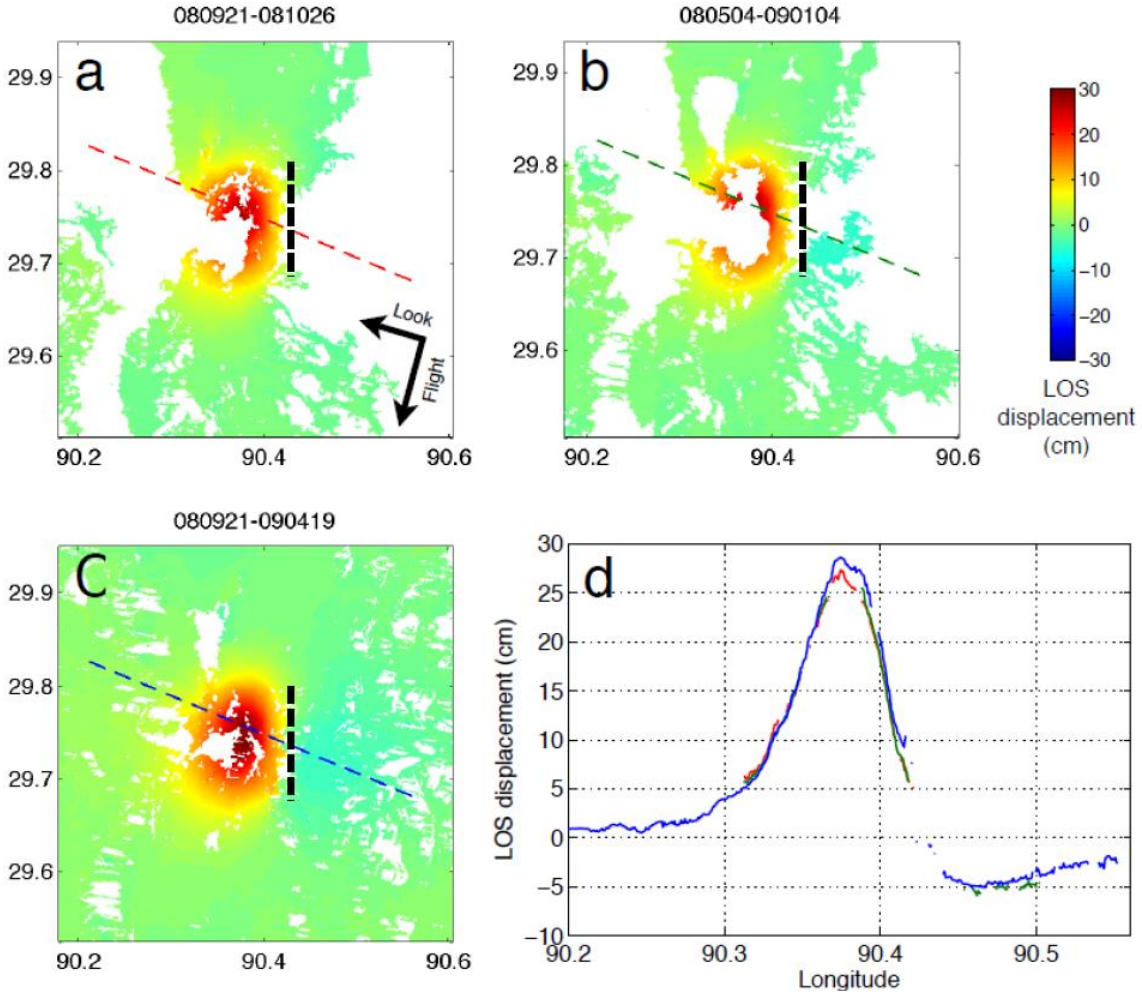

Figure 3. 3. (a)-(c) Coseismic interferograms inverted for coseismic slip. Long & short arrows in (a) show descending satellite flight direction and look direction, respectively. Black dashed lines mark the inferred fault trace at surface. SAR acquisition dates are shown above each interferogram in yymmdd format. Positive range change represents motion away from the satellite, while negative range change indicates motion towards the satellite. (d) Profiles showing coseismic line-of-sight displacement through the centre of the deformed area. Red, green and blue displacement profiles correspond to dashed lines in (a), (b) and (c), including 20, 90, and 215 days of postseismic deformation, respectively (see Fig. 3.2).

3.2.2 Aftershocks

The aftershock dataset we use for temporal analysis is from the China Earthquake Data Centre (hereafter referred to as CEDC). It provides earthquake location, local magnitude and phase information free online (http://data.earthquake.cn/data/). Among the recorded aftershocks, most occurred within 100 days following the mainshock (Fig. 3.4). We compare the temporal evolution of postseismic slip and aftershocks, considering events until 2010 August 31.

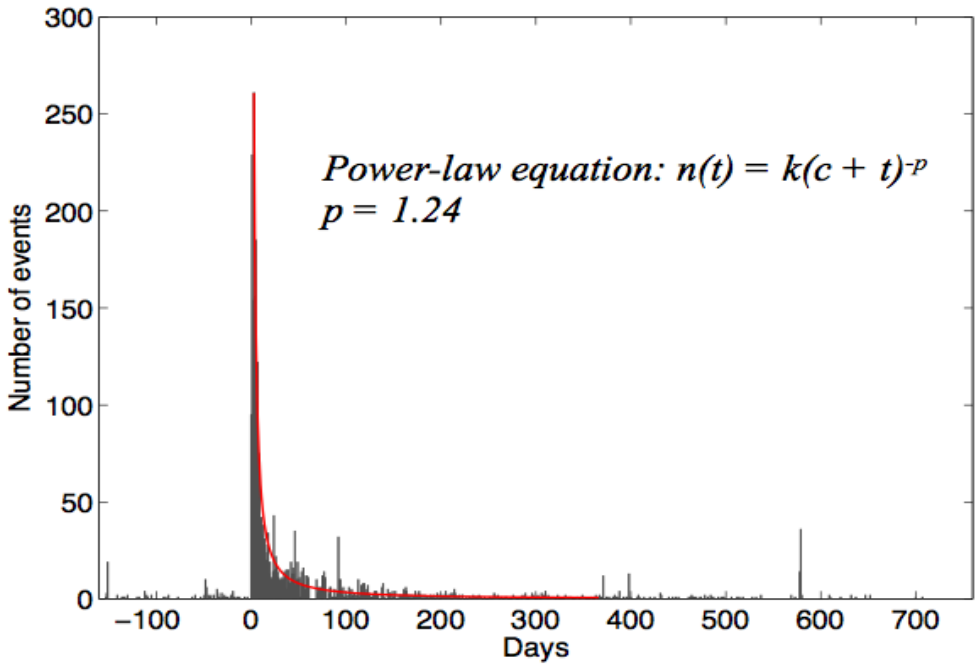

Figure 3. 4. Number of seismic events in the range N29.25° - 30.25°, E90.00° - 90.70° that occurred between 2008 May 1 and 2010 August 31 as a function of time. Red line is a power law fit to the first year of aftershocks, from the third day (with maximum number of aftershocks) after the mainshock onwards. All events are taken from the China Earthquake Data Centre (http://data.earthquake.cn/data/).

Fig. 3.4 shows the number of CEDC-recorded aftershocks, $n(t)$, as a function of time t for the first year following the mainshock. The curve fit to aftershocks (between the third day to the end of the first year since the main shock) using a power-law equation:

$$n(t) = k(c + t)^{-p}, \quad (3.3)$$

where *k, c, p* are constants, gives a *p* value of 1.24. The *p* value falls near the higher end of the typical range of other aftershock sequences (Dieterich, 2007), but we note that it is lower than for the L'Aquila event (D' Agostino et al., 2012), another moderate-size normal faulting earthquake. The two largest aftershocks occurred on 2008 October 6 and 2008 October 8, with local magnitude 5.5 and 5.7 respectively. The cumulative moment released by the first year of aftershocks is 4.68×10^{17} N m, which represents 13 per cent of the energy released by the mainshock. The cumulative aftershock moment during the period spanned by the postseismic data is only 5 per cent.

3.3 Coseismic slip inversion method

From the noise-corrected co-seismic interferograms, we aim to estimate the following source parameters for the Damxung earthquake: location (centre of fault trace), strike, dip, rake, upper and lower depth of the fault, fault length and slip. Both a homogeneous elastic half space (Okada, 1985) and a layered elastic half space (Wang et al., 2003) are considered. For both Earth models, we first carried out a non-linear inversion to estimate all of the fault parameters listed above, with uniform slip across the fault plane. We then carried out a linear inversion for distributed slip, holding other parameters fixed.

3.3.1 Homogeneous crust

3.3.1.1 Uniform slip model

We first assume uniform coseismic slip on a rectangular plane in an elastic half-space. The three unwrapped coseismic interferograms are down-sampled using a

quadtree algorithm (Jónsson et al., 2002) to give 4793 pixels in total, greatly reducing the computational effort in the inversion. The influence of residual spatially-correlated atmospheric noise is accounted for by the weighting matrix derived from Cholesky factorisation (Harris & Segall, 1987) of the inverse of the data covariance matrix. The covariance matrix is calculated from the 1D covariance equation that best describes the autocorrelation between every pair of pixels at a given distance in the non-deforming area (Lohman & Simons, 2005). A simulated annealing algorithm (Jónsson et al., 2002) is employed to find the global optimal model that minimizes the objective function, which is the sum of squares of weighted residuals (observed minus predicted displacements). The downhill simplex method (Nelder & Mead, 1965) is used to test models returned by the simulated annealing method to avoid

Table 3. 1. Source parameters derived from joint inversion of three Envisat interferograms, assuming uniform slip on rectangle buried in homogeneous and layered crust. InSAR results (Liu et al., 2012; Elliott et al., 2010) and seismic source parameters are also listed for comparison.

Parameters	Homogeneous crust (this study)	Layered crust (this study)	Homogeneous crust (Liu et al., 2012)	Homogeneous crust (Elliott et al., 2010)	USGS	GCMT
X (km) [a]	0.45 ± 0.05	0.76 ± 0.30	0.26 ± 0.02	0.58 ± 0.1	-18.73	7.36
Y (km) [a]	2.87 ± 0.11	2.55 ± 0.71	2.42 ± 0.05	3.55 ± 0.1	24.62	-7.54
Strike(°)	179.4 ± 0.5	180.0 ± 2.3	182.2 ± 0.2	181 ± 1	180	178
Dip(°)	54.8 ± 0.6	54.1 ± 2.9	54.4 ± 0.3	47 ± 1	48	53
Rake(°)	-114.6 ± 1.8	-108.4 ± 12.1	-111.7 ± 0.7	-115 ± 2	-119	-122
Top (km) [b]	5.18 ± 0.09	5.63 ± 0.46	4.54 ± 0.04	4.0 ± 0.1	-	-
Bottom (km) [b]	10.30 ± 0.21	10.47 ± 1.55	10.95 ± 0.05	10.7 ± 0.2	-	-
Length (km)	8.81 ± 0.14	8.99 ± 0.80	9.58 ± 0.07	10.4 ± 0.2	-	-
Slip (m)	1.76 ± 0.10	1.90 ± 0.55	1.33 ± 0.02	1.0	-	-
Moment (10^{18} N m)	3.13 ± 0.18	3.29 ± 0.95	3.23	3.1 ± 0.1	3.4	3.65

[a] X,Y are the central coordinates of the fault's upper edge projected to the surface. Reference point is at N29.728 E90.424.
[b] Top, Bottom are the depth of the upper and lower edge of the fault plane, respectively.

local minima (Wright et al., 1999). The optimal model is listed in Table 3.1. To determine parameter errors (e.g. Funning et al., 2005; Devlin et al., 2012), 100 simulated sets of spatially-correlated noise (Wright et al., 2003) are added to the displacement data, and then the optimal model is derived for each of the perturbed data sets using the hybrid simulated annealing and downhill simplex algorithm. Parameter errors are estimated from the obtained distributions by taking the standard deviations (Fig. S3.2). It is noted that the error estimation here considers only the contribution from atmospheric noise, as implemented by Liu et al. (2012) and Elliott et al. (2010), for the purpose of comparing different studies. Other parameters, such as the assumed elastic structure and downsampling method, may also affect the estimated errors. As discussed in Section 3.5.1, considering the layered elastic structure of the crust may affect estimates of the maximum slip depth, although the difference does not exceed 1 km in the case studied here.

3.3.1.2 Distributed slip model

Although residuals for the uniform slip model are generally small, as discussed in Section 3.5.1, we see localized residuals near the fault, especially around the southern end. To reduce residuals and obtain a more realistic slip model with distributed slip, we solved for slip on multiple fault patches using a linear inversion approach.

We initially fixed the rake at the value derived from the uniform slip model. Fault orientation parameters (location, strike and dip) were also fixed. We impose a non-negative slip constraint to obtain the slip distribution on the fault plane. The fault length and down-dip width were extended, then the plane was discretized into 19 along-strike and 20 down-dip patches, each with size 1 km × 1 km. Using the Okada elastic dislocation model (Okada, 1985), a Green's function matrix was calculated, which contains the predicted line-of-sight changes at each location in the displacement dataset produced by unit slip on each fault patch. The Laplacian operator was used to smooth the slip solution, and its effect was controlled by the

smoothing factor, *k*, which also controls a constraint of zero slip on the side and lower edges of the fault plane (Jónsson et al., 2002). A resolution test (Fig. S3.3) indicates that slip at shallow down-dip depth (0-5 km) can be well-resolved in spatial pattern and amplitude, while slip at intermediate depth (5-11 km) is generally well-recovered (small smearing with surrounding patches). Deeper slip patches (12-20 km) are smeared to a greater extent and may be mislocated.

We also solve for the slip vector by allowing variable rake. From the uniform slip modelling, we infer that the rake is between -45° and -135°. So, by calculating Green's functions for unit slip in these two end-member directions, the component of slip in each direction can be estimated (e.g. Ryder et al., 2010). Through vector calculation, we obtained both the direction and magnitude of slip on each fault patch.

3.3.2 Layered crust

The models described above consider the crust as a homogeneous elastic half-space, using the Okada model (Okada, 1985). The effect of the layered elastic structure of the Earth on inversion of geodetic data has been widely discussed and tested (e.g. Savage, 1987; Wald et al., 1996; Simons et al., 2002; Fialko, 2004b; Zhao et al., 2004; Amoruso et al., 2004; Hearn & Bürgmann, 2005). It is generally found that incorporating depth dependence of elastic moduli can increase estimates of centroid depth and estimated moment compared to those obtained for an Okada half-space model. Thus, we consider local seismic velocity structures proposed by various studies outlined below, and implement an inversion for a layered crust.

Yuan et al. (1997) used recordings from INDEPTH II, GEDEPTH (German Depth Profiling of Tibet and the Himalayas), and the permanent broadband Lhasa station to image the lithospheric structure of southern Tibet. The key feature of the velocity profile at station A36 (closest to the fault trace) is: a crustal low-velocity zone north

of the Yarlu-Zangbo suture (at depths ~ 13 – 30 km); a Moho depth of 70 – 80 km; and an S wave velocity of ~ 2.6 km/s down to a depth of ~ 2.5 km, and ~ 3.5 km/s at greater depths down to ~ 13 km (refer to fig. 5 of Yuan et al., 1997). Kola-Ojo & Meissner (2001) compared a velocity profile derived from GEDEPTH data with that at A36 from Yuan et al. (1997), showing a much lower S wave velocity in the upper ~ 20 km of crust (refer to fig. 5 of Kola-Ojo & Meissner, 1997). Using surface wave dispersion analysis, Rapine et al. (2003) found significant variation in the crustal velocity structure of southern and northern Tibet. The Lhasa terrane (where the 2008 Damxung earthquake occurred), with an S wave velocity of 2.75 km/s in the upper ~ 5 km, has a low-velocity zone of 3.35 km/s in the middle crust between 20 – 30 km (refer to fig. 6 of Rapine et al., 2003).

Taking the above studies into consideration, we construct a simplified model as follows: an upper layer, 4 km thick with low seismic velocities, overlying an elastic half-space with higher velocities. Table 3.2 summarises the model parameters. The V_p/V_s ratios are consistent with a Poisson's ratio of 0.25 (Owens & Zandt, 1997; Kind et al., 2002). Layer densities (ρ) are estimated from an empirical velocity-density relationship (Berteussen, 1977):

$$\rho = 0.77 + 0.32 \times V_p \,, \qquad (3.4)$$

To account for the layered nature of the crust, we utilize the software EDGRN/EDCMP (Wang et al., 2003), instead of the commonly-used Okada model (Okada, 1985), in the objective function to calculate line-of-sight displacements. It is demonstrated that the improved algorithm can retrieve synthetic source parameters well (see Table S3.2 and Fig. S3.4 for details of the test). The Fortran code EDGRN/EDCMP was developed by Wang et al. (2003) to compute displacements due to slip on a rectangular dislocation in a layered elastic medium. It comprises two modules: EDGRN calculates Green's functions at different depths for specified observation locations, by superposing the effect of each point source. The required

input includes P wave velocities, S wave velocities and densities for each layer. The thickness of each layer should also be specified. EDCMP reads Green's functions passed from EDGRN, and calculates static deformation at given positions according to the input fault parameters.

Table 3. 2. Seismic velocity and density structure for the simplified elastic crustal model, which consists of two layers, an upper layer with low velocity and a lower elastic half-space with higher velocity.

Layer No.	Thickness (km)	V_p (km/s)	V_s (km/s)	Density (g/cm^3)	Rigidity (GPa)	Young's modulus (GPa)
1	4	4.75	2.74	2.29	17.19	43.00
2	infinite	6.02	3.47	2.69	32.39	81.05

The modelling approach used for the layered case to derive distributed slip was otherwise the same as that used for the homogeneous case. Fault parameters (location, strike and dip) derived from the uniform-slip model (Fig. S3.5) assuming a layered crust were passed to the EDCMP module to build Green's functions. Here, the fault plane was also discretized into 1 km^2 squares. Following the computation of the Green's functions, the inversion procedure is the same as that described in Section 3.3.1.2 to derive a slip distribution for the homogeneous crust case.

3.4 Postseismic deformation time-series and afterslip inversion

We selected 17 differential interferograms (Table S3.1) with good coherence to construct postseismic deformation time-series spanning 2008 October 26 to 2010 August 22, and consisting of 11 time intervals. Each unwrapped interferogram was down-sampled by a factor of 10. Next, a least squares inversion for line-of-sight distance change at every pixel during each time interval was performed using the following equation:

$$\begin{pmatrix} G \\ kT \end{pmatrix} m = \begin{pmatrix} d \\ 0 \end{pmatrix}, \tag{3.5}$$

where G is a matrix of ones and zeros referencing the interferogram time intervals, m is a vector of the displacement at each time that we need to derive, k is a temporal smoothing factor that controls the effect of the smoothing operator T, and d is a vector of line-of-sight displacement (Berardino et al., 2002; Schmidt & Bürgmann, 2003; Philibosian & Simons, 2011; Barnhart & Lohman, 2012). The smoothing operator T is a matrix constructed assuming a first-order linear increment of displacement in the time domain. By plotting RSS (residual sum of squares) misfit versus model time-series roughness for different smoothing factors, we chose the value that allows both parameters to be low. Pixels that cannot be solved by the system because of rank deficiency or insufficient finite values were assigned no value. The gap in SAR coverage between the event and first acquisition date was filled by extending the displacement backwards, assuming a linear displacement gradient for the first 21 days (Ryder et al., 2007). We note that the linear approximation likely underestimates the real displacement values by a small amount. Finally, line-of-sight displacement maps at successive dates with reference to the common scene were produced by summing displacements in appropriate time intervals.

Postseismic deformation time-series reveal localized deformation on the southern part of the fault (Fig. 3.5). The maximum line-of-sight displacement reaches ~ 3 cm adjacent to the inferred coseismic fault trace in the hanging wall side one year after the earthquake. Together with the change in sign of line-of-sight displacements across the fault trace (Fig. 3.5), this information implies that afterslip on the fault plane that ruptured coseismically is the most likely mechanism responsible for the near field postseismic deformation, rather than viscoelastic relaxation, which would produce a circular uplift across the fault as described in Section 3.6. The displacement in the footwall is not obvious, because its magnitude is much smaller

than that in the hanging wall. An exponential fit of the form $A(1 - e^{-t/\tau})$ to the cumulative average displacement of the hanging wall pixels (boxed in Fig. 3.5) gives a decay time τ of ~ 227 days (Fig. 3.6).

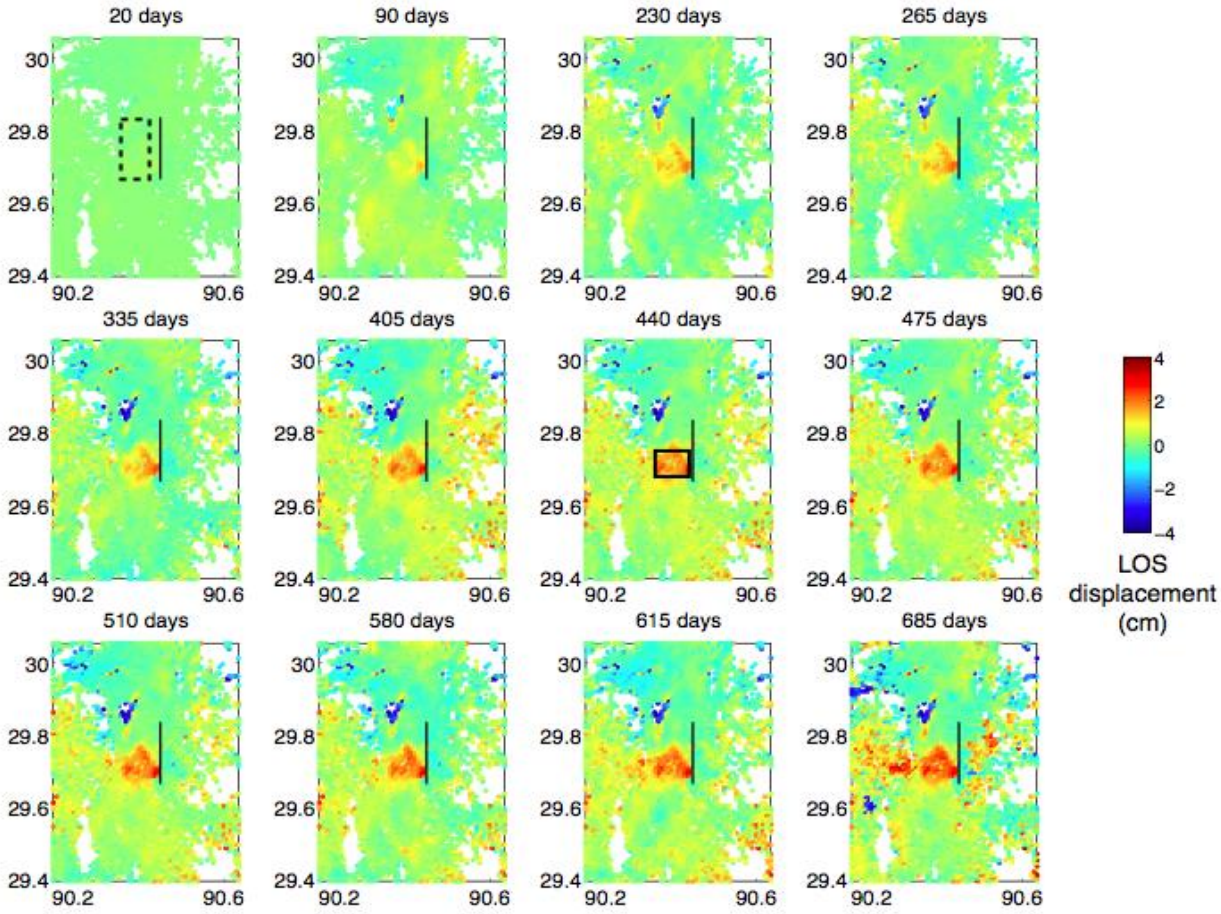

Figure 3. 5. Postseismic deformation time-series. The first panel is the linearly back-projected LOS displacement between the earthquake and the first SAR acquisition after the earthquake, with dashed box as the surface projection of the fault plane. Positive range change represents motion away from the satellite, while negative range change indicates motion towards the satellite. Black line represents the fault trace inferred in this study. Pixels in the black box on the hanging-wall (440 days deformation map) are averaged for cumulative line-of-sight displacement calculation in Fig. 3.6. Days refer to number of days after earthquake on 2008 October 6.

We invert the time-series for cumulative time-dependent afterslip. We do not include the last epoch, which has relatively large noise on the hanging wall side of the fault. A model considering crustal layering is adopted, with the same velocity structure as that used in the inversion for the coseismic slip distribution (Table 3.2). Source parameters are inherited as the coseismic rupture from Section 3.3.2.

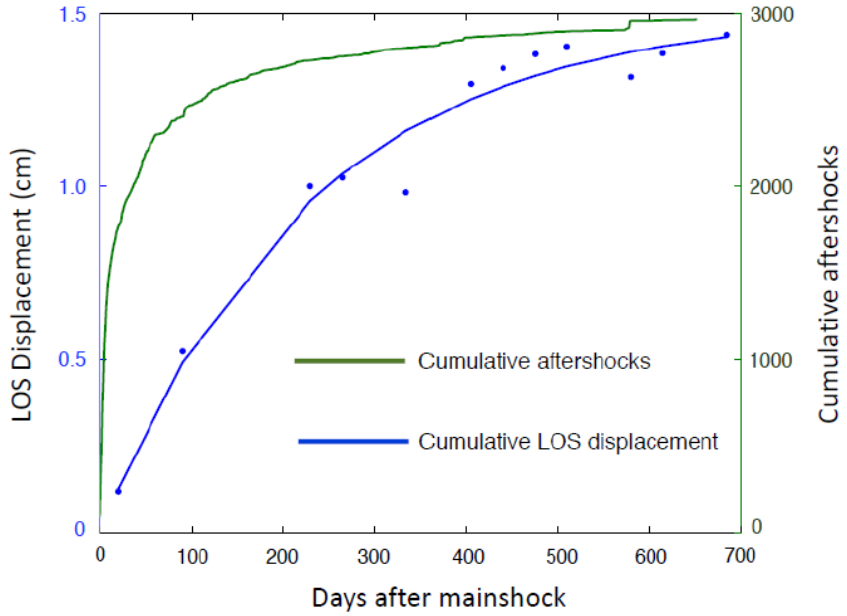

Figure 3. 6. Cumulative number of aftershocks and cumulative line-of-sight postseismic displacement as a function of time. Cumulative postseismic displacement is the average value of pixels in the black box in Fig. 3.5.

3.5 Inversion results

3.5.1 Coseismic inversion

The model of uniform slip on a rectangular fault plane buried in a homogeneous crust reproduces the line-of-sight surface displacements well, with RMS misfits of 1.43, 1.10 and 1.62 cm respectively for the three interferograms. The RMS is larger than that of the original interferograms, which is ~ 0.6 cm as derived from the 1-D covariance function of the far-field interferogram noise. Errors in inferred fault parameters are generally small (Table 3.1). The estimated fault plane strikes nearly north-south, dips to the west at 54.8°, and is buried with its top edge at a down-dip depth of ~ 5 km. This result is consistent with other InSAR studies of the earthquake source parameters (Elliott et al., 2010 ; Liu et al., 2012; Sun et al., 2011), but differs from that deduced by Wu et al. (2011), who suggests that the east-dipping boundary fault ruptured based on seismicity and ground motion data. Uniform slip including

crustal layering gives parameters of fault location, strike and dip comparable to those derived from homogeneous crustal model. The RMS misfits between predicted and observed displacement are 2.02, 1.46 and 1.43 cm for the three interferograms.

The distributed slip model with fixed rake positivity constraint generally shows the same slip pattern for both crustal models (Figs 3.7a and b). Slip greater than 1.0 m occurs mainly between 6 and 12 km down-dip distance, but the peak slip from the homogeneous crust model is ~ 30 cm larger than that from the layered crust model. Several patches on the shallow southern part of the fault show a maximum of 0.5 m slip. RMS misfits between predicted and observed displacement for the homogeneous crust model are 1.23, 1.07 and 1.44 cm, and 1.23, 1.06 and 1.45 cm for layered crust model.

The slip vector is solved for both crustal models (Figs 3.7d and e). Again, as for the model with fixed rake, the general slip patterns are similar: the primary slip patch tapers to the upper northern part of the fault. The maximum slip for the layered model is 2.22 m at a down-dip depth of 9.5 km, and for the homogeneous model the maximum is 2.38 m at 8.5 km depth. The oblique slip on the deep northern part of the fault plane may be an artifact caused by residual noise localized in the northern part of the hanging wall. We run the inversion 100 times to invert the 100 sets of realistic noise-perturbed data for slip distribution on each patch (Wright et al., 2003; Barnhart & Lohman, 2013). The estimated error on each patch is one standard deviation of the derived 100 slip values. All errors are less than 8 cm (Figs 3.7g and h). The overall area of slip in the layered model is slightly larger and deeper than that for homogeneous one. The moment release of the layered crust slip model is 3.67×10^{18} N m, and 3.60×10^{18} N m for the homogeneous crust model, both equivalent to a M_w 6.3 earthquake. The RMS misfits are slightly reduced relative to the fixed rake case: 1.20, 1.04, 1.41 cm for the homogeneous crustal model, and 1.21, 1.03, and 1.42 for the layered model.

The above analysis demonstrates that the InSAR data for this event are not able to distinguish between homogeneous and layered crustal models, in terms of goodness of fit. This is possibly due to the fact that the coseismic slip is mainly buried beneath the upper low-rigidity layer. However, when the previously-mentioned independent geophysical evidence for layering is taken into account, estimated slip is deeper and has smaller magnitude than for a homogeneous model.

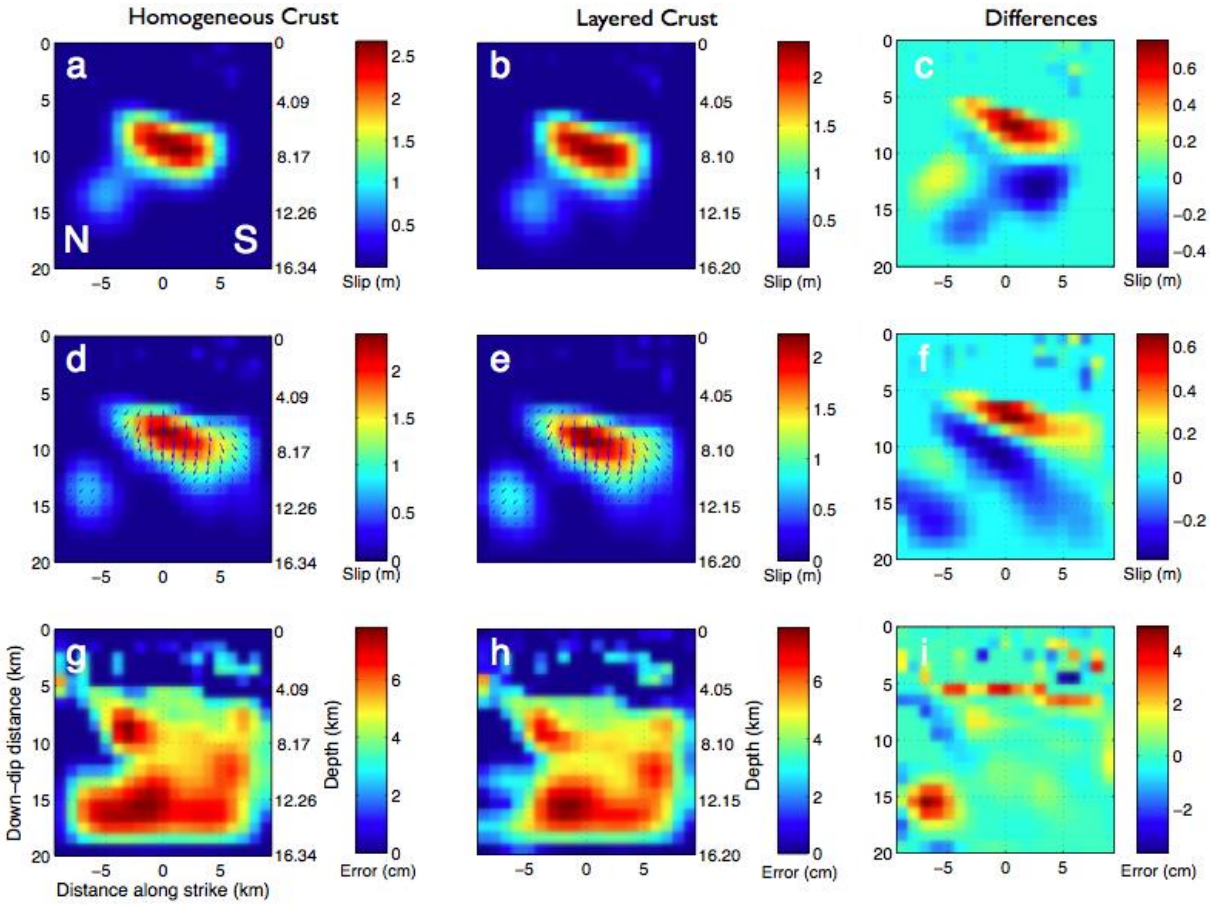

Figure 3. 7. Modelled slip distribution on the fault plane. (a) and (b) assume fixed rake and (c) is the difference between (a) and (b), while (d) and (e) assume variable rake with arrows marking the slip direction, and (f) is the difference between (d) and (e). (g) and (h) are estimated errors of distributed slip models with variable rake and (i) is the difference between (g) and (h). Panels on left are derived from homogeneous crust model and panels in the middle from layered crust model.

Fig. 3.8 shows the observed and modelled coseismic line-of-sight displacements, as well as the residuals for the distributed slip model with variable rake in a layered crust. The hanging wall residuals for the three coseismic interferograms show a

consistent trend, from negative in the date pair 080921 – 081026, nearly zero in 080504 – 090104, to positive in 080921 – 090419. This indicates that the slip model reproduces the second interferogram (080504 – 090104) best, and moderately overestimates the 'real' coseismic slip. The residuals for the coseismic interferogram spanning 215 days after the earthquake (080921 – 090419) show a positive line-of-sight displacement (consistent with additional subsidence) in the hanging wall of the rupture, which may suggest a contribution of afterslip that we explore in detail below. The negative residuals in the near field at the southern end of the fault may be a result of a simplified fault geometry.

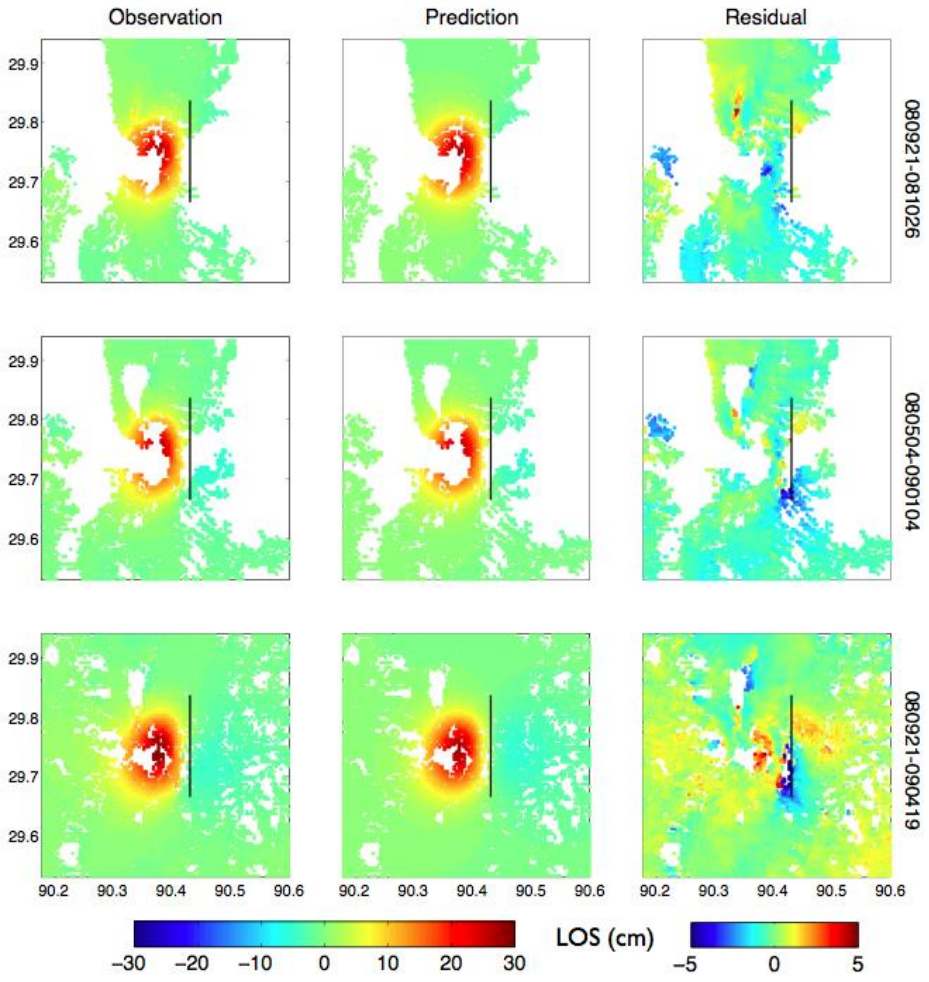

Figure 3. 8. InSAR observations and model prediction from slip distribution model with variable rake in a layered crust. Residuals are shown in the third column. Black lines mark fault trace. SAR acquisition dates are in yymmdd format on the right side of each residual map. Positive range change represents motion away from the satellite, while negative range change indicates motion towards the satellite.

3.5.2 Afterslip inversion

The afterslip inversion results show some stable spatial features (Fig. 3.9). Three patches A, B and C appear in all time-series epochs. The shallowest patch A sits at the southern part of the fault, at a down-dip distance of 3 – 5 km. This patch smears with the other two patches in the second to fifth epochs. Patch B is located at a down-dip depth of 6-8 km, overlapping with the upper edge of the coseismic slip model. The third and largest patch C lies roughly down-dip and just south of the rupture at 10 – 15 km depth. The spatial pattern of this deep-seated patch is not stable, as the third to fifth epochs show variable depth range, likely due to the fact that it is harder to consistently resolve this deeper slip patch.

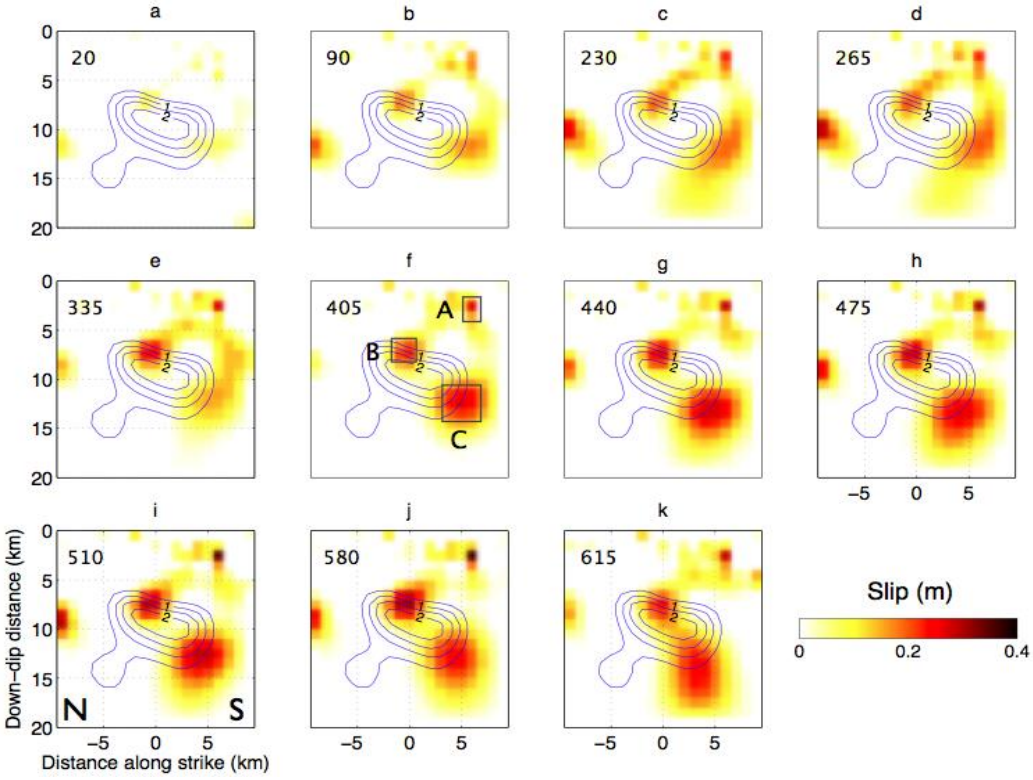

Figure 3. 9. Cumulative transient afterslip estimated for the date of each postseismic SAR acquisition using the layered model, compared with the coseismic slip distribution derived from the layered crust model with fixed rake (blue contours, labels in metres). A, B and C are three spatially stationary patches discussed in the text. Numbers at the upper left corner indicate days since mainshock.

The RMS misfits between modelled and observed postseismic displacements for each epoch are smaller than 0.73 cm. The postseismic deformation time-series is satisfactorily reproduced (Fig. S3.6, Fig. S3.7). Afterslip errors are estimated by re-running the inversion of noise-perturbed time-series 100 times to obtain a slip value distribution for each patch. The standard deviation of each patch is plotted as a separate time-series in Fig. S3.8, showing that the spatial distribution of error is similar to that of afterslip. For patch A, the error is < 10 cm. For patch B, the error doesn't increase significantly with time, and for patch C, the error is obviously larger than that for patches A and B, and increasing with time. The largest error for each epoch appears at variable depth on the most northern part of the fault. This may result from the residual atmospheric noise in the north-west part of the hanging wall being mapped into the slip distribution. Error calculation and analysis indicate that afterslip patches A and B are well-resolved, and when dealing with afterslip deeper than a down-dip depth of 11 km, slip features should be treated with caution.

The upper two afterslip patches generally have not migrated much spatially over the timespan of observations. While there is an apparent tendency of patch C to migrate downwards along the fault plane with time (Fig. 3.9), as was inferred for the Izmit earthquake (Bürgmann et al., 2002), the fault slip is poorly resolved below the depth of 10 – 12 km (see Fig S3.3 of the Supplementary Materials). Deeper afterslip (down-dip depth > 15 km) on the down-dip extension of the coseismic rupture is not found.
The cumulative maximum slip averaged over the boxed elements shown in Fig. 3.9(f) after 615 days is ~ 20 cm for all three patches (Fig. 3.10). The total afterslip moment is 3.76×10^{17} N m, which is ~ 10 per cent of the moment inferred from coseismic interferograms. Exponential fits to the cumulative afterslip of the three patches give an increasing decay time with depth (Fig. 3.10). The overall moment release evolves with an exponential decay time of 154 days (Fig. 3.11). The obvious discontinuity of the moment release at 335 days and 405 days after the mainshock might be a result of over-correction of atmospheric and orbital noise, which in turn may underestimate

the afterslip. This underestimation can also be seen from the fits to averaged afterslip of each patch (Fig. 3.10). We should note that both afterslip and moment are expected to be larger than presented here, because the linear estimation of the first 20 days of deformation would likely have underestimated the initial postseismic deformation.

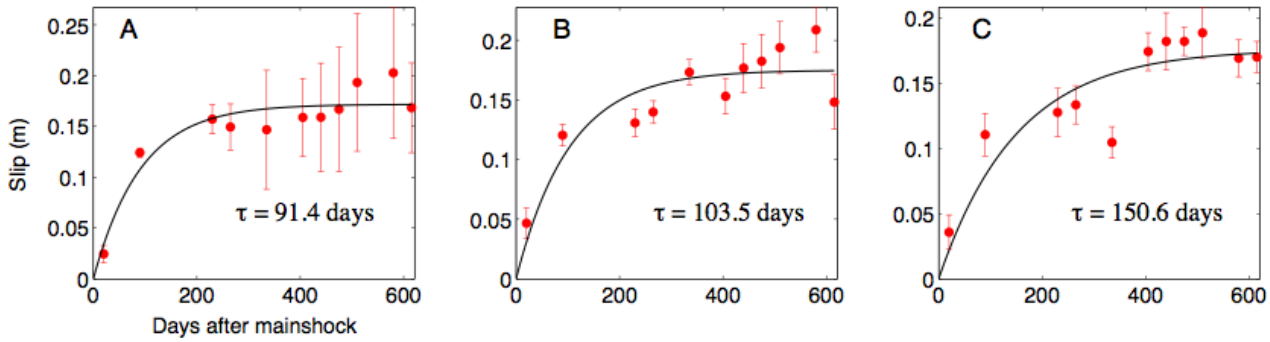

Figure 3. 10. Afterslip evolution of patches A, B and C, with best-fit exponential curve. The error at every epoch is the standard deviation of the slip magnitude for the patches boxed in Fig. 3.9(f).

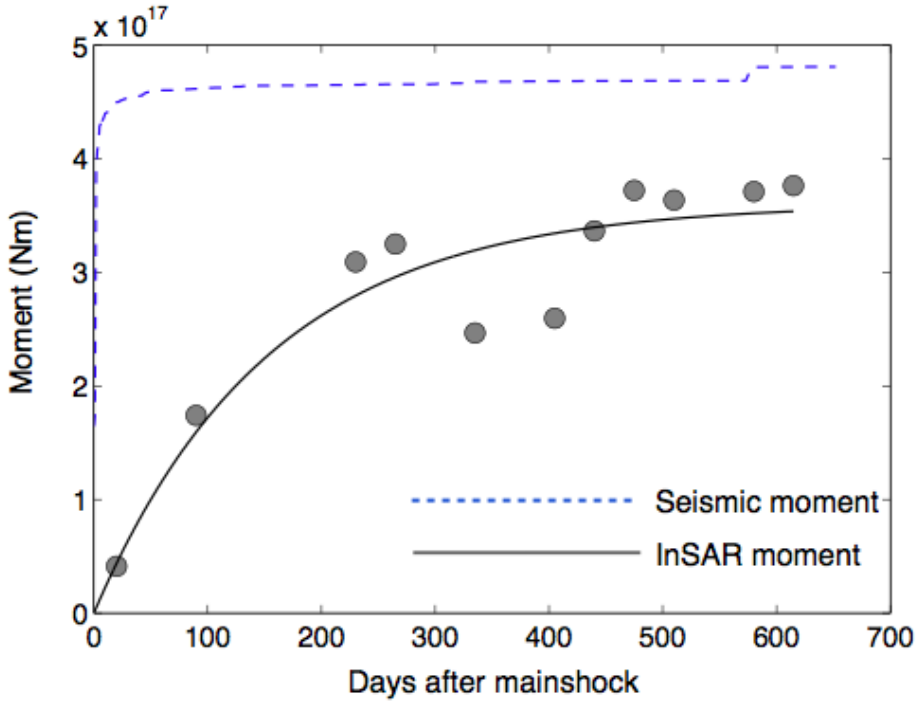

Figure 3. 11. Time evolution of cumulative postseismic moment released by afterslip (grey dots, with best-fit exponential marked by black line) and aftershocks (blue dashed line).

3.6 Viscoelastic modelling

The mid/lower crustal and/or upper mantle viscosity of the Tibetan Plateau has been estimated from InSAR studies of several moderate to large earthquakes that occurred in recent years (e.g. Ryder et al., 2007; Ryder et al., 2010; Ryder et al., 2011; Wen et al., 2012; Yamasaki & Houseman., 2012). However, the earthquakes studied are mainly strike-slip, and involve faults located generally in regions close to the margins of the Tibetan Plateau. Thus, the viscosity of the interior of Tibet is not well established. Here, we adopt the same method as used by Ryder et al. (2010) to constrain local strength beneath the elastic upper crust in southern Tibet.

We use the software PSGRN/PSCMP written by Wang et al. (2006) to simulate the postseismic line-of-sight displacement due to viscoelastic stress relaxation. PSGRN/PSCMP shares the same work flow as the coseismic deformation modelling software EDGRN/EDCMP descried earlier. It includes two modules: PSGRN calculates Green's functions and PSCMP calculates postseismic displacements at given time. In the PSGRN module, the user can input the seismic velocities and viscosities of different layers. The code is designed to implement a Burger's rheology, which is a Kelvin-Voigt body and a Maxwell body in series. To model Maxwell relaxation, the transient viscosity (dashpot of the Kelvin-Voigt body) is set as zero, while the steady state viscosity (dashpot of the Maxwell body) is non-zero (Wang et al., 2006). This software has been employed to study many earthquakes to infer lithospheric rheology from geodetic observations of postseismic deformation (e.g. Barbot et al., 2008, 2010; Xiong et al., 2010; Hoechner et al., 2011; Wen et al., 2012).

In order to obtain a general idea of the postseismic surface expression of viscoelastic relaxation below the seismogenic zone, we first run a forward model by inputting an arbitrary viscosity (1×10^{18} Pa s) of a Maxwell viscoelastic half-space under a 15-

km-thick elastic upper crust. We use our coseismic slip model derived for a layered earth (Fig. 3.7e) and the rheology parameters shown in Table 3.3. We find that circular uplift is broadly distributed over the fault trace (Fig. 3.12c), while subsidence occurs in the far field, as is also evident for other normal-faulting earthquakes studied by Nishimura & Thatcher (2003), Gourmelen & Amelung (2005) and Ryder et al. (2010). The uplift is the surface response to material at depth flowing in towards the faulted area. In our postseismic deformation time-series, we find no clear evidence of such uplift over the fault, so direct estimation of the optimal viscosity is not possible. However, we can still estimate a lower bound on the viscosity of the mid/lower crust, by running multiple viscoelastic models with different viscosities of the Maxwell half-space (Ryder et al., 2010).

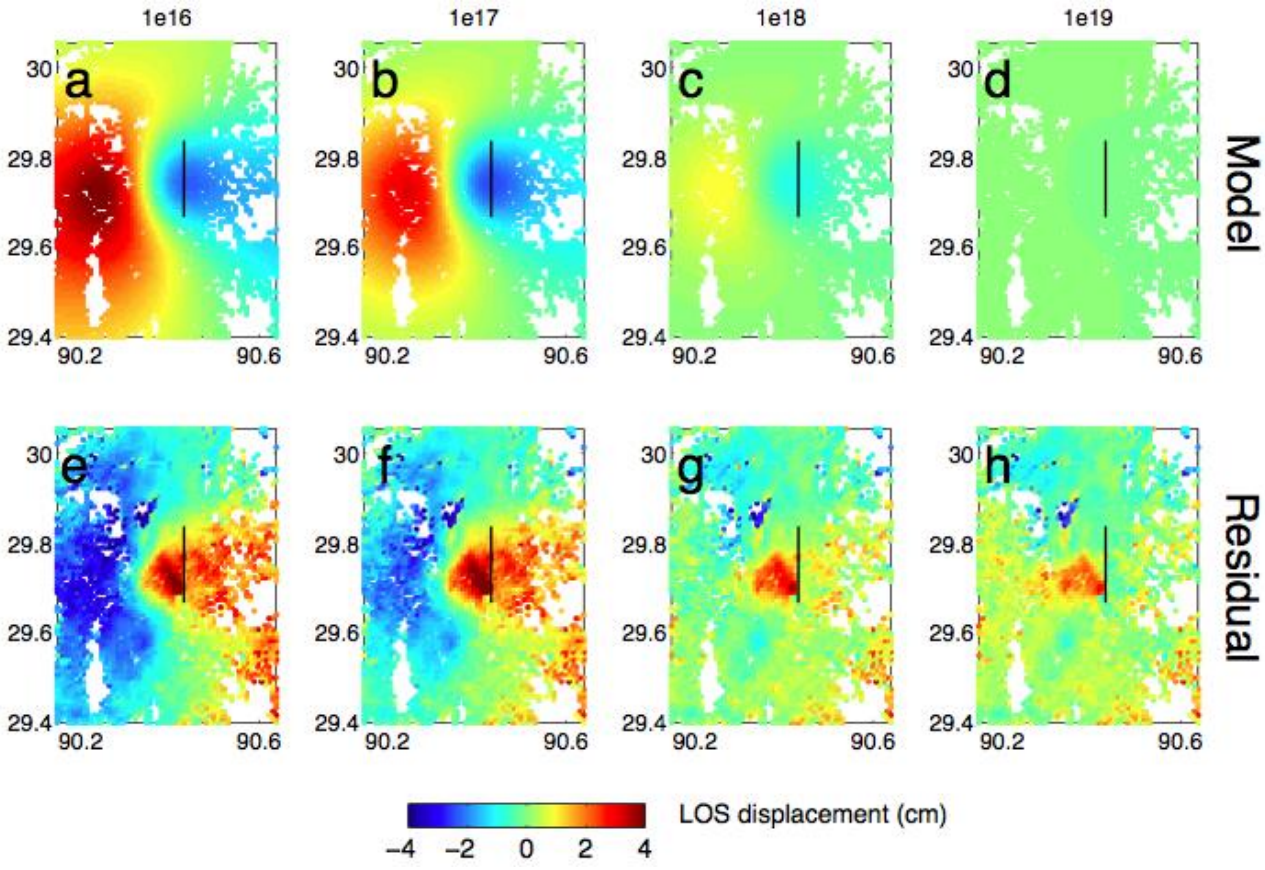

Figure 3. 12. (a) - (d) Modelled postseismic line-of-sight displacements due to viscoelastic relaxation at 615 days after the mainshock, using variable viscosities (Pa s) marked as the title of each figure. (e) - (h) Residuals between the cumulative postseismic deformation at 615 days after the mainshock (sub-figure titled 615 days in Fig. 3.5) and the modelled deformation due to viscoelastic relaxation in the mid/lower crust. Positive range change represents motion away from the satellite, while negative range change indicates motion towards the satellite.

The elastic layer thickness is set to 15 km (Ryder et al., 2007, 2010) and elastic parameters are the same as those used for the coseismic slip inversion in a layered earth. For a range of viscosities varying between 1×10^{16} and 2×10^{19} Pa s, we simulate the transient postseismic displacements and calculate the RMS misfit between the modelled viscoelastic displacements and the postseismic deformation time-series. The modelled displacements for the 615 days epoch are shown in Figs 3.12(a)-(d), for viscosities of 10^{16}, 10^{17}, 10^{18} and 10^{19} Pa s, respectively. Figs 3.12 (e)-(h) show the residuals between cumulative line-of-sight displacement and modelled viscoelastic displacement for variable viscosities. When a larger viscosity is applied, the expected viscoelastic relaxation signal is smaller, leaving the residual as close as to the displacement caused by afterslip (e.g. Figs 3.12g and h). The viscosity beneath which the RMS misfit value begins to rise steeply is taken as the lower bound on the Maxwell viscosity (Ryder et al., 2010). Fig. 3.13 shows the RMS misfit values as a function of viscosity. The RMS misfit levels off at high viscosities, as the modelled displacements become insignificant with respect to the interferograms. The lower bound obtained is 1×10^{18} Pa s. Errors are the standard deviations of the RMS misfit distributions derived by re-running the residual calculation 100 times for noise-perturbed deformation time-series. The errors in RMS misfit values are generally smaller than ~ 0.023 cm.

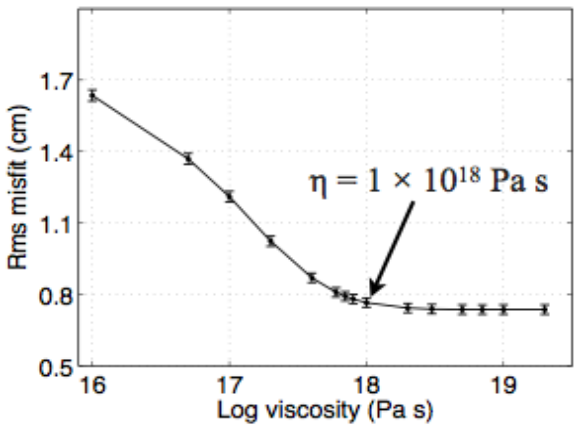

Figure 3. 13. Plot of RMS misfit versus log viscosity. Errors are the standard deviations of the RMS misfit distributions derived by perturbing postseismic deformation time-series with 100 sets of realistic noise, and re-running 100 times the calculation of residual between modelled and observed displacements.

3.7 Discussion

3.7.1 Layered crust versus homogeneous crust

The Damxung earthquake occurred in the north-central part of the Yadong-Gulu rift. The availability of seismic velocity estimates for the study area offers a chance to apply the layered crust model to derive earthquake source parameters. The INDEPTH II project carried out a thorough seismic survey along this part of the Tibetan Plateau, and there are many published results on the imaged crustal and/or mantle structure. These studies allow us to reasonably estimate the velocities. Lateral elasticity heterogeneity across the fault plane is left for further consideration.

Our uniform slip model assuming a homogeneous crust has similar source parameters as those obtained by other studies of this earthquake, as summarized by Liu et al. (2012) and shown in Table 3.1. When taking layering into consideration, the uniform slip model gives a different fault size (53.7 km^2 for layered crust *vs* 55.2 km^2 for homogeneous crust) and a slightly different slip direction (54.1° *vs* 54.8°). If we further derive distributed slip, both crustal models give spatially similar patterns of slip (Fig. 3.7). For the slip models with variable rake, the peak slip patch of the layered model locates at a depth of 7.7 km, and the maximum magnitude is 2.2 m, while for the homogeneous model, they are 6.9 km and 2.4 m, respectively. This result is in accordance with the synthetic test by Hearn & Bürgmann (2005), highlighting the importance of considering the layered characteristics of the crust. The seismic moment estimated for both crustal models are ~ 3.60×10^{18} N m, equivalent to a M_w 6.3 earthquake.

3.7.2 Coseismic slip, afterslip and aftershocks

It has been observed in previous studies of normal faulting events that afterslip tends to occur at the edges of the coseismic slip zone (D'Agostino et al., 2012; Copley et

al., 2012). In this study, afterslip patch A (Fig. 3.9) appears in the upper layer of the layered elastic crust, which may represent the response of the shallow fault to stress change and/or redistribution of shallow material. Patches B and C sit near the upper and lower southern edges of the coseismic slip. We note that the afterslip under a down-dip depth of 11 km is relatively poorly resolved, as revealed by the error analysis in section 3.5.2. For this earthquake, none of the slip patches are much deeper than the coseismic slip, which is also the case for other normal faulting earthquakes studied geodetically, such as the 2009 M_w 6.3 L' Aquila earthquake (D' Agostino et al., 2012), the 2008 M_w 6.4 Nima-Gaize earthquake (Ryder et al., 2010), and the 1959 M_w 7.3 Hebgen Lake, Montana earthquake (Nishimura & Thatcher, 2003). Together these might indicate that shallow afterslip is responsible for the near-field postseismic displacement of normal faulting events. In general, the possibility of deep afterslip on the down-dip extension of coseismic fault planes needs to be further investigated.

The three localized afterslip patches locate at different depths and are distributed along the fault, showing no obvious correlation with depth as suggested by the rate and state friction law (Tse & Rice, 1986; Scholz, 2002), according to which depth-dependent frictional properties should limit afterslip to above and below the main coseismic rupture. This inconsistency was also found in the study of the L'Aquila earthquake, and was interpreted as being caused by additional complexity of fault properties relative to a depth-dependent frictional model (D' Agostino et al., 2012). We infer that the frictional properties on the fault differ not only in the down-dip direction, but also laterally along strike.

Given that we have no InSAR observations for the first 20 days of postseismic deformation, we are not able to constrain the spatial pattern of afterslip in this very early phase, although we did a linear back projection of the postseismic deformation. There are two possible scenarios for these first 20 days: (i) the afterslip is spatially

stable, and similar to that for later epochs; (ii) the afterslip migrates following the mainshock into surrounding regions. Studies on other earthquakes, such as the 2005 Nias-Simeulue earthquake (Hsu et al., 2006), the 2004 Parkfield earthquake (Johnson et al., 2006) and the 2011 Tohoku-Oki earthquake (Ozawa et al., 2012), show that afterslip inverted from very early postseismic geodetic observation is generally spatially stable, and so we infer that the second scenario proposed above is less likely for the 2008 Damxung earthquake.

The temporal evolution of afterslip and aftershocks of the Damxung earthquake are different. Cumulative aftershock numbers decay faster than the cumulative line-of-sight deformation (Fig. 3.6). Similarly, Fig. 3.11 shows that the decaying rate of cumulative seismic moment calculated from the CEDC catalogue is faster than that of cumulative moment released by afterslip. The study of the 1999 Chi-Chi earthquake by Perfettini & Avouac (2004) suggests that afterslip governs the temporal evolution of aftershocks. This does not appear to hold for the Damxung earthquake, which may be a consequence of the different earthquake type (thrusting versus normal faulting), or the different fault zone environment. Aftershock relocation in future may help characterise the spatial relationship between afterslip and aftershocks, and better reveal the temporal correlation by selection of only those aftershocks within a certain distance from the fault plane.

3.7.3 Viscosity constraints for the deep crust of southern Tibet

InSAR measurements of postseismic deformation provide a unique opportunity to study the mid/lower crustal rheology of Tibet. Postseismic deformation for a number of earthquakes in Tibet has been effectively modelled to constrain the crustal and/or mantle strength of the plateau (Ryder et al., 2007, 2010, 2011; Wen et al., 2012). Ryder et al. (2007) modelled viscoelastic relaxation following the 1997 M_w 7.5 Manyi earthquake, and inferred an effective viscosity of $3 – 10 \times 10^{18}$ Pa s beneath a

15 km elastic layer. Studies by Ryder et al. (2011) and Wen et al. (2012) of the postseismic transients following the 2001 M_w 7.9 Kokoxili earthquake found steady-state viscosities of about 10^{19} Pa s. A robust lower bound of 3×10^{17} Pa s was placed on the mid/lower crustal viscosity of central Tibet from modelling of viscoelastic relaxation in a Maxwell half-space following the 2008 Nima-Gaize earthquake (Ryder et al., 2010). The viscosities in the range of $3 \times 10^{17} – 2 \times 10^{19}$ Pa s fall in the central part of the range of $10^{16} – 10^{21}$ Pa s estimated for the plateau by modelling of present-day topography, margin relief of the Tibetan Plateau and GPS records of interseismic surface movement (Clark & Royden, 2000; Shen et al., 2001; Clark et al., 2005b; Copley & Mckenzie, 2007; Bendick et al., 2008; Hilley et al., 2009; Zhang et al., 2009).

In the present study, a lower bound of 1×10^{18} Pa s is inferred for the mid/lower crust viscosity of this part of the Yadong-Gulu rift, which is consistent with estimates for other parts of the plateau. It is noted that in the viscoelastic modelling, a thinner elastic layer (e.g. ~ 13 km as defined by the depth of the base of the Damxung rupture) would push the lower bound of the mid/lower crust viscosity slightly higher than that estimated here. We notice that several other moderate to large normal faulting earthquakes occurred along this rift since the last century, e.g. the 1952 M 7.5 Gulu earthquake located at northern end of the rift and the 1992 M_w 6.2 Nyemu earthquake to the south of the 2008 Damxung earthquake. Modelling of InSAR-recorded late postseismic deformation of these events would enable further probing of lithospheric rheology of different sections of this specific long-enduring seismic zone, and thus facilitate understanding of the earthquake cycle.

3.8 Conclusions

This study uses InSAR observations to investigate the coseismic and postseismic surface deformation associated with the 2008 M_w 6.3 Damxung earthquake in Tibet.

The coseismic deformation pattern revealed by InSAR confirms that a west-dipping normal fault on the eastern margin of the Yadong-Gulu rift is responsible for this event. Inversion of multiple Envisat data assuming both homogeneous and layered crustal models yields comparable coseismic slip distribution patterns, revealing a blind rupture below a down-dip depth of ~ 5 km. The maximum slip for the layered model is smaller and deeper, while the moment release values calculated from both models are similar (~ 3.60×10^{18} N m). For the postseismic period, localised line-of-sight increase in the hanging wall of the southern part of the rupture can be well reproduced by three afterslip patches located at different positions on the fault plane. Localised afterslip patches are located in the shallow upper crust and at the top and bottom edges of the coseismic slip, revealing frictional heterogeneities in both down-dip and along-strike directions of the fault. Our afterslip model also excludes deep afterslip (> 15 km) on the down-dip extension of the fault. Afterslip moment within the first 615 days is at least ~ 11 per cent of the moment released by coseismic slip. The temporal evolution of aftershocks and afterslip are not linearly correlated. By modelling viscoelastic relaxation in a Maxwell-half space, we place a lower bound of 1×10^{18} Pa s on the viscosity of the mid/lower crust of this part of the Yadong-Gulu rift. Continued postseismic deformation modelling of other normal faulting events that occurred along this rift system will allow for rheological strength mapping and earthquake risk assessment of this active seismic zone.

Acknowledgements

We thank the editor, Prof. Duncan Agnew, and two anonymous reviewers for their constructive suggestions. Envisat SAR data are provided by the ESA (European Space Agency) through CAT–1 proposal (proposal ID C1P. 5119). Figure 3.1 was generated using open-access software GeoMapApp. Lidong Bie acknowledges financial support from the University of Liverpool and the China Scholarship Council. We also thank Rongjiang Wang (GFZ Potsdam) for help with

PSGRN/PSCMP installation, and the Seismology Group at the University of Liverpool for useful discussions.

Chapter 4

Recent seismic and aseismic activity in the Ashikule stepover zone, NW Tibet

Lidong Bie and Isabelle Ryder

School of Environmental Sciences, University of Liverpool, UK. E-mail l.bie@liv.ac.uk

Geophysical Journal International, 2014, 198(3): 1632-1643. doi: 10.1093/gji/ggu230

Summary

Three large earthquakes occurred in the Ashikule stepover zone, NW Tibet in 2008 (M_w 7.1), 2012 (M_w 6.2) and 2014 (M_w 6.9). In this paper we use InSAR data to examine the 2008 event in detail, and place it in the context of both recent/possible future events and regional tectonic environment. We present InSAR data covering the coseismic and postseismic phases of the 2008 event, and invert for slip distributions during both phases in order to examine the spatial relationship between earthquake rupture and afterslip. To account for the curved rupture trace as mapped in the field, we model the slip on a non-planar fault. A change in slip sense from left-lateral in the north to extensional in the south is consistent with the focal mechanism of aftershocks. We find that afterslip occurs around the perimeter of the coseismic slip, although in a patchy way, as seen in other normal faulting case studies. We calculate the Coulomb stress changes imparted by the 2008 earthquake on neighboring faults, including stress loading on the subsequent rupture zones of the 2012 and 2014 earthquakes. We also compute the combined loading effect of the 2008, 2012 and 2014 earthquakes on the nearby Altyn Tagh Fault, which hasn't experienced a major earthquake since early last century. This study demonstrates that stepover zone

failure can increase stresses on bounding strike-slip faults, which likely has relevance in analogous tectonic environments elsewhere in the world.

Keywords: Radar interferometry; Dynamics and mechanics of faulting; Time-series analysis; Seismicity and tectonics; Asia

4.1 Introduction

On 2008 March 20, the M_w 7.1 Yutian earthquake occurred in the western Kunlun mountains, NW Tibet. Among recent earthquakes on the Tibetan plateau, the Yutian earthquake stands out as it was the largest normal faulting event (Elliott et al., 2010). Its epicentre locates between the Ashikule basin and Guliya ice cap (Fig. 4.1), bounded by two major sinistral strike-slip fault systems: the Altyn Tagh and the Longmu-Gozha Co faults (Taylor & Yin, 2009; Styron et al., 2010). Further north, the Tarim basin collides with, and may currently be underthrusting (Zhao et al., 2011) beneath, the Tibetan terranes. This region has experienced another two M_w 6.0+ earthquakes since the occurrence of 2008 Yutian earthquake. A M_w 6.2 normal faulting earthquake occurred ~ 100 km to east, and a M_w 6.9 earthquake showing pure left-lateral strike-slip motion as reported by the USGS (U.S. Geological Survey) occurred on 2014 February 12, ~ 110 km to the NE of the 2008 Yutian earthquake.

Several Interferometric Synthetic Aperture Radar (InSAR) studies have been carried out to investigate the coseismic surface deformation patterns, and to invert for source parameters (Elliott et al., 2010; Furuya & Yasuda, 2011; Zhang et al., 2011; Wang et al., 2013) for the 2008 Yutian earthquake. Elliott et al. (2010) proposed a slip model consisting of three rectangular planar faults with varying strike directions. To overcome the mechanically incompatible overlapping of rectangular faults, Furuya & Yasuda (2011) presented a non-planar fault source model. To reduce the local

modelling residual, they added a second WSW-striking sinistral fault to the north of the main rupture, although such a fault has not been documented in the field.

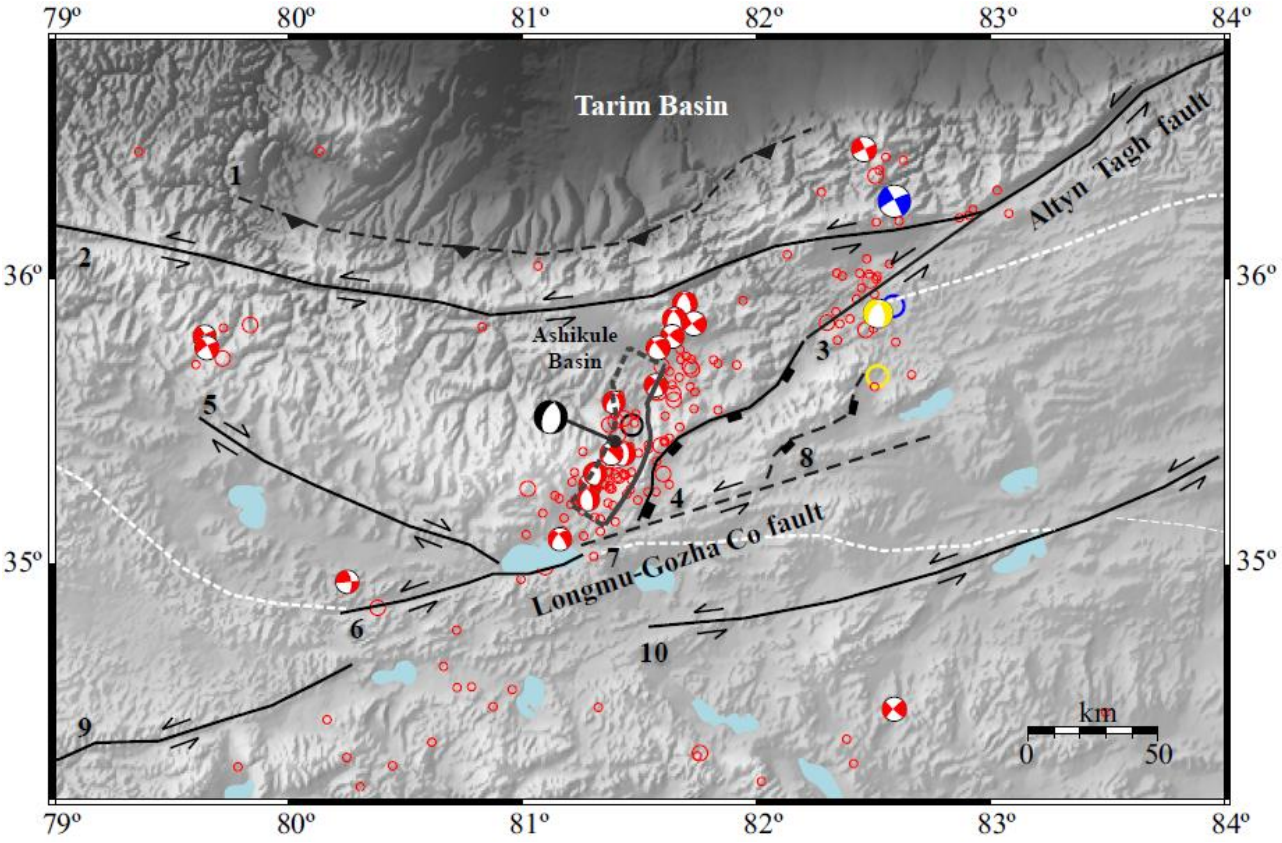

Figure 4. 1. (a) Tectonic map of the Yutian region. Black solid lines and white dashed lines are fault traces and suture lines, respectively, modified from Styron et al. (2010). Black dashed lines are additional faults as shown in Xu et al. (2013). Number on the left side of each fault marks the fault ID in Table S4.2 for Coulomb stress change calculations. Main shock and aftershock focal mechanisms from the Global CMT catalogue are shown, together with locations (circles) from the USGS earthquake archive (http://earthquake.usgs.gov/earthquake/search/). Earthquakes with $M > 4$ from 2008 March 20 until 2014 March 22 in the USGS archive are plotted. Circle size is scaled with earthquake magnitude (largest event M_w 7.1). Global CMT focal mechanisms (plotted in GCMT locations) of the 2008, 2012 and 2014 mainshocks are marked in black, yellow and blue, respectively, and corresponding USGS locations are marked in the same color. Grey line delineates the 2008 Yutian earthquake surface rupture and dashed box is the surface projection of the rupture plane from this study.

A recent field investigation conducted by Xu et al. (2013) mapped the surface rupture trace in detail. They divided the rupture into three segments with variable strikes and similar slip directions (see fig. 2 in Xu et al., 2013). The northern segment generally strikes to the SSW with vertical and left-lateral slip components, expressing right-

stepping transtensional breaks. The SSE-striking middle segment is dominated by normal faulting with a minor left-lateral component. The southern segment extends SSW and the main geomorphological feature is oblique normal fault scarps. Both field mapping and InSAR observations suggest that the rupture may extend further south into the glaciated area (Elliott et al., 2010; Xu et al., 2013).

The Global Centroid Moment Tensor (GCMT) catalogue places the event ~ 25 km west of the rupture trace (Fig. 4.1). The moment tensor solution has a nodal plane striking 203° and dipping 52° to NW, with a rake of -74°. The GCMT estimate of the mainshock seismic moment is 5.43×10^{19} N m, which corresponds to a moment magnitude of 7.1. The GCMT locations for aftershocks show consistency in aligning linearly along the strike of the fault rupture (Fig. 4.1). In the north, three aftershock focal mechanisms suggest an oblique sense of motion on faults striking either NW or NE, whereas in the central and southern portions, normal faulting mechanisms dominate with minor exceptions, such as the one close to the mainshock. The moment tensor solutions offer a first-order knowledge of the faulting type along the rupture and help constrain the fault geometry.

In this paper, after presenting a revised coseismic rupture model that takes recent field mapping into account, we present new postseismic InSAR data and derive a deformation time-series, from which an afterslip model is obtained. The spatial relationship between afterslip and coseismic slip distribution is discussed. Furthermore, we investigate how the Yutian rupture brought about static stress changes on major neighboring faults, including stress loading on the subsequent rupture zones of the 2012 and 2014 earthquakes. The tectonic background of the Yutian earthquake is discussed, and examples of similar tectonic settings in Tibet and elsewhere are presented. Through this study, we aim to investigate how stepover zone failure can alter the state of stress in the surrounding crust.

4.2 InSAR data

To investigate static ground motions associated with the Yutian earthquake, we used InSAR observations spanning the earthquake with different look directions from two sensors. Details of coseismic interferograms used by this study are listed in Table 4.1. We constructed two ascending L-band ALOS interferograms (tracks 514 and 515), and two C-band Envisat interferograms (ascending track 155 and descending track 477), using the ROI_PAC software (Rosen et al., 2004). All coseismic interferograms show a positive line-of-sight (LOS) displacement (away from the satellite) on the hanging wall side of the fault (Fig. 4.2). The maximum LOS displacement observed by ALOS is ~ 2.0 m, close to the central section of the fault. For all interferograms, the signal coherence on the footwall is poor due to the decorrelation caused by glaciated high relief. To model the coseismic data, the four interferograms are down-sampled to 9408 points in total using a quadtree algorithm (Jónsson et al., 2002).

Table 4. 1. Coseismic SAR image pairing for the 2008 M_w 7.1 Yutian earthquake.

Satellite	Flight direction	Track no.	Date 1 (yyyy/mm/dd)	Date 2 (yyyy/mm/dd)
ALOS	Ascending	515	2008/01/26	2008/04/27
ALOS	Ascending	514	2008/02/24	2008/05/26
Envisat	Ascending	155	2008/02/22	2008/05/02
Envisat	Descending	477	2007/04/01	2008/04/20

To build up a postseismic deformation time-series for the Yutian earthquake, we selected postseismic interferograms with relatively good coherence. Table S4.1 lists the date pairings of 11 postseismic interferograms for Envisat ascending track 155 covering 2008 May 2 (44 days after the mainshock) to 2009 November 13. There are two obvious near-field features for the postseismic interferograms, taking interferogram 080502-090626 as an example (Fig. S4.1a): a curved lobe with negative LOS displacement locates close to the northern end of the fault, and a belt

with positive LOS displacement sits at the southern end. Interferograms constructed with independent SAR acquisitions show similar features at the same position (e.g. interferogram 080606-090731 shown in Fig. S4.1b). This similarity suggests that the two main features represent displacement due to subsurface processes, rather than localized phase differences caused by atmospheric disturbance. As in the coseismic case, the footwall side is largely decorrelated.

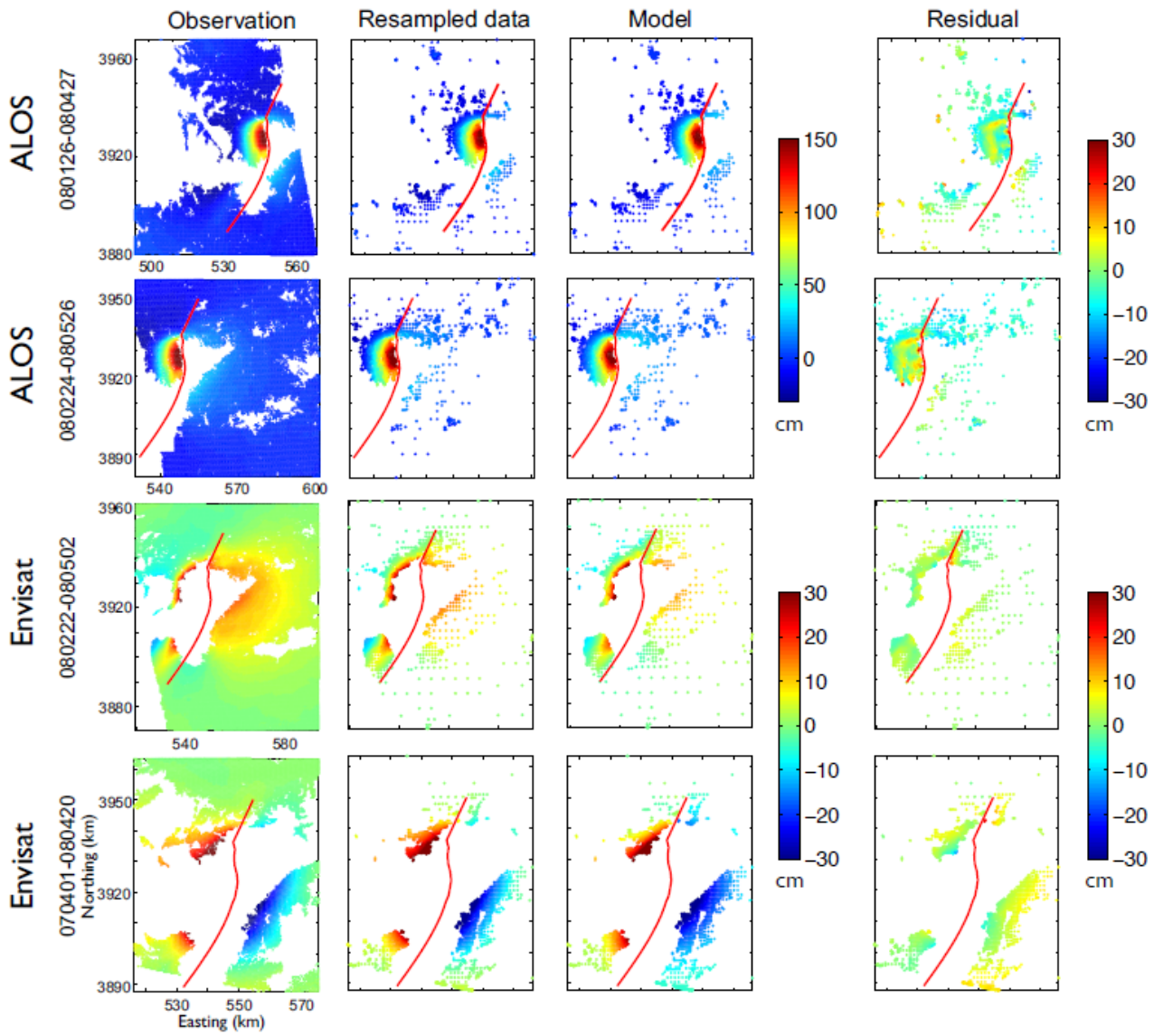

Figure 4. 2. The observed, downsampled and modelled InSAR coseismic data for the 2008 M_w 7.1 Yutian earthquake. The fourth column shows the residuals between the model and observation. Date pairing for each interferogram is shown on the left, with track information listed in Table 4.1. Red line marks the fault trace from this study.

Since the amplitude of the coseismic signal in the line-of-sight direction is sufficiently large (up to ~ 2.0 m), we do not attempt to correct for atmospheric errors contained in the coseismic interferograms. However, given the small amplitude and long wavelength of the postseismic signal, there may be a component of topography-correlated atmospheric noise. Before building up a postseismic deformation time-series, we therefore use the same procedure as described in Bie et al. (2014) for noise reduction. The atmospheric error is modelled by assuming a linear relationship between elevation and atmospheric delay, and the orbital error is approximated as a bi-linear ramp. Then, both errors are jointly modelled and subtracted from every postseismic interferogram. Regular grid downsampling by a factor of 10 is implemented for each interferogram (Ryder et al., 2007) to reduce the computation effort. Then, a similar least-squares inversion method as described in Bie et al. (2014) is adopted to perform the calculation for LOS displacement at every pixel during each time interval. Finally, LOS displacement maps at successive dates with reference to a common scene (in this case, the SAR acquisition on 2008 May 2) are produced by summing displacements in relevant time intervals.

4.3 Inversion method

The non-planar characteristic of the Yutian rupture requires that we construct the fault geometry a priori. We therefore follow Furuya & Yasuda (2011) in adopting a curved fault geometry. The surface trace of our source geometry generally respects the rupture mapped by Xu et al. (2013) for the central and southern sections, while the ‘en echelon’ transtensional pattern mapped along the northern section is simplified. The southern end of the fault is extended to where the change in sign of LOS displacement diminishes. In contrast to the short northern fault of Elliott et al. (2010), which left significant localized residual, we also extended the northern section. Different from Furuya & Yasuda (2011), who set the lower edge of the fault straight to avoid geometrical complication, we assume the bottom edge to be a down-

dip extension of the surface fault trace (e.g. Roten et al., 2011). Here the dip of the non-planar fault is approximated as that of the rectangle constructed by the four corner vertices.

We subdivided the non-planar fault into a collection of triangular dislocation elements (TDEs), rather than the common choice of rectangular dislocation elements (Okada, 1985). The non-planar fault was constructed and meshed using the CUBIT 14.0 geometry and mesh generation toolkit (http://cubit.sandia.gov). Because slip inversion resolution is poorer at depth, the mesh here need not be as dense as that at the top (Fig. S4.2). To achieve this, we set more (less) controlling vertices on the top (bottom) edge and the upper (lower) parts of the two sides. The size ratio of the TDEs at top and bottom is approximately 0.7.

For both the coseismic and postseismic cases, we solve for slip magnitude and direction on each TDE. Green's functions for normal and left-lateral components are computed by associating unit slip on individual TDEs with surface displacements at individual observation locations in a homogeneous elastic half-space (Meade, 2007). As shown by field investigation (Xu et al., 2013), the slip only has left-lateral and normal-fault components, and so a non-negative least-squares inversion scheme is applied. We use a Laplacian operator to smooth the adjacent dislocations and its effect is controlled by a factor *k*, for which the value is chosen by identifying the corner of the roughness versus misfit L-curve (e.g. Segall & Harris, 1987). To estimate the slip distribution error, we make 100 data sets perturbed by spatially-correlated synthetic noise (Wright et al., 2003) and rerun the non-negative least-squares inversion.

4.4 InSAR modelling results

4.4.1 Coseismic slip distribution model

Using the modelling approach described above, we explore different possible geometries, varying the dip angles independently at 5° intervals between 45° and 60°. Our preferred fault dips at 50° to the west. Fig. 4.2 shows the preferred results of the coseismic inversion that generates the lowest residual. The observed unwrapped interferograms are displayed on the left hand side, the optimal modelled LOS displacement is shown in the middle, and the residual is on the right hand side. The model successfully reproduces the main features of the coseismic deformation field, and the RMS (root mean square) misfits for the four interferograms are 7.0, 7.3, 3.4 and 4.6 cm respectively. The RMS is larger than that of the original interferograms, which is ~ 0.7 cm as derived from the 1-D covariance function of the far-field interferogram noise. A systematic along-strike residual in the hanging wall of the faults is present in the two ALOS residual maps (Fig. 4.2), but is absent in two Envisat residual maps due to incoherence in the hanging wall. This occurrence of systematic along-strike residual may be due to a listric sub-surface fault geometry, which is not modelled here. In addition, there is a positive residual of ~ 10 cm in the LOS direction in the footwall of the fault in track 477, which is also seen in the study by Furuya & Yasuda (2011). We interpret this as unmodelled atmospheric noise and/or unwrapping errors.

Our preferred source geometry and slip models are shown in Fig. 4.3. The normal slip component is dominant (Fig. 4.3b), with maximum amplitude approximately three times larger than the strike-slip component (Fig. 4.3a). Most slip occurs on the central segment over a depth range of 0 – 15 km, and the peak slip of 5.6 m is at 2.5 – 5 km depth (Fig. 4.3c). We also found that the slip distribution is characterized by a general rotation of the slip direction, which changes from normal faulting on the central and southern segments to left-lateral strike slip motion on the northern segment of the rupture (Fig. 4.3c). This is consistent with the trend shown by GCMT aftershock focal mechanisms (Fig. 4.1). The moment release is 4.99×10^{19} Nm, equivalent to a M_w 7.1 earthquake. Error analysis shows that the maximum standard deviation is ~ 8.0 cm, in the north lower corner and the shallow southern segment

(Fig. 4.3d). Slip on the central segment (where major slip occurs) is well retrieved, with the 1σ uncertainty generally ≤ 5 cm.

4.4.2 Afterslip model

The time-series in Fig. 4.4 reveals two localised hanging wall deformation features at the northern and southern ends of the fault, respectively. We plot the absolute average cumulative displacement of the pixels boxed in the two deformation features (boxes shown in Fig. 4.4a) in Fig. 4.4(k), showing a similar increasing trend and amplitude. This indicates that both features could be controlled by the same subsurface process, such as afterslip. A logarithmic function $U(t) = a \ln(1 + t/\tau)$ is applied to fit the postseismic deformation time-series using a non-linear least-squares method. Here, $U(t)$ is the displacement at time t since the mainshock, a is a constant and τ is the characteristic decay constant. For the northern and southern deformation patches, the decay constants τ are 70.7 d and 19.6 d, respectively. We note that viscoelastic relaxation would produce a circular uplift pattern across the normal fault (Ryder et al., 2010; Bie et al., 2014), unlike the pattern observed here. The difference in sign of the LOS displacements at the fault ends suggests a variation in postseismic slip direction, as for the coseismic case.

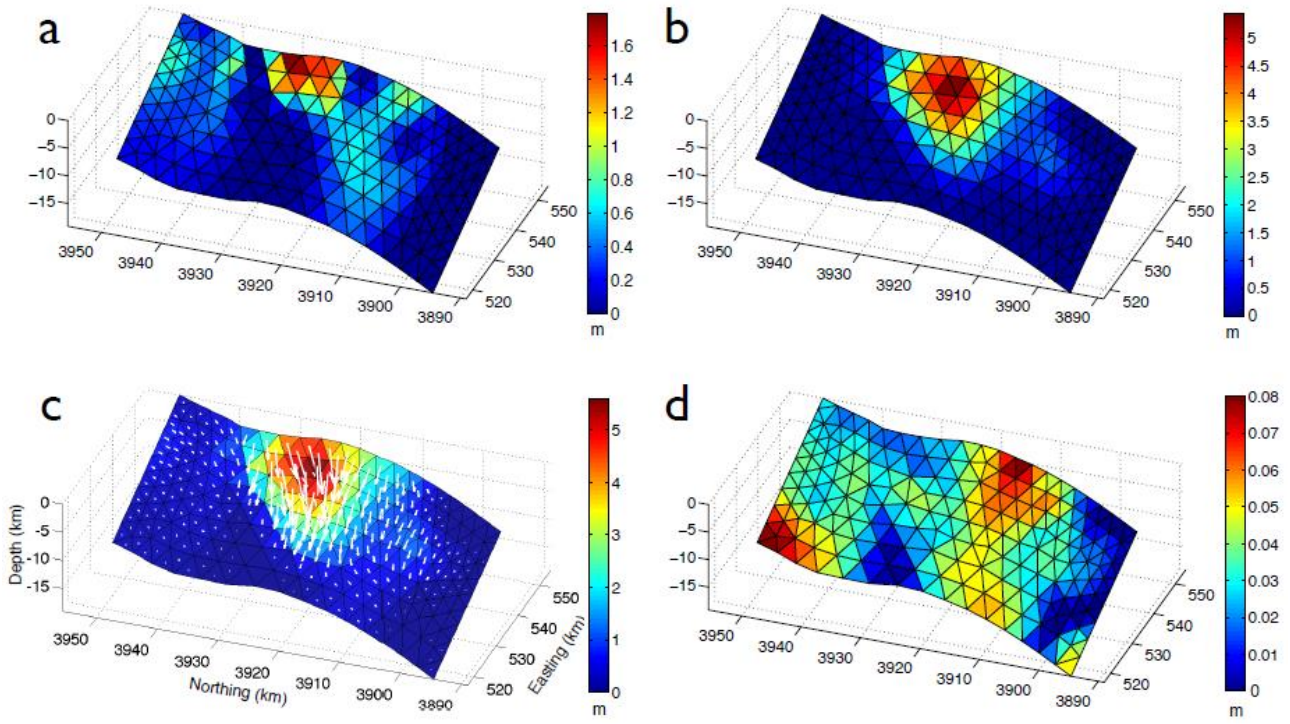

Figure 4. 3. Coseismic slip model for the 2008 Yutian earthquake from inversion of all four coseismic interferograms shown in Fig. 4.2. (a) Left-lateral strike slip component. (b) Normal faulting component. (c) Total slip on each TDE with slip direction marked by white vectors. (d) 1-sigma uncertainty for the slip distribution as shown in Fig. 4.3c.

We invert the postseismic deformation transients for afterslip in a similar way to the coseismic slip inversion. The results of the postseismic inversion are shown in Fig. 4.5. Two main features seen in the InSAR observations are well reproduced: one negative lobe close to the northern end of fault trace and a positive belt next to the southern end. The maximum RMS residual is 0.54 cm for the last epoch (Fig. 4.5k), and the minimum is 0.06 cm for the first epoch. The residual mainly appears in the vicinity of the northern segment (Fig. 4.5k), implying a geometrical complexity for this segment (e.g. an 'en echelon' pattern) as mapped by Xu et al. (2013). We note that there exists a residual with displacement sign change on the hanging wall near the bend between the northern and central segments. This could be due to the geometrical complexity and/or existence of an additional buried small fault striking in an E-W direction.

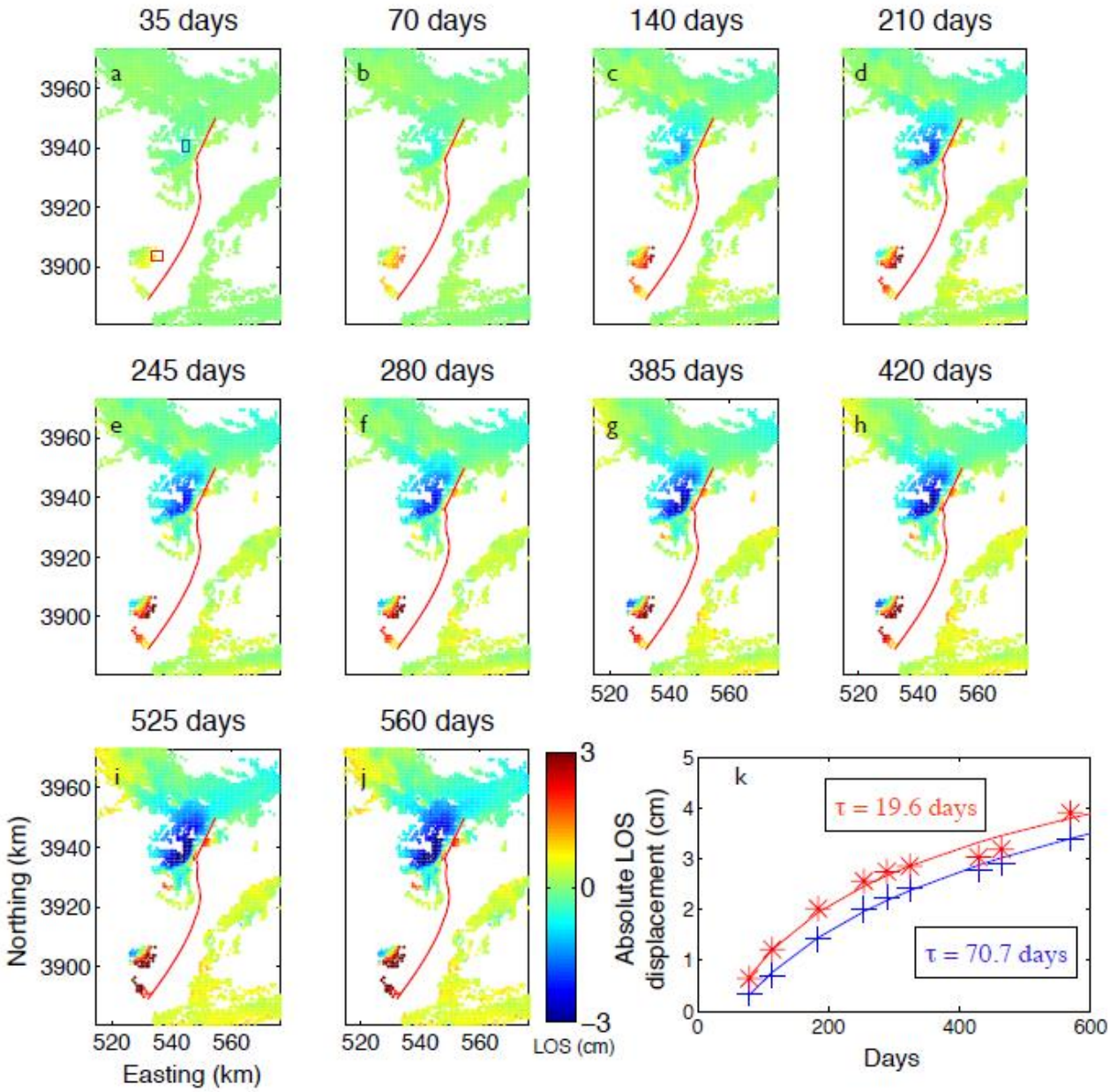

Figure 4. 4. (a) - (j) Postseismic deformation time-series. Title of each subfigure represents days since the first postseismic SAR acquisition on 2008 May 2 (44 d after the main shock). Red line marks the fault trace inferred in this study. (k) Cumulative postseismic displacement as a function of time. Red and blue dots correspond to absolute average values of pixels in the red and blue boxes in Fig. 4.4a, respectively. The best-fit logarithmic functions are marked by red and blue lines with corresponding relaxation times (τ) shown.

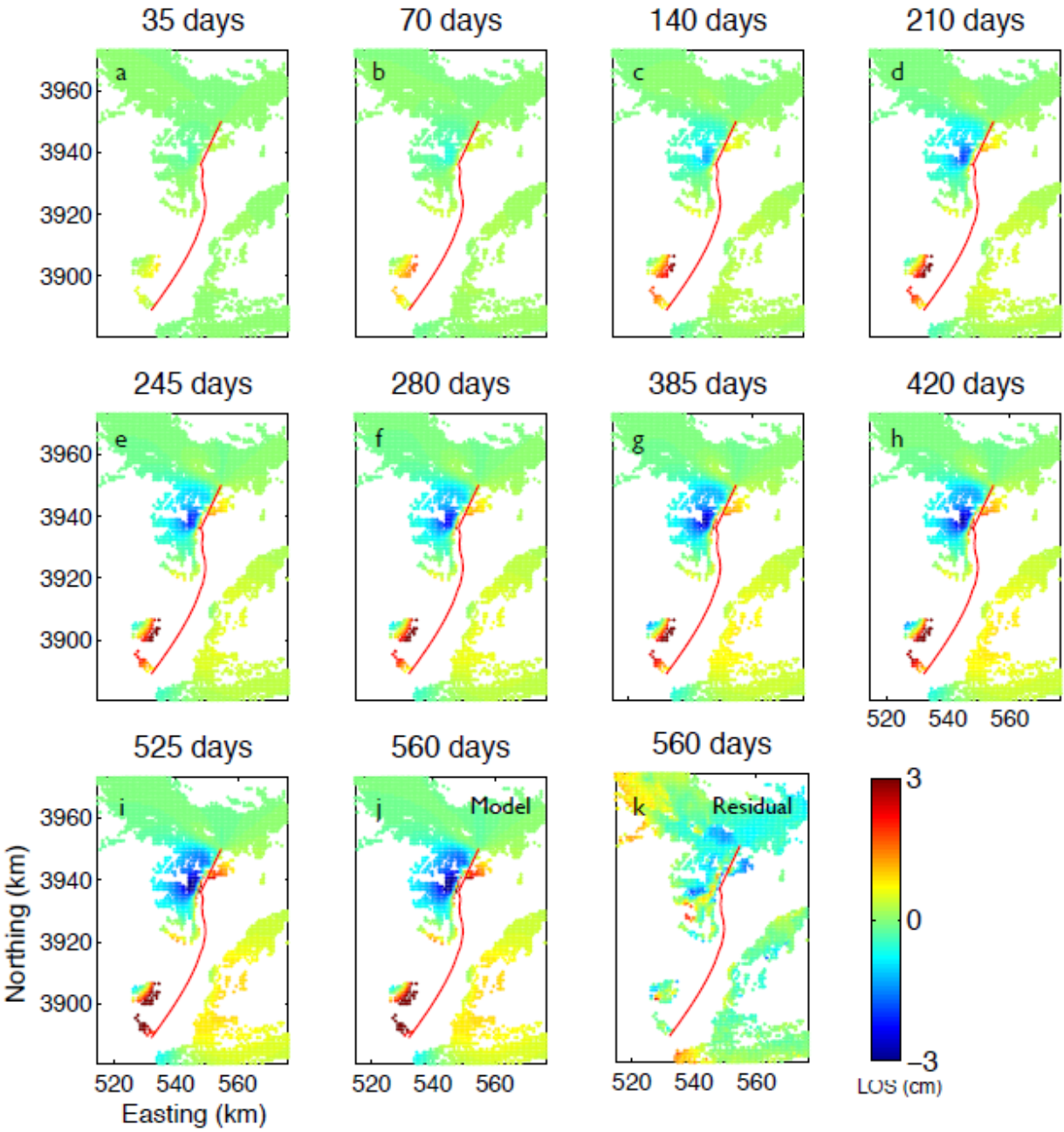

Figure 4. 5. (a) - (j) Modelled postseismic deformation time-series. Red line marks the fault trace inferred in this study. (k) Residual between modelled (Fig. 4.5j) and observed (Fig. 4.4j) postseismic deformation for the last epoch in time-series. Residuals for other epochs are shown in Fig. S4.4.

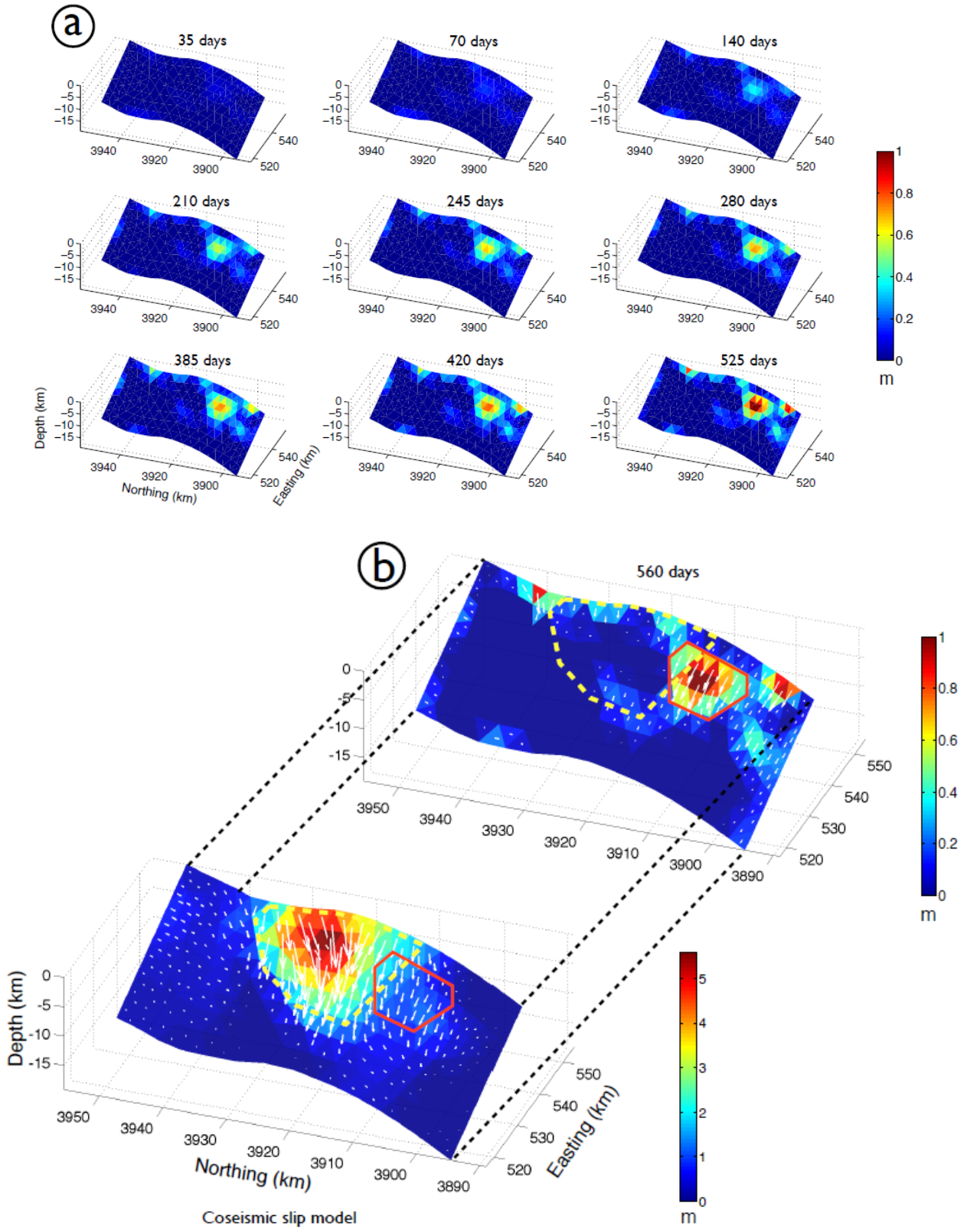

Figure 4. 6. (a) Afterslip distribution models for the first nine epochs, corresponding to Figs. 4.4a-i. (b) A 3D comparison view between the afterslip model for the last postseismic deformation epoch and the coseismic slip model. White vectors indicate the slip direction scaled with the slip magnitude. Yellow dashed contour encompasses the area with coseismic slip greater than ~ 2 m, and red solid line depicts the location of the largest afterslip patch.

Fig. 4.6 displays the afterslip distribution models. The main concentration of slip appears in the south at depths of ~ 2 – 9 km. The maximum afterslip is ~ 1.1 m, at 560 d since the reference SAR acquisition date. The sense of slip varies from left-lateral in the north to pure normal in the south, in agreement with the spatial variation of coseismic slip direction (Fig. S4.3). The cumulative afterslip moment is 6.6×10^{18} Nm, 13 per cent of that released by the mainshock. Through logarithmic fit to the postseismic deformation time-series, the averaged cumulative displacements for the first 44 d since the mainshock are 1.27 cm and 2.14 cm for the northern and southern deformation features, respectively. The cumulative displacement in the first 44 d since the mainshock is approximately half that of the total displacement from first postseismic SAR acquisition to the end of the current time-series. Thus, if we further include the energy released between the mainshock and the first postseismic SAR acquisition, a moment release of ~ 3.3×10^{18} Nm is expected. In total, the cumulative afterslip moment could reach 20 per cent of the coseismic moment release.

4.5 Coulomb stress change modelling

Stress changes associated with an earthquake have been demonstrated to induce or retard the seismic activity of surrounding regions (Freed, 2005). To examine the effect of the 2008 Yutian earthquake on neighbouring faults, we quantify whether these faults are brought closer to or moved away from failure by calculating the Coulomb stress changes (Scholz, 2002) according to:

$$\Delta\sigma_f = \Delta\tau + \mu'\Delta\sigma_n\,, \qquad (4.1)$$

where $\Delta\tau$ and $\Delta\sigma_n$ are shear and normal stress changes resolved on the receiver faults, and μ' is the apparent friction. We assume a μ' of 0.4, as is commonly assumed for a major strike-slip environment (Freed, 2007).

We calculate the changes in Coulomb stress contributed by the coseismic and postseismic phases of the 2008 Yutian earthquake. One significant difference to most other Coulomb stress change calculations is that we use a non-planar source model for the Yutian earthquake rather than rectangular dislocation sources. Meade (2007) gives explicitly the analytic expressions for strains due to slip on a triangular dislocation buried in an elastic half-space. Here we use these expressions to calculate strain, after which the stress changes can be derived according to Hooke's law. Then, the stresses are resolved on receiver faults. The geometry and slip directions of receiver faults listed in Table S4.2 are compiled from Styron et al. (2010) and Xu et al. (2013). Our calculations are carried out at a depth of 8 km, although the Coulomb stress changes are not sensitive to this value.

Fig. 4.7 shows the Coulomb stress change along major neighboring fault segments. Positive Coulomb stress changes resulting from coseismic rupture of the Yutian earthquake are mainly along structures in the southwest and northeast part of the map, where the Longmu-Gongza Co fault and the Altyn Tagh fault lie (Fig. 4.7a). The 2012 earthquake epicentre falls close to a zone of negative Coulomb stress change, suggesting that the occurrence of the 2012 normal faulting earthquake cannot be explained in terms of Coulomb stress change due to the 2008 Yutian earthquake. The epicentre of 2014 M_w 6.9 earthquake and its aftershocks align well with a splay left-lateral strike-slip fault (numbered 3 in Fig. 4.1) of the major left-lateral Altyn Tagh fault. Considering its location and slip sense – which agrees with the GCMT focal mechanism for the 2014 event – we argue that the splay fault is responsible for the occurrence of the earthquake. As illustrated in Fig. 4.7(a), the 2014 earthquake occurred on a segment where the 2008 earthquake exerted a positive Coulomb stress change.

We also test how the Coulomb stress change on the surrounding faults was modified by the 2012 M_w 6.2 earthquake and the 2014 M_w 6.9 earthquake. Although the current

lack of SAR acquisitions following the 2012 and 2014 earthquakes prevents us from inverting for detailed coseismic slip models, we estimate rupture length and width from empirical relations (Wells & Coppersmith, 1994), and uniform slip from the seismic moment release (Table S4.3). Figs 4.7(b) and (c) show the preliminary results of Coulomb stress change calculations on neighbouring faults caused by the 2012 normal faulting earthquake and 2014 strike-slip earthquake. The 2012 normal faulting earthquake adds a positive Coulomb stress change to the 2014 strike-slip earthquake rupture, although the change is an order of magnitude smaller than that imposed by the 2008 Yutian earthquake. The 2014 rupture mainly affects the stress change on the Altyn Tagh fault to the east of the junction (Fig. 4.7c). Collectively, Fig. 4.7(d) shows the combined effect of the three earthquakes.

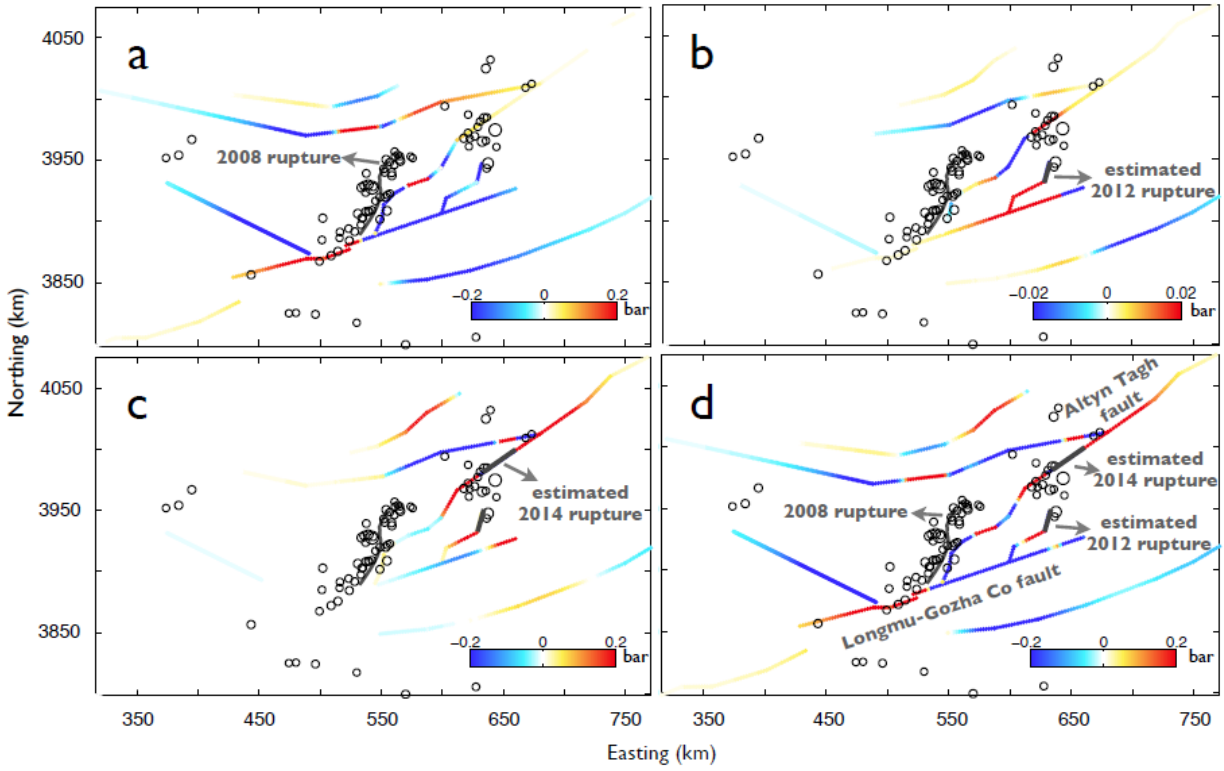

Figure 4. 7. Coulomb stress changes along faults surrounding the three recent earthquakes (ruptures marked by grey solid lines and labeled accordingly) at a depth of 8 km. An apparent friction coefficient of 0.4 is used. Here, the Coulomb stress change calculation considers: (a) the coseismic and postseismic stress change induced by the 2008 M_w 7.1 earthquake; (b) the coseismic stress change imparted by the estimated 2012 rupture; (c) the coseismic stress change brought about by the estimated 2014 rupture; and (d) the combined stress change caused by the three earthquakes mentioned above. Black circles, scaled by magnitude and shown at their USGS archive location, denote earthquakes (with $M \geq 4.5$) that occurred between 2008 March 20 and 2014February 23.

4.6 Discussion

4.6.1 Spatial pattern of coseismic slip and afterslip models

The generally NS-striking normal fault and its rupture in 2008 demonstrate a local extensional stress field. We notice that a local stress field perturbation occurred on the northern segment: as shown in Fig. S4.3, both coseismic and postseismic slip models of the 2008 Yutian earthquake show a changing slip direction from left-lateral on the northern segment to extensional on the central and southern segments. The aftershock focal mechanisms from the GCMT catalogue show a first-order similarity in fault slip direction with the InSAR modelling results (Fig. 4.1). In the vicinity of the northern segment, at least three focal mechanisms have a nodal plane dipping to the NW with a left-lateral strike-slip component.

As found for other normal faulting earthquakes (e.g. Copley et al., 2012; D'Agostino et al., 2012; Bie et al., 2014), the resolved afterslip patches mainly distribute around the coseismic rupture, though in patches rather than being continuous (Fig. 4.6b). The patchiness of the afterslip distribution implies that the frictional properties controlling aseismic slip are highly heterogeneous across the fault surface. The major cluster of afterslip patches is on the southern segment, in the upper ~ 8 km of the coseismic fault plane. The same area marked in the coseismic model also shows locally elevated slip amplitude, implying that current coseismic slip model may account for some early postseismic deformation. On the northern and central segments, several shallow afterslip patches reach the surface. Although a small amount of afterslip appears downdip of the coseismic rupture, we tend to believe that for normal faulting earthquakes, shallow afterslip is the major source responsible for the near-field postseismic deformation.

4.6.2 Driving stresses behind the Yutian earthquake

What causes the E-W extension in Tibet is a long-debated question. Multiple explanations have been proposed, such as gravitational collapse (e.g. Molnar & Tapponnier, 1978; Molnar & Lyon-Caen, 1989), convective removal of the lower mantle lithosphere (England & Houseman, 1989), basal shear due to Indian Plate indention (McCaffrey & Nabelek, 1998; Ratschbacher et al., 2011; Copley et al., 2011), and simple shear induced by lower crustal flow (Zhang et al., 2013). Elliott et al. (2010) preferred the gravitational spreading model to explain the occurrence of the Yutian earthquake, in consideration of the extraordinarily high elevation (> 5000 m) of the epicentral area. Furuya & Yasuda (2011) attributed the Yutian rupture to extensional stress release in a stepover zone controlled by a large sinistral strike slip fault system.

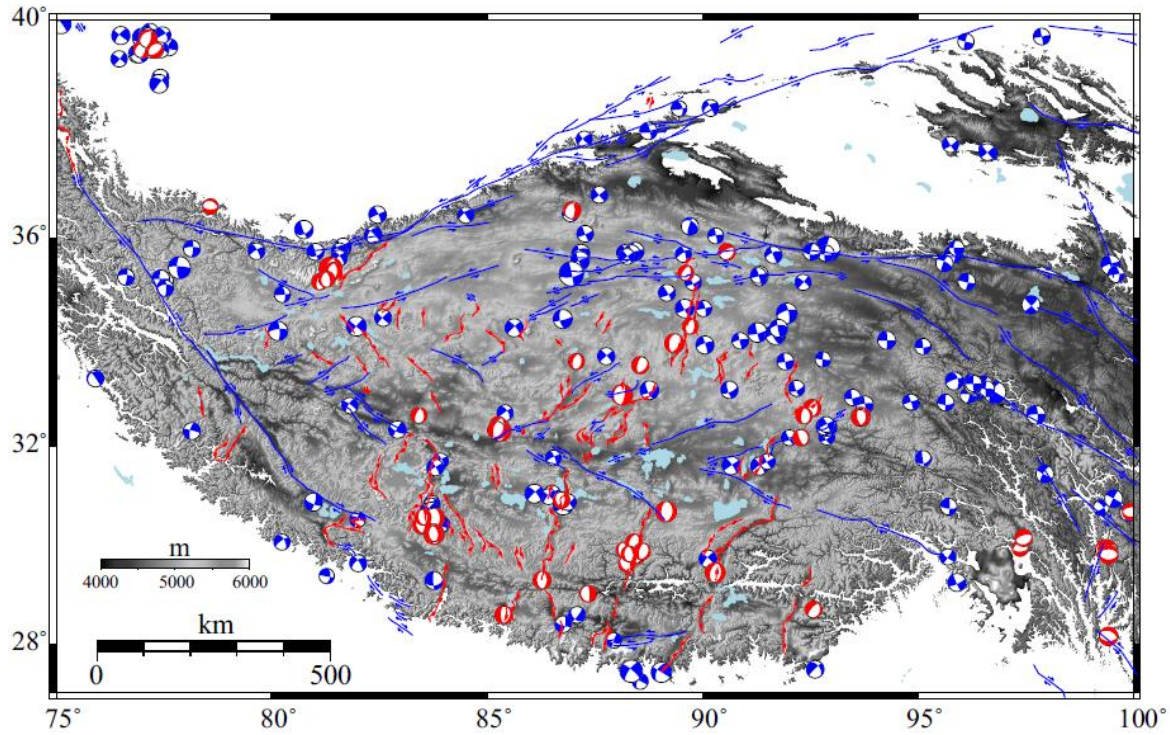

Figure 4. 8. (a) Distribution of focal mechanisms across the Tibetan Plateau since 1972 from the GCMT catalogue, overlain on GTOPO30 topography. Earthquakes included are restricted to those with solutions near pure-normal and pure strike-slip (that is, rake is within 20° of the pure sense of slip). Red are extensional solutions and blue are strike-slip solutions. Strike-slip faults and normal faults as mapped in the field are marked in blue and red, respectively. Elevations below 4000 m and above 6000 m are set to white, to sharpen the relief in the plateau interior.

We note that strike-slip and normal fault earthquakes appear in close proximity in many places in Tibet (Fig. 4.8), for example along the Bangong-Nujiang suture zone, and in the epicentral areas of the 2008 Yutian, Nima and Zhongba earthquakes. This is in general agreement with geologically mapped fault structures (Fig. 4.8). In the Lhasa terrane, north-trending rifts are kinematically linked with right-slip faults near the Bangong-Nujiang suture, and to the north of the suture, NNE-striking normal faults merge with left-slip faults (Taylor et al., 2003). The Yutian rupture inferred from this study is bounded by the left-slip Altyn Tagh fault and Longmu-Gozha Co fault (Fig. 4.1). Another correlation between the two types of earthquake is that both release most of their energy at elevations above 4500 m (see fig. 20 of Elliott et al., 2010). It is reasonable to postulate that normal and strike-slip faults are closely linked kinematically. Given that the 2008 Yutian earthquake locates in a stepover zone linking large strike-slip faults, it seems that its occurrence could be explained by its regional tectonic environment, instead of or in addition to gravity-driven collapse. It is possible that the bending of the Altyn Tagh fault also influences the kinematic behaviour of the Yutian fault, although we prefer to explain the Yutian earthquake by means of a stepover zone closely linked to the Altyn Tagh fault and the Longmu-Gozha Co fault at its northern and southern ends, respectively.

4.6.3 Stepover zone failure and stress transfer on the Altyn Tagh fault

Through the Coulomb stress change calculations (Fig. 4.7), we identify parts of bounding strike-slip faults on which the positive Coulomb stress increase is greatest, e.g. the west segment of the Longmu Gozha Co fault and the Altyn Tagh fault segment to east of the junction (Fig. 4.7d). For a stepover zone as illustrated in Fig. 4.9(a), failure of stepover faults has the potential to trigger earthquake rupture on ‘en echelon’ strike-slip faults. Indeed, the occurrence of a M_w 6.9 strike-slip earthquake on an adjacent fault 6 yr after the Yutian event was likely a case of static stress triggering. How the stepovers and linking dip-slip faults affect rupture propagation

between strike-slip faults has been modelled and discussed widely, to shed light on their role as either barriers or preferred nucleation points (e.g. Harris et al., 1991; Harris & Day, 1993; Oglesby, 2005; Duan & Oglesby, 2006). One of the most studied regions is the western end of the North Anatolian fault, Turkey, where the August 1999 Izmit earthquake occurred (e.g. Armijo et al., 2002; Duman et al., 2005). Here, our results may have important implications from the other side: namely, that the failure of extensional stepovers could potentially trigger earthquakes along strike-slip faults.

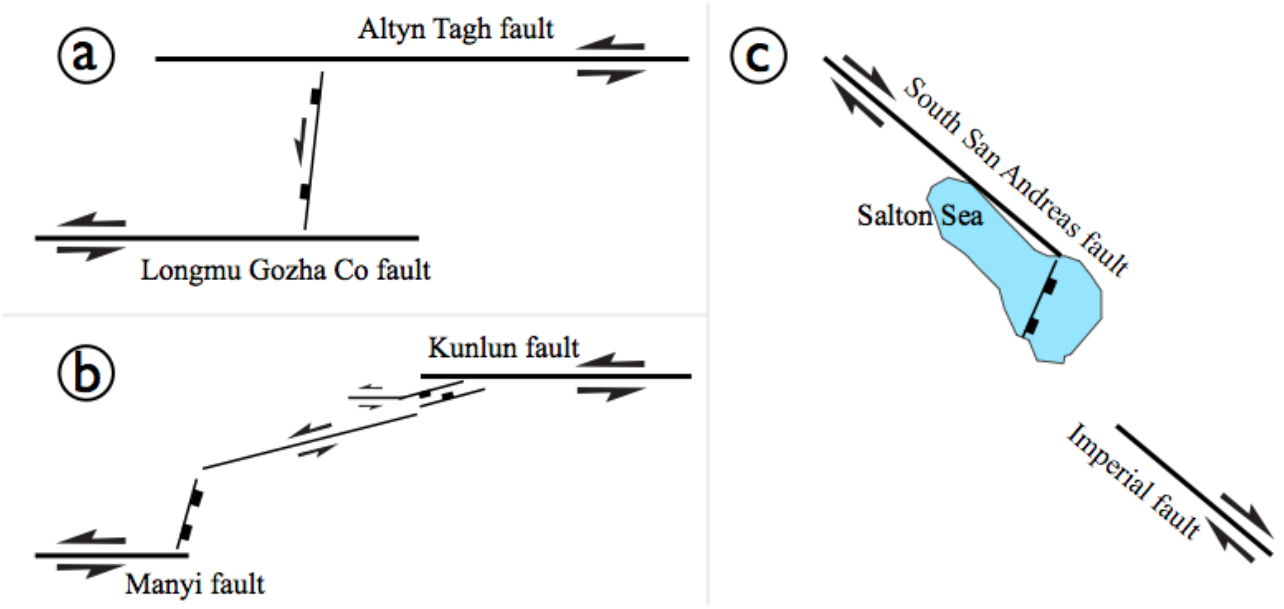

Figure 4. 9. Schematic models of step-over zones: (a) where the 2008 Yutian earthquake ruptured; (b) where the sinistral Manyi fault and the western end of Kunlun fault are linked (modified from fig. 1 of Lasserre et al. 2005); and (c) the pull-apart between the dextral south San Andreas fault and Imperial fault (modified from fig. 1 in Hole, 2011).

Our study gives a hint about potential seismicity dynamics in regions with similar tectonic configuration on the Plateau and elsewhere. On the northern Tibetan Plateau, strike-slip faults are broadly distributed and segmented by extensional stepovers. As illustrated in Fig. 4.9(b), for example, the Manyi fault and the western end of Kunlun fault are linked by a complex stepover zone with multiple normal faults (Tapponnier et al., 2001; Xu et al., 2002; Lasserre et al., 2005). According to Antolik et al. (2004)

and Lasserre et al. (2005), the rupture of 2001 M_w 7.8 Kokoxili earthquake was probably initiated by stepover zone failure at the western end of the Kunlun fault preceding the main moment release. In California, the southern San Andreas fault (SSAF) terminates in an extensional stepover zone beneath the Salton Sea (Fig. 4.9c). Brothers et al. (2011) studied flood-induced active fault movement in the stepover zone and its loading on the SSAF, and found that Coulomb stress change on the SSAF increased at least 14 bars, sufficient to trigger an earthquake.

It is clear that recent seismic and aseismic activities in the Ashikule stepover zone significantly increases the Coulomb stress change on the Altyn Tagh fault to the east of the junction with the fault splay (Fig. 4.7d). Historically, there was a pair of large earthquakes with magnitude 7.1 in 1924 along this segment of the Altyn Tagh fault, ~ 150 km to the NE of the 2014 earthquake (Engdahl & Villasenor, 2002). The absence of major earthquakes since then may indicate that this segment is likely at a mid to late stage of its seismic cycle. Assuming a slip rate of 10 mm/yr (Elliott et al., 2008; He et al., 2013), a slip deficit close to 1 m has accumulated since the 1924 events, and our preliminary calculation also indicates that it would take ~ 40 yrs to accumulate a similar amount of stress (~ 0.2 bars) on the Altyn Tagh fault as that caused by the earthquakes considered in this study. InSAR-recorded ground deformation will help better constrain the fault location, geometry and slip distribution model for the 2014 earthquake, thus enabling a refinement of the Coulomb stress change map and facilitating seismic risk assessment.

4.7 Conclusions

We presented coseismic and new postseismic InSAR data for the 2008 M_w 7.1 Yutian earthquake. Our revised model of fault geometry and coseismic slip takes field-mapped ruptures into account. From the InSAR data we produced a postseismic time-series covering ~ 1.5 years following the mainshock, and generated a time-series of

afterslip. For both coseismic and postseismic phases, normal slip occurs in the middle and southern segments, while left-lateral slip occurs in the northern segment. This is in accordance with focal mechanisms of aftershocks. Afterslip mainly occurs in a patchy rim around the top half of the mainshock rupture, indicating heterogeneity in fault frictional properties. Coulomb stress changes on neighbouring faults are calculated from the non-planar source model. We demonstrate from a static stress change perspective that the 2012 M_w 6.2 normal faulting earthquake was likely not triggered by the 2008 event. Conversely, the 2008 rupture brought the region of the 2014 event closer to failure. Collectively, the 2008 and 2014 earthquakes have brought part of the Altyn Tagh fault closer to failure. Putting the 2008 Yutian earthquake in a more general tectonic context, we conclude that failure of stepover zone normal faults could bring 'en echelon' strike-slip faults closer to rupture. Similar interactions between strike-slip faults and extensional stepover zones are expected to apply in similar tectonic environments both on the Tibetan Plateau and elsewhere in the world.

Acknowledgements

Lidong Bie is supported by a joint scholarship from the China Scholarship Council and the University of Liverpool. Fig. 4.1 and Fig. 4.8 were made using GMT (Wessel & Smith, 1998). Envisat data are from the ESA, Category-1 project 5199. ALOS data are from the ASF L1 datapool.

Chapter 5

Deep postseismic viscoelastic relaxation excited by an intraslab normal fault earthquake in the Chile subduction zone

Lidong Bie[*1], Isabelle Ryder[1], Marianne Metois[2]

[1]*School of Environmental Sciences, University of Liverpool, UK.*

[2] *Instituto Nazionale di Geofisica e Vulcanologia, Centro Nazionale Terremoti, Via di Vigna Murata, 605, Rome, Italy.*

E-mail: l.bie@liv.ac.uk

Manuscript prepared for submission

Abstract

The 2005 M_w 7.8 Tarapaca earthquake was the result of normal faulting on a west-dipping plane at a depth of ~ 90 km within the subducting slab of the North Chilean gap that partially ruptured in 2014. We use Envisat observations of nearly four years of postseismic deformation following the earthquake, together with some survey GPS measurements, to investigate the viscoelastic relaxation response of weak layers to the coseismic stress. We constrain the rheological structure by testing various 3D models, taking into account the vertical and lateral heterogeneities in viscosity that one would expect in a subduction zone environment. A viscosity of $4 – 8 \times 10^{18}$ Pa s for the continental asthenosphere fits both InSAR line-of-sight (LOS) and GPS horizontal displacements reasonably well. In order to test whether the Tarapaca earthquake and associated postseismic relaxation could have triggered the recent Iquique sequence, we computed the Coulomb stress change induced by the co- and post-seismic activities following the Tarapaca earthquake on the megathrust interface

(which ruptured in the 2014 *M* 8.2 Iquique earthquake) and nodal planes of its *M* 6.7 preshock. These calculations show that static stress triggering by the Tarapaca earthquake may act as an indirect trigger for the Iquique earthquake, via loading of the *M* 6.7 preshock. We demonstrate the feasibility of using deep intraslab earthquakes to constrain subduction zone rheology. Continuing geodetic observation following the 2014 Iquique earthquake may further validate the rheological parameters obtained here.

5.1 Introduction

One of the key factors that influence understanding of the physics governing megathrust earthquake cycles is our limited knowledge of subduction zone rheology. Theoretically, stresses induced by megathrust earthquakes will be relaxed in any weak layers beneath the upper crust. Postseismic deformation produced by this viscoelastic relaxation process (VER) may be modeled to constrain the rheology. Recent advances in the spatial and temporal coverage of geodetic measurements have seen transient deformation following several megathrust earthquakes being explicitly investigated to infer rheological properties at various subduction zones (e.g. Pollitz et al., 2008; Hu & Wang, 2012; Sun et al., 2014; Trubienko et al., 2014).

Intermediate depth earthquakes represent another type of event in subduction zones that rupture within the subducting slab at depths of 70 to 300 km. Large intermediate-depth earthquakes also induce stresses, which will gradually be released by VER in any nearby weak layer(s), and produce transient deformation that could be indicative of subduction zone rheology. To test the feasibility of using normal faulting earthquakes to constrain subduction zone rheology, we investigate InSAR and GPS observations following the 2005 magnitude 7.8 Tarapaca earthquake, which occurred ~ 100 km inland from the coast in northern Chile (Fig. 5.1). Seismological and

geodetic studies identify this earthquake to have occurred on a shallow west-dipping intraslab fault at ~ 90 km depth (Peyrat et al., 2006; Delouis & Legrand, 2007).

In this region, the Nazca plate subducts beneath the South American plate at a rate of ~ 7 cm/yr. Studies of interseismic deformation show that this segment of plate boundary is overall highly locked, with a local decrease of the coupling in front of Iquique (e.g. Chlieh et al., 2011; Béjar-Pizarro et al., 2013; Métois et al., 2013). In April 2014, the magnitude 8.2 Iquique earthquake occurred ~ 100 km offshore and partially released the strain accumulated on the shallow interface since the last big earthquake in 1877 (e.g. Ruiz et al., 2014; Schurr et al., 2014; Bürgmann, 2014).

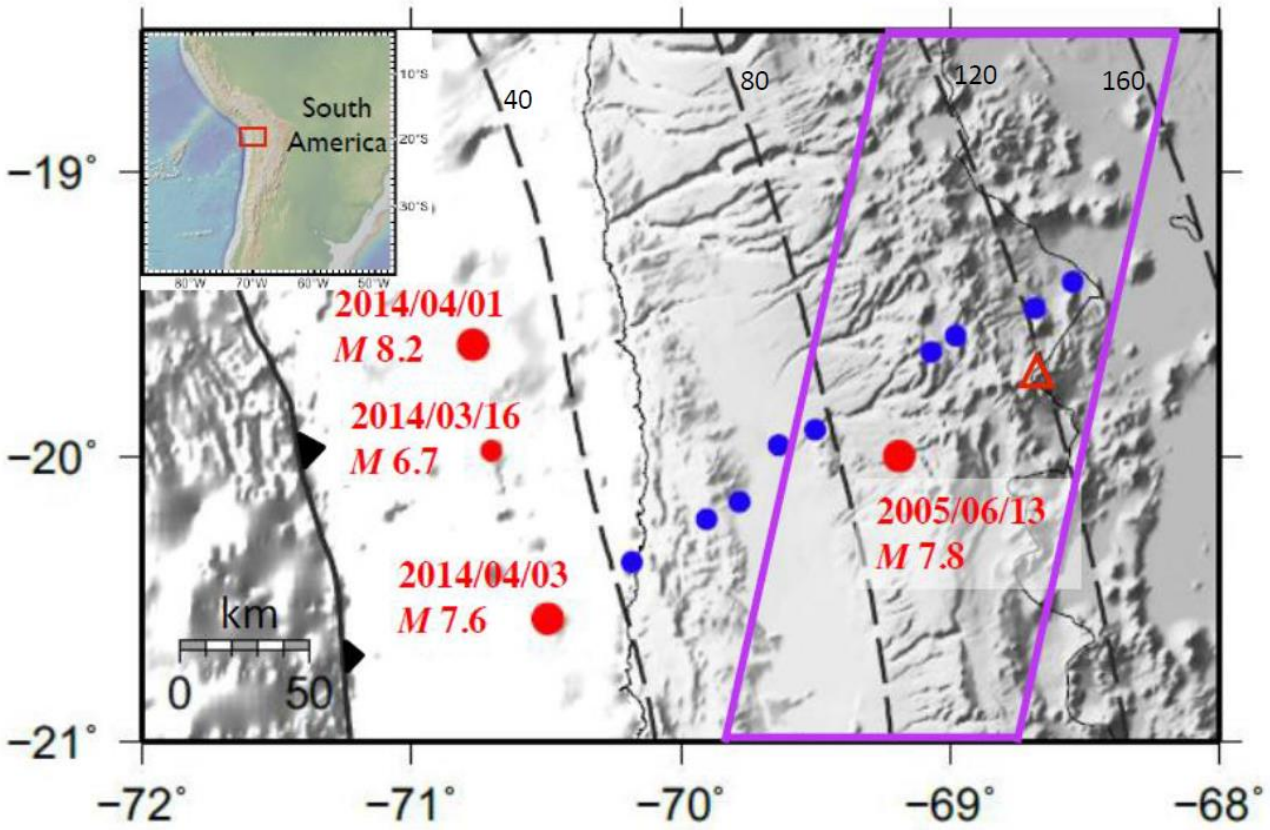

Figure 5. 1. Topographic map of the northern Chile subduction zone. Grey dashed contours represent the depth of the subducting Nazca plate in 40 km intervals, from slab1.0 (Hayes et al., 2012). Red dots mark the locations of earthquakes in this study. Red triangle marks the location of the Sillajhuay volcano. Blue dots are survey-mode GPS locations (Métois et al., 2013). Purple lines delineate the area covered by InSAR data shown in Fig. 5.2. Inset figure shows the study region relative to South America.

The other aspect of this work is to investigate the stress perturbation effect of intraslab earthquakes on the megathrust interface. The occurrence of the 2014 Iquique earthquake provides a natural opportunity for that purpose. We assess the static stress change brought about by the 2005 Tarapaca earthquake and subsequent VER, and explore whether the 2014 Iquique earthquake, or the energetic foreshock sequence in the preceding months, may have been triggered by the 2005 Tarapaca earthquake.

5.2 Data and rate map

5.2.1 InSAR data

We collect all postseismic SAR images from the C-band Envisat satellite spanning ~ 4 yrs from July 2005 to August 2009. In total, 29 SAR acquisitions from track 96 are processed, each with a swath nearly 500 km long, large enough to give a good coverage of the potential VER-induced long-wavelength ground displacement. Given the relatively arid regional environment and sparse vegetation, the coherence is generally good, leading to a total of 135 interferograms produced using the JPL/Caltech software ROI_PAC (Rosen et al., 2004). Topographic phase is removed using the 3-arc-second DEM from the Shuttle Radar Topography Mission (Farr et al., 2007). The interferograms are unwrapped using a branch-cut method (Goldstein & Werner, 1998).

The detection of low-amplitude, long-wavelength postseismic signals has in general been limited by atmospheric delays and imprecise orbits (Jolivet et al., 2014). To mitigate the atmospheric delay effect, we adopt the method described by Walters et al. (2013) and Jolivet et al. (2014). We estimate the phase delay caused by water vapor difference using data from the Medium-Resolution Imaging Spectrometer (MERIS) instrument aboard the Envisat satellite, and that caused by spatial variation

of atmospheric pressure using the ERA-Interim global atmospheric model provided by the European Centre for Medium-Range Weather Forecasts (ECMWF). The effective use of MERIS data requires a largely cloud-free (< 25 per cent cloud) weather condition, which constrains the number of usable interferograms to 45 (Fig. S1 and Table S2). After correction for atmospheric noise, uncertainties associated with the satellite orbits are removed assuming a linear phase ramp across the interferogram. Removal of a linear ramp should not compromise any postseismic signal, although the effect of plate interface creep may be reduced.

Given the depth of the earthquake (~ 90 km), any postesismic signal is expected to be small (i.e. few millimetres). Considering the low signal-to-noise ratio, we chose to build a deformation rate map, rather than a time-series. The rate map is produced by averaging the added phase of 45 noise-corrected interferograms over their total time span. Out of the 45 interferograms, pixels coherent in at least 40 interferograms are stacked to produce a rate map.

The rate map shows two notable features (Fig. 5.2). One is the circular negative line-of-sight change associated with activity at Sillajhuay volcano, with a peak rate of ~ 1.4 cm/yr. The other feature is a broad-scale negative millimeter-level line-of-sight change over the area of the coseismic rupture. Given that Envisat data are most sensitive to vertical component and the fault's orientation, the negative change can be mostly attributed to uplift, in contrast to the circular zone of subsidence that occurred coseismically (Peyrat et al., 2006). This contrast of coseismic and postseismic displacement is a first hint that the postseismic relaxation mechanism is VER. In Section 5.3 below, we run models to explore whether VER is a viable mechanism.

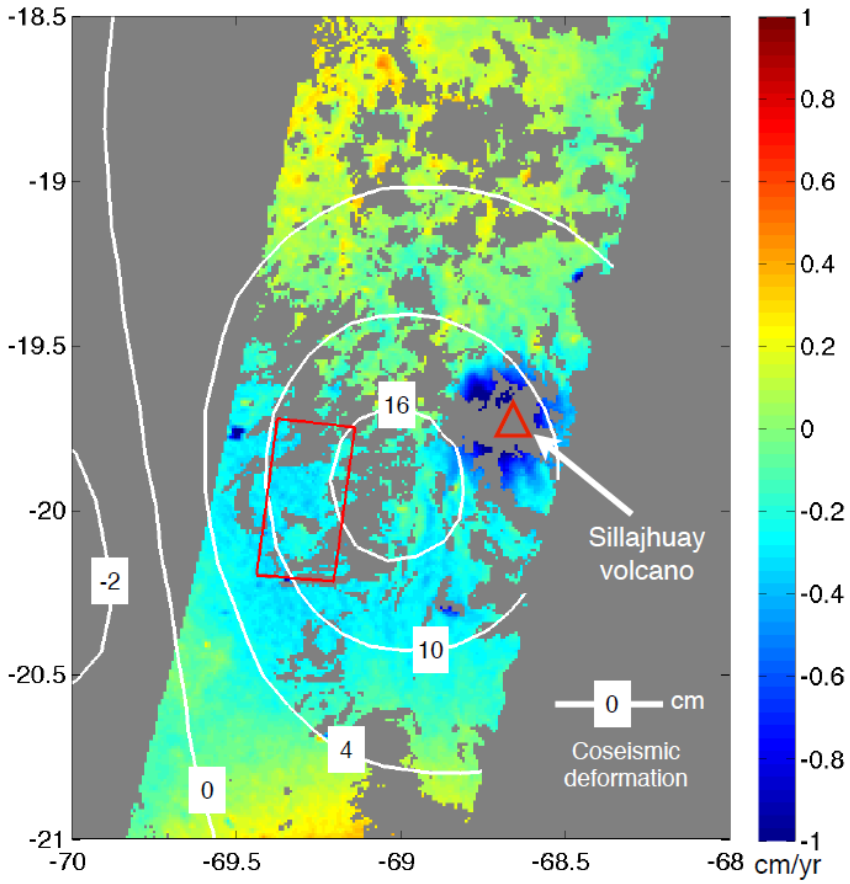

Figure 5. 2. Rate map constructed from postseismic Envisat interferograms from June 2005 to March 2009, as listed in Table S5.2. Warm colours indicate LOS motion away from the satellite. Coseismic deformation of the Tarapaca earthquake is shown by white contours, with positive values representing motion away from the satellite. Red rectangle is the surface projection of the Tarapaca rupture from Peyrat et al. (2006). Red triangle marks the location of the Sillajhuay volcano.

5.2.2 GPS data

In this study, we take advantage of the long-standing campaign measurements of the GPS network installed by Chilean and French teams in North Chile starting in the 1990's (Ruegg et al., 1996). Indeed, one profile composed of 9 benchmarks traverses the epicentral area of the Tarapaca earthquake (Ruegg et al., 1996; Chlieh et al., 2004; Métois et al., 2013) from the coast to the vicinity of the Sillajhuay volcano in a northeast direction (Fig. 5.1). Measurements have been conducted on this network

before the Tarapaca earthquake, in 1996 and 2000, with an additional measurement in 2002 for two stations. Altogether, all benchmarks have been measured at least twice preseismicly on a 3 or 6 years time span. The next survey was carried out in the month following the Tarapaca earthquake that took place on 13 June 2005, and subsequent measurements were conducted in 2010 and 2012.

We process all these data following the method described in Métois et al. (2013) using the GAMIT-GLOBK software (King & Bock, 2002), and obtain horizontal velocities before and after the 2005 Tarapaca earthquake (Fig. 5.3a, and Table S5.3 & S5.4). Velocities calculated first in the ITRF 2008 (Altamimi et al., 2011) are then rotated into a fixed South America reference frame as defined by the absolute pole from the NNR Nuvel-1A model (DeMets Gordon, 1994).

The large uncertainties associated with the pre-Tarapaca velocities (Table S5.3) are mostly due to the bad quality of orbits and reference frame stations prior to 1997, to poor-quality antenna calibration models, and to the fact that the observation sessions were often shorter than an entire day (in particular for the first 1996 campaign). However, the large time-span covered by the measurements gives us confidence in these velocities. We observe a significant difference between the pre- and post-Tarapaca velocities (Fig. 5.3b and Table S5.5). The residual velocities are systematic and produce a divergent pattern away from the epicentral area (Fig. 5.3b) that is consistent with the regional inflation observed with InSAR (see section 5.2.1). We therefore interpret this change in velocity before and after the Tarapaca earthquake as mostly due to the postseismic VER following the mainshock. However, part of this residual motion could be due to rapid afterslip in the weeks following the mainshock, or due to changes in the degree of interseismic coupling on the plate interface, as indicated by the increase in velocity changes towards the coast. The divergent pattern centred on the Tarapaca epicentre speaks in favor of a signal dominated by postseismic VER, and we will test this hypothesis in the following modelling section.

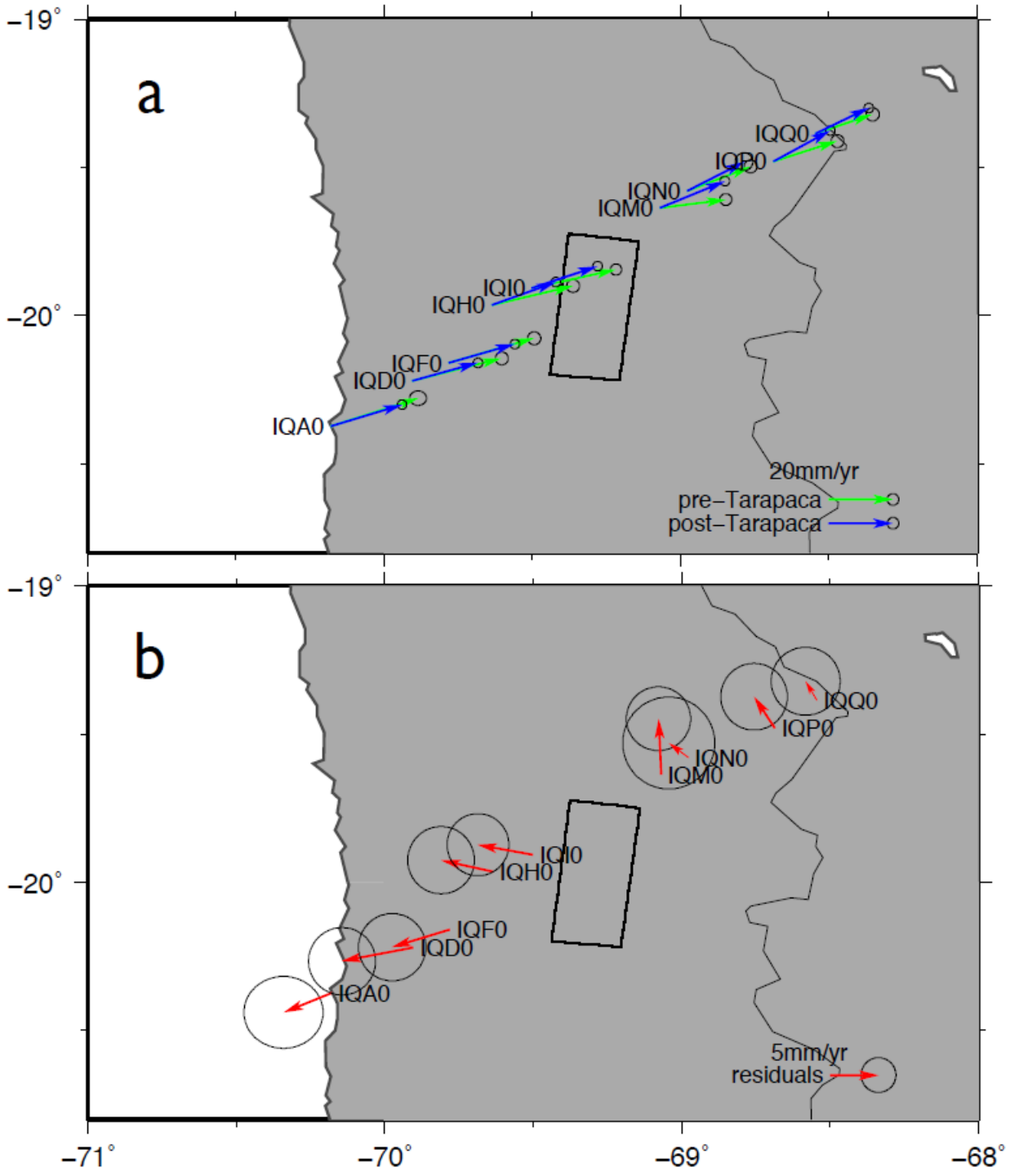

Figure 5. 3. (a) Horizontal velocities relative to stable South America from survey mode GPS measurements before and after the Tarapaca earthquake. (b) Difference between the pre- and post-mainshock displacements shown in (a) (see Table S5.3 – S5.5). Black rectangle is the surface projection of the Tarapaca rupture from Peyrat et al. (2006).

5.3 Modelling

5.3.1 VER modelling

Seismic tomography studies in this region reveal two important features of the subduction zone rheology. The first is a uniform low P-wave attenuation for the forearc, extending eastward to longitude -69°. In accordance with low surface heat flow values, the low attenuation indicates a cold and stagnant forearc. The second is a ~ 45 km-thick layer beneath the magmatic arc with high P-wave attenuation, interpreted as being composed of partial melts ascending from mantle asthenosphere (Schurr et al., 2003). The 2005 Tarapaca earthquake occurred within the subducted rigid oceanic lithosphere. Given its proximity to the weak layer, there is a good chance that any coseismic stress perturbation excited a VER process. To model the VER-induced surface displacement, we used the software RELAX, a 3-D semi-analytic package which can incorporate lateral rheological heterogeneity (Barbot & Fialko, 2010).

Our model configuration is shown on a cross section perpendicular to the trench in Fig. 5.4. The elastic layers of the continental and subducted oceanic lithosphere are both set to have a thickness of 40 km. A Poisson's ratio of 0.25 is assumed, and a uniform shear modulus of 63.4 GPa is set for the entire model (Hetland & Zhang, 2014). As an input, the coseismic slip model we adopted is from Peyrat et al. (2006), as summarized in Table S5.1. Assuming a Maxwell viscoelastic rheology, we fixed the oceanic mantle viscosity at 1×10^{20} Pa s, which is similar to the global mantle average (Moucha et al., 2007), as used by Wang et al. (2012). Forward modelling tests show that decreasing the viscosity of the oceanic mantle increases the RMS misfit (Fig. S5.2). The rheological parameters we aimed to constrain include the size of the strong forearc H_A (zone A), the thickness H_B and viscosity η_B of the weak layer below the magmatic arc (zone B), and the viscosity of the area η_C (zone C) beneath zone B.

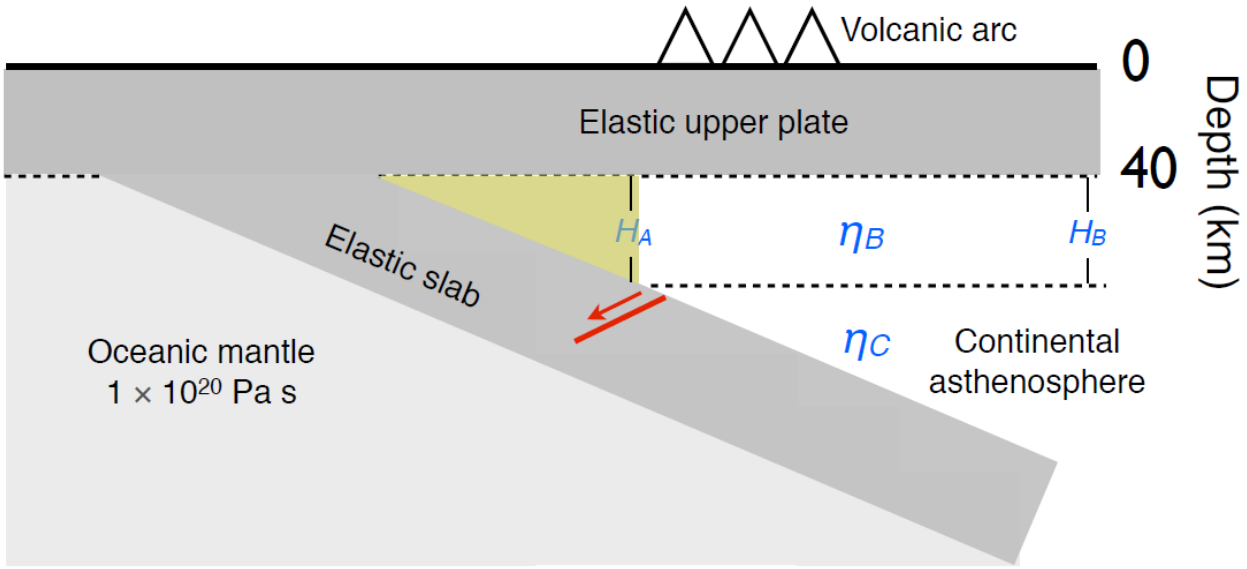

Figure 5. 4. Schematic cross-section perpendicular to the trench, showing the rheological structure constrained in this study. Yellow triangle represents the cold and stagnant part of the forearc (zone A). Parameters (H_A, H_B, η_B and η_C) in blue are variables to infer. Oceanic mantle viscosity is fixed, but its effect on surface deformation is tested and shown in Fig. S5.2.

In order to obtain a model that fits the first-order spatial pattern as revealed by InSAR observations, we progressively test various 3D rheological models in four steps (Fig. 5.5). For each step, the root-mean-square (RMS) misfit is plotted against the parameter we are trying to constrain. Here, the area of Sillajhuay volcano is masked out before calculating RMS, to avoid the potential influence of volcanic deformation on the RMS computation. In the first step, we infer the best-fit size of zone A, while keeping the viscosities η_B of zone B and η_C of zone C as 4×10^{18} Pa s. Zone A is treated as elastic, consistent with seismic studies (Schurr et al., 2003). Then, in the second step, we vary the thickness H_B of zone B and find that a value between 40 km and 50 km fits the observations well. In this step, zone B is taken to be an elastic layer. Subsequently, we test different viscosities η_C for zone C, and a viscosity of 8×10^{18} Pa s gives a minimum RMS (Fig. 5.5c). For zone B, we impose a lower bound viscosity η_B of 5×10^{19} Pa s, since lower values rapidly increase the RMS misfit (Fig. 5.5d). We also test for a viscoelastic zone A, by decreasing its viscosities to the same as zones B and C. In this case, the predicted displacement pattern differs markedly

from the observations (Fig. S5.2). Due to the guided method we use to constrain multiple paprameters, it is likely that trade-offs between different parameters exist. For example, decreasing the oceanic mantle viscosity while increasing the viscosities of η_C and η_C may also fit the InSAR data. In Chapter 6, we further discuss possible geodetic solutions in bettern constraining the oceanic mantle viscosity.

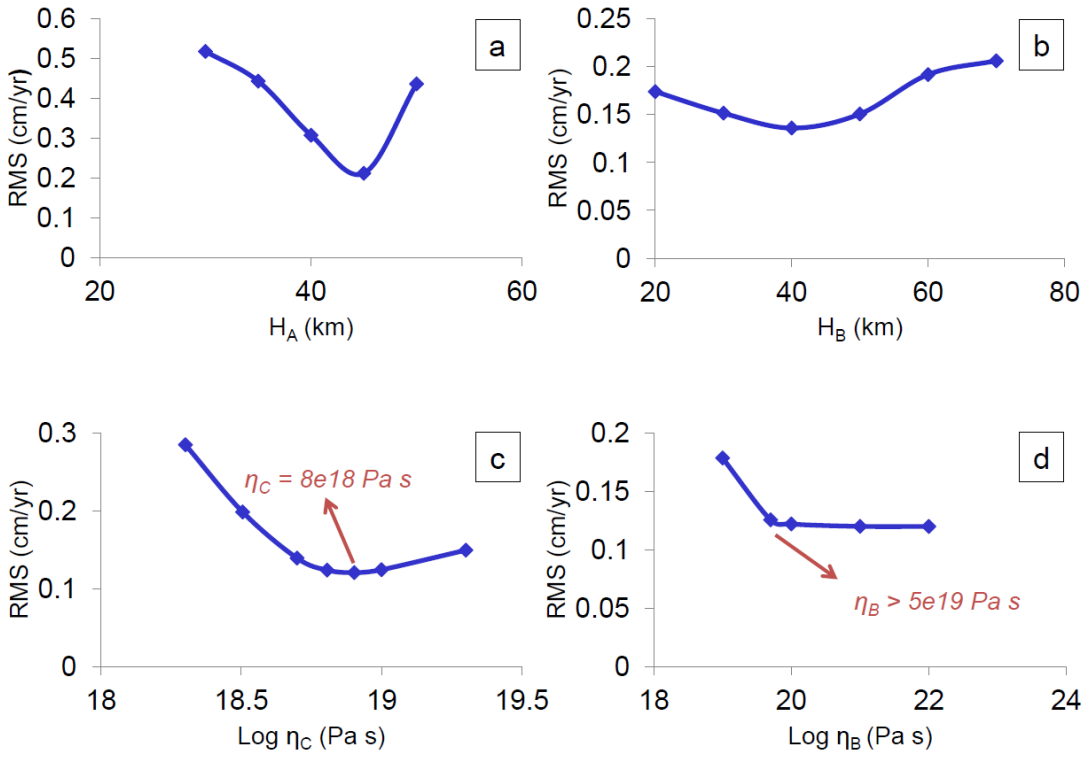

Figure 5. 5. RMS misfit curves derived during modelling. (a) RMS misfit versus thickness of zone A. Zone B and C are viscoelastic layers with fixed viscosity of 4×10^{18} Pa s. (b) RMS misfit versus thickness of zone B. Zone B is fixed as being elastic, while η_C is 4×10^{18} Pa s. (c) RMS misfit versus viscosity of zone C. (d) RMS misfit versus viscosity of zone B. Viscosity of zone C is fixed at 8×10^{18} Pa s, as derived in Fig. 5.5(c).

To validate our model, we compare the forward-modelled horizontal displacements with the GPS data, which is the difference between the mean interseismic velocity before and after the Tarapaca earthquake. As shown in Fig. 5.6(a), the InSAR-derived viscosity η_C of 8×10^{18} Pa s for zone C gives a very good azimuthal fit to the GPS displacements, but the amplitudes are under-predicted. The azimuthal alignment demonstrates that VER contributed at least part of the GPS-recorded postseismic

deformation. A model conducted with a lower viscosity η_C of 4×10^{18} Pa s fits better the amplitude of the GPS data, but produces a systematic anti-clockwise bias in azimuth for sites located northeast of the fault (Fig. 5.6b). We note that the RMS calculated for InSAR data differ less than 0.025 cm/yr for models with viscosities η_C

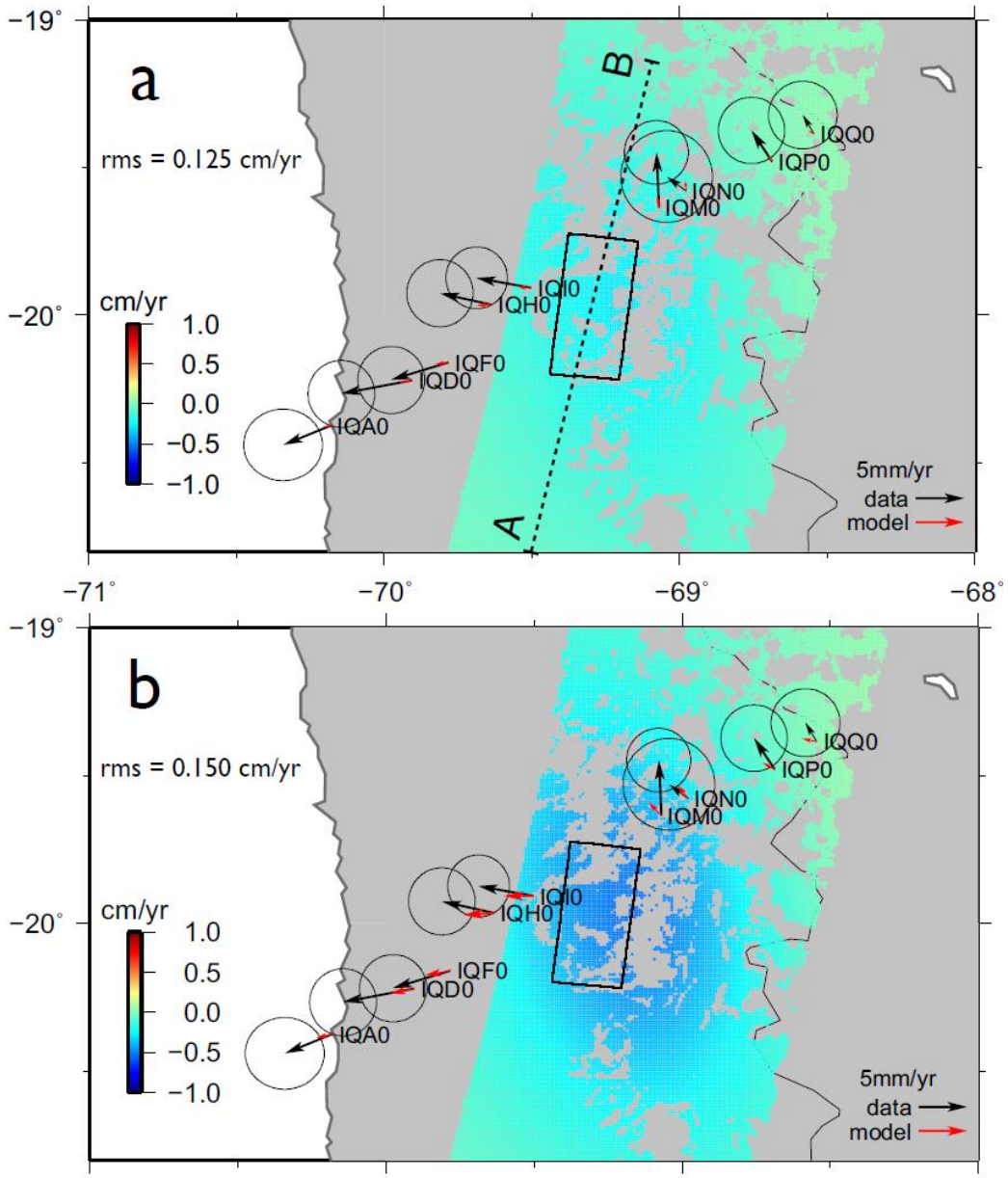

Figure 5. 6. Modelled rate map of InSAR LOS displacement and GPS horizontal displacements (red arrows) with zone C viscosity η_C of: (a) 8×10^{18} Pa s; (b) 4×10^{18} Pa s. Other parameters are: H_A = H_B = 45 km, $\eta_B = 5 \times 10^{19}$ Pa s. Black arrows are the same as shown in Fig. 5.3(b). Black dashed line marked as A-B in (a) denotes the profile in Fig. 5.8. RMS misfit between model and InSAR data is given with unit cm/yr. Fig. 5.6(a) is reproduced in Fig. S5.7, but with the modelled GPS displacement scaled by 4 times, in order to clearly show the agreement in azimuth.

of 4×10^{18} and 8×10^{18} Pa s. With a lower viscosity in zone C, the predicted InSAR displacement is slightly larger in amplitude in comparison to the observations (Fig. S5.4). We discuss further this relative inconsistency between InSAR and GPS data in Section 5.4.1.

5.3.2 Static stress change modelling

Static stress transfer is one of the mechanisms that can explain the occurrence of earthquakes following other events. In addition to coseismic stress changes, postseismic processes such as viscoelastic relaxation also modify the stress loading on surrounding faults (Steacy et al., 2005). The 2014 Iquique earthquake and its main *M* 6.7 preshock occurred about 9 years after the 2005 Tarapaca earthquake. The proximity of these events both in space (Fig. 5.1) and time offers a good opportunity to evaluate the possibility of static stress triggering.

To do so, we calculate the Coulomb stress change caused by the Tarapaca earthquake and its postseismic VER process on the subduction shallow interface and preshock nodal planes, based on the equation:

$$\Delta\sigma_f = \Delta\tau + \mu'\Delta\sigma_n \,, \qquad (5.1)$$

where $\Delta\tau$ and $\Delta\sigma_n$ are shear and normal stress changes, and μ' is the apparent friction. We assume a value for μ' of 0.4, and note that changing this value does not affect qualitatively the stress loading pattern.

We choose the 2014 Iquique rupture plane from the coseismic model proposed by Hayes et al. (2014). As there is currently no consensus on the rupture plane of the *M* 6.7 preshock, we projected stress changes onto both nodal planes derived from moment tensor inversion by Fuenzalida et al. (2014). Fig. 5.7(a) shows the Coulomb

stress change superimposed on the slip models for the Iquique earthquake and its largest aftershocks, and the aftershock distribution from Schurr et al. (2014). It is apparent that most aftershocks and the majority of slip locate in a negative stress zone, implying a lack of direct triggering effect for the mainshock. Stresses resolved onto the two pre-shock nodal planes show a positive loading on the shallow NNW-dipping one (Fig. 5.7c). Hayes et al. (2014) propose that the *M* 6.7 preshock imparted a positive stress on the plate interface where the *M* 8.2 Iquique earthquake occurred. We further propose here that the 2005 Tarapaca earthquake may have acted as an indirect trigger of the 2014 Iquique earthquake, via loading on the preshock.

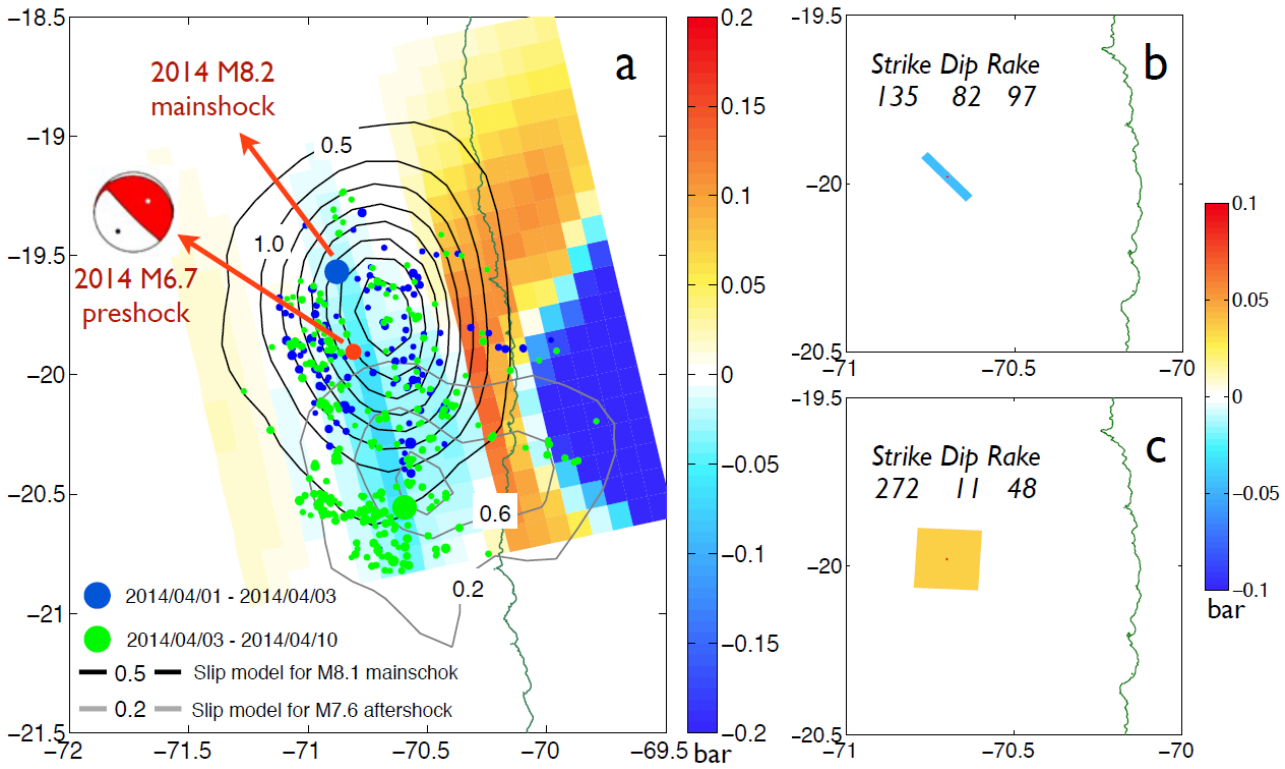

Figure 5. 7. Coulomb stress changes induced by the co- and post-seismic deformation associated with the Tarapaca earthquake. (a) Stress change on the subduction interface. Aftershock distribution, and slip models for the *M* 8.2 Iquique earthquake and its *M* 7.6 aftershock, are from Schurr et al. (2014). (b) and (c) Stress change on the nodal planes of the *M* 6.7 preshock.

5.4 Discussion

5.4.1 Likely sources of uncertainties

In this study, we have used an intermediate-depth intraslab normal faulting earthquake to constrain the northern Chile subduction zone rheological structure. Our models successfully retrieve the first-order spatial pattern of the geodetically-recorded surface deformation. While a model with a viscosity of 8×10^{18} Pa s for zone C fits well the InSAR displacement and GPS horizontal direction, it underpredicts the GPS amplitude. Decreasing the viscosity for zone C to 4×10^{18} Pa s increases the RMS misfit between InSAR model and data by ~ 0.025 cm/yr, but the fit in GPS amplitude is improved. This inconsistency may be accounted for by several sources of uncertainty.

The first source of uncertainty comes from the data assumption. The assumption that the GPS-recorded difference of interseismic velocity is merely caused by the post-Tarapaca VER effect excludes the likely change in subduction zone coupling. Temporal variation in interseismic coupling has been seen in other subduction zones, for example, on the Nicoya subduction interface (Feng et al., 2012) and at northeastern Japan (e.g. Mavrommatis et al., 2014; Nishimura et al., 2004), and could be present in North Chile as suggested by Ruiz et al. (2014). In our case, the degree of coupling may change as a result of stress perturbation due to the Tarapaca earthquake and its postseismic VER process, and/or the physical properties of the plate interface itself.

The second source of uncertainty is related to the regional complexity in rheology. In our model, we did not consider possible viscosity heterogeneity in the NS direction. As shown in seismic tomography studies (see fig. 5 in Schurr et al., 2003), seismic attenuation varies at different latitudes, indicating heterogeneous rheology. The heterogeneity can also be inferred from profiles drawn parallel to the satellite flight

direction across the deformed area. As shown in Fig. 5.8, decreasing the viscosity for zone C produces a better fit to the data on the left hand-side (corresponding to the southern part), while on the right hand side (northern side), the model deviates from the data. It suggests a likely increase of viscosity from south to north. Our models with uniform asthenospheric viscosity 8×10^{18} Pa s and 4×10^{18} Pa s could potentially act as two end-member situations, demonstrating that a slight change in viscosity can alter the observable deformation.

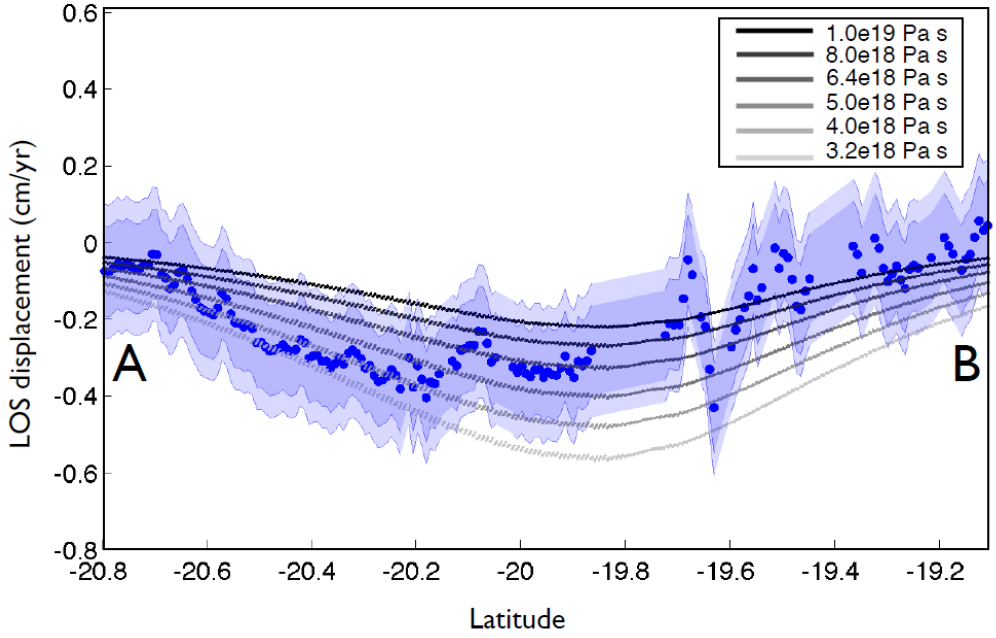

Figure 5. 8. LOS displacement changes with different viscosity for the continental asthenosphere along the A-B profile shown in Fig. 5.6(a). Blue dots show the LOS displacement rate along the profile. Higher viscosities provide a better a better fit to the northern part of the zone. The inner error bound (deep blue area) is a theoretical standard deviation derived from estimates by Li et al. (2006) of the MERIS data accuracy, and the outer bound (light blue area) is from Bennartz & Fischer (2001).

Third, given the low signal-to-noise ratio, any correction for noise in the InSAR data could potentially introduce extra errors by overestimating/underestimating the atmospheric contribution and phase ramp. As suggested by Bennartz & Fischer (2001), the theoretical accuracy of MERIS water vapor retrieval is 1.6 mm, which equals ~ 11 mm of uncertainty in the Envisat look direction. Li et al. (2006) also find

that the standard deviation of the difference between MERIS water vapor retrieval and GPS-measured zenith delay is 1.1 mm, corresponding to ~ 7.4 mm of atmospheric delay. Stacking of interferograms further reduces the atmospheric noise, and thus improves the theoretical accuracy of the rate map by $N^{-0.5}$, where N denotes the number of interferograms being stacked (Zebker et al., 1997). Assuming a similar error for each interferogram used in this study, the theoretical error of our rate map is ~ 1.7 mm/yr or ~ 1.2 mm/yr, based on the MERIS accuracy reported by Bennartz & Fischer (2001) and Li et al. (2006), respectively (Fig. 5.8). In comparison to the reported uncertainties of MERIS water vapor retrieval, a standard deviation of ~ 1.5 mm/yr between our model using 4×10^{18} Pa s for zone C and the rate map is not significant. Taking the above factors into consideration, we suggest a likely range of viscosity of $4 – 8 \times 10^{18}$ Pa s rather than stating a definite value.

5.4.2 Subduction zone rheology

Despite the uncertainties discussed above, our modelling constrains the local rheological structure in several aspects. The forearc (zone A), boardered to the east by a relatively weak lower crust and mantle lithosphere, must have high strength. Our model also requires that the lower crust and mantle lithosphere are at least an order of magnitude stronger than the asthenosphere beneath. Synthetic tests with low viscosity for zones A and B produce a different sense of motion at the surface, incompatible with the observations (Fig. S5.3).

Our inference of an asthenospheric viscosity of $4 – 8 \times 10^{18}$ Pa s is consistent with estimates from recent postseismic studies of megathrust earthquakes. Klein et al. (2014) investigated the GPS-recorded postseismic deformation following the 2010 Maule earthquake in Chile, and obtained a Maxwell viscosity of 3×10^{18} Pa s for the asthenospheric mantle. In the study of postseismic deformation following the 1960 *M* 9.5 Valdivia, Chile earthquake, Ding & Lin (2014) obtained four increasing

asthenosphere viscosities corresponding to four different observation periods after the earthquake. Their minimum value of 2×10^{18} Pa s, derived from the first four years of observation right after the earthquake, agrees well with the viscosity we inferred from the same period of observation after the Tarapaca earthquake. This consistency validates our estimation of the short-term viscosity by fitting the averaged early postseismic deformation over a short time scale (~ 4 yrs in both cases), although we agree with the likely non-linear stress-dependency of viscosity in the long term (Bürgmann & Dresen, 2008). An effective way to further test and modify current models of rheological structure would be to investigate postseismic deformation following the 2014 Iquique earthquake.

The regional rheological model inferred from geodetic observation shows consistency with independent constraints from seismic attenuation studies, especially in the contrast between the viscosity of zone A and B. Schurr & Rietbrock (2004) proposed that a strong forearc nose (zone A) acts as a barrier that obstructs the trenchward flow of hot asthenospheric mantle, and thus restricts the volcanic front to the east. According to the linearity of the volcanic front along the slab depth contour of ~ 90 km in northern Chile, we suggest that, in this part of the subduction zone, a strong forearc nose is a persistent structure that sits on top of the subducted slab to a depth of ~ 90 km.

5.4.3 Interplay of different earthquake types in a subduction zone environment

Stress transfer has been successful in explaining the occurrence of megathrust earthquakes in subduction zone earthquake cycles (e.g. Ding & Lin, 2014). When considering stress transfer between adjacent cycles and between different phases of each cycle, it is also necessary to consider the roles played by other types of earthquakes that occur within the subduction zone. Large intraslab normal fault earthquakes are expected at the downdip edge of the coupled subduction segment

(Astiz et al., 1988; Lay et al., 1989). Previous studies focused mainly on how the normal fault events themselves interact with the megathrust earthquake cycle (e.g. Kausel & Campos., 1992; Gardi et al., 2006). Here, we also investigated the stress loading due to VER processes following large intraslab events.

In the case of the Tarapaca earthquake, the coseismic-only stress loading is heterogeneous across the area of the coseismic rupture in the Iquique earthquake (Fig. S5.5a). Postseismic VER exerts a positive stress change that overlaps with the Iquique rupture, but is mostly downdip of it (Fig. S5.6a). For the upper two thirds of the plate interface, stress loading due to postseismic VER is negative. Taken together, the combined stress loading is mostly negative on the Iquique mainshock rupture, showing that the postseismic Tarapaca VER process dominates the Coulomb stress change across the Iquique rupture on the plate interface. On the nodal planes of the *M* 6.7 preshock, the coseismic stress loading (Fig. S5.5b and c) from the Tarapaca earthquake is ~ 8 times larger than that from the postseismic VER process (Fig. S5.6b and c). The combined stress change projected on the shallow-dipping nodal plane of the preshock is positive and reaches ~ 0.05 bar. As mentioned earlier, the *M* 6.7 preshock positively loaded the 2014 Iquique rupture plane (Hayes et al., 2014). Together, these lines of enquiry imply that, via loading of the *M* 6.7 preshock fault, the static stress change from the Tarapaca earthquake may have acted as an indirect trigger for the Iquique earthquake. At a late stage of the earthquake cycle when interseismic stress accumulation is high, even a small stress perturbation may initiate the subsequent failure of a long-coupled segment.

5.5 Conclusions

We take advantage of InSAR and GPS measurements covering the 2005 intraslab Tarapaca earthquake epicentral area in North Chile, before and after the main shock, to investigate the related postseismic relaxation effect. Our study demonstrates that

such a deep normal faulting intraslab earthquake generates a measurable deformation at the surface that helps constrain the subduction zone rheology. We show that a continental asthenosphere with viscosity of $4 – 8 \times 10^{18}$ Pa s underlying the lower crust, together with a mantle lithosphere of viscosity $> 5 \times 10^{19}$ Pa s and a strong forearc zone for the continental part, retrieve well the observed deformation pattern in North Chile. Calculation of Coulomb stress change on the 2014 Iquique rupture and its preshock nodal planes indicates that the static stress change from the Tarapaca earthquake and its postseismic VER may have acted as an indirect trigger for the Iquique earthquake, shedding new light on the overall sequence of seismic activity.

Acknowledgements

MERIS data and ECMWF ERA-Interim data are from the British Atmospheric Data Centre (BADC). We thank all the researchers, engineers and students from French-Chilean LiA Montessus de Ballore (LIA-MB) that took part in the GPS fieldwork, in particular J.C Ruegg who installed the first network, and C. Vigny and A. Socquet who subsequently developed the network.

Chapter 6

Discussion and conclusions

This chapter discusses several aspects raised from the studies of three normal faulting earthquakes. First, I discuss the characteristics of seismic and aseismic slip on normal faults. Rupture characteristics, such as shallow slip deficit and depth dependence on magnitude, are investigated by compiling several geodetically-studied normal fault earthquakes. The spatial relationship between afterslip and coseismic slip is discussed, and the spatial pattern is related to earthquake mechanics. I also discuss postseismic deformation mechanisms by compiling normal faulting earthquakes with postseismic geodetic measurements. Then, I examine spatial and temporal differences in rheology estimated using various techniques for different parts of the Tibetan Plateau. Third, I discuss the influence of subduction zone rheology on earthquake cycle deformation, and potential techniques and methods for investigation of oceanic mantle viscosity. Finally, I suggest future work before drawing conclusions.

6.1 Sesimic and aseismic slip on normal faults

6.1.1 Characteristics of normal fault coseismic slip

Wide applications of modern geodetic techniques provide detailed measurements of crustal deformation caused by earthquakes. Coseismic slip models can be derived from these observations based on elastic dislocation theory. I compiled coseismic slip models for 8 normal faulting earthquakes in different regions, in order to investigate whether there exists a systematic depth-dependence of seismic moment release. The moment magnitudes of these earthquakes fall within a range of 6.2 – 7.1. The seismic moment release is calculated for every depth interval (chosen as the size of patch

used in each study), and then normalized with reference to the largest moment release.

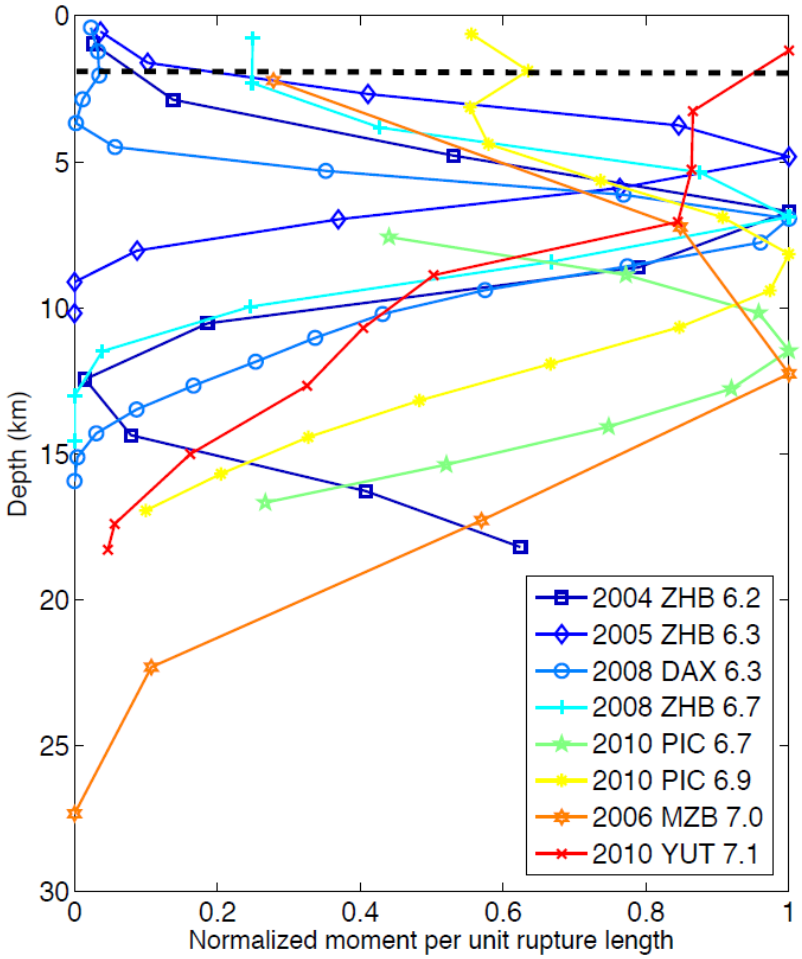

Figure 6. 1. Normalised seismic moment per unit rupture length, as a function of depth, for 8 normal faulting earthquakes. Slip models for the 2004, 2005 and 2008 ZHB (Zhongba) earthquakes are from Ryder et al. (2012), and those for the 2008 DAX (Damxung) earthquake, 2010 PIC (Pichilemu) earthquake doublets, 2006 MZB (Mozambique) earthquake, and 2010 YUT (Yutian) earthquake are from Bie et al. (2014), Ryder et al. (2012), Copley et al. (2012) and Bie et al. (2014), respectively. Black dashed line marks the depth of 2 km.

Fig. 6.1 shows the normalized seismic moment per unit rupture length, as a function of depth. A strong depth variation of coseismic slip can be found. For all but the 2008 Yutian earthquake, the maximum seismic moment release occurs at depths of 5 – 12 km. There is no clear relationship between earthquake magnitude and depth of maximum slip. Taking 20 per cent of the maximum coseismic moment release as a threshold, the majority of slip concentrates at depths of ~ 2 – 18 km. This range is

consistent with the global seismogenic thickness of 14 ± 5 km estimated from a large compilation of coseismic geodetic observations (Wright et al., 2013).

In all cases except the 2008 Yutian and 2004 Zhongba earthquakes, coseismic slip gradually decays both upwards and downwards. This trend is similar to that found by Fialko et al. (2005) for several large strike-slip earthquakes. Above the maximum slip zone, slip decays more slowly for large earthquakes, for example, the 2008 M_w 6.7 Zhongba and 2010 M_w 6.9 Pichilemu earthquakes. Specifically for the 2008 M_w 7.1 Yutian earthquake, the maximum coseismic moment release appears in the uppermost 5 km. For the above three earthquakes, the coseismic rupture extended to the surface. At the bottom of the seismogenic layer, two earthquakes show a discrepancy in comparison to others. One is the 2004 M_w 6.2 Zhongba earthquake, for which the moment release decays first to nearly zero at a depth of ~ 12 km, and then rapidly increases to 60 per cent of the maximum at ~ 18 km. This feature is probably caused by interferogram noise being mapped into the slip model. As shown by Ryder et al. (2012), slip modelled at the bottom shows strike-slip rather than the major normal-faulting motion, indicating a possible artefact. For other earthquakes, slip decreases to a minimum above 20 km depth, with the exception of the 2006 M_w 7.0 Mozambique earthquake, where slip extends to a depth of ~ 27 km (Copley et al., 2012). The large slip depth of the Mozambique earthquake is probably related to the relatively large seismogenic thickness of the western branch of the East African Rift System (Craig et al., 2011). The other possibility is that the patch size of 5 km used in the model is larger than other models compiled here. So it is reasonable to postulate that a finer grid would modify the depth variation. It is also noted that the Mozambique earthquake ruptured an unusually steep normal fault at ~ 75°, which may influence the depth extent of coseismic slip.

A physical model to explain the shallow slip deficit is that velocity-strengthening frictional properties of the upper layer arrests the propagation of coseismic rupture (Marone et al., 1991; Marone, 1998). The model proposed by Marone et al. (1991)

comprises a mature zone of unconsolidated fault gouge (exhibiting velocity strengthening) sitting on top of consolidated fault gouge (exhibiting velocity weakening and hosting the majority of coesismic slip distribution). Several factors may influence whether or not the coseismic rupture can reach the surface, including the thickness of the velocity-strengthening zone, stress drop in the velocity-weakening zone, and preseismic stress level in the shallow crust (Fialko et al., 2005). It is also possible that surface rupture of the M_w 7.1 Yutian earthquake is related to the dynamic weakening mechanism. If so, the Yutian earthquake might represent a minimum size of event that is required to promote sufficient dynamic weakening to allow rupture reaching the surface (Faulkner et al., 2011).

How coseismic slip deficit is compensated during the normal fault earthquake cycle remains an open question to be solved. For strike-slip faults, interseismic and postseismic creep is generally found below the seismogenic depth. In contrast, afterslip models of the Damxung and Yutian earthquakes show no clearly-resolvable deeper slip. Additionally, no geodetic observation of interseismic creep of any normal fault is reported. The absence of such observation is probably caused by a slow interseismic rate of continental normal faults, beyond the current capacity of geodetic observation. Shallow slip deficit receives more attention, given its closeness to surface geodetic observations, and the implications of strain accumulation at shallow depth. Although shallow afterslip can partially accommodate the slip deficit, other mechanisms, such as distributed elastic deformation (secondary structure(s) involved) and/or plastic shallow deformation, and interseismic creep at all phases of the earthquake cycle, need to be invoked to explain the remaining deficit (Fialko et al., 2005; Kaneko & Fialko, 2011). If only part of the shallow deficit can be accommodated, the essential question related to seismic hazard is whether strain accumulation (how much) at shallow depth can lead to a shallow earthquake (how large).

6.1.2 What is the main postseismic deformation mechanism for normal faults?

How are coseismically-induced stresses relaxed during the postseismic phase? For the first two normal fault earthquakes in this thesis, short wavelength postseismic deformation seems prevalent within ~ 30 km of the fault. Shallow afterslip is thus the most plausible mechanism that can explain the deformation. The Tarapaca earthquake was located at a depth of ~ 90 km, near the continental lower crust/upper mantle, which is considered to be weak. The postseismic deformation across the fault's surface projection shows a broad uplift pattern, favoring the mechanism of viscoelastic relaxation, though I do not exclude the possibility of localised slip on or in the slab. A compilation of normal fault earthquakes with postseismic studies is made to investigate what factors might affect our determination of the plausible postseismic deformation mechanism.

Tables 6.1 lists 11 normal fault earthquakes with post-seismic measurements. In spite of a limited number of samples, the compilation suggests that afterslip tends to be the only visible postseismic mechanism associated with shallow earthquakes smaller than M_w 7.2. The Umbria-Marche earthquake is an exception, with VER being proposed to account for the far field GPS-recorded displacement that cannot be recovered by an afterslip-only model, although the latter is the major postseismic mechanism. The rheological model features a 5 – 12 km-thick transition zone with viscosity of 1×10^{18} Pa s under an 8 km-thick upper crust (Riva et al., 2007). The special case of the Umbria-Marche earthquake may be related to the existence of a regional-scale weak layer.

When earthquakes get larger than M_w 7.2, VER induced ground deformation reaches an observable degree. Even ~ 40 yrs after the Gulu earthquake, VER-related postseismic deformation is still observable. At this late stage, kinematic slip on the fault plane cannot reproduce the observations, ruling out the possibilities of afterslip

and/or interseismic slip (Ryder et al., 2014). The 2005 Tarapaca earthquake occurred within the subducted slab, close to the weak continental lower crust/upper mantle. Although its great depth of ~ 90 km may reduce the displacement observed at the surface, other factors, such as its large magnitude and the low viscosity of weak layers, may trade off against the impact of depth and produce an observable VER signal.

Table 6. 1. Compilation of normal fault earthquakes with postseismic geodetic studies. Aspects not specifically studied in a particular paper are marked as N/A. Depth and moment magnitude are from the USGS catalogue, except the Gulu earthquake, for which the moment magnitude is from Ryder et al. (2014) and depth is from Engdahl & Villasenor (2002).

Name	**Date**	M_w	**Depth**	**Afterslip**	**VER**	**Viscosity**	**Reference**
Umbria-Marche	1997/09/26	6.0	10	Yes	Yes	1×10^{18}	Riva et al., 2007
Damxung	2008/10/06	6.3	12	Yes	No	$> 1 \times 10^{18}$	Chapter 3
L'Aquila	2009/04/06	6.3	8.8	Yes	No	N/A	D'Agostino et al., 2012
Nima-Gize	2008/01/09	6.4	10	Yes	No	$> 3 \times 10^{17}$	Ryder et al., 2012
Athens	1995/05/13	6.6	14	Yes	No	N/A	Atzori et al., 2008
Pichilemu	2010/03/11	6.9	11	Yes	No	N/A	Bie et al., *in prep*
Mozambique	2006/02/22	7.0	11	Yes	No	$> 2 \times 10^{19}$	Copley et al., 2012
Yutian	2008/03/10	7.1	10	Yes	No	N/A	Chapter 4
Hebgen Lake	1959/08/17	7.2	10	Yes	Yes	$4 \times 10^{18\pm0.5}$	Nishimura & Thatcher, 2003
Gulu	1952/08/17	7.4	35	No	Yes	$5 - 10 \times 10^{19}$	Ryder et al., 2014
Tarapaca	2005/06/13	7.8	90	N/A	Yes	$4 - 8 \times 10^{18}$	Chapter 5

To summarize, whether VER is excited depends on the magnitude and depth of the earthquake, and rheological properties of the materials near the coseismic rupture. Shallow normal faulting earthquakes with magnitude smaller than 7.2 do not produce large enough stress to excite observable VER deformation. When the earthquake is larger in magnitude (> M_w 7.2) and close to the weak layer(s), VER-generated observable surface deformation may be used to constrain rheological structure; otherwise, only a lower bound on viscosity can be estimated (e.g. Bie et al., 2014; Copley et al., 2012; Ryder et al., 2012).

6.1.3 Coseismic slip, afterslip and friction laws

In this thesis, time-dependent afterslip models are derived for two normal faulting earthquakes from transient postseismic InSAR observations. Afterslip following the M_w 6.3 Damxung earthquake is mainly composed of three patches, surrounding the main coseismic rupture. The depth extent of the afterslip ranges from 11 km to the surface. For the M_w 7.1 Yutian earthquake, afterslip patches appear mainly in the northern and southern segments, while the coseismic rupture dominates in the central segment. Similar to the Damxung earthquake, most afterslip patches do not extend deeper than the coseismic rupture. For both earthquakes, the major afterslip patches increase in magnitude over time, but do not migrate significantly.

Complementary spatial patterns between co- and post-seismic slip have been found in other normal faulting earthquake studies. In the study of the 2006 M_w 7.0 Mozambique earthquake, Copley et al. (2012) found that afterslip appears above the main coseismic slip zone from depths of ~ 10 km towards the surface (fig. 7 of Copley et al., 2012). The 2009 M_w 6.3 L' Aquila earthquake in Italy is one of the most extensively studied normal fault earthquakes, with various combinations of datasets having been applied. D' Agostino et al. (2012) investigated the spatial and temporal evolution of afterslip inverted from InSAR and GPS data, separately and together, and found four major afterslip patches at various depths around the coseismic rupture. Gualandi et al. (2014) obtained a similar afterslip distribution by employing a principle component decomposition-based method to invert GPS data only. Further inclusion of high-precision leveling data into joint inversion with InSAR and GPS data corroborates the above two afterslip models (Cheloni et al., 2014). In summary, for these normal faulting earthquakes, afterslip does not extend deeper than the coseismic rupture, and is complementary to the main coseismic slip zone in a patchy way.

The appearance of afterslip at shallow depth and an upwards decrease in coseismic slip agree with the rate-state friction law, according to which the velocity-strengthening behavior of shallow sedimentary layers arrests coseismic slip but favours aseismic slip (Marone et al., 1991). However, our case studies and others' mentioned above show two aspects that may challenge the rate-state friction law. First, afterslip patches locate at various depths, not just above the coseismic rupture, but also at seismogenic depth. For example, two major afterslip patches appear at down-dip depths of 5 – 15 km in the Damxung earthquake and the southern major afterslip patch locates at the same depth as the maximum coseismic rupture in the Yutian earthquake. Second, sustained afterslip is found overlapping with the coseismic rupture, which contradicts the theoretical boundary between velocity-weakening and velocity-strengthening regions. Although one may argue that smoothing applied in inversion procedures could smear the slip distribution, Johnson et al. (2012) carried out an unsmoothed inversion of postseismic displacement following the 2011 Tohoku-Oki earthquake, and were unable to produce a model that fit the observations without extending to historical rupture zones (velocity-weakening zones).

The above two aspects seem to suggest that fault frictional properties vary not only in the downdip direction, but also laterally along strike. Similar to the asperity model suggested to explain frictional behavior of subduction megathrusts (e.g. Lay et al., 1982; Bilek & Lay 2002), continental normal faults may also consist of both frictional stable and unstable areas at seismogenic depth. The boundary between areas with different frictional properties may not be sharp, but vary in a continuous fashion (Fig. 6.2). In this way, the unexpected (according to rate-state friction law) afterslip in the velocity-weakening zone may be explained. Another possibility is that geometric irregularities of the fault can also arrest coseismic slip and promote afterslip. In the case of the Yutian earthquake, as seen from the postseismic deformation, two major deformation features appear near where the fault changes its

strike direction (Fig. 4.6b). Accordingly, the inverted model shows that major afterslip patches concentrate at the fault's bends, where the coseismic slip tapers.

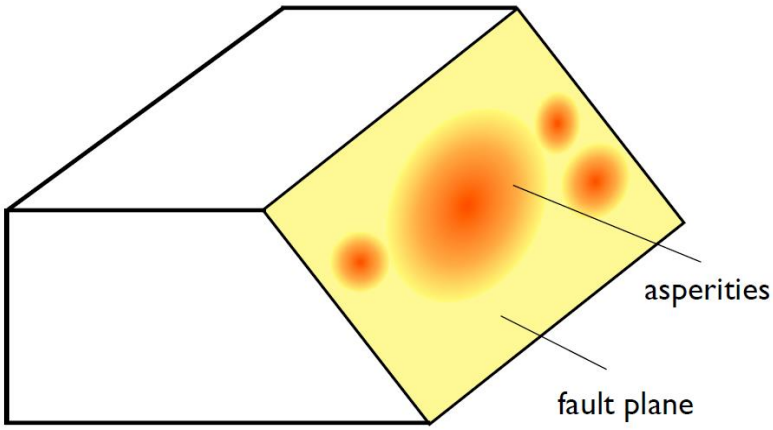

Figure 6. 2. A conceptual model showing asperities on a normal fault plane. The frictional property shows a continuous, rather than sharp change, and along-strike heterogeneity.

The above discussion treats the rate-state friction law as appropriate to explain earthquake rupture. However, it may not be suitable to extrapolate the phenomenological descriptions of friction at low slip rate beyond earthquake nucleation (Faulkner et al., 2011). Experiments conducted by Faulkner et al. (2011) on clay-rich sediments illustrate that the rate-state friction law only controls earthquake nucleation, and has little to do with earthquake propagation. Coseismic weakening due to thermal processes may allow the propagation of coseismic rupture through the rate-strengthing portions (e.g. Faulkner et al., 2011; Noda & Lapusta, 2013). Following this line of argument, the overlap between co- and post-seismic slip summarized here for a number of normal faulting earthquakes may not necessarily contradict the rate-state friction law, but only requires other parameters describing the coseismic rupture propagation.

6.2 Lithospheric rheology of the Tibetan Plateau

Multiple models have been raised to describe how the Tibetan Plateau deforms. The block model treats the plateau as being composed of a number of small plates moving along major strike-slip faults (e.g. Tapponnier et al., 1982, 2001; Thatcher, 2007). In the continuum model, the lithosphere is regarded as a continuum with distributed deformation driven by boundary and interior forces (e.g. England & Molnar, 2005; Copley, 2008). The channel flow model with a weak lower crust explains the flat topography in the plateau interior and different topographic gradients at the plateau margins (e.g. Royden et al., 1997; Clark & Royden, 2000).

One critical difference between these models is the depth-variation of the rheology, and its role in driving the lithospheric deformation. As direct measurement of deep rheological properties is difficult, large efforts have been made in geophysical imaging of the physical state of the Tibetan lithosphere. Seismic and magnetotelluric studies provide extensive evidence indicating the presence of weak layers in the mid- and/or lower crust, or even upper mantle, depending on the locations (Klemperer, 2006). Although the above geophysical methods and numerical models can provide constraints on the mechanical properties, no definite imaging of the viscous flow process has been presented until Ryder et al. (2014) showed unequivocal InSAR observations of active postseismic flow in a weak lower crust and/or upper mantle.

Geodetic observation of postseismic deformation is usually investigated to put constraints on rheological properties of the crust and upper mantle. Here, I compile all postseismic VER studies of earthquakes across the Tibetan Plateau, together with rheology estimates from other modelling efforts, such as shoreline changes (e.g. England et al., 2013; Shi et al., 2015) and topographic constraints (e.g. Shen et al., 2001; Clark et al., 2005a). By comparing viscosity estimates at different time-scales, I investigate the consistency between long- and short-term rheology. I also discuss the possible lateral heterogeneity of rheology within the plateau and discuss its tectonic implications.

Clark & Royden (2000) postulated that a weak channel exists within the Tibetan crust, whose viscosity must be lower than 10^{16} Pa s if its thickness is ~ 10 – 20 km. These authors suggest that the thin weak lower channel accommodates significant lateral flow and reduces the transmission of stresses through the weak layer, resulting in decoupling between the mantle and the upper crust, thus maintaining a low topographic relief across Tibet. However, the effect of a thicker channel is not tested. In most recent studies of rheology on the time scale of decades, a thin ductile channel located in the middle crust is not favored (Ryder et al., 2014; Doin et al., 2015). Instead, the estimated viscosity of ~ 10^{19} Pa s may allow the entire lower crust to flow on geological time scale, supporting the notion by England et al. (2013) that the low-viscosity thin channel is not necessary to explain the low topographic relief of Tibet. In addition, the thickness of 15 km assigned for the ductile 'channel' in geological modelling (e.g. Clark & Royden, 2000; Clark et al., 2005a) should not be applied without justification in short-term viscoelastic modelling. For the above reasons, unlike the compilations made by Huang et al. (2014) and Shi et al. (2015), I use the relationship between lower crustal viscosity (η) and thickness (h), h^3/η (eq 4 in Clark & Royden, 2000), to scale viscosities derived for very thin layers up to values more appropriate for thicker layers. This makes the different studies more comparable and mitigates the effects of trade-offs between viscosity and thickness.

6.2.1 Rheology estimates from various studies

In northern Tibet, rheological estimates mostly come from geodetic observations before and/or after the 1997 M_w 7.6 Manyi earthquake (e.g. Ryder et al., 2007; Yamasaki & Houseman, 2012; DeVries & Meade, 2013) and the 2001 M_w 7.8 Kokoxili earthquake (e.g. Ryder et al., 2011; Wen et al., 2012; DeVries & Meade, 2013; Hilley et al., 2009). On the time scale of years to decades, inferred lower crustal viscosities across most of the studies lie in the range of $1 \times 10^{18} – 5 \times 10^{19}$ Pa s. Yamasaki & Houseman (2012) fits equivalently well the InSAR postseismic

displacement time-series of the Manyi earthquake by using a depth-dependent viscosity model, and suggests that the viscosity decreases exponentially from 1.2 × 10^{21} Pa s at 10 km (top of the viscoelastic layer) to 1.6 × 10^{18} Pa s at 60 km (the Moho depth). The range estimated by Yamasaki & Houseman (2012) between 1.6 × 10^{18} – 1.2 × 10^{21} Pa s encompasses other geodetic estimates. The viscosity of the 20 km-thick channel sandwiched between elastic layers in DeVries & Meade (2013) is estimated to be smaller than 3 × 10^{18} Pa s. However, using the relationship h^3/η to scale it to a 60 km-thick viscoelastic layer gives a viscosity < 2.4 × 10^{19} Pa s (Fig. 6.3).

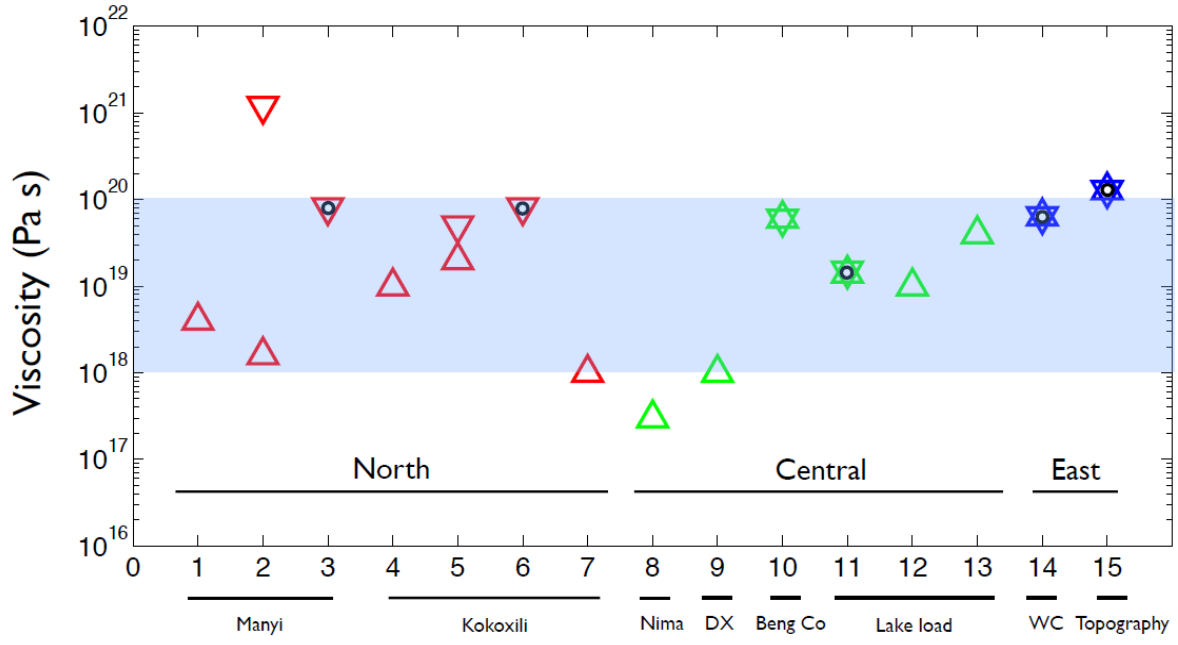

Figure 6. 3. A synoptic diagram showing viscosity estimates for the lower crust and/or upper mantle of the Tibetan Plateau on different time scales. Upward-pointing triangles represent the lower bound of viscosity, and downward-pointing triangles represent the upper bound. Where the viscosity is estimated as a value rather than a range is denoted by a hexagram. Red, green, and blue colors represent estimates for northern, central and eastern part of the Tibetan Plateau. Black circles mark those viscosity estimates that are scaled up according to the relationship between weak layer viscosity (η) and thickness (h), h^3/η. When scaling relationship is applied, the thickness h is fixed at 60 km. DX and WC represent the Damxung and the Wenchuan earthquake, respectively. The number of the x-axis refers to the cited studies: 1, Ryder et al. (2007); 2, Yamasaki & Houseman (2012); 3, DeVries & Meade (2013); 4, Ryder et al. (2011); 5, Wen et al. (2012); 6, DeVries & Meade (2013); 7, Hilley et al. (2009); 8, Ryder et al. (2010); 9, Bie et al. (2014); 10, Ryder et al. (2014); 11, Doin et al. (2015); 12, Shi et al. (2015); 13, England et al. (2013); 14, Huang et al. (2014); 15, Clark et al. (2005a).

In central Tibet, postseismic deformation following two moderate normal faulting earthquakes (Nima and Damxung earthquakes) constrains the lower crustal viscosity to be greater than ~ 10^{17} Pa s (e.g. Ryder et al., 2010; Bie et al., 2014). A late postseismic InSAR observation following two 1950s earthquakes can be best explained by viscoelastic relaxation in the lower crust and/or upper mantle (Ryder et al., 2014). If a 60 km-thick viscoelastic lower crust is assumed, the optimal Maxwell viscosity is 6×10^{19} Pa s, equivalent to estimates from geological modelling by Clark et al. (2005a). Geodetic short time scale observation is supplemented by three studies of shoreline rebound of the lakes in central Tibet on the time scale of kiloyears. England et al. (2013) found from GPS field measurements and optical image interpretation that there are no measurable paleoshoreline distortions of the Zhari Namtso and other lakes in central Tibet. The horizontality of the shorelines can be explained by elastic support of the lake load, but requires the elastic part of the crust to exceed 15 – 25 km. This value is greater than the long-term elastic thickness, which is less than ~ 10 km for central Tibet (England et al., 2013). Instead, a preferred alternative mechanism that explains the paleoshoreline horizontality is viscous stress arising from flow in the lower crust. Depending on the boundary condition beneath the lower crust, the minimum allowable lower crustal viscosity decreases with increasing thickness of viscoelastic layer. For a viscoelastic lower crust of 60 km (similar to that of Ryder et al., 2014) sandwiched by elastic layers, the viscosity is required to be greater than 4×10^{19} Pa s to support the lake load. This lower bound is similar to 1×10^{19} Pa s which is estimated by Shi et al. (2015) from palaeoshoreline studies of the Siling Co, another large lake ~ 400 km ENE of the Zhari Nam Co lake. Based on ~ 20 years of InSAR observation of ground motion associated with water load increase since 2000, Doin et al. (2015) propose that the best mechanism that explains the ground motion is viscoelastic relaxation of a weak channel in the deep crust above a rigid mantle. The optimal Maxwell viscosity is 1 – 3×10^{18} Pa s for a ductile lower crust with thickness between 25 – 40 km. Although this value is at least one order of magnitude smaller than estimates from England et

al. (2013) and Shi et al. (2015), scaling the viscosity against the thickness to 60 km gives a range of 1.4 – 1.5 × 10^{19} Pa s, close to the previously-estimated lower bound. Considering the decadal time scale of the InSAR observations, the estimate of 1.4 – 1.5 × 10^{19} Pa s is consistent with that on the millennial time scale of England et al. (2013).

In the eastern part of plateau, two avenues for investigating lower crustal mechanical properties provide either short- or long-term rheological estimates. One approach is investigating how flow dynamics affect topographic variation (e.g. Clark et al., 2005; Cook & Royden, 2008), and the other is looking at postseismic ground deformation following the 2008 Wenchuan earthquake (Huang et al., 2014). At the eastern margin of the plateau, strong Sichuan Basin crust diverts the flow of material towards the south-eastern and north-eastern corners, where crustal strength is weak. As a result of the strength contrast between the plateau and the basin, the eastern margin is characterized by a steep topographic gradient, while to the northwest and southwest of the Sichuan basin, the margin decreases more gently in elevation. The anomalously high topographic gradient requires lower crustal flow with a viscosity of 2 × 10^{18} Pa s within a 15 km channel (Clark et al., 2005). Huang et al. (2014) set up a 3D rheological model to accommodate the mid- to far-field horizontal GPS-recorded deformation. The 3D model considers the strength contrast at the margin, with the lower crustal viscosity for the plateau two orders of magnitude smaller than that for the upper mantle of the Sichuan basin. For the plateau, the weak lower crust is treated as a 15 km channel with a Maxwell viscosity of 1 × 10^{18} Pa s overlying a strong upper mantle with viscosity 1 × 10^{19} Pa s. Scaling the short- and long-term viscosity to a 60 km ductile layer gives viscosities of 6.4 × 10^{19} Pa s and 1.28 × 10^{20} Pa s, respectively. The short term value used by Huang et al. (2014) agrees well with that derived by Ryder et al. (2014) for central Tibet, while the long-term viscosity of Clark et al. (2005a) is only slightly larger than that estimated at millennial time scales (Fig. 6.3).

6.2.2 Temporal and spatial characteristics of lower crustal rheology and its implications

The synopsis shown in Fig. 6.3 suggests a general consistency in estimates for the lower crustal viscosity of order 10^{19} Pa s on short time scales. For longer time scales, the viscosity is within one order of magnitude difference from the estimates at short time scales. As introduced in Chapter 2, laboratory rock mechanics experiments suggest that lower crustal rocks may exhibit a power-law rheological behavior. In this case, the viscosity would increase with time as coseismic stresses are relaxed postseismically. The small increase in viscosity across time scales as indicated here (10^{18} – 10^{20} Pa s) may suggest that the early stage postseismic measurement of viscosity (transient) is not overwhelmingly smaller than the long term viscosity (steady-state). Indeed, in some postseismic studies, a Burgers rheology that assumes that the transient viscosity is one order of magnitude smaller than the steady-state viscosity is sufficient to fit the geodetic observations (e.g. Hearn et al., 2009; Ryder et al., 2011).

In addition to the temporal variation, estimated lower crustal viscosities show small differences across the plateau. We note that in northern Tibet, the viscosity of the weak layer is mostly constrained by interseismic and/or postseimic geodetic observations following major strike-slip earthquakes assuming a stratified Earth model. In the postseismic study of the 1999 İzmit/Düzce earthquakes on the North Anatolian fault, Yamasaki et al. (2014) found that the presence of a localized weak zone with finite width beneath the fault can explain well the proximity to the fault of maximum postseismic velocities. The viscosity of the finite weak zone is ~ $10^{18 \pm 0.3}$ Pa s and the background viscosity is greater than ~ 10^{20} Pa s. The lateral contrast of viscosity is about two orders of magnitude. This may raise the question about what spatial scale is represented by the viscosity estimates from the two strike-slip earthquakes in northern Tibet assuming a stratified Earth. In other words, lower crustal strength may be heterogeneous laterally on a local to regional scale. Further

investigation using other rheological models to fit postseismic displacement following the two events would be of value.

6.3 Subduction zone rheology

In this section, I will discuss first the influence of rheology on the subduction zone earthquake cycle. The contribution of VER to interseismic and postseismic deformation is highlighted by a review of recent studies. Given that current inferences on subduction zone rheology largely concentrate on the continental portion, I further discuss potential techniques that could shed light on the near-trench deformation that is indicative of oceanic mantle viscosity.

6.3.1 Effect of viscosity on the subduction zone earthquake cycle

Subduction zone rheology plays an important role in the dynamics of the so-called subduction factory (Hirth & Kohlstedt, 2003). An elastic subduction earthquake cycle model consists of coseismic rupture, interseismic locking and afterslip phases. To further accommodate the horizontal motion as revealed by postseismic GPS observations, viscoelastic relaxation beneath the elastic lithosphere is included in the subduction earthquake cycle model (Wang et al., 2012).

Including VER in the subduction earthquake cycle challenges seismic hazard estimation based on purely elastic rebound theory. Because VER processes affect the state of stress on the plate interface and within the overriding plate, if VER is the dominant postseismic mechanism especially on a time scale of decades, its influence on the stress state should be more profound than afterslip. Sun et al. (2014) show that even short-term (~ 3 yrs) postseimic seafloor GPS observations near the trench reflect a major contribution from viscoelastic relaxation, rather than afterslip for the 2011 Tohoku-Oki earthquake. Similarly, gravity field variation requires a dominance of

VER even in the first year after the 2004 Sumatra earthquake (Broerse et al., 2015). If such a prevalence of VER deformation is attributed totally to elastic behavior (e.g. rate-strengthening afterslip), one would possibly over- or under-estimate afterslip downdip and updip of the seismic rupture, eventually leading to a biased understanding of the megathrust frictional properties. The challenge is therefore to distinguish the relative contribution of afterslip and VER to postseismic deformation, and finding out what physical properties control the spatial and temporal change in dominance.

In addition to postseismic VER, the weak part of the mantle also takes part in the interseismic phase of the subduction earthquake cycle. As stress builds up on the seismogenic part of the plate interface, it is simultaneously partially relaxed by nearby weak layers. Thus, the interseismic surface deformation is a combination of elastic and viscoelastic deformation. Li et al. (2015) showed that treating the combined deformation solely as elastic tends to overestimate the interseismic locking depth. In turn, the interseismic locking model, which has implications for potential seismic hazard, could be biased.

As an essential input for geodynamic and earthquake cycle models, constraints on viscosity draw lots of efforts from the geodesy community trying to fit surface deformation before and after major megathrust earthquakes with predictions from various rheological models. Chapter 1, 2 and 5 mentioned some of the studies on the 2004 Sumatra, 2011 Tohoku-Oki and 2010 Maule earthquakes. Chapter 5 presents the first geodetic study of VER deformation induced by a deep intraslab normal faulting earthquake. The demonstrated feasibility of using deep normal fault earthquakes to constrain subduction zone rheology opens new avenues for similar investigations. More importantly, the stress loading on the plate interface and upper crust due to the deep normal faulting earthquake strongly suggests that a comprehensive subduction earthquake cycle should consider elastic and viscoelastic

effects brought about not just by megathrust earthquakes, but also other types of large events in subduction systems.

6.3.2 Oceanic mantle viscosity

Current geodetic constraints on subduction zone rheology concentrate mostly on the continental part by fixing the oceanic viscosity (e.g. Hu et al., 2004), or ignore lateral heterogeneity but treat the oceanic and continental weak parts as a whole (e.g. Ding & Lin, 2014). Laboratory experiments suggest that oceanic mantle viscosity can be up to an order of magnitude higher than that of the continental side (Hirth & Kohlstedt, 2003). The fact that most GPS sites locate inland far away from the trench may limit their sensitivity to VER contribution from the oceanic mantle, thus resulting in a weak constraint on the oceanic mantle viscosity. Two possible solutions exist for a better constraint on oceanic mantle rheology.

One is the development of techniques in monitoring postseismic deformation near the trench, such as seafloor geodesy (Bürgmann & Chadwell, 2014). New techniques applied near the trench can provide unequivocal evidence for VER following megathrust earthquakes, because general subsidence (the reverse of the postseismic uplift expected after shallow normal fault earthquakes) is expected across the trench if VER is the dominant postseismic mechanism. Additionally, one can potentially distinguish the contribution from oceanic and continental mantle to postseismic deformation, given that the observation is closer to the oceanic part than in land-based techniques. Gravitational change due to ongoing postseismic redistribution of mass can also be incorporated to infer oceanic viscosity (e.g. Broerse et al., 2015). This technique overcomes the limitation of InSAR, which has the issue of decorrelation over water and offers a large-scale observation of postseismic deformation. Indeed, Broerse et al. (2015) find that the contrast in temporal behavior of GPS and gravity observations requires an order of magnitude higher viscosity in

the oceanic asthenosphere than that in the continental mantle. This finding is consistent with experimental studies (Hirth & Kohlstedt, 2003) and support the model set-up described in Chapter 5 for the Tarapaca earthquake.

The other solution to constrain oceanic viscosity is to monitor postseismic deformation following earthquakes that occur in oceanic crust. In this way, the GPS sites inland may record postseismic deformation due to VER in the oceanic mantle. Of course, the earthquake should be large enough to induce VER in the oceanic mantle, and GPS sites in the forearc should still be close enough to the trench. An ongoing study of this type is reported by Hu et al. (2014), which tries to constrain the Indian oceanic mantle viscosity using one year of postseismic deformation following the 2012 M_w 8.6 Wharton Basin earthquake sequence. This strike-slip earthquake sequence ruptured multiple near-orthogonal faults, ~ 100 km west of the Sumatra subduction zone (Hill et al., 2015). A 50 – 80 km thick asthenosphere with a Maxwell viscosity of $2 – 8 \times 10^{18}$ Pa s is inferred above the Indian oceanic mantle, which has a steady-state viscosity of $5 – 50 \times 10^{20}$ Pa s.

6.4 Further work

6.4.1 Interseismic deformation of normal faults

In this thesis the coseismic and postseismic phases of normal faults are explicitly investigated, leaving space for further investigation on the interseismic deformation mechanism of normal faults. A large quantity of interseismic locking models have been published for strike-slip faults on the basis of geodetic observations (as summarized by Wright et al., 2013). Strike-slip faults are commonly modelled as being locked from the surface to a certain depth, below which slip occurs aseismically and loads the fault. Estimates on locking depth for normal faults from geodetic measurements are sparse in the literature. It is reasonable to ask whether the

assumption of aseismic motion down-dip of the seismogenic part is applicable to normal faults.

An important difference between normal faults and strike-slip faults is that normal faults may become listric at depth. If gravitational force is the major driving factor for extension, aseismic slip on the near-horizontal portion may be less likely while the steep shallow part is locked, unless the frictional resistance is dramatically low. Basal shear traction, resulting from directed ductile flow, may be responsible for generation of the sub-horizontal structure and motion on it (Yin, 1989). Geodetic measurements may help evaluate the geometry of normal faults, as is being widely implemented for coseismic deformation. However, current GPS and InSAR accuracy at the millimetre level and atmospheric noise at the centimetre level may act together to limit the effectiveness of constraining the geometry and low interseismic slip rate from interseismic geodetic measurements.

I run a preliminary test on using InSAR to measure interseismic deformation of a major normal fault bounding the western side of the Yinchuan graben, west of the Ordos block in NE China. The extensional rate is estimated at ~ 2.9 ± 1 mm/yr since the late Pliocene (Zhang et al., 1998). The fault is likely responsible for the *M* 8 Pingluo earthquake in 1739. Preliminary stacking results show no obvious fault-related deformation. This could be due to the much lower signal-to-noise ratio in comparison to similar studies on strike-slip faults.

6.4.2 Towards a global lithospheric strength map from InSAR

InSAR shows great potential in mapping lithospheric rheology, as demonstrated in this thesis and others. The techniques introduced in Chapter 3 can be applied in tectonically-active continental areas, such as the Alpine-Himalayan orogenic belt, where large earthquakes are not uncommon (Fig. 6.4). Even for earthquakes that

occurred ~ 50 years before the first ever satellite SAR acquisition, postseismic VER deformation can be well-retrieved unambiguously (Ryder et al., 2014). The archive of the last ~ 25 years of SAR data is a treasure that needs to be fully explored for certain intervals of postseismic deformation. The newly-launched Sentinel-1 constellations and ALOS-2 satellite will also provide a wealth of new data with a short revisit time of 6 and 14 days, respectively. Together with other geodetic measurements, these new-generation satellites can provide temporally-extended postseismic observations of previous large earthquakes, and thoroughly capture early postseismic activity for new earthquakes.

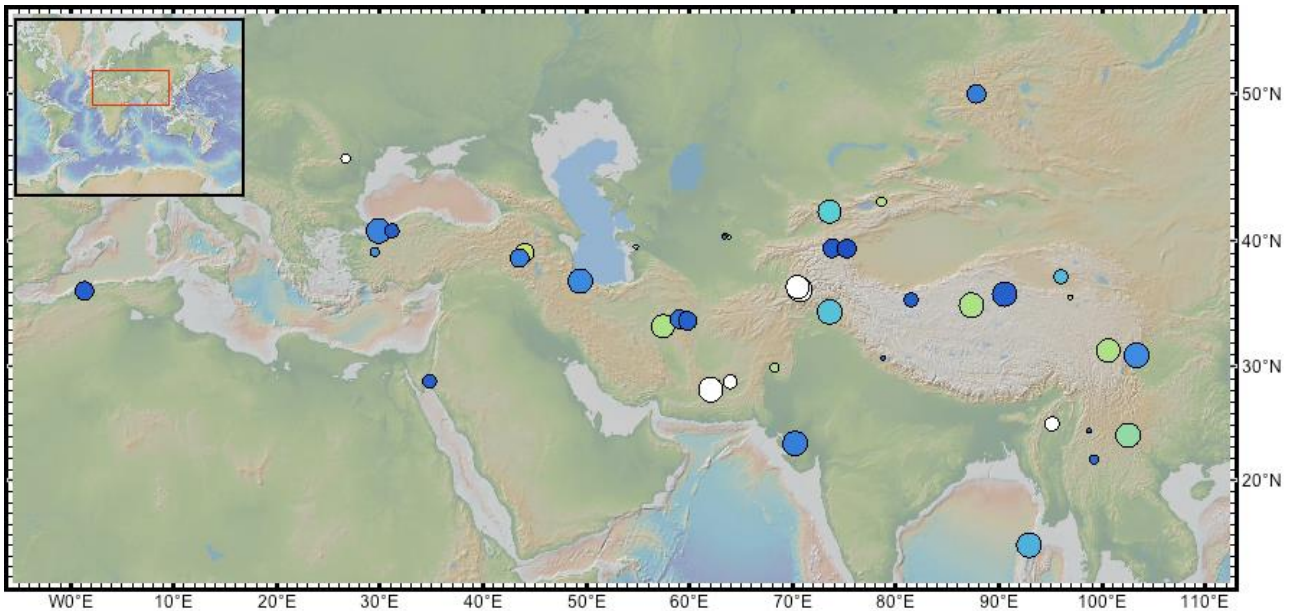

Figure 6. 4. Earthquakes with M > 7.0 (1900-2013) on the Alpine-Himalayan orogenic belt. This map is produced from GeoMapApp, with data from ANSS earthquake catalogue. Colour of circles represents the earthquake depth: the darker the colour, the shallower the earthquake. Circle size is scaled with the earthquake magnitude.

6.4.3 Comprehensive subduction earthquake cycle model

The work in this thesis on the Tarapaca earthquake demonstrates that postseismic deformation observed by InSAR following deep normal faulting earthquakes can be used to constrain subduction zone rheology. The occurrence of the 2014 Iquique

earthquake offers a chance to test the rheological structure I find here. Continuing geodetic monitoring of postseismic deformation should yield further constraints on the rheological structure for this part of the northern Chilean subduction zone.

Future investigations of postseismic deformation following the Tarapaca earthquake should attempt to resolve the discrepancy between modelled postseismic deformation time-series and the GPS recordings (Fig. 6.5). As shown by GPS data at site PICB, the rapid decay at an early postseismic stage might indicate either a lower transient viscosity than the steady-state viscosity or transient motions on the slab triggered by the Tarapaca earthquake. While RELAX is not capable of modelling a Burgers rheology, a finite element model with two viscosities may be required to reconcile the predicted and observed short-term postseismic deformation time-series.

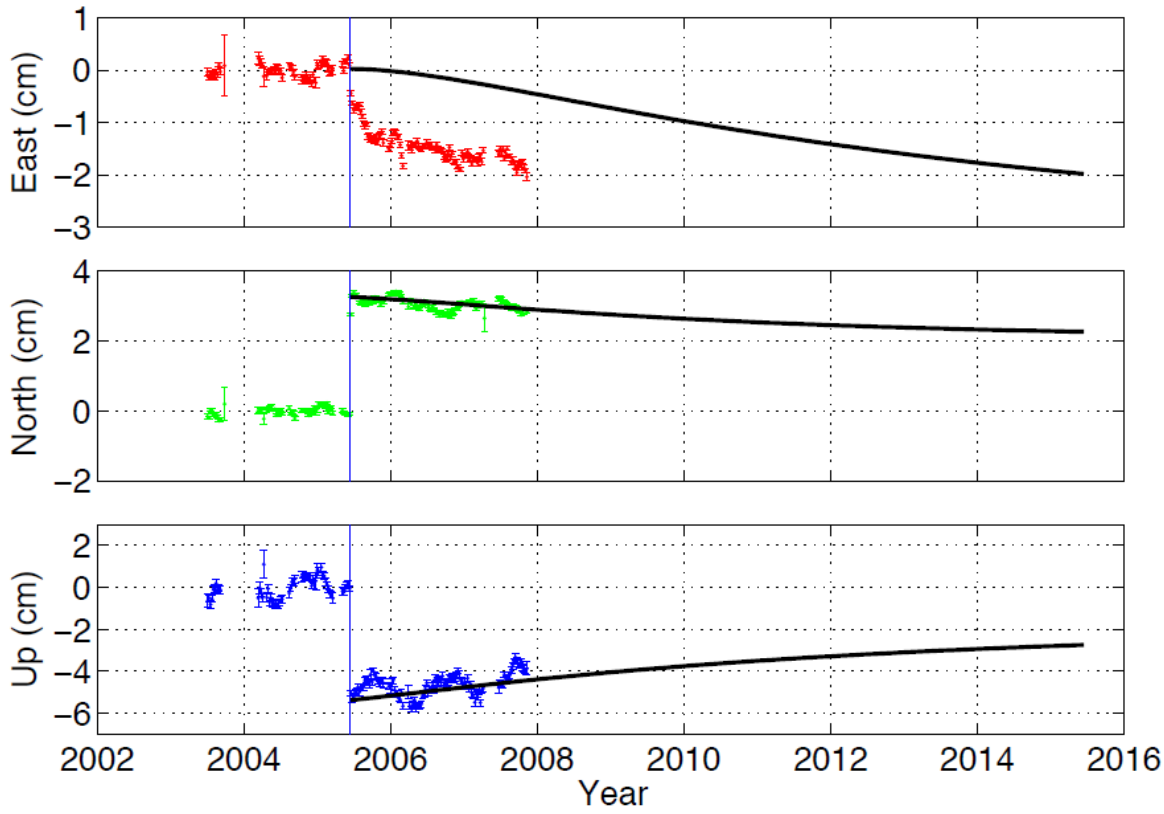

Figure 6. 5. Comparison of modelled (black lines) and observed postseismic displacement time-series at GPS site PICB. GPS recordings are detrended with respect to the pre-Tarapaca interseismic slope. Rapid decay clearly seen from the east component indicates an early stage transient deformation.

Whether it is universally applicable to use intraslab normal faulting earthquakes to constrain subduction zone rheology depends on several factors that influence the detection of postseismic deformation caused by viscoelastic relaxation. The signal amplitude is controlled by the location and magnitude of the intraslab earthquake. If the intraslab earthquake is too deep, small in magnitude and/or away from weak layers, the postseismic signal may be out of the detection capability of geodetic techniques. Atmospheric noise is another issue that should be handled carefully in order to obtain a convincing signal. A match in the observed spatial pattern of deformation with a forward model prediction is merely a first step. Independent geodetic observations, for example, from different SAR sensors, various tracks, and different techniques (e.g. GPS observations) are further needed to consolidate the findings.

The interaction between intraslab normal faulting earthquakes and megathrust earthquakes suggests that a comprehensive subduction zone earthquake cycle model should consider not just great megathrust earthquakes on the plate interface, but also earthquakes in the subducted slab, and potentially their postseismic activities. Such a comprehensive earthquake cycle model will influence earthquake hazard assessments in subduction zones.

6.5 Conclusions

In this thesis, I have systematically explored various phases of earthquake cycle deformation for normal faults in different tectonic settings. Below I will firstly summarize some technical updates I made in this thesis, which can help future derivation of slip models from geodetic observations, and then outline some key findings that may contribute to the knowledge of earthquake physics.

In the study of the 2008 M_w 6.3 Damxung earthquake, I built up an automatic nonlinear inversion strategy that considers the layered elastic structure of the upper crust. In comparison to the homogeneous Earth model, the layered crustal model yields a comparable slip distribution pattern, but a slightly deeper centroid with smaller maximum slip. The strategy can be easily adapted in future use for fast retrieval of fault parameters and seismic moment release. Application of triangular dislocation modelling in the slip inversion for the 2008 M_w 7.1 Yutian earthquake demonstrated its capability in producing a fault geometry consistent with aftershock distribution and surface rupture.

The slip inversion for the Damxung earthquake shows a blind rupture below a downdip depth of ~ 5 km. A summary of geodetically-studied moderate-to-large normal fault earthquakes demonstrates the existence of shallow slip deficit, similar to that found by Fialko et al. (2005) for several large strike-slip earthquakes. The only exception in our compilation is the M_w 7.1 Yutian earthquake, where maximum coseismic moment release occurs in the uppermost 5 km.

For the continental normal faulting earthquakes investigated in this thesis, afterslip is the dominant mechanism responsible for the postseismic ground motion. Afterslip patches tend to appear in close proximity to, but no deeper than, the coseismic rupture. Partial overlap between co- and post-seismic slip might indicate the presence of a transition zone between areas with rate-weakening and rate-strengthening frictional behavior.

Transient deformation following normal fault earthquakes provides opportunities to constrain lower crust and/or upper mantle rheology. Assuming a Maxwell viscoelastic half-space beneath an elastic upper crust, VER-induced transient deformation is characterized by a circular uplift pattern across the fault's trace. Although there is no observable VER-related deformation for the Damxung earthquake, a lower bound of 1×10^{18} Pa s is placed on the mid/lower crust of central

Tibet. For the Tibetan Plateau, various studies of transient deformation favour a thickened lower crust with viscosity estimates falling in a range of 10^{18} – 10^{20} Pa s. The short time-scale estimate is compatible with geodynamic models, if the channel thickness is scaled up to the same as for the short-term models.

Chapter 5 presents the first geodetic study on postseismic deformation following an intraslab normal faulting earthquake in the Chilean subduction zone. A set of 45 interferograms is stacked, after atmospheric noise correction using MERIS and ERA-Interim data, to obtain a postseismic rate map. The rate map shows a broad elliptical uplift feature across the fault's surface projection. A line of interseismic GPS survey measurements before and after the 2005 Tarapaca earthquake indicates postseismic activity following the Tarapaca earthquake. A lower bound of 5×10^{19} Pa s is obtained for the continental lower crust and upper mantle by testing various combinations of rheological parameters, while fixing the oceanic mantle viscosity at 1×10^{20} Pa s. A weak continental asthenosphere with a viscosity of $4 – 8 \times 10^{18}$ Pa s is required to fit the geodetic measurements. Comparison of modelled deformation profiles against the data indicates a likely increase in asthenosphere viscosity along the fault's striking direction (from south to north).

Earthquake interaction is explored based on computations of static stress changes. The 2008 M_w 7.1 Yutian earthquake is followed by another two events in 2012 (M_w 6.2) and 2014 (M_w 6.9) in the Ashikule stepover zone, bounded by a series of strike-slip faults. The 2012 earthquake locates in a zone of negative Coulomb stress change calculated from the non-planar source model of the 2008 Yutian earthquake. Both the 2008 and 2012 normal faulting earthquakes positively load the region of the 2014 strike-slip event, suggesting that failure of stepover zone normal faults could bring 'en echelon' strike-slip faults closer to failure. Collectively, the three recent large earthquakes increase the Coulomb stress change by ~ 0.2 bars on a locked segment of the Altyn Tagh fault, where two M 7.1 earthquakes took place in 1924. This segment

of the Altyn Tagh fault has not experienced a large earthquake since 1924, and a slip deficit close to 1 m has accumulated, assuming a slip rate of 10 mm/yr.

To investigate the interplay of different types of earthquakes in a subduction zone, I computed the Coulomb stress change induced by the co- and post-seismic activities following the Tarapaca earthquake. The Coulomb stress changes are resolved on both the megathrust interface (which ruptured in the 2014 *M* 8.2 Iquique earthquake), and nodal planes of the *M* 6.7 preshock, which is regarded as a trigger of the Iquique earthquake by Hayes et al. (2014). Although the plate interface is negatively stressed by the Tarapaca earthquake, a shallow-dipping nodal plane of the *M* 6.7 preshock is positively stressed by ~ 0.03 bars. It shows that static stress triggering by the Tarapaca earthquake may act as an indirect trigger for the Iquique earthquake, via loading of the *M* 6.7 preshock. The interplay demonstrated here implies that comprehensive subduction zone earthquake cycle models should consider other types of earthquakes in addition to megathrust events.

From the case studies and discussion presented in this thesis, one can see that to fully understand the whole spectrum of earthquake cycle, it is necessary to push the limit of current geodetic ability in measuring small-amplitude transient deformation. I anticipate that future development of new geodetic mapping tools and advanced data analysis techniques will boost our knowledge of earthquake physics, and ultimately seismic hazard assessment.

Bibliography

Altamimi, Z., Collilieux, X. & Métivier, L., 2011. ITRF2008: an improved solution of the international terrestrial reference frame, *J. Geod.*, 85(8), 457-473.

Amoruso, A., Crescentini, L. & Fidani, C., 2004. Effects of crustal layering on source parameter inversion from coseismic geodetic data, *Geophys. J. Int.*, 159(1), 353-364.

Antolik, M., Abercrombie, R. E. & Ekström, G., 2004. The 14 November 2001 Kokoxili (Kunlunshan), Tibet, earthquake: Rupture transfer through a large extensional step-over, *Bull. seism. Soc. Am.*, 94(4), 1173-1194.

Armijo, R., Meyer, B., Navarro, S., King, G. & Barka, A., 2002. Asymmetric slip partitioning in the Sea of Marmara pull-apart: a clue to propagation processes of the North Anatolian Fault? *Terra Nova*, 14(2), 80-86.

Armijo, R., Tapponnier, P., Mercier, J. L. & Tong-Lin, H., 1986. Quaternary extension in southern Tibet: Field observations and tectonic implications, *J. geophys. Res.*, 91(B14), 13803-13872.

Árnadóttir, T., Jónsson, S., Pollitz, F. F., Jiang, W. & Feigl, K. L., 2005. Postseismic deformation following the June 2000 earthquake sequence in the south Iceland seismic zone, *J. geophys. Res.*, (1978–2012), 110(B12).

Astiz, L., Lay, T. & Kanamori, H., 1988. Large intermediate-depth earthquakes and the subduction process, *Phys. Earth planet. Inter.*, 53(1), 80-166.

Atzori, S., Manunta, M., Fornaro, G., Ganas, A. & Salvi, S., 2008. Postseismic displacement of the 1999 Athens earthquake retrieved by the Differential Interferometry by Synthetic Aperture Radar time series, *J. geophys. Res.*, 113(B9).

Avouac, J. P., 2015. From geodetic imaging of seismic and aseismic fault slip to dynamic modelling of the seismic cycle, *Annu. Rev. Earth planet Sci.*, 43(1), 233–271, doi:10.1146/annurev-earth-060614-105302.

Barbot, S. & Fialko, Y., 2010. Fourier-domain Green's function for an elastic semi-infinite solid under gravity, with applications to earthquake and volcano deformation, *Geophys. J. Int.*, 182(2), 568-582.

Barbot, S., Fialko, Y. & Bock, Y., 2009. Postseismic deformation due to the M_w 6.0 2004 Parkfield earthquake: Stress-driven creep on a fault with spatially variable rate-and-state friction parameters, *J. geophys. Res.*, 114(B7).

Barbot, S., Hamiel, Y. & Fialko, Y., 2008. Space geodetic investigation of the coseismic and postseismic deformation due to the 2003 M_w 7.2 Altai earthquake: Implications for the local lithospheric rheology, *J. geophys. Res.*, 113(B3), B03403.

Barnhart, W. D. & Lohman, R. B., 2012. Regional trends in active diapirism revealed by mountain range-scale InSAR time series, *Geophys. Res. Lett.*, 39(8).

Barnhart, W. D. & Lohman, R. B., 2013. Phantom earthquakes and triggered aseismic creep: Vertical portioning of strain during earthquake sequences in Iran, *Geophys. Res. Lett.*, 40, 819-823.

Béjar-Pizarro, M., Socquet, A., Armijo, R., Carrizo, D., Genrich, J. & Simons, M., 2013. Andean structural control on interseismic coupling in the North Chile subduction zone, *Nature Geoscience*, 6(6), 462-467.

Bendick, R., McKenzie, D. & Etienne, J., 2008. Topography associated with crustal flow in continental collisions, with application to Tibet, *Geophys. J. Int.*, 175(1), 375-385.

Bennartz, R. & Fischer, J., 2001. Retrieval of columnar water vapour over land from backscattered solar radiation using the Medium Resolution Imaging Spectrometer, *Remote Sens. Environ.*, 78(3), 274-283.

Berardino, P., Fornaro, G., Lanari, R. & Sansosti, E., 2002. A new algorithm for surface deformation monitoring based on small baseline differential SAR interferograms, *IEEE Trans. Geosci. Remote Sens.*, 40(11) 2375-2383.

Berteussen, K, A., 1977. Moho depth determinations based on spectral ratio analysis of NORSAR long period P waves, *Phys. Earth Planet. Interiors*, 15, 13-27.

Bevis, M., Businger, S., Chiswell, S., Herring, T. A., Anthes, R. A., Rocken, C. & Ware, R. H., 1994. GPS meteorology: Mapping zenith wet delays onto precipitable water, *J. Appl. Meteorol.*, 33(3), 379-386.

Bevis, M., Businger, S., Herring, T., Rocken, C., Anthes, R. & Ware, R., 1992. GPS meteorology-Remote sensing of atmospheric water vapor using the Global Positioning System, *J. geophys. Res.*, 97(D14), 15787-15801.

Bie et al., InSAR observations of postseismic activities following the Pichilemu earthquakes, Chile, *in prep*.

Bie, L. & Ryder, I., 2014. Recent seismic and aseismic activity in the Ashikule stepover zone, NW Tibet. *Geophys. J. Int.*, 198(3), 1632-1643.

Bie, L., Ryder, R., Nippress, S. E. J. & Burgmann, R., 2014. Coseismic and post-seismic activity associated with the 2008 M_w 6.3 Damxung earthquake, Tibet, constrained by InSAR, *Geophys. J. Int.*, 196(2), 788-803.

Bilek, S. L. & Lay, T., 2002. Tsunami earthquakes possibly widespread manifestations of frictional conditional stability, *Geophys. Res. Lett.*, 29(14), doi:10.1029/2002GL015215.

Broerse, T., Riva, R., Simons, W., Govers, R. & Vermeersen, B., 2015. Postseismic GRACE and GPS observations indicate a rheology contrast above and below the Sumatra slab, *J. geophys. Res.*, 120, doi:10.1002/2015JB011951.

Brothers, D., Kilb, D., Luttrell, K., Driscoll, N. & Kent, G., 2011. Loading of the San Andreas fault by flood-induced rupture of faults beneath the Salton Sea, *Nat. Geosci.*, 4(7), 486-492.

Bürgmann, R., 2014. Earth science: Warning signs of the Iquique earthquake, *Nature*, 512, 258-259. doi:10.1038/nature13655.

Bürgmann, R. & Chadwell, D., 2014. Seafloor geodesy, *Annu. Rev. Earth planet Sci.,* 42, 509-534.

Bürgmann, R. & Dresen, G., 2008. Rheology of the lower crust and upper mantle: Evidence from rock mechanics, geodesy, and field observations, *Annu. Rev. Earth planet Sci.,* 36(1), 531.

Bürgmann, R., Ergintav, S., Segall, P., Hearn, E. H., McClusky, S., Reilinger, R. E., Woith, H. & Zschau, J., 2002. Time-dependent distributed afterslip on and deep below the Izmit earthquake rupture, *Bull. Seism. Soc. of Am.,* 92(1), 126-137.

Bürgmann, R., Rosen, P. A. & Fielding, E. J., 2000. Synthetic aperture radar interferometry to measure Earth's surface topography and its deformation, *Annu. Rev. Earth planet Sci.,* 28(1), 169-209.

Byerlee, J., 1978. Friction of rocks, *Pure Appl. Geophys.,* 116(4-5), 615-626.

Cavalié, O., Doin, M. P., Lasserre, C. & Briole, P., 2007. Ground motion measurement in the Lake Mead area, Nevada, by differential synthetic aperture radar interferometry time series analysis: Probing the lithosphere rheological structure, *J. geophys. Res.,* 112(B3), B03403.

Cavalié, O., Lasserre, C., Doin, M. P., Peltzer, G., Sun, J., Xu, X. & Shen, Z. K., 2008. Measurement of interseismic strain across the Haiyuan fault (Gansu, China), by InSAR, *Earth Planet. Sci. Lett.,* 275(3), 246-257.

Chang, W. L., Smith, R. B. & Puskas, C. M., 2013. Effects of lithospheric viscoelastic relaxation on the contemporary deformation following the 1959 M_w 7.3 Hebgen Lake, Montana, earthquake and other areas of the intermountain seismic belt, *Geochem. Geophys. Geosyst.,* 14(1), 1-17.

Cheloni, D., Giuliani, R., D'Anastasio, E., Atzori, S., Walters, R. J., Bonci, L., D' Agostino, N., Mattone, M., Calcaterra, S., Gambino, P., Deninno, F., Maseroli, R. & Stefanelli, G., 2014. Coseismic and post-seismic slip of the 2009 L'Aquila (central Italy) M_w 6.3 earthquake and implications for seismic potential along the Campotosto fault from joint inversion of high-precision levelling, InSAR and GPS data, *Tectonophysics,* 622, 168-185.

Chlieh, M., De Chabalier, J. B., Ruegg, J. C., Armijo, R., Dmowska, R., Campos, J. & Feigl, K. L., 2004. Crustal deformation and fault slip during the seismic cycle in the North Chile subduction zone, from GPS and InSAR observations, *Geophys. J. Int.,* 158(2), 695-711.

Chlieh, M., Perfettini, H., Tavera, H., Avouac, J. P., Remy, D., Nocquet, J. M. & Bonvalot, S., 2011. Interseismic coupling and seismic potential along the Central Andes subduction zone, *J. geophys. Res.,* 116(B12), Doi: 10.1029/2010JB008166.

Clark, M. K., Bush, J. W. & Royden, L. H., 2005a. Dynamic topography produced by lower crustal flow against rheological strength heterogeneities bordering the Tibetan Plateau, *Geophys. J. Int.,* 162(2), 575-590.

Clark, M. K., House, M. A., Royden, L. H., Whipple, K. X., Burchfiel, B. C., Zhang, X. & Tang, W., 2005b. Late Cenozoic uplift of southeastern Tibet, *Geology,* 33, 525-528.

Clark, M. K. & Royden, L. H., 2000. Topographic ooze: Building the eastern margin of Tibet by lower crustal flow, *Geology,* 28(8), 703-706.

Cocco, M., Pacheco, J., Singh, S. K. & Courboulex, F., 1997. The Zihuatanejo, Mexico, earthquake of 1994 December 10 (M = 6.6): source characteristics and tectonic implications, *Geophys. J. Int.*, 131(1), 135-145.

Cook, K. L. & Royden, L. H., 2008. The role of crustal strength variations in shaping orogenic plateaus, with application to Tibet, *J. geophys. Res.*, 113(B8).

Copley, A., 2008. Kinematics and dynamics of the southeastern margin of the Tibetan Plateau, *Geophys. J. Int.*, 174(3), 1081-1100.

Copley, A., Avouac, J. P. & Wernicke, B. P., 2011. Evidence for mechanical coupling and strong Indian lower crust beneath southern Tibet, *Nature*, 472(7341), 79-81.

Copley, A., Hollingsworth, J. & Bergman, E., 2012. Constraints on fault and lithosphere rheology from the coseismic slip and postseismic afterslip of the 2006 M_w 7.0 Mozambique earthquake, *J. geophys. Res.*, 117(B3), B03404.

Copley, A. & McKenzie, D., 2007. Models of crustal flow in the India–Asia collision zone, *Geophys. J. Int.*, 169(2), 683-698.

Craig, T. J., Jackson, J. A., Priestley, K. & McKenzie, D., 2011. Earthquake distribution patterns in Africa: their relationship to variations in lithospheric and geological structure, and their rheological implications, *Geophys. J. Int.*, 185(1), 403-434.

Davis, J. L., Herring, T. A., Shapiro, I. I., Rogers, A. E. E. & Elgered, G., 1985. Geodesy by radio interferometry: Effects of atmospheric modeling errors on estimates of baseline length, *Radio sci.*, 20(6), 1593-1607.

D'Agostino, N., Cheloni, D., Fornaro, G., Giuliani, R. & Reale, D., 2012. Space-time distribution of afterslip following the 2009 L'Aquila earthquake, *J. geophys. Res.*, 117(B2), B02402.

Delouis, B. & Legrand, D., 2007. M_w 7.8 Tarapaca intermediate depth earthquake of 13 June 2005 (northern Chile): Fault plane identification and slip distribution by waveform inversion. *Geophys. Res. Lett.*, 34(1). doi:10.1029/2006GL028193.

DeMets, C., Gordon, R. G., Argus, D. F. & Stein, S., 1994. Effect of recent revisions to the geomagnetic reversal time scale on estimates of current plate motions, *Geophys. Res. Lett.*, 21(20), 2191-2194.

Deng, J., Gurnis, M., Kanamori, H. & Hauksson, E., 1998. Viscoelastic flow in the lower crust after the 1992 Landers, California, earthquake, *Science*, 282(5394), 1689-1692.

Devlin, S., Isacks, B. L., Pritchard, M. E., Barnhart, W. D. & Lohman, R. B., 2012. Depths and focal mechanisms of crustal earthquakes in the central Andes determined from teleseismic waveform analysis and InSAR, *Tectonics*, 31(2).

DeVries, P. M. & Meade, B. J., 2013. Earthquake cycle deformation in the Tibetan plateau with a weak mid-crustal layer, *J. geophys. Res.*, 118(6), 3101-3111.

Dieterich, J. H., 1979. Modeling of rock friction: 1. Experimental results and constitutive equations, *J. geophys. Res.*, 84(B5), 2161-2168.

Dieterich, J. H., 2007. Applications of rate- and state-dependent friction to models of fault slip and earthquake occurrence, *Treatise on Geophysics*, 4, 107-129.

Ding, M. & Lin, J., 2014. Post-seismic viscoelastic deformation and stress transfer after the 1960 M 9.5 Valdivia, Chile earthquake: effects on the 2010 M8. 8 Maule, Chile earthquake, *Geophys. J. Int.*, doi:10.1093/gji/ggu048.

Ding, X. L., Li, Z. W., Zhu, J. J., Feng, G. C. & Long, J. P., 2008. Atmospheric effects on InSAR measurements and their mitigation, *Sensors*, 8(9), 5426-5448.

Doin, M. P., Lasserre, C., Peltzer, G., Cavalié, O. & Doubre, C., 2009. Corrections of stratified tropospheric delays in SAR interferometry: Validation with global atmospheric models, *J. Appl. Geophys.*, 69(1), 35-50.

Doin, M. P., Twardzik, C., Ducret, G., Lasserre, C., Guillaso, S. & Jianbao, S., 2015. InSAR measurement of the deformation around Siling Co Lake: Inferences on the lower crust viscosity in central Tibet, *J. geophys. Res.*, 120, doi:10.1002/2014JB011768.

Duan, B. & Oglesby, D. D., 2006. Heterogeneous fault stresses from previous earthquakes and the effect on dynamics of parallel strike-slip faults, *J. geophys. Res.*, 111(B5), doi:10.1029/2004JB003298.

Duman, T. Y., Emre, O., Dogan, A. & Ozalp, S., 2005. Step-over and bend structures along the 1999 Duzce earthquake surface rupture, North Anatolian fault, Turkey, *Bull. Seism. Soc. Am.*, 95(4), 1250-1262.

Elliott, J. R., Biggs, J., Parsons, B. & Wright, T. J., 2008. InSAR slip rate determination on the Altyn Tagh Fault, northern Tibet, in the presence of topographically correlated atmospheric delays, *Geophys. Res. Lett.*, 35(12). doi:10.1029/2008GL033659

Elliott, J. R., Nissen, E. K., England, P. C., Jackson, J. A., Lamb, S., Li, Z., Oehlers, M. & Parsons, B., 2012. Slip in the 2010-2011 Canterbury earthquakes, New Zealand, *J. geophys. Res.*, 117(B3).

Elliott, J. R., Walters, R. J., England, P. C., Jackson, J. A., Li, Z. & Parsons, B, 2010. Extension on the Tibetan plateau: recent normal faulting measured by InSAR and body wave seismology, *Geophys. J. Int.*, 183(2), 503-535.

Engdahl, E.R. & Villaseñor, A., 2002. Global seismicity: 1900-1999, in *International Handbook of Earthquake and Engineering Seismology, Part A, Chapter 41*, pp. 665-690, eds Lee, W.H.K., Kanamori, H., Jennings, P.C. & Kisslinger, C., Academic Press, Boston.

England, P. & Houseman, P., 1989. Extension during continental convergence, with application to the Tibetan plateau, *J. geophys. Res.*, 94, 17561-17579.

England, P. & Molnar, P., 1997. Active deformation of Asia: from kinematics to dynamics, *Science*, 278(5338), 647-650.

England, P. & Molnar, P., 2005. Late Quaternary to decadal velocity fields in Asia, *J. geophys. Res.*, 110(B12).

England, P. C., Walker, R. T., Fu, B. & Floyd, M. A., 2013. A bound on the viscosity of the Tibetan crust from the horizontality of palaeolake shorelines, *Earth planet Sci. Lett.*, 375, 44-56.

Farr, T. G. *et al.*, 2007. The Shuttle Radar Topography Mission, *Rev. Geophys.*, 45(2).

Faulkner, D. R., Mitchell, T. M., Behnsen, J., Hirose, T. & Shimamoto, T., 2011. Stuck in the mud? Earthquake nucleation and propagation through accretionary forearcs, *Geophys. Res. Lett.*, 38(18).

Feng, L., Newman, A. V., Protti, M., González, V., Jiang, Y. & Dixon, T. H., 2012. Active deformation near the Nicoya Peninsula, northwestern Costa Rica, between 1996 and 2010: Interseismic megathrust coupling, *J. geophys. Res.*, 117(B6).

Fialko, Y., 2004a. Evidence of fluid-filled upper crust from observations of postseismic deformation due to the 1992 M_w 7. 3 Landers earthquake, *J. geophys. Res.*, 109(B8).

Fialko, Y., 2004b. Probing the mechanical properties of seismically active crust with space geodesy: Study of the coseismic deformation due to the 1992 M_w 7.3 Landers (southern California) earthquake, *J. geophys. Res.*, 109(B3).

Fialko, Y., 2006. Interseismic strain accumulation and the earthquake potential on the southern San Andreas fault system, *Nature*, 441(7096), 968-971.

Fialko, Y., Sandwell, D., Simons, M. & Rosen, P., 2005. Three-dimensional deformation caused by the Bam, Iran, earthquake and the origin of shallow slip deficit, *Nature*, 435(7040), 295-299.

Fialko, Y., Simons, M. & Agnew, D., 2001. The complete (3-D) surface displacement field in the epicentral area of the 1999 M_w7. 1 Hector Mine earthquake, California, from space geodetic observations, *Geophys. Res. Lett.*, 28(16), 3063-3066.

Freed, A.M., 2005. Earthquake triggering by static, dynamic and postseismic stress transfer, *Annu. Rev. Earth Planet. Sci.*, 33, 335-367.

Freed, A. M., Ali, S. T. & Bürgmann, R., 2007. Evolution of stress in Southern California for the past 200 years from coseismic, postseismic and interseismic stress changes, *Geophys. J. Int.*, 169(3), 1164-1179.

Freed, A. M., Bürgmann, R., Calais, E., Freymueller, J. & Hreinsdóttir, S., 2006. Implications of deformation following the 2002 Denali, Alaska, earthquake for postseismic relaxation processes and lithospheric rheology, *J. geophys. Res.*, 111(B1).

Fuenzalida, A., Tavera, H., Ruiz, S., Ryder, I., Fernandez, E., Garth, T., Neto, O. D. L., Métois, M., De Angelis, S. & Rietbrock, A., 2014. Nucleation of the 2014 Pisagua, N. Chile earthquake: seismic analysis of the foreshock sequence. *American Geophysical Union*, Fall Meeting 2014. Abstract #S31D-4456.

Funning, G. J., Parsons, B., Wright, T. J., Jackson, J. A. & Fielding, E. J., 2005. Surface displacements and source parameters of the 2003 Bam (Iran) earthquake from Envisat advanced synthetic aperture radar imagery, *J. geophys. Res.*, 110(B9).

Furuya, M. & Yasuda, T., 2011. The 2008 Yutian normal faulting earthquake (M_w 7.1), NW Tibet: Non-planar fault modeling and implications for the Karakax Fault, *Tectonophysics,* 511(3), 125-133.

Gardi, A., Lemoine, A., Madariaga, R. & Campos, J., 2006. Modeling of stress transfer in the Coquimbo region of central Chile, *J. geophys. Res.,* 111(B4), Doi:10.1029/2004JB003440.

Goetze C., 1978. The mechanisms of creep in olivine, *Phil. Trans. R. Soc. Lond. A.,* 288, 99–119.

Goldstein, R. M., Zebker, H. A. & Werner, C. L., 1988. Satellite radar interferometry: Two-dimensional phase unwrapping, *Radio Sci.,* 23(4), 713-720.

Gonzalez-Ortega, A., Fialko, Y., Sandwell, D., Alejandro Nava-Pichardo, F., Fletcher, J., Gonzalez-Garcia, J., Lipovsky, B., Floyd, M. & Funning, G., 2014. El Mayor-Cucapah (M_w 7.2) earthquake: Early near-field postseismic deformation from InSAR and GPS observations, *J. geophys. Res.,* 119(2), 1482-1497.

Gourmelen, N. & Amelung, F., 2005. Postseismic mantle relaxation in the central Nevada seismic belt, *Science,* 310(5753), 1473-1476.

Gray, A. L., Mattar, K. E. & Sofko, G., 2000. Influence of ionospheric electron density fluctuations on satellite radar interferometry, *Geophys. Res. Lett.,* 27(10), 1451-1454.

Gualandi, A., Serpelloni, E. & Belardinelli, M. E., 2014. Space-time evolution of crustal deformation related to the M_w 6.3, 2009 L'Aquila earthquake (central Italy) from principal component analysis inversion of GPS position time-series, *Geophys. J. Int.,* doi: 10.1093/gji/ggt522.

Hampel, A. & Hetzel, R., 2015. Horizontal surface velocity and strain patterns near thrust and normal faults during the earthquake cycle: The importance of viscoelastic relaxation in the lower crust and implications for interpreting geodetic data, *Tectonics,* 34(4), 731-752.

Hanssen, R. F., 2001. *Radar Interferometry: Data Interpretation and Error Analysis,* Kluwer Academic Publishers.

Harris, R. A. & Day, S. M., 1993. Dynamics of fault interaction: Parallel strike-slip fault, *J. geophys. Res.,* 98, 4461-4472.

Harris, R. A., & Segall, P., 1987. Detection of a locked zone at depth on the Parkfield, California, segment of the San Andreas fault, *J. geophys. Res.,* 92(B8), 7945-7962.

Harris, R. A., Archuleta, R. J. & Day, S. M., 1991. Fault steps and the dynamic rupture process: 2-D numerical simulations of a spontaneously propagating shear fracture, *Geophys. Res. Lett.,* 18, 893-896.

Hayes, G. P., Herman, M. W., Barnhart, W. D., Furlong, K. P., Riquelme, S., Benz, H. M., Bergman, E., Barrientos, S., Earle, P. & Samsonov, S., 2014. Continuing megathrust earthquake potential in Chile after the 2014 Iquique earthquake, *Nature,* 512(7514), 295-298.

Hayes, G. P., Wald, D. J. & Johnson, R. L., 2012. Slab1. 0: A three-dimensional model of global subduction zone geometries. *J. geophys. Res.,* 117(B1). doi:10.1029/2011JB008524.

He, J., Vernant, P., Chéry, J., Wang, W., Lu, S., Ku, W., Xia, W. & Bilham, R., 2013. Nailing down the slip rate of the Altyn Tagh fault, *Geophys. Res. Lett.*, 40(20), 5382-5386.

Hearn, E. H. & Bürgmann, R., 2005. The effect of elastic layering on inversions of GPS data for coseismic slip and resulting stress changes: Strike-slip earthquakes, *Bull. seism. Soc. Am.*, 95(5), 1637-1653.

Hearn, E. H., Bürgmann, R. & Reilinger, R. E., 2002. Dynamics of Izmit earthquake postseismic deformation and loading of the Düzce earthquake hypocenter, *Bull. seism. Soc. Am.*, 92(1), 172-193.

Hearn, E. H., McClusky, S., Ergintav, S. & Reilinger, R. E., 2009. Izmit earthquake postseismic deformation and dynamics of the North Anatolian Fault Zone, *J. geophys. Res.*, 114(B8).

Hetland, E. A. & Zhang, G., 2014. Effect of shear zones on post-seismic deformation with application to the 1997 M_w 7.6 Manyi earthquake, *Geophys. J. Int.,* doi:10.1093/gji/ggu127.

Hill, E. M., Yue, H., Barbot, S., Lay, T., Tapponnier, P., Hermawan, I., Hubbard, J., Banerjee, P., Feng, L., Natawidjaja, D. & Sieh, K., 2015. The 2012 M_w 8.6 Wharton Basin sequence: A cascade of great earthquakes generated by near-orthogonal, young, oceanic mantle faults, *J. geophys. Res.*, doi:10.1029/2014JB011703.

Hill, D. P. & Prejean, S., 2015. Dynamic triggering. In: Kanamori H., editor. *Treatise on Geophysics*. 2nd edn. Elsevier, Vol. 4.

Hilley, G. E., Johnson, K. M., Wang, M., Shen, Z. K. & Bürgmann, R., 2009. Earthquake–cycle deformation and fault slip rates in northern Tibet, *Geology*, 37(1), 31-34.

Hirth, G. & Kohlstedt, D., 2003. Rheology of the upper mantle and the mantle wedge: A view from the experimentalists. Inside the subduction Factory, Vol. 138, 83-105, ed. Eiler J., *American Geophysical Union*, Monograph.

Hoechner, A., Sobolev, S. V., Einarsson, I. & Wang, R., 2011. Investigation on afterslip and steady state and transient rheology based on postseismic deformation and geoid change caused by the Sumatra 2004 earthquake, *Geochem. Geophys. Geosyst.*, 12(7), Q07010.

Hole, J. A., 2011. Earthquake hazards: Rivers, rifts and ruptures, *Nat. Geosci.*, 4(7), 428-429.

Hsu, Y. J., Bechor, N., Segall, P., Yu, S. B., Kuo, L. C. & Ma, K. F., 2002. Rapid afterslip following the 1999 Chi-Chi, Taiwan earthquake, *Geophys. Res. Lett.*, 29(16), 1-4.

Hsu, Y. J., Simons, M., Avouac, J. P., Galetzka, J., Sieh, K., Chlieh, M., Natawidjaja, D., Prawirodirdjo, L. & Bock, Y., 2006. Frictional afterslip following the 2005 Nias-Simeulue earthquake, Sumatra, *Science*, 312(5782), 1921-1926.

Hu, Y., Bürgmann, R., Banerjee, P. & Wang, K., 2014. Viscoelastic Postseismic Deformation Following the 2012 M_w 8.6 East Indian Ocean Earthquake, *American Geophysical Union*, Fall Meeting 2014, abstract #S11B-4344

Hu, Y. & Wang, K., 2012. Spherical-Earth finite element model of short-term postseismic deformation following the 2004 Sumatra earthquake, *J. geophys. Res.*, 117(B5).

Hu, Y., Wang, K., He, J., Klotz, J. & Khazaradze, G., 2004. Three-dimensional viscoelastic finite element model for postseismic deformation of the great 1960 Chile earthquake, *J. geophys. Res.*, 109(B12).

Huang, M. H., Bürgmann, R. & Freed, A. M., 2014. Probing the lithospheric rheology across the eastern margin of the Tibetan Plateau. *Earth planet Sci. Lett*., 396, 88-96.

Jaeger, J. C., Cook, N. G. & Zimmerman, R., 2009. Fundamentals of rock mechanics, John Wiley & Sons.

Johanson, I. A., Fielding, E. J., Rolandone, F. & Bürgmann, R., 2006. Coseismic and postseismic slip of the 2004 Parkfield earthquake from space-geodetic data, *Bull. Seism. Soc. Am.*, 96(4B), S269-S282.

Johnson, K. M., Bürgmann, R. & Larson, K., 2006. Frictional properties on the San Andreas fault near Parkfield, California, inferred from models of afterslip following the 2004 earthquake, *Bull. Seism. Soc. Am., 96*(4B), S321-S338.

Johnson, K. M., Fukuda, J. I. & Segall, P., 2012. Challenging the rate-state asperity model: Afterslip following the 2011 M 9 Tohoku-oki, Japan, earthquake, *Geophys. Res. Lett.*, 39(20).

Jolivet, R., Agram, P. S., Lin, N. Y., Simons, M., Doin, M. P., Peltzer, G. & Li, Z., 2014. Improving InSAR geodesy using global atmospheric models, *J. geophys. Res.*, 119(3), 2324-2341.

Jónsson, S., Segall, P., Pedersen, R. & Björnsson, G., 2003. Post-earthquake ground movements correlated to pore-pressure transients, *Nature*, 424(6945), 179-183.

Jónsson, S., Zebker, H., Segall, P. & Amelung, F., 2002. Fault slip distribution of the 1999 M_w 7.1 Hector Mine, California, earthquake, estimated from satellite radar and GPS measurements, *Bull. seism. Soc. Am.*, 92(4), 1377-1389.

Jung, H., Green II, H. W. & Dobrzhinetskaya, L. F., 2004. Intermediate-depth earthquake faulting by dehydration embrittlement with negative volume change, *Nature*, 428(6982), 545-549.

Kaneko, Y. & Fialko, Y., 2011. Shallow slip deficit due to large strike-slip earthquakes in dynamic rupture simulations with elasto-plastic off-fault response, *Geophys. J. Int.*, 186(3), 1389-1403.

Kato, A., Obara, K., Igarashi, T., Tsuruoka, H., Nakagawa, S. & Hirata, N., 2012. Propagation of slow slip leading up to the 2011 M_w 9.0 Tohoku-Oki earthquake, *Science*, 335(6069), 705-708.

Kausel, E. & Campos, J., 1992. The M_s = 8 tensional earthquake of 9 December 1950 of northern Chile and its relation to the seismic potential of the region, *Phys. Earth planet. Inter.*, 72(3), 220-235.

Kind, R., Yuan, X., Saul, J., Nelson, D., Sobolev, S. V., Mechie, J., Zhao, W., Kosarev, G., Ni, J., Achauer, U & Jiang, M., 2002. Seismic images of crust and upper mantle beneath Tibet: Evidence for Eurasian plate subduction, *Science*, 298(5596), 1219-1221.

King, G. C., Stein, R. S. & Lin, J., 1994. Static stress changes and the triggering of earthquakes, *Bull. seism. Soc. Am.,* 84(3), 935-953.

King, R. W. & Bock, Y., 2002. Documentation for the GAMIT Analysis Software, release 10.0. Massachusetts Institute of Technology, Cambridge, MA.

Kirby, S., Engdahl, R. E. & Denlinger, R., 1996. Intermediate-depth intraslab earthquakes and arc volcanism as physical expressions of crustal and uppermost mantle metamorphism in subducting slabs. in *Subduction: Top to Bottom*, American Geophysical Union, Geophys. Monogr., Vol. 96, Washington, DC.

Klein, E., Fleitout, L., Vigny, C. & Garaud, J. D., 2014. Postseismic Deformations Associated with Maule Earthquake and the Mechanical Properties of the Asthenosphere and Subduction Interface. *American Geophysical Union,* Fall Meeting 2014. Abstract #G43B-0511.

Klemperer, S., 2006. Crustal flow in Tibet: Geophysical evidence for the physical state of Tibetan lithosphere, and inferred patterns of active flow, *Geol. Soc. Spec. Publ.,* 268, 39–70.

Kola-Ojo, O. & Meissner, R., 2001. Southern Tibet: Its deep seismic structure and some tectonic implications, *J. Asian Earth Sci.,* 19(1), 249-256.

Lasserre, C., Peltzer, G., Crampé, F., Klinger, Y., Van der Woerd, J. & Tapponnier, P., 2005. Coseismic deformation of the 2001 M_w = 7.8 Kokoxili earthquake in Tibet, measured by synthetic aperture radar interferometry, *J. geophys. Res.,* 110(B12). DOI: 10.1029/2004JB003500.

Lay, T., Astiz, L., Kanamori, H. & Christensen, D. H., 1989. Temporal variation of large intraplate earthquakes in coupled subduction zones, *Phys. Earth planet. Inter.,* 54(3), 258-312.

Lay, T., Kanamori, H. & Ruff, L., 1982. The asperity model and the nature of large subduction zone earthquakes, *Earthqu. Predict. Res.,* 1, 3-71.

Lemoine, A., Madariaga, R. & Campos, J., 2002. Slab-pull and slab-push earthquakes in the Mexican, Chilean and Peruvian subduction zones, *Phys. Earth planet. Inter.,* 132(1), 157-175.

Li, S., Moreno, M., Bedford, J., Rosenau, M. & Oncken, O., 2015. Revisiting viscoelastic effects on interseismic deformation and locking degree: a case study of the Peru-North Chile subduction zone, *J. geophys. Res.,* 120, 4522–4538. doi:10.1002/2015JB011903.

Li, Z., Muller, J. P., Cross, P., Albert, P., Fischer, J. & Bennartz, R., 2006. Assessment of the potential of MERIS near-infrared water vapour products to correct ASAR interferometric measurements, *Int. J. Remote Sens.,* 27(2), 349-365.

Lin, Y. N. N., Sladen, A., Ortega-Culaciati, F., Simons, M., Avouac, J. P., Fielding, E. J., Brooks, B. A., Bevis, M., Genrich, J., Rietbrock, A., Vigny, C., Smalley, R. & Socquet, A., 2013. Coseismic and postseismic slip associated with the 2010 Maule Earthquake, Chile: Characterizing the Arauco Peninsula barrier effect, *J. geophys. Res.,* 118(6), 3142-3159.

Liu, Y., Xu, C., Wen, Y., He, P. & Jiang, G., 2012. Fault rupture model of the 2008 Dangxiong (Tibet, China) M_w 6.3 earthquake from Envisat and ALOS data, *Adv. Space Res.,* 50, 952-956.

Lohman, R. B. & Simons, M., 2005. Some thoughts on the use of InSAR data to constrain models of surface deformation: Noise structure and data downsampling, *Geochem. Geophys. Geosyst.*, 6(1), Q01007.

Marone, C. J., 1998. Laboratory-derived friction laws and their application to seismic faulting, *Annu. Rev. Earth Planet. Sci.*, 26(1), 643-696.

Marone, C. J., Scholtz, C. H. & Bilham, R., 1991. On the mechanics of earthquake afterslip, *J. geophys. Res.*, 96(B5), 8441-8452.

Massonnet, D. & Feigl, K. L., 1998. Radar interferometry and its application to changes in the Earth's surface, *Rev. Geophys.*, 36, 441-500.

Mavrommatis, A. P., Segall, P. & Johnson, K. M., 2014. A decadal-scale deformation transient prior to the 2011 M_w 9.0 Tohoku-Oki earthquake, *Geophys. Res. Lett.*, 41(13), 4486-4494.

McCaffrey, R. & Nabelek, J., 1998. Role of oblique convergence in the active deformation of the Himalayas and southern Tibet plateau, *Geology*, 26(8), 691-694.

Meade, B. J., 2007. Algorithms for the calculation of exact displacements, strains, and stresses for triangular dislocation elements in a uniform elastic half space, *Computers & Geosciences*, 33(8), 1064-1075.

Métois, M., Socquet, A., Vigny, C., Carrizo, D., Peyrat, S., Delorme, A., Maureira, E., Valderas-Bermejo, M.-C. & Ortega, I., 2013. Revisiting the North Chile seismic gap segmentation using GPS-derived interseismic coupling, *Geophys. J. Int.*, 194(3), 1283-1294.

Molnar, P., England, P. & Martinod, J., 1993. Mantle dynamics, uplift of the Tibetan Plateau, and the Indian monsoon, *Rev. Geophys.*, 31(4), 357-396.

Molnar, P. & Lyon-Caen, H., 1989. Fault plane solu- tions of earthquakes and active tectonics of the Tibetan plateau and its margins, *Geophys. J. Int.*, 99, 123-153.

Molnar, P. & Tapponnier, P., 1978. Active tectonics of Tibet, *J. geophys. Res.*, 83, 5361-5375.

Moucha, R., Forte, A. M., Mitrovica, J. X. & Daradich, A., 2007. Lateral variations in mantle rheology: implications for convection related surface observables and inferred viscosity models, *Geophys. J. Int.*, 169(1), 113-135.

Nelder, J. A. & Mead, R., 1965. A simplex method for function minimization, *The Computer J*, 7(4), 308-313.

Nelson, K. D., et al., 1996. Partially molten middle crust beneath southern Tibet: Synthesis of project INDEPTH results, *Science*, 274(5293), 1684-1688.

Nishimura, T., Hirasawa, T., Miyazaki, S. I., Sagiya, T., Tada, T., Miura, S. & Tanaka, K., 2004. Temporal change of interplate coupling in northeastern Japan during 1995-2002 estimated from continuous GPS observations, *Geophys. J. Int.*, 157(2), 901-916.

Nishimura, T. & Thatcher, W., 2003. Rheology of the lithosphere inferred from postseismic uplift following the 1959 Hebgen Lake earthquake, *J. geophys. Res.*, 108(B8), 2389.

Noda, H. & Lapusta, N., 2013. Stable creeping fault segments can become destructive as a result of dynamic weakening, *Nature*, 493(7433), 518-521.

Oglesby, D. D., 2005. The dynamics of strike-slip step-overs with linking dip-slip faults, *Bull. Seism. Soc. Am.,* 95(5), 1604-1622.

Okada, Y., 1985. Surface deformation due to shear and tensile faults in a half-space, *Bull. seism. Soc. Am.,* 75, 1135-1154.

Okada, Y., 1992. Internal deformation due to shear and tensile faults in a half-space, *Bull. seism. Soc. Am.,* 82(2), 1018-1040.

Owens, T. J. & Zandt, G., 1997. Implications of crustal property variations for models of Tibetan plateau evolution, *Nature,* 387(6628), 37-43.

Ozawa, S., Nishimura, T., Munekane, H., Suito, H., Kobayashi, T., Tobita, M. & Imakiire, T., 2012. Preceding, coseismic, and postseismic slips of the 2011 Tohoku earthquake, Japan, *J. geophys. Res.,* 117(B7), B07404.

Parsons, T., 2005. A hypothesis for delayed dynamic earthquake triggering, *Geophys. Res. Lett.,* 32(4).

Peltzer, G., Rosen, P., Rogez, F. & Hudnut, K., 1996. Postseismic rebound in fault step-overs caused by pore fluid flow, *Science,* 273, 1202-1204.

Peltzer, G., Rosen, P., Rogez, F. & Hudnut, K., 1998. Poroelastic rebound along the Landers 1992 earthquake surface rupture, *J. geophys. Res.,* 103(B12), 30131-30145.

Perfettini, H. & Avouac, J.P., 2004. Postseismic relaxation driven by brittle creep: A possible mechanism to reconcile geodetic measurements and the decay rate of aftershocks, application to the Chi-Chi earthquake, Taiwan, *J. geophys. Res.,* 109, B2, B02304.

Peyrat, S., Campos, J., De Chabalier, J. B., Perez, A., Bonvalot, S., Bouin, M. P., Legrand, D., Nercessian, A., Charade, O., Patau, G., Clévédé, E., Kausel, E., Bernard, P. & Vilotte, J. P., 2006. Tarapacá intermediate-depth earthquake (M_w 7.7, 2005, northern Chile): A slab-pull event with horizontal fault plane constrained from seismologic and geodetic observations, *Geophys. Res. Lett.,* 33(22).

Philibosian, B. & Simons, M., 2011. A survey of volcanic deformation on Java using ALOS PALSAR interferometric time series, *Geochem. Geophys. Geosyst.,* 12(11), Q11004.

Pollitz, F., 2005. Transient rheology of the upper mantle beneath central Alaska inferred from the crustal velocity field following the 2002 Denali earthquake, *J. geophys. Res.,* 110, B08407.

Pollitz, F., Banerjee, P., Grijalva, K., Nagarajan, B. & Bürgmann, R., 2008. Effect of 3-D viscoelastic structure on post-seismic relaxation from the 2004 *M* = 9.2 Sumatra earthquake. *Geophys. J. Int.,* 173(1), 189-204.

Pollitz, F. F., Peltzer, G. & Bürgmann, R., 2000. Mobility of continental mantle: Evidence from postseismic geodetic observations following the 1992 Landers earthquake, *J. geophys. Res.,*105(B4), 8035-8054.

Pollitz, F. F. & Sacks, I. S., 2002. Stress triggering of the 1999 Hector Mine earthquake by transient deformation following the 1992 Landers earthquake, *Bull. seism. Soc. Am.,* 92(4), 1487-1496.

Ramon, D., Cazier, L. & Santer, R., 2003. The surface pressure retrieval in the MERIS O_2 absorption: Validation and potential improvements. In Geoscience and Remote Sensing Symposium, 2003. IGARSS'03. Proceedings. 2003 IEEE International (Vol. 5, pp. 3126-3128). IEEE.

Rapine, R., Tilmann, F., West, M., Ni, J. & Rodgers, A., 2003. Crustal structure of northern and southern Tibet from surface wave dispersion analysis, *J. geophys. Res.,* 108(B2), 2120.

Ratschbacher, L., 2011. Rifting and strike-slip shear in central Tibet and the geometry, age and kinematics of upper crustal extension in Tibet. in *Growth and Collapse of the Tibetan Plateau,*Vol. 353, pp. 127-163, eds Gloaguen, R. & Ratschbacher, L. et al., Geol. Soc, London, Special Publications.

Reid, H. F., 1910. The mechanics of the earthquake (Vol. 2). Carnegie institution of Washington.

Reilinger, R., 1986. Evidence for postseismic viscoelastic relaxation following the 1959 *M* = 7.5 Hebgen Lake, Montana, earthquake, *J. geophys. Res.,* 91(B9), 9488-9494.

Reilinger, R. E., Ergintav, S., Bürgmann, R., McClusky, S., Lenk, O., Barka, A., Gurkan, O., Hearn, L., Feigl, K. L., Cakmal, R., Aktug, B., Ozener, H. & Töksoz, M. N., 2000. Coseismic and postseismic fault slip for the 17 August 1999, *M* = 7.5, Izmit, Turkey earthquake, *Science,* 289(5484), 1519-1524.

Resor, P. G., Pollard, D. D., Wright, T. J. & Beroza, G. C., 2005. Integrating high-precision aftershock locations and geodetic observations to model coseismic deformation associated with the 1995 Kozani-Grevena earthquake, Greece, *J. geophys. Res.,* 110(B9).

Rippe, D. & Unsworth, M., 2010. Quantifying crustal flow in Tibet with magnetotelluric data, *Phys. Earth planet. Inter.,* 179**,** 107–121.

Riva, R. E. M., Borghi, A., Aoudia, A., Barzarghi, R., Sabadini, R. & Panza, G. F., 2007. Viscoelastic relaxation and long-lasting afterslip following the 1997 Umbria-Marche (central Italy) earthquakes, *Geophys. J. Int.,* 169, 534-546.

Rosen, P. A., Henley, S., Peltzer, G. & Simons, M., 2004. Update repeat orbit interferometry package released, *Eos Trans*. AGU, 85, 47, doi:10.1029/2004EO050004.

Roten, D., Olsen, K. B., Pechmann, J. C., Cruz-Atienza, V. M. & Magistrale, H., 2011. 3D simulations of *M* 7 earthquakes on the Wasatch fault, Utah, Part I: Long-period (0-1 Hz) ground motion, *Bull. Seism. Soc. Am.,* 101(5), 2045-2063.

Rousset, B., Barbot, S., Avouac, J. P. & Hsu, Y. J., 2012. Postseismic deformation following the 1999 Chi-Chi earthquake, Taiwan: Implication for lower-crust rheology, *J. geophys. Res.,* 117(B12).

Royden, L. H., Burchfiel, B. C., King, R. W., Wang, E., Chen, Z., Shen, F. & Liu, Y., 1997. Surface deformation and lower crustal flow in eastern Tibet, *Science,* 276(5313), 788-790.

Ruegg, J. C., Campos, J., Armijo, R., Barrientos, S., Briole, P., Thiele, R., Arancibia, M., Canuta, J., Duquesnoy, T., Chang, M., Lazo, D., Lyon-Caen, H., Ortlieb, L., Rossignol, J. C. & Serrurier, L., 1996. The M_w = 8.1 Antofagasta (North Chile) earthquake of July 30, 1995: First results from teleseismic and geodetic data, *Geophys. Res. Lett.,* 23(9), 917-920.

Ruiz, S., Metois, M., Fuenzalida, A., Ruiz, J., Leyton, F., Grandin, R., Vigny, C., Madariaga, R. & Campos, J., 2014. Intense foreshocks and a slow slip event preceded the 2014 Iquique M_w 8.1 earthquake, *Science,* 345(6201), 1165-1169.

Ryder, I., Bürgmann, R. & Fielding, E., 2012. Static stress interactions in extensional earthquake sequences: An example from the South Lunggar Rift, Tibet, *J. geophys. Res.*, 117(B9).

Ryder, I., Bürgmann, R. & Pollitz, F., 2011. Lower crustal relaxation beneath the Tibetan Plateau and Qaidam Basin following the 2001 Kokoxili earthquake, *Geophys. J. Int.,* 187(2), 613-630.

Ryder, I., Bürgmann, R. & Sun, J., 2010. Tandem afterslip on connected fault planes following the 2008 Nima-Gaize (Tibet) earthquake, *J. geophys. Res.,* 115(B3), B03404.

Ryder, I., Parsons, B., Wright, T. J. & Funning, G. J., 2007. Post-seismic motion following the 1997 Manyi (Tibet) earthquake: InSAR observations and modelling, *Geophys. J. Int.,* 169(3), 1009-1027.

Ryder, I., Wang, H., Bie, L. & Rietbrock, A., 2014. Geodetic imaging of late postseismic lower crustal flow in Tibet, *Earth planet Sci. Lett.,* 404, 136-143.

Sandwell, D. T., Sichoix, L. & Smith, B., 2002. The 1999 Hector Mine earthquake, southern California: Vector near-field displacements from ERS InSAR, *Bull. seism. Soc. Am.,* 92(4), 1341-1354.

Savage, J.C., 1987. Effect of crustal layering upon dislocation modeling, *J. geophys. Res.,* 92(B10), 10 595–10 600.

Savage, J. C. & Svarc, J. L., 2009. Postseismic relaxation following the 1992 M 7. 3 Landers and 1999 M 7. 1 Hector Mine earthquakes, southern California, *J. geophys. Res.,* 114(B1).

Savage, J. C., Svarc, J. L. & Yu, S. B., 2005. Postseismic relaxation and transient creep, *J. geophys. Res.,* 110(B11).

Schmidt, D. A. & Bürgmann, R., 2003. Time-dependent land uplift and subsidence in the Santa Clara valley, California, from a large interferometric synthetic aperture radar data set, *J. geophys. Res.,* 108(B9), 2416.

Scholz, C. H., 2002. *The mechanics of earthquakes and faulting*, Cambridge University Press.

Schurr, B., Asch, G., Hainzl, S., Bedford, J., Hoechner, A., Palo, M., Wang, R., Moreno, M., Bartsch, M., Zhang, Y., Oncken, O., Tilmann, F., Dahm, T., Victor, P., Barrientos, S. & Vilotte, J. P., 2014. Gradual unlocking of plate boundary controlled initiation of the 2014 Iquique earthquake, *Nature,* 512, 299-302. doi:10.1038/nature13681.

Schurr, B., Asch, G., Rietbrock, A., Trumbull, R. & Haberland, C. H., 2003. Complex patterns of fluid and melt transport in the central Andean subduction zone revealed by attenuation tomography, *Earth planet Sci. Lett.,* 215(1), 105-119.

Schurr, B. & Rietbrock, A., 2004. Deep seismic structure of the Atacama basin, northern Chile, *Geophys. Res. Lett.,* 31(12).

Segall, P., 2000. Earthquake and volcano deformation, Princeton University Perss.

Segall, P., Bürgmann, R. & Matthews, M., 2000. Time-dependent triggered afterslip following the 1989 Loma Prieta earthquake, *J. geophys. Res.,* 105(B3), 5615-5634.

Segall, P. & Harris, R., 1987. Earthquake deformation cycle on the San Andreas fault near Parkfield, California, *J. geophys. Res.,* 92(B10), 10511-10525.

Shen, F., Royden, L. H. & Burchfiel, B. C., 2001. Large-scale crustal deformation of the Tibetan Plateau, *J. geophys. Res.,* 106(B4), 6793-6816.

Shen, Z. K., Wang, M., Li, Y., Jackson, D. B., Yin, A., Dong, D. & Fang, P., 2001. Crustal deformation along the Altyn Tagh fault system, western China, from GPS, *J. geophys. Res.,* 106, 30.

Shi, X., Kirby, E., Furlong, K. P., Meng, K., Robinson, R. & Wang, E., 2015. Crustal strength in central Tibet determined from Holocene shoreline deflection around Siling Co, *Earth planet Sci. Lett.,* 423, 145-154.

Simons, M., Fialko, Y. & Rivera, L., 2002. Coseismic deformation from the 1999 M_w 7.1 Hector Mine, California, earthquake as inferred from InSAR and GPS observations, *Bull. seism. Soc. Am.,* 92(4), 1390-1402.

Steacy, S., Gomberg, J. & Cocco, M., 2005. Introduction to special section: Stress transfer, earthquake triggering, and time-dependent seismic hazard, *J. geophys. Res.,* 110(B5).

Steketee, J. A., 1958. On Volterra's dislocations in a semi-infinite elastic medium, *Can. J. Phys.,* 36(2), 192-205.

Styron, R., Taylor, M. & Okoronkwo, K., 2010. Database of active structures from the Indo-Asian collision, *Eos, Trans. Amer. Geophys. Union,* 91(20), 181.

Sun, J., Johnson, K. M., Cao, Z., Shen, Z., Bürgmann, R. & Xu, X, 2011. Mechanical constraints on inversion of coseismic geodetic data for fault slip and geometry: Example from InSAR observation of the 6 October 2008 M_w 6.3 Dangxiong-Yangyi (Tibet) earthquake, *J. geophys. Res.,* 116(B1), B01406.

Sun, T., Wang, K., Iinuma, T., Hino, R., He, J., Fujimoto, H., Kido, M., Osada, Y., Miura, S., Ohta, Y. & Hu, Y., 2014. Prevalence of viscoelastic relaxation after the 2011 Tohoku-oki earthquake, *Nature,* 514(7520), 84-87.

Tapponnier, P., Peltzer, G., Le Dain, A. Y., Armijo, R. & Cobbold, P., 1982. Propagating extrusion tectonics in Asia: new insights from simple experiments with plasticine, *Geology,* 10(12), 611-616.

Tapponnier, P., Xu, Z., Roger, F., Meyer, B., Arnaud, N., Wittlinger, G. & Yang, J., 2001. Oblique stepwise rise and growth of the Tibet Plateau, *Science,* 294(5547), 1671-1677.

Taylor, M. & Yin, A., 2009. Active structures of the Himalayan-Tibetan orogen and their relationships to earthquake distribution, contemporary strain field, and Cenozoic volcanism, *Geosphere,* 5(3), 199-214.

Taylor, M., Yin, A., Ryerson, F. J., Kapp, P. & Ding, L., 2003. Conjugate strike-slip faulting along the Bangong-Nujiang suture zone accommodates coeval east-west extension and north-south shortening in the interior of the Tibetan Plateau, *Tectonics,* 22(4), doi:10.1029/2002TC001361.

Thatcher, W., 2007. Microplate model for the present-day deformation of Tibet, *J. geophys. Res.,* 112(B1).

Thatcher, W., 2009. How the continents deform: the evidence from tectonic geodesy, *Annu. Rev. Earth Planet. Sci.,* 37, 237-262.

Thatcher, W. & Rundle, J. B., 1984, A viscoelastic coupling model for the cyclic deformation due to periodically repeated Earthquakes at subduction zones, *J. geophys. Res.,* 89(B9), 7631–7640, doi:10.1029/JB089iB09p07631.

Trubienko, O., Garaud, J. D. & Fleitout, L., 2014. Models of postseismic deformation after megaearthquakes: the role of various rheological and geometrical parameters of the subduction zone, *Solid Earth Discussions,* 6(1), 427-466.

Tse, S. T. & Rice, J. R., 1986. Crustal earthquake instability in relation to the depth variation of frictional slip properties, *J. geophys. Res.,* 91(B9), 9452-9472.

Wald, D.J., Heaton, T.H. & Hudnut, K.W., 1996. The slip history of the 1994 Northridge, California, earthquake determined from strong-motion, teleseismic, GPS, and leveling data, *Bull. seism. Soc. Am.,* 86(1B), S49–S70.

Walters, R. J., Elliott, J. R., D'Agostino, N., England, P. C., Hunstad, I., Jackson, J. A., Parsons, B., Phillips, R. J. & Roberts, G., 2009. The 2009 L'Aquila earthquake (central Italy): A source mechanism and implications for seismic hazard, *Geophys. Res. Lett.,* 36(17).

Walters, R. J., Elliott, J., Li, Z. & Parsons, B., 2013. Rapid strain accumulation on the Ashkabad fault (Turkmenistan) from atmosphere-corrected InSAR, *J. geophys. Res.,* 118, 3674-3690, doi:10.1002/jgrb.50236.

Wang, C., Shan, X., Wang, C., Ding, X., Zhang, G., & Masterlark, T., 2013. Using finite element and Okada models to invert coseismic slip of the 2008 M_w 7.2 Yutian earthquake, China, from InSAR data, *J. Seismol.,* 17(2), 347-360, doi:10.1007/s10950-012-9324-5.

Wang, H., Elliott, J. R., Craig, T. J., Wright, T. J., Liu-Zeng, J. & Hooper, A., 2014. Normal faulting sequence in the Pumqu-Xainza Rift constrained by InSAR and teleseismic body-wave seismology, *Geochem. Geophys. Geosyst.,* 15(7), 2947-2963.

Wang, K., Hu, Y. & He, J., 2012. Deformation cycles of subduction earthquakes in a viscoelastic Earth, *Nature,* 484(7394), 327-332.

Wang, R., Martín, F. L. & Roth, F., 2003. Computation of deformation induced by earthquakes in a multi-layered elastic crust-FORTRAN programs EDGRN/EDCMP, *Computers & Geosciences,* 29(2), 195-207.

Wang, R., Martín, F. L. & Roth, F., 2006. PSGRN/PSCMP–a new code for calculating co-and post-seismic deformation, geoid and gravity changes based on the viscoelastic-gravitational dislocation theory, *Computers & Geosciences,* 32(4), 527-541.

Wells, D. L. & Coppersmith, K. J., 1994. New empirical relationships among magnitude, rupture length, rupture width, rupture area, and surface displacement, *Bull. Seism. Soc. Am.,* 84(4), 974-1002.

Wen, Y., Li, Z., Xu, C., Ryder, I. & Bürgmann, R., 2012. Postseismic motion after the 2001 M_w 7.8 Kokoxili earthquake in Tibet observed by InSAR time series, *J. geophys. Res.,* 117(B8), B08405.

Wessel, P. & Smith, W. H., 1998. New, improved version of Generic Mapping Tools released, *EOS, Trans. Am. Geophys. Un.,* 79(47), 579-579.

Wright, T. J., Elliott, J. R., Wang, H. & Ryder, I., 2013. Earthquake cycle deformation and the Moho: Implications for the rheology of continental lithosphere, *Tectonophysics,* 609, 504-523.

Wright, T. J., Lu, Z. & Wicks, C., 2003. Source model for the M_w 6.7, 23 October 2002, Nenana Mountain earthquake (Alaska) from InSAR, *Geophys. Res. Lett.,* 30(18), doi:10.1029/2003GL018014.

Wright, T. J., Parsons, B., Jackson, J., Haynes, M., Fielding, E., England, P. & Clarke, P., 1999. Source parameters of the 1 October 1995 Dinar (Turkey) earthquake from SAR interferometry and seismic body wave modelling, *Earth Planet. Sci. Lett.,* 172, 23–37.

Wu, Z. H., Ye, P. S., Barosh, P. J. & Wu, Z. H., 2011. The October 6, 2008 M_w 6.3 magnitude Damxung earthquake, Yadong-Gulu rift, Tibet, and implications for present-day crustal deformation within Tibet, *J. Asian Earth Sci.,* 40(4), 943-957.

Xiong, X., Shan, B., Zheng, Y. & Wang, R., 2010. Stress transfer and its implication for earthquake hazard on the Kunlun Fault, Tibet, *Tectonophysics,* 482(1), 216-225.

Xu, X., Chen, W., Ma, W., Yu, G. & Chen, G., 2002. Surface rupture of the Kunlunshan earthquake (M_s 8.1), northern Tibetan plateau, China, *Seism. Res. Lett.,* 73(6), 884-892.

Xu, X., Tan, X., Yu, G., Wu, G., Fang, W., Chen, J., Song, H. & Shen, J., 2013. Normal- and oblique-slip of the 2008 Yutian earthquake: Evidence for eastward block motion, northern Tibetan Plateau, *Tectonophysics,* 584, 152-165.

Yamasaki, T. & Houseman, G. A., 2012. The crustal viscosity gradient measured from post-seismic deformation: a case study of the 1997 Manyi (Tibet) earthquake, *Earth Planet. Sci. Lett.,* 351, 105-114.

Yamasaki, T., Wright, T. J. & Houseman, G. A., 2014. Weak ductile shear zone beneath a major strike-slip fault: Inferences from earthquake cycle model constrained by geodetic observations of the western North Anatolian Fault Zone, *J. geophys. Res.,* 119(4), 3678-3699.

Yin, A., 1989. Origin of regional, rooted low-angle normal faults: A mechanical model and its tectonic implications, *Tectonics*, 8(3), 469-482.

Yin, A., Kapp, P. A., Murphy, M. A., Manning, C. E., Harrison, T. M., Grove, M., Ding, L., Deng, X. & Wu, C., 1999. Significant late Neogene east-west extension in northern Tibet, *Geology*, 27(9), 787-790.

Yuan, X., Ni, J., Kind, R., Mechie, J. & Sandvol, E., 1997. Lithospheric and upper mantle structure of southern Tibet from a seismological passive source experiment, *J. geophys. Res.*, 102, 27491-27500.

Zebker, H. A., Rosen, P. A. & Hensley, S., 1997. Atmospheric effects in interferometric synthetic aperture radar surface deformation and topographic maps, *J. geophys. Res.*, 102(B10), 7547-7563.

Zhang, C., Cao, J. & Shi. Y., 2009. Studying the viscosity of lower crust of Qinghai-Tibet Plateau according to post-seismic deformation, *Sci. China, Ser. D*, 52(3), 411-419.

Zhang, G., Qu, C., Shan, X., Zhang, G., Song, X., Wang, R., Li, Z & Hu, J., 2011. The coseismic Insar measurements of 2008 Yutian earthquake and its inversion for the fault flip, *Chin. J. Geophys.*, 54(6), 757-765.

Zhang, Y. Q., Mercier, J. L. & Vergély, P., 1998. Extension in the graben systems around the Ordos (China), and its contribution to the extrusion tectonics of south China with respect to Gobi-Mongolia, *Tectonophysics*, 285(1), 41-75.

Zhang, Z., Chen, Y., Yuan, X., Tian, X., Klemperer, S. L., Xu, T., Bai, Z., Zhang, H., Wu, J. & Teng, J., 2013. Normal faulting from simple shear rifting in South Tibet, using evidence from passive seismic profiling across the Yadong-Gulu Rift, *Tectonophysics*, 606, 178-186.

Zhao, S., Müller, R. D., Takahashi, Y. & Kaneda, Y., 2004. 3-D finite-element modelling of deformation and stress associated with faulting: Effect of inhomogeneous crustal structures, *Geophys. J. Int.*, 157(2), 629-644.

Zhao, W., Kumar, P., Mechie, J., Kind, R., Meissner, R., Wu, Z., Shi, D., Su, H., Xue, G., Karplus, M. & Tilmann, F., 2011. Tibetan plate overriding the Asian plate in central and northern Tibet, *Nat. Geosci.*, 4(12), 870-873.

Appendix

Supplementary Tables and Figures for Chapter 3

Table S3.1. Envisat aquisitions (a) and interferograms (b) used in this study for the 2008 Damxung earthquake.

a

Envisat Acquisition Dates (yyyy/mm/dd)	
2008/05/04	2009/11/15
2008/09/21	2009/12/20
2008/10/26	2010/01/24
2009/01/04	2010/02/28
2009/04/19	2010/05/09
2009/05/24	2010/06/13
2009/06/28	2010/08/22
2009/09/06	

b

Interferogram Pairs (yymmdd - yymmdd)	
Coseismic	Postseismic
080504 - 090104	081026 - 090104
080921 - 081026	090104 - 090524
080921 - 090419	090104 - 091115
	090628 - 090906
	090628 - 100509
	090628 - 100613
	090906 - 100124
	090906 - 100509
	090906 - 100613
	091115 - 100124
	091115 - 100509
	091115 - 100613
	091220 - 100228
	091220 - 100822
	100124 - 100509
	100124 - 100613
	100509 - 100613

Table S3.2. Synthetic input source parameters and inversion results for the test of simulated annealing and downhill simplex algorithm considering the effects of crustal layering. A rectangular normal fault buried beneath 4 km with uniform slip of 5 m is used to forward model surface displacements. Displacements are perturbed with synthetic noise and inverted for source parameters using the improved algorithm. Location and fault geometry parameters are well-retrieved.

Parameters	Input	Inversion
X (km) [a]	0	-0.09 ± 0.34
Y (km) [a]	0	-0.12 ± 0.69
Strike(°)	180	179.98 ± 2.88
Dip(°)	45	46.51 ± 3.30
Rake(°)	-90	-90.90 ± 10.24
H_min (km) [b]	4	4.34 ± 0.41
Width (km) [b]	5	4.21 ± 0.99
Length (km)	8	7.60 ± 1.21
Slip (m)	5	6.64 ± 1.68
Moment (10^{18} Nm)	6.28	6.18 ± 0.79

[a] X,Y are the central coordinates of the fault's upper edge projected to the surface. Reference point is at N29.728 E90.424.
[b] Top, Bottom are the depth of the upper and lower edge of the fault plane, respectively.

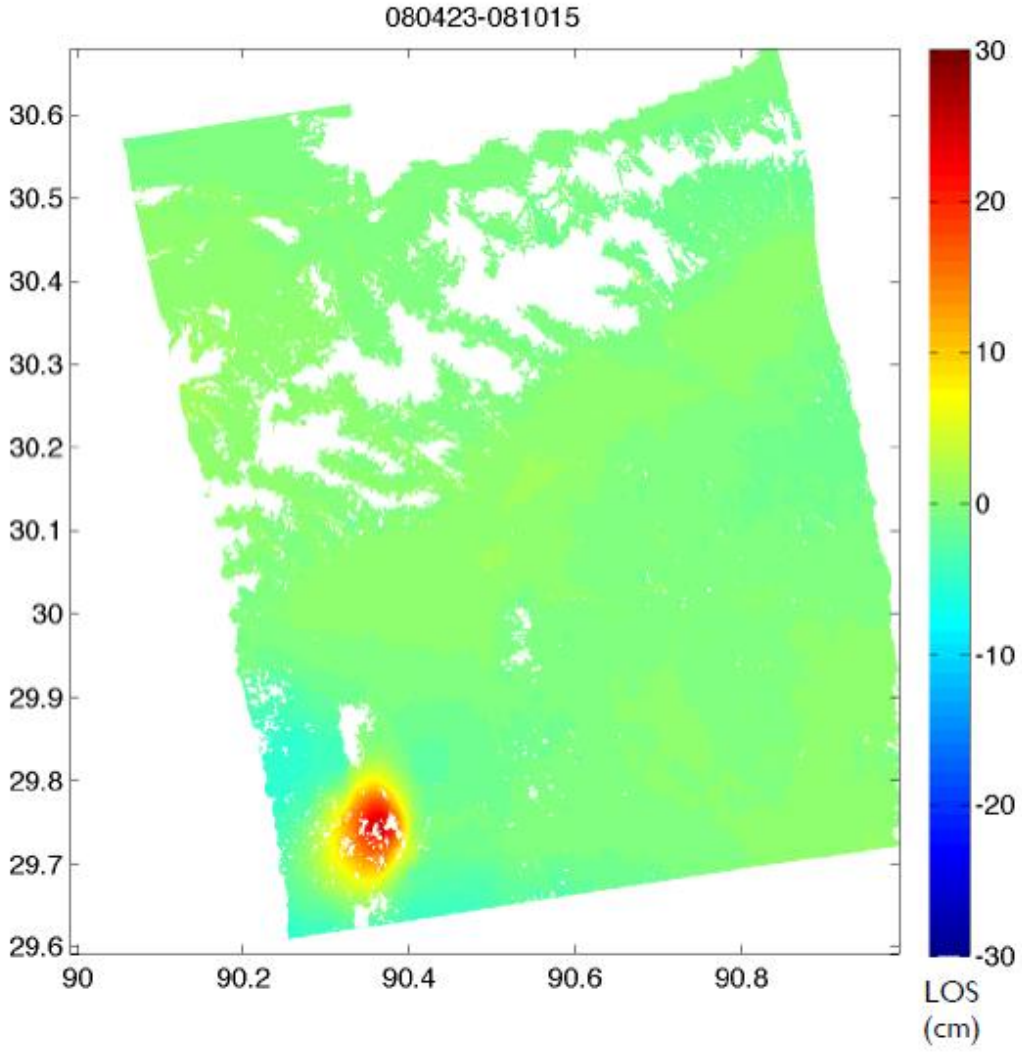

Figure S3.1. Ascending interferogram track 26. Positive range change represents motion away from the satellite, while negative range change indicates motion towards the satellite.

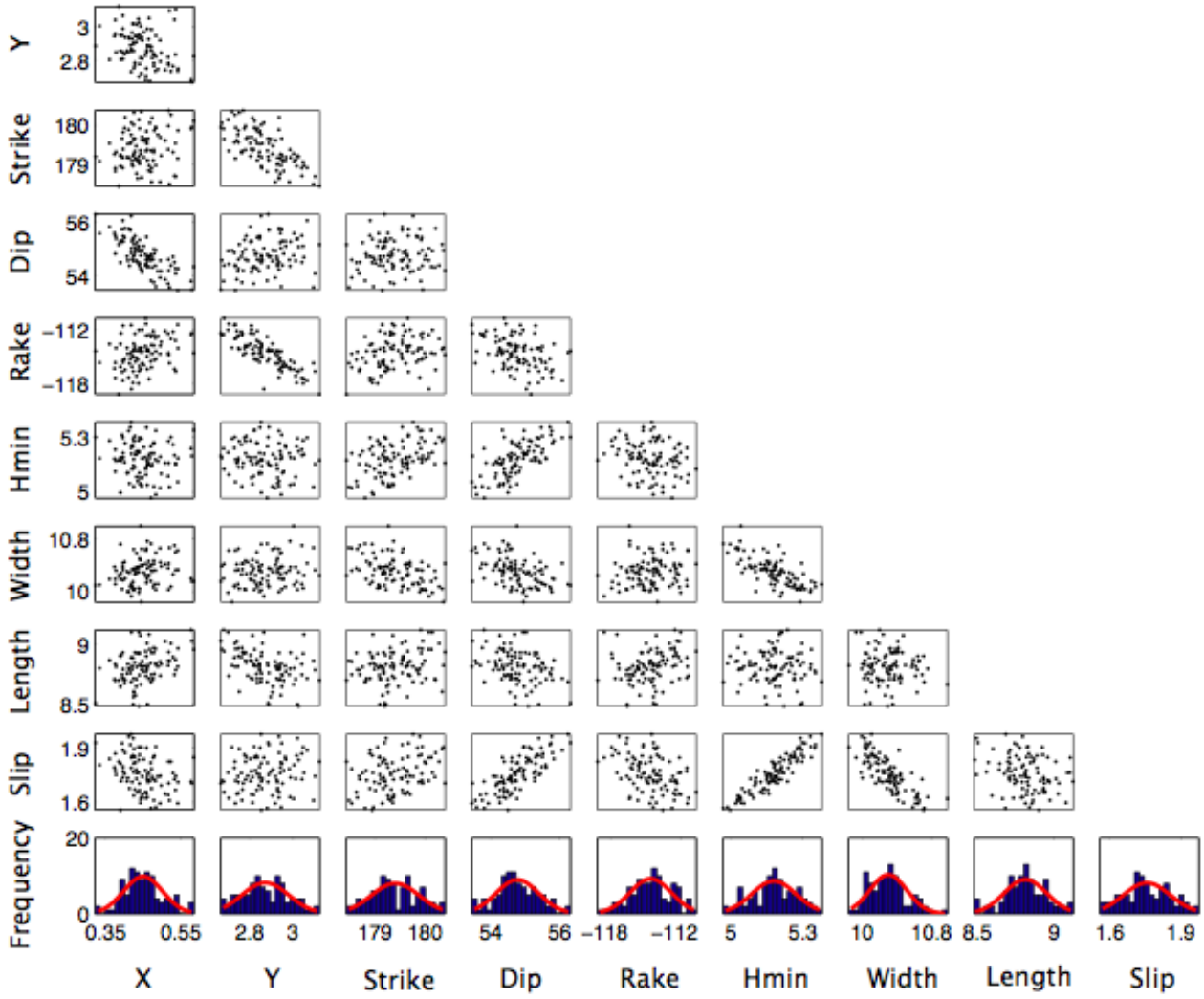

Figure S3.2. Tradeoffs and uncertainties of source parameters for the uniform slip model assuming a homogeneous crust. Red curves in the last row are the Gaussian fit to the distribution of source parameters. Unit of each parameter is the same as that in Table 3.1.

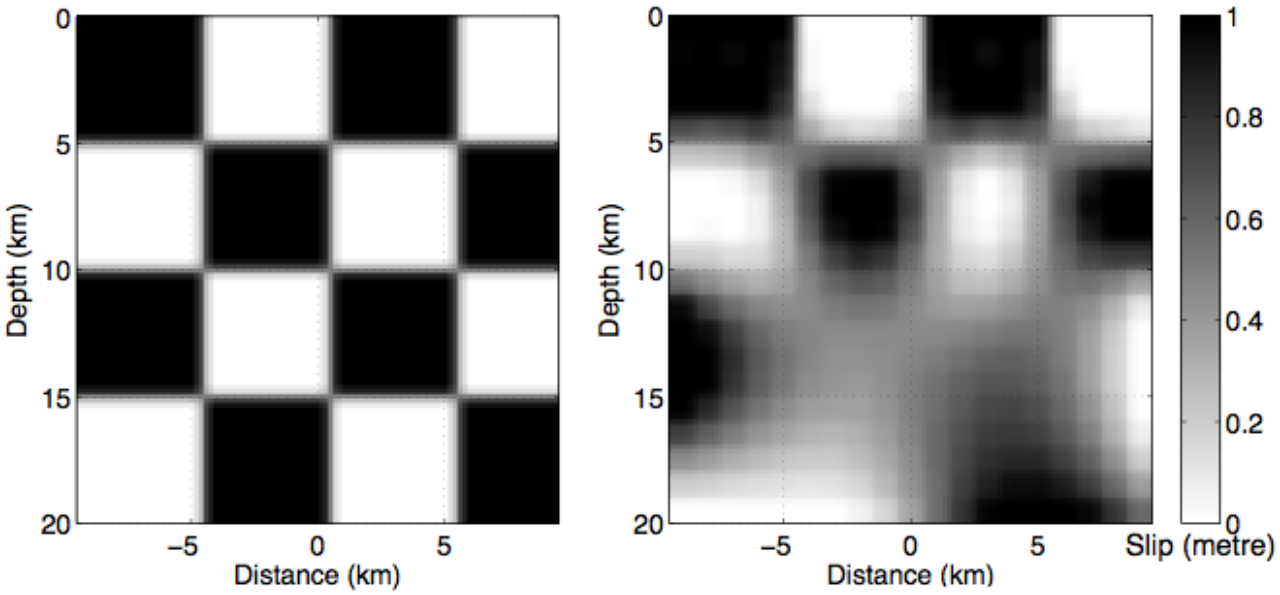

Figure S3.3. Resolution test employing a checkerboard pattern. Left side is the input slip distribution and right side is the recovered slip distribution.

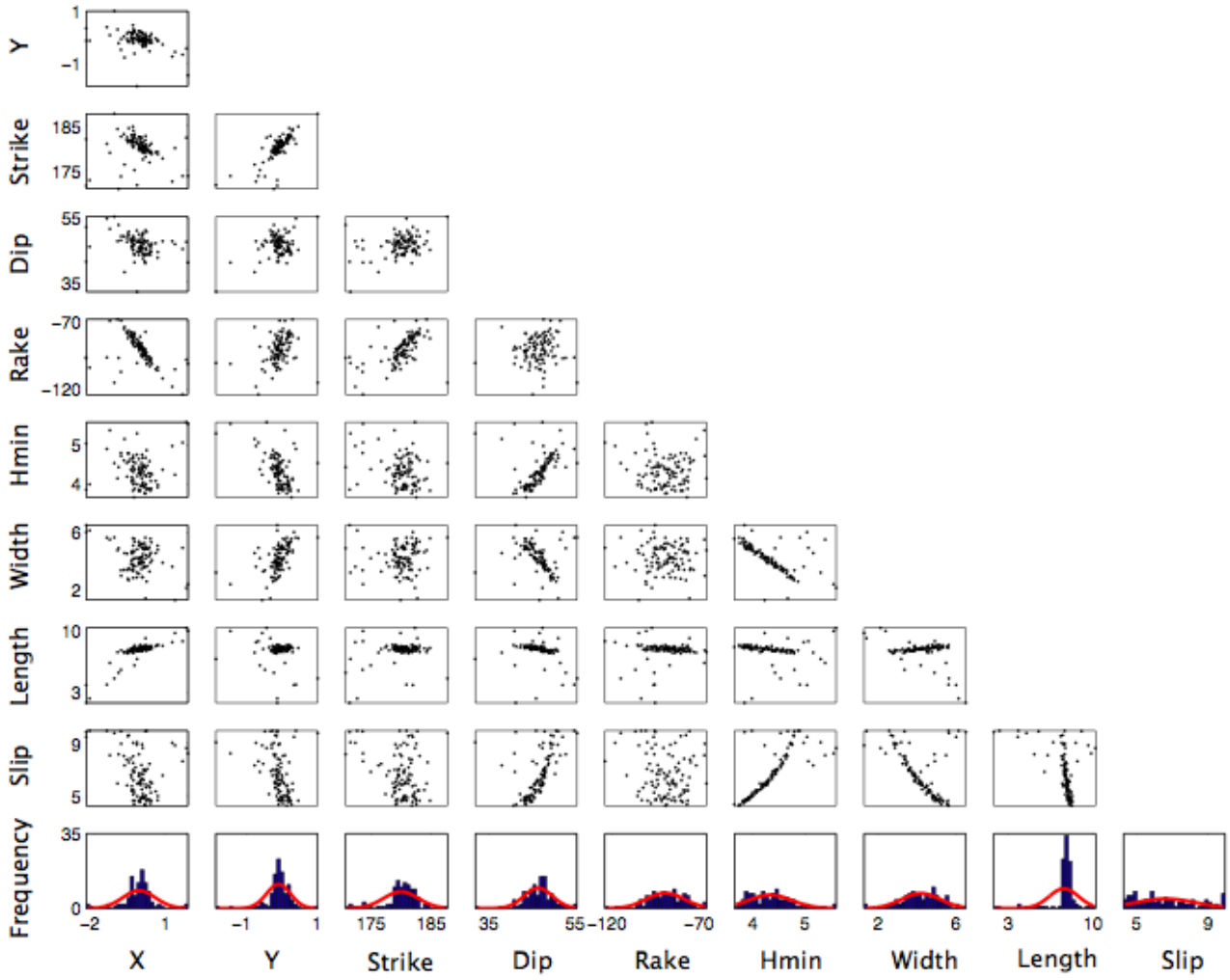

Figure S3.4. Tradeoffs and uncertainties of synthetic source parameters (Table S3.2) for the uniform slip model assuming a homogeneous crust. 100 synthetic noise perturbed datasets are inverted for source parameters distribution. Red curves in the last row are the Gaussian fit to the distribution of source parameters. Unit of each parameter is the same as that in Table 3.1.

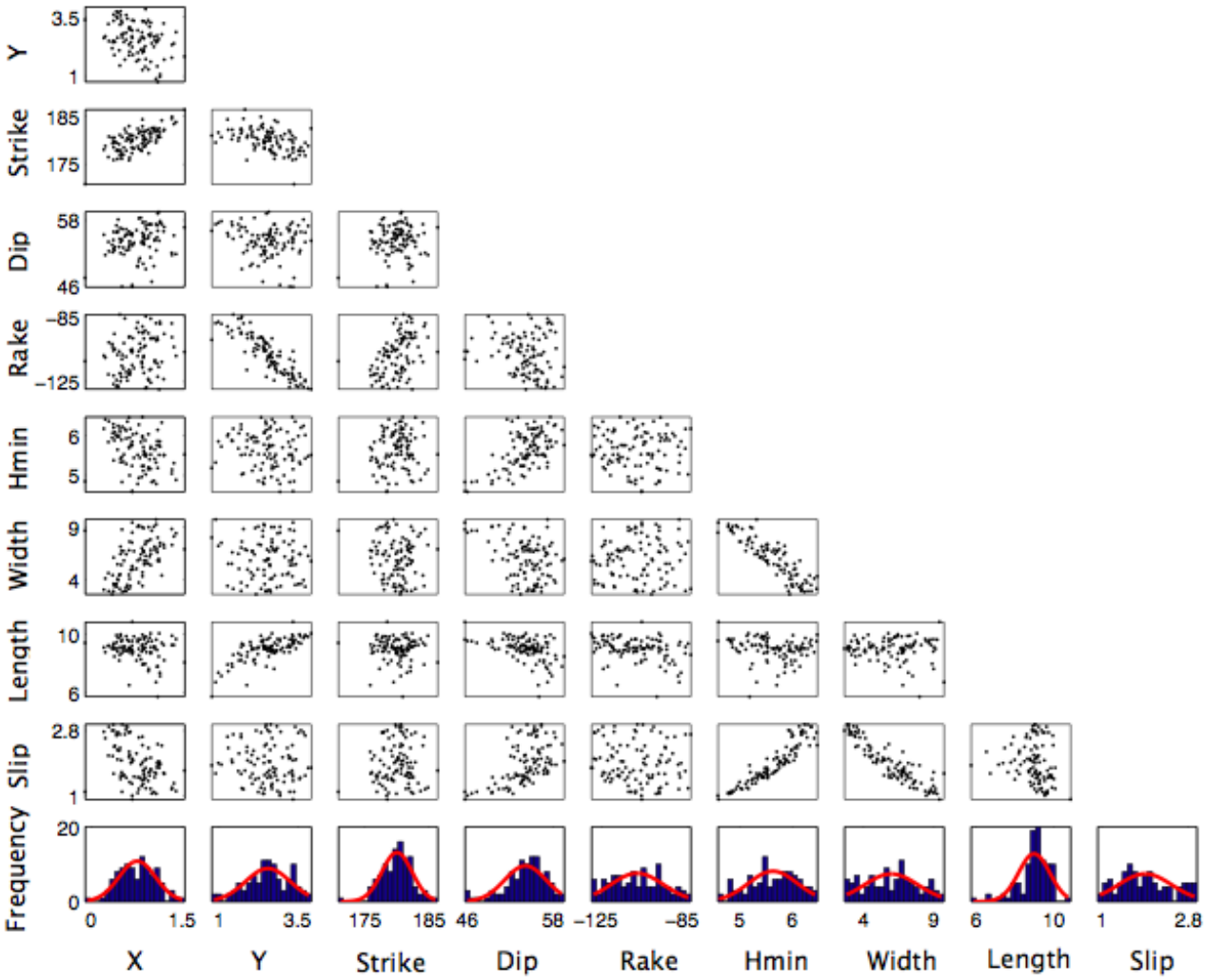

Figure S3.5. Tradeoffs and uncertainties of source parameters for the uniform slip model assuming a layered crust. Red curves in the last row are the Gaussian fit to the distribution of source parameters. Unit of each parameter is the same as that in Table 3.1.

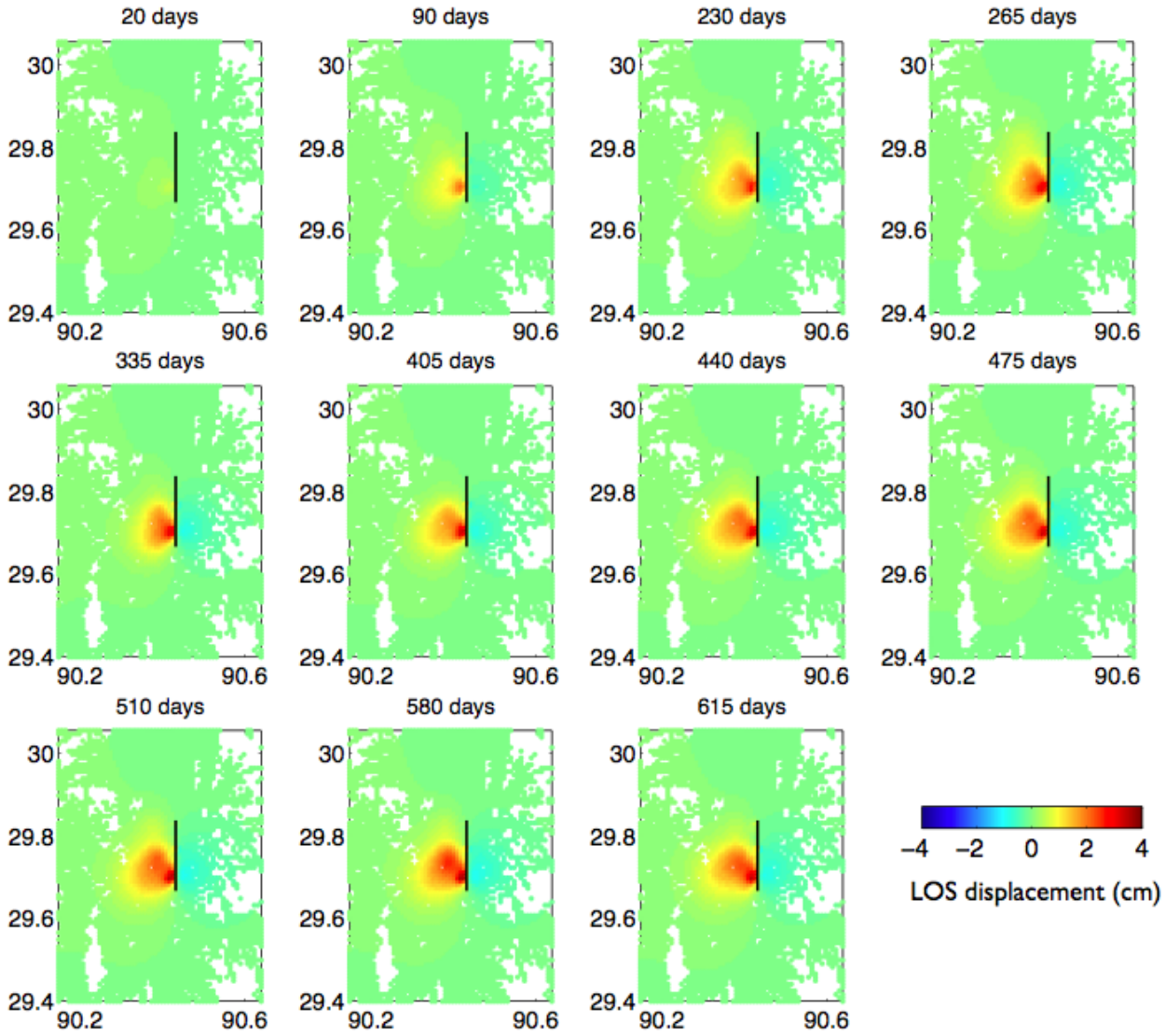

Figure S3.6. Modelled postseismic deformation time-series from afterslip distribution shown in Fig. 3.9. Black line represents the fault trace inferred in this study. Title of each sub-figure refers to number of days after earthquake on 2008 October 6.

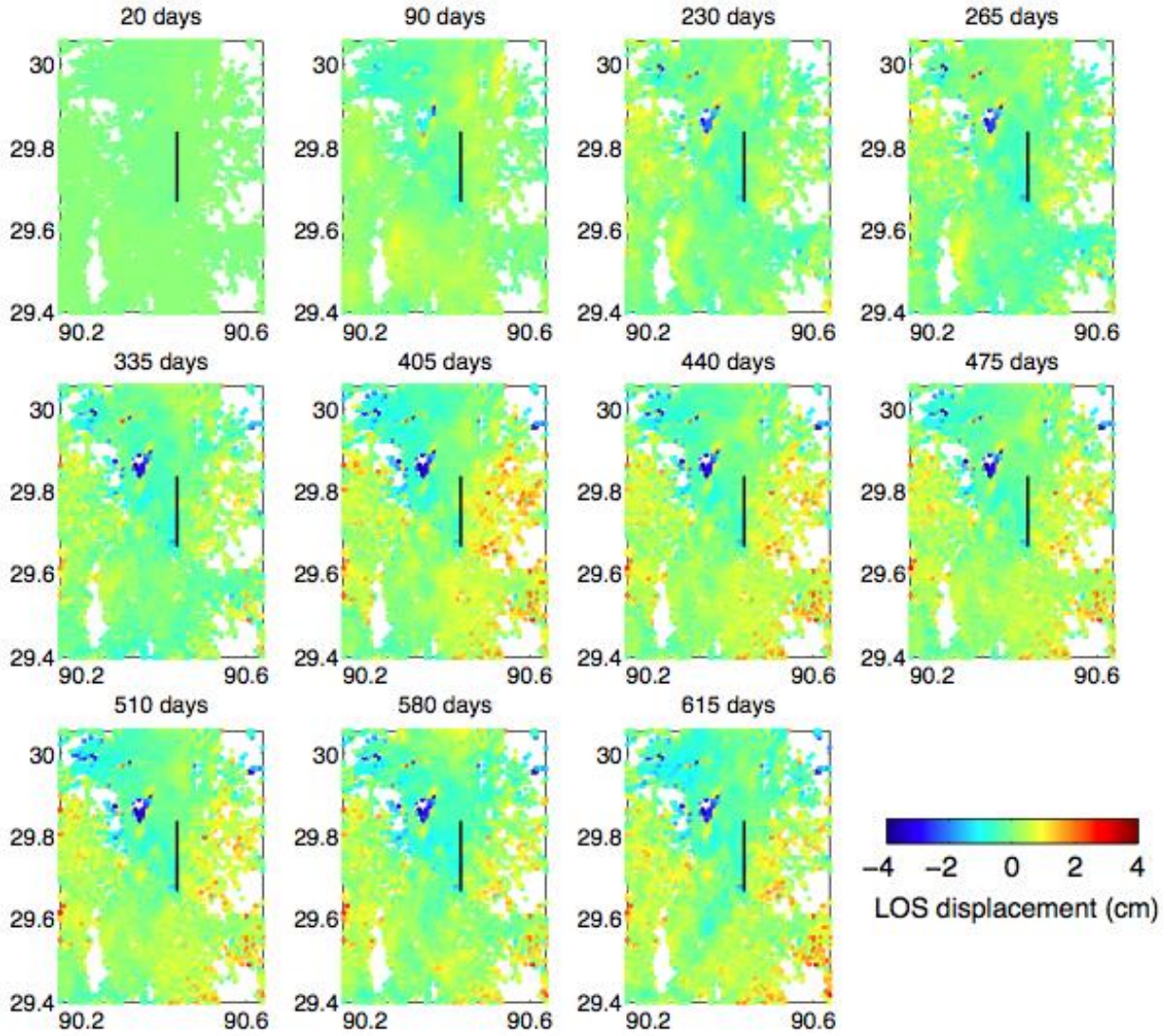

Figure S3.7. Residual between the original postseismic deformation time-series (Fig. 3.5) and the forward-modelled postseismic deformation time-series (Fig. S3.6). Title of each sub-figure refers to number of days after earthquake on 2008 October 6.

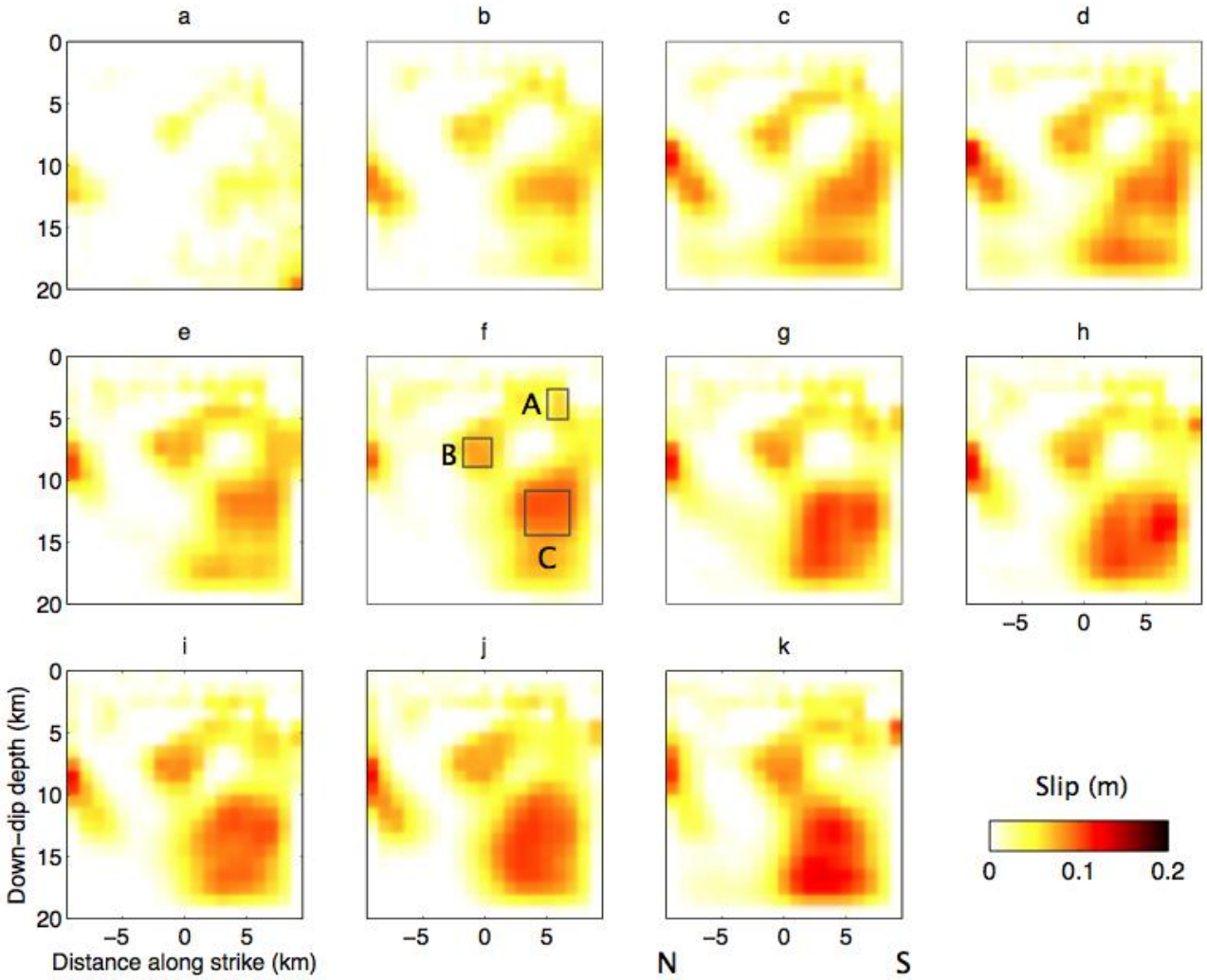

Figure S3.8. Afterslip errors at each SAR acquisition. Error here is the standard deviation of the afterslip distributions derived by inverting 100 sets of realistic noise perturbed postseismic deformation time-series.

Supplementary Tables and Figures for Chapter 4

Table S4.1. Postseismic interferograms from Envisat ascending track 155 used to construct a postseismic deformation time series for the 2008 M_w 7.1 Yutian earthquake.

Postseismic interferogram pairs (yymmdd-yymmdd)
080502-090626
080502-091009
080502-091113
080606-090102
080606-090626
080711-080919
080711-090522
080711-091009
080919-090522
080919-091113
081128-090206

Table S4.2. Receiver fault geometry for Coulomb stress change calculation. ID refers to the fault numbered in Fig. 4.1. Each fault is subdivided into multiple segments with different strikes.

ID: 1; Segments: 6; Kegang Fault						
Start_Lat	Start_Lon	End_Lat	End_Lon	Strike	Dip	Rake
36.273	79.76	36.172	80.20	105.75	45	90
36.172	80.20	36.083	81.092	96.78	45	90
36.083	81.092	36.164	81.517	76.60	45	90
36.164	81.517	36.268	81.779	63.73	45	90
36.268	81.779	36.41	81.972	47.53	45	90
36.41	81.972	36.546	82.271	60.42	45	90
ID: 2; Segments: 7; Altyn Tagh Fault						
Start_Lat	Start_Lon	End_Lat	End_Lon	Strike	Dip	Rake
36.187	79	35.875	80.869	101.11	90	0
35.875	80.869	35.942	81.568	83.05	90	0
35.942	81.568	36.115	82.093	67.68	90	0
36.115	82.093	36.238	82.998	80.18	90	0
36.238	82.998	36.472	83.431	56.01	90	0
36.472	83.431	36.651	83.655	45.08	90	0
36.651	83.655	36.783	83.9999	64.38	90	0
ID: 3; Segments: 1; Altyn Tagh Fault splay						
Start Lat	Start Lon	End Lat	End Lon	Strike	Dip	Rake
35.836	82.241	36.238	82.998	56.48	90	0
ID: 4; Segments: 7						
Start Lat	Start Lon	End Lat	End Lon	Strike	Dip	Rake
35.155	81.494	35.261	81.553	24.44	50	-90
35.261	81.553	35.364	81.573	9.00	50	-90
35.364	81.573	35.446	81.666	42.72	50	-90
35.446	81.666	35.506	81.798	60.79	50	-90
35.506	81.798	35.552	81.97	71.76	50	-90
35.552	81.97	35.631	82.089	50.74	50	-90
35.631	82.089	35.836	82.241	31.00	50	-90

ID: 5; Segments: 1						
Start_Lat	Start_Lon	End_Lat	End_Lon	Strike	Dip	Rake
35.517	79.617	35.006	80.899	115.65	90	180
ID: 6; Segments: 3; Longmu Gozha Co Fault Middle						
Start Lat	Start Lon	End Lat	End Lon	Strike	Dip	Rake
34.829	80.221	34.968	80.875	75.29	90	0
34.968	80.875	34.968	81.027	89.96	90	0
34.968	81.027	35.036	81.258	70.17	90	0
ID: 7; Segments: 1; Longmu Gozha Co Fault East						
Start Lat	Start Lon	End Lat	End Lon	Strike	Dip	Rake
35.065	81.231	35.47	82.76	71.59	90	0
ID: 8; Segments: 3						
Start_Lat	Start_Lon	End_Lat	End_Lon	Strike	Dip	Rake
35.305	82.093	35.409	82.135	18.22	50	-90
35.409	82.135	35.52	82.413	63.80	50	-90
35.52	82.413	35.659	82.458	14.74	50	-90
ID: 9; Segments: 4; Longmu Gozha Co Fault West						
Start Lat	Start Lon	End Lat	End Lon	Strike	Dip	Rake
34.309	79	34.371	79.174	66.61	90	0
34.371	79.174	34.377	79.445	88.39	90	0
34.377	79.445	34.503	79.927	72.28	90	0
34.503	79.927	34.648	80.271	62.79	90	0
ID: 10; Segments: 6						
Start_Lat	Start_Lon	End_Lat	End_Lon	Strike	Dip	Rake
34.781	81.539	34.812	81.953	84.67	90	0
34.812	81.953	34.874	82.344	78.95	90	0
34.874	82.344	34.973	82.774	74.19	90	0
34.973	82.774	35.157	83.411	70.38	90	0
35.157	83.411	35.272	83.741	66.80	90	0
35.272	83.741	35.38	83.979	60.85	90	0

Table S4.3. Estimated fault parameters for the 2012 M_w 6.2 normal faulting earthquake and the 2014 M_w 6.9 strike-slip earthquake, used as input for the calculation of Coulomb stress change. It is assumed here that the rupture on the northern segment of the fault numbered with ID 8 in Fig. 4.1 is responsible for the 2012 earthquake and, since it is an extensional event, that the rupture is buried beneath a depth of 4 km. For the 2014 earthquake, we assume that the rupture on fault numbered with ID 3 in Fig. 4.1 is responsible and, since it is strike-slip, that the rupture extended to the surface. Fault geometries are the same as listed in Table S4.2. Other parameters are listed below.

Event year	Length (km)	Width (km)	Uniform slip (m)	Rigidity (GPa)	Moment (Nm)
2012	15.95	10.00	0.49	3.23	2.5×10^{18}
2014	36.00	12.70	1.90	3.23	2.8×10^{19}

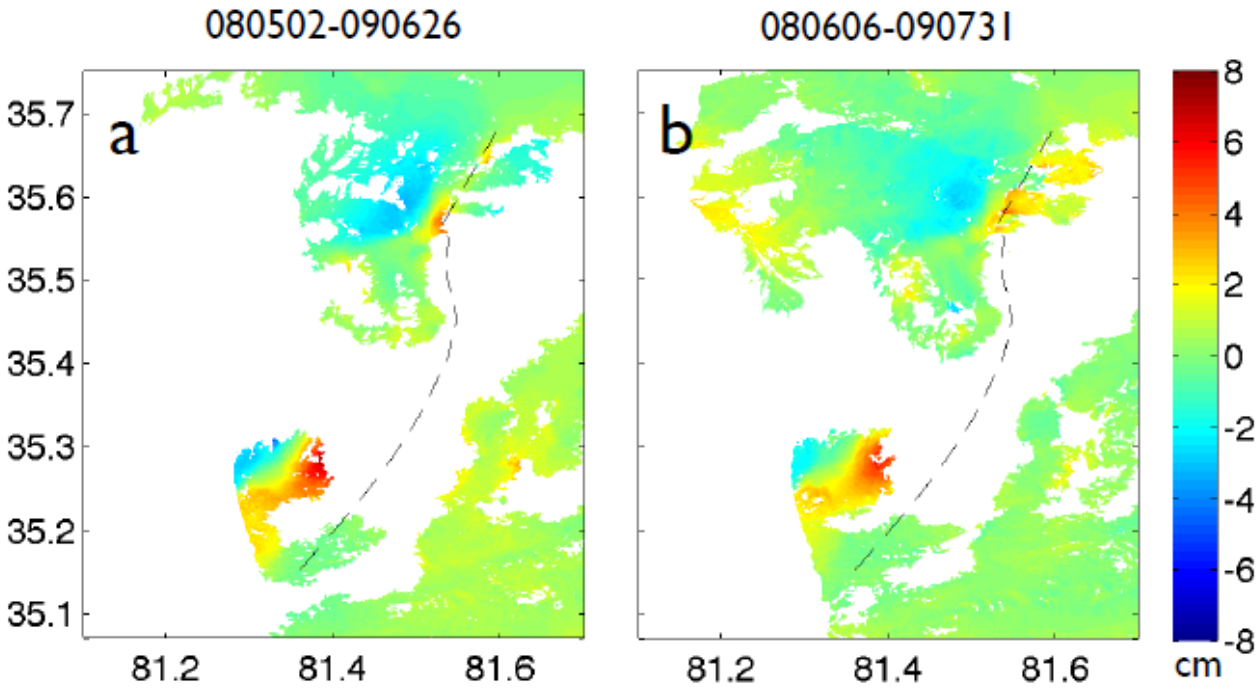

Figure S4.1. Postseismic interferograms for Envisat ascending track 155 with date pairing: (a) 080502-090626; and (b) 080606-090731. Positive range change represents motion away from the satellite, while negative range change indicates motion towards the satellite. Black dashed line marks the fault trace inferred from this study.

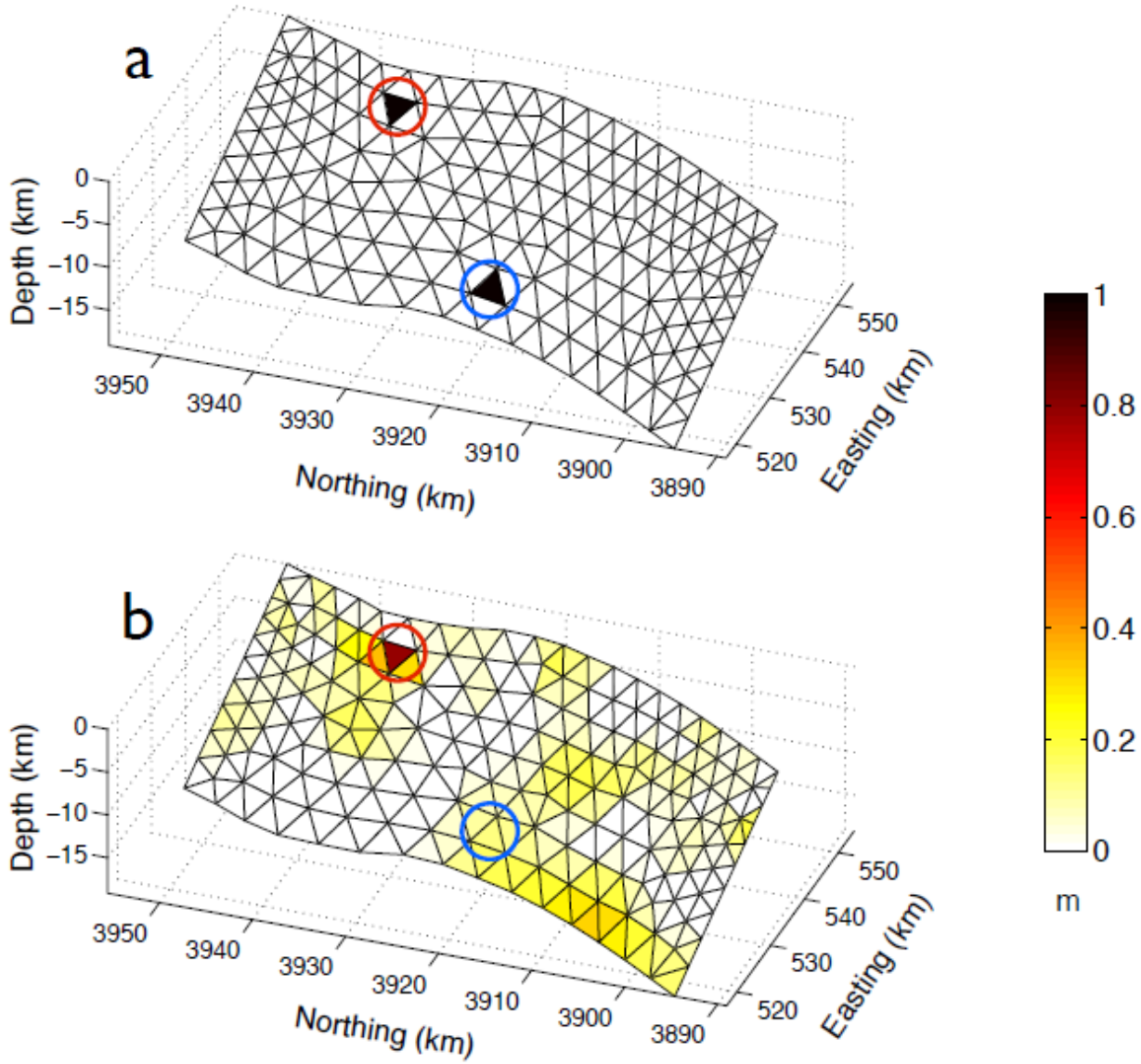

Figure S4.2. Resolution test showing that unit slip at shallow depth can be well retrieved (red circle), but the deeper one is smeared out (blue circle). (a) Input slip model; (b) Recovered slip model.

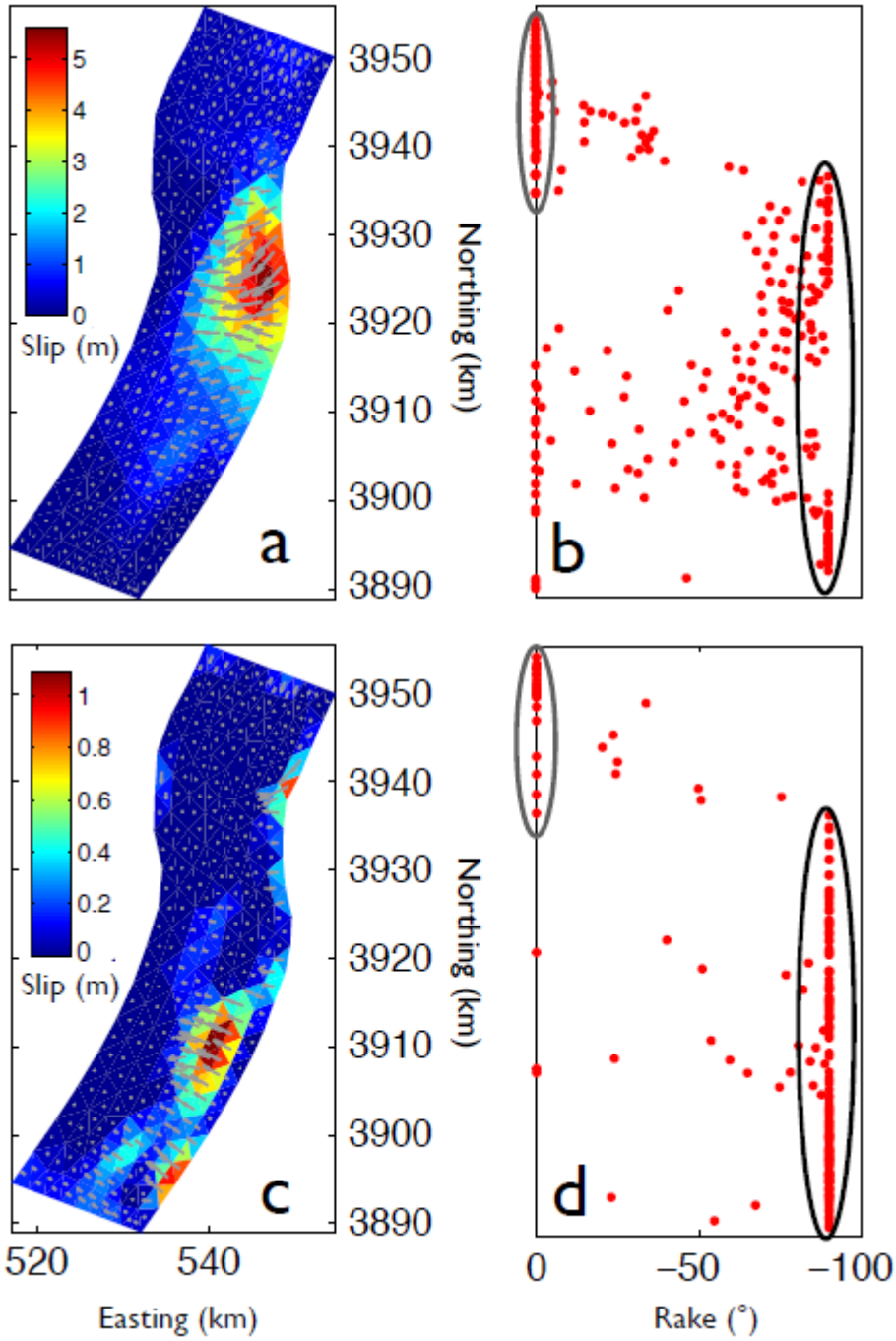

Figure S4.3. Surface projection of the coseismic (a) and postseismic (c) slip distribution models. Grey arrow on each TDE shows the slip direction. (b) and (d) show the slip direction on each TDE as a function of northing, where the grey ellipse circles the northern segment of the fault with mainly left-lateral slip, and black ellipse depicts the central and southern segments with major normal sense of slip.

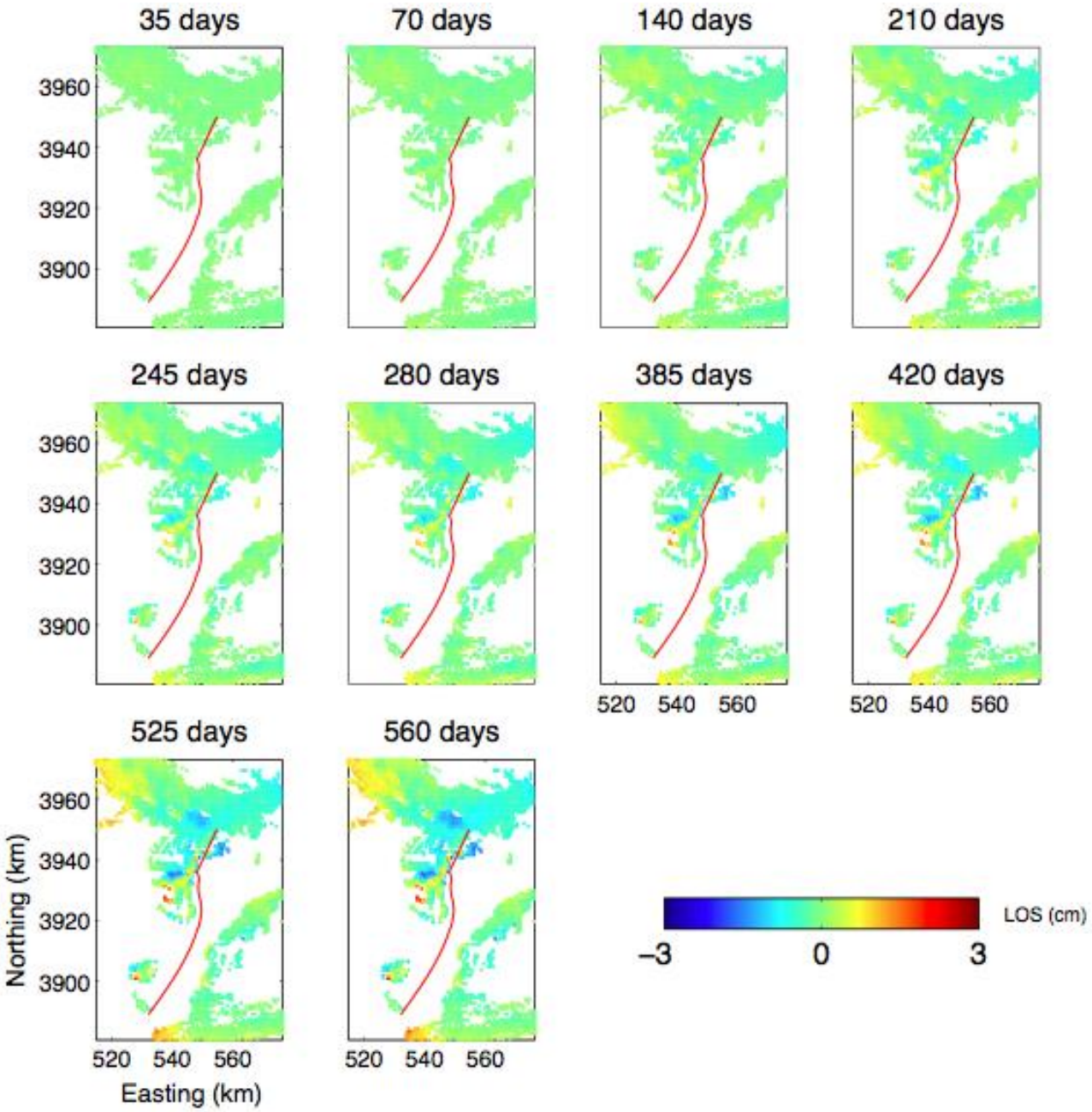

Figure S4.4. Residual between modelled (Figs. 4.5a-j) and observed (Figs. 4.4a-j) postseismic deformation time series. Red line marks the fault trace inferred in this study.

Supplementary Tables and Figures for Chapter 5

Table S5.1. Source parameters of the 2005 M_w 7.8 Tarapaca earthquake (Peyrat et al., 2006), used as input for VER modelling.

Length (km)	Width (km)	Top depth (km)	Strike	Dip	Rake	Slip (m)
54	24	90	189	24	-74	6.5

Table S5.2. List of postseismic interferograms stacked for rate map.

Postseismic interferogram pairs (yymmdd - yymmdd)	
050718 - 050926	070723 - 071105
050718 - 051031	070723 - 080602
050718 - 081124	070723 - 080811
050822 - 070618	070723 - 081020
050822 - 070827	070723 - 090309
050822 - 080811	070827 - 080811
050926 - 051031	070827 - 081020
050926 - 081124	071105 - 071210
051031 - 060703	071105 - 080602
051031 - 081124	071105 - 080707
070129 - 071105	071105 - 080811
070129 - 071210	071105 - 081020
070129 - 080707	071105 - 090309
070129 - 081020	071210 - 080707
070129 - 090309	071210 - 081020
070618 - 070723	071210 - 090309
070618 - 070827	080602 - 080811
070618 - 080602	080602 - 081020
070618 - 080707	080707 - 081020
070618 - 080811	080707 - 090309
070618 - 081020	080811 - 081020
070618 - 090309	081020 - 090309
070723 - 070827	

Table S5.3. Pre-Tarapaca GPS velocities in mm/yr relative to stable South America as defined by NNR-Nuvel1A model. The original velocities were calculated in ITRF2008.

STATION	LON	LAT	Ve	Vn	σe	σn	Measurements	Time-span
IQA0	-70.18	-20.373	27.19	8.72	1.46	1.25	2	1996.915- 2000.8
IQD0	-69.904	-20.221	27.78	7.05	1.11	1.12	2	1996.915-2000.8
IQF0	-69.781	-20.160	26.51	7.70	1.12	1.12	2	1996.915-2000.8
IQH0	-69.636	-19.964	25.23	5.93	1.11	1.12	2	1996.915-2000.8
IQI0	-69.501	-19.907	26.13	5.75	0.96	0.97	3	1996.915-2002.556
IQM0	-69.07	-19.636	20.54	2.55	1.03	1.02	3	1996.915-2002.556
IQN0	-68.978	-19.579	19.78	7.56	1.12	1.12	2	1996.915-2000.8
IQP0	-68.686	-19.481	19.87	6.39	1.11	1.11	2	1996.915-2000.8
IQQ0	-68.544	-19.387	17.71	6.03	1.17	1.14	2	1996.915-2000.8

Table S5.4. Post Tarapaca GPS velocities in mm/yr relative to stable South America as defined by NNR-Nuvel1A model. The original velocities were calculated in ITRF2008.

STATION	LON	LAT	Ve	Vn	σe	σn	Measurements	Time-span
IQA0	-70.18	-20.373	22.22	6.70	0.82	0.82	3	2005.501-2012.288
IQD0	-69.904	-20.221	20.40	5.66	0.82	0.82	2	2005.501-2012.288
IQF0	-69.781	-20.160	20.54	5.89	0.82	0.82	3	2005.501-2012.288
IQH0	-69.636	-19.964	19.86	7.11	0.81	0.82	3	2005.501-2012.288
IQI0	-69.501	-19.907	20.43	6.78	0.82	0.82	3	2005.501-2012.288
IQM0	-69.07	-19.636	20.28	8.30	0.82	0.82	3	2005.501-2012.288
IQN0	-68.978	-19.579	17.76	9.05	1.53	1.53	2	2010.458-2012.288
IQP0	-68.686	-19.481	17.71	9.66	0.81	0.81	3	2005.501-2012.288
IQQ0	-68.544	-19.387	16.53	8.02	0.82	0.82	3	2005.501-2012.288

Table S5.5. Residual velocities (post-pre Tarapaca earthquake) in mm/yr interpreted as postseismic deformation in this study. Velocities are relative to stable South America as defined by NNR-Nuvel1A model.

STATION	LON	LAT	Re	Rn	σre	σrn
IQA0	-70.18	-20.373	-4.97	-2.02	2.28	2.07
IQD0	-69.904	-20.221	-7.38	-1.39	1.93	1.94
IQF0	-69.781	-20.160	-5.97	-1.81	1.94	1.94
IQH0	-69.636	-19.964	-5.37	1.18	1.92	1.94
IQI0	-69.501	-19.907	-5.7	1.03	1.78	1.79
IQM0	-69.07	-19.636	-0.26	5.75	1.85	1.84
IQN0	-68.978	-19.579	-2.02	1.49	2.65	2.65
IQP0	-68.686	-19.481	-2.16	3.27	1.92	1.92
IQQ0	-68.544	-19.387	-1.18	1.99	1.99	1.96

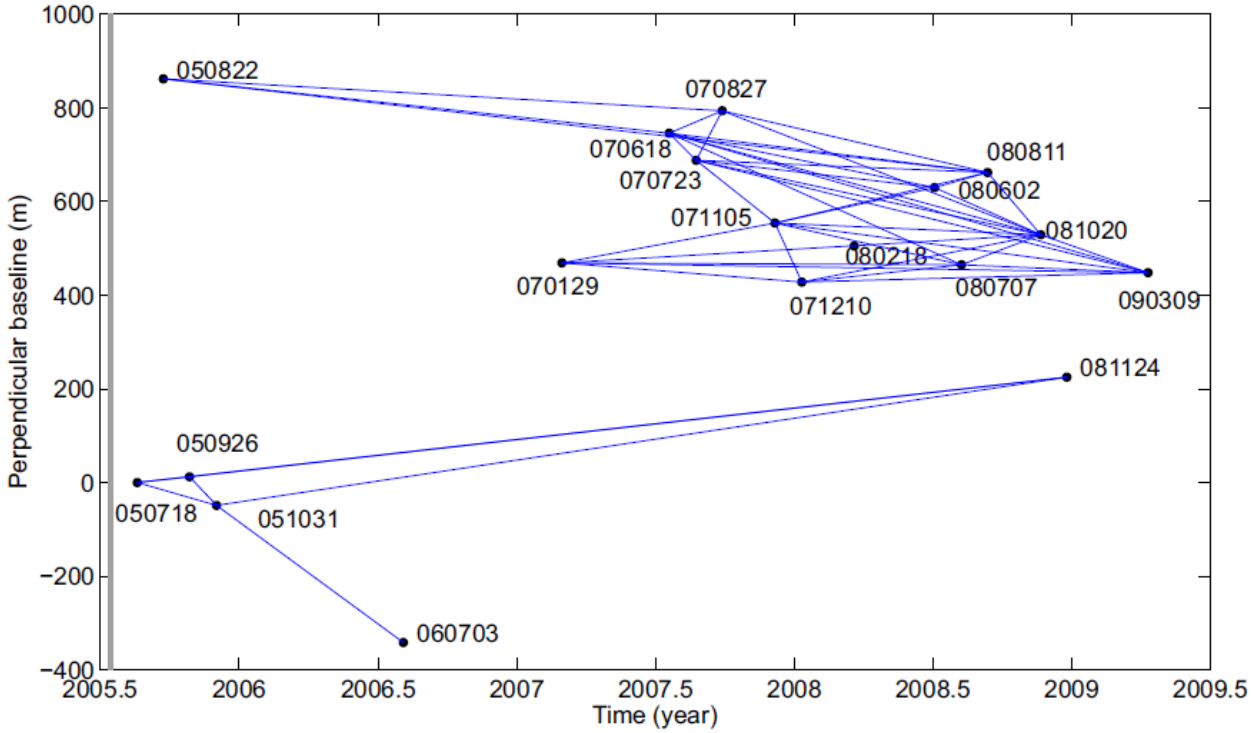

Figure S5.1. Perpendicular baseline-time plots for the 45 Envisat interferograms (Table S5.2) used for rate map construction. Grey line marks the Tarapaca earthquake on 2005 June 13.

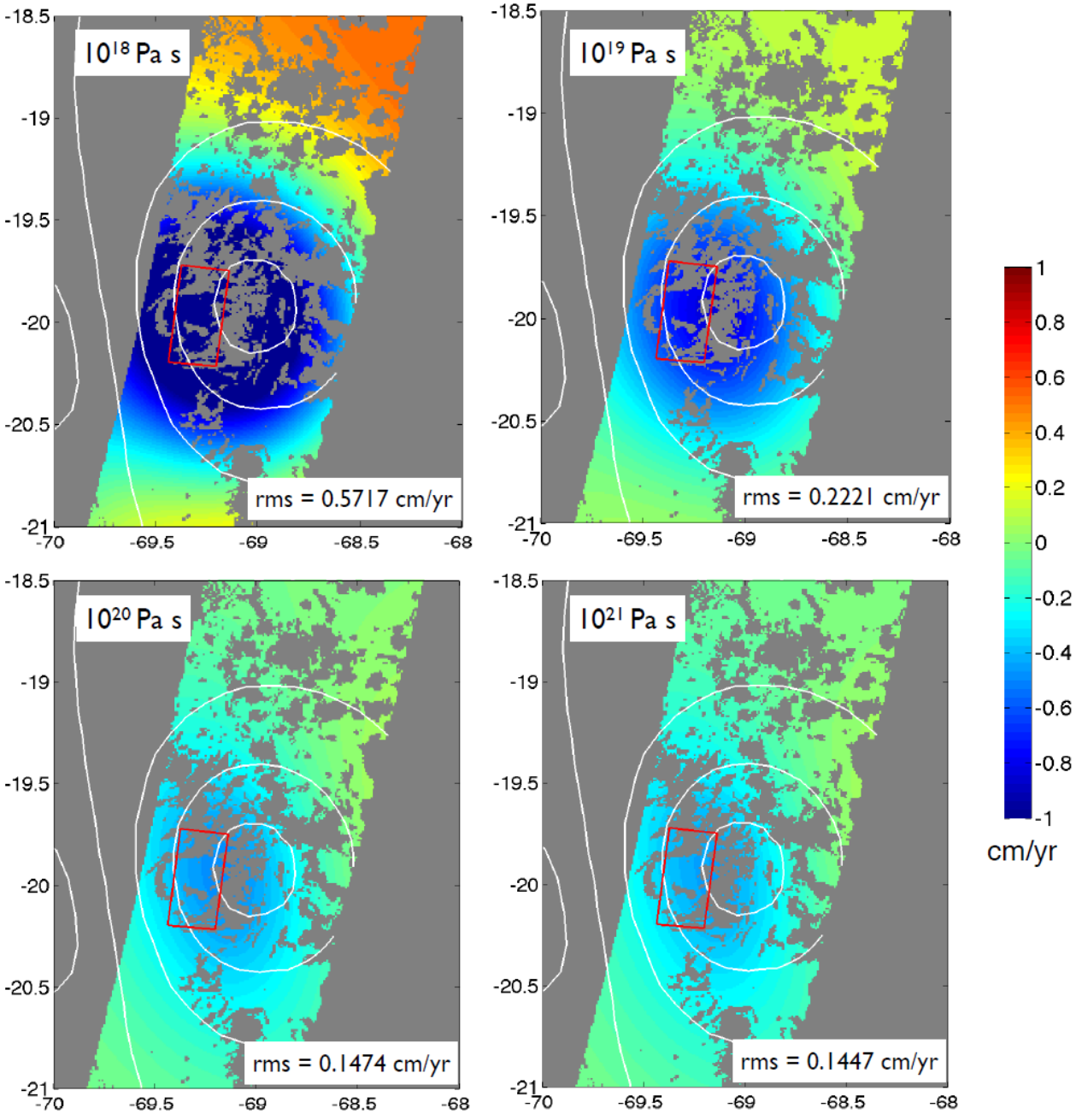

Figure S5.2. Modelled LOS displacements with various viscosity inputs for the oceanic mantle. Oceanic mantle viscosity is shown in top-left corner of each subfigure. Other parameters are same as used for Fig. 5.6(b). Warm colours indicate LOS motion away from the satellite. Coseismic deformation of the Tarapaca earthquake is shown by the same white contours as in Fig. 5.2. Red rectangle is the surface projection of the Tarapaca rupture from Peyrat et al. (2006). RMS misfit between InSAR model and data is given for each case in the lower right corner.

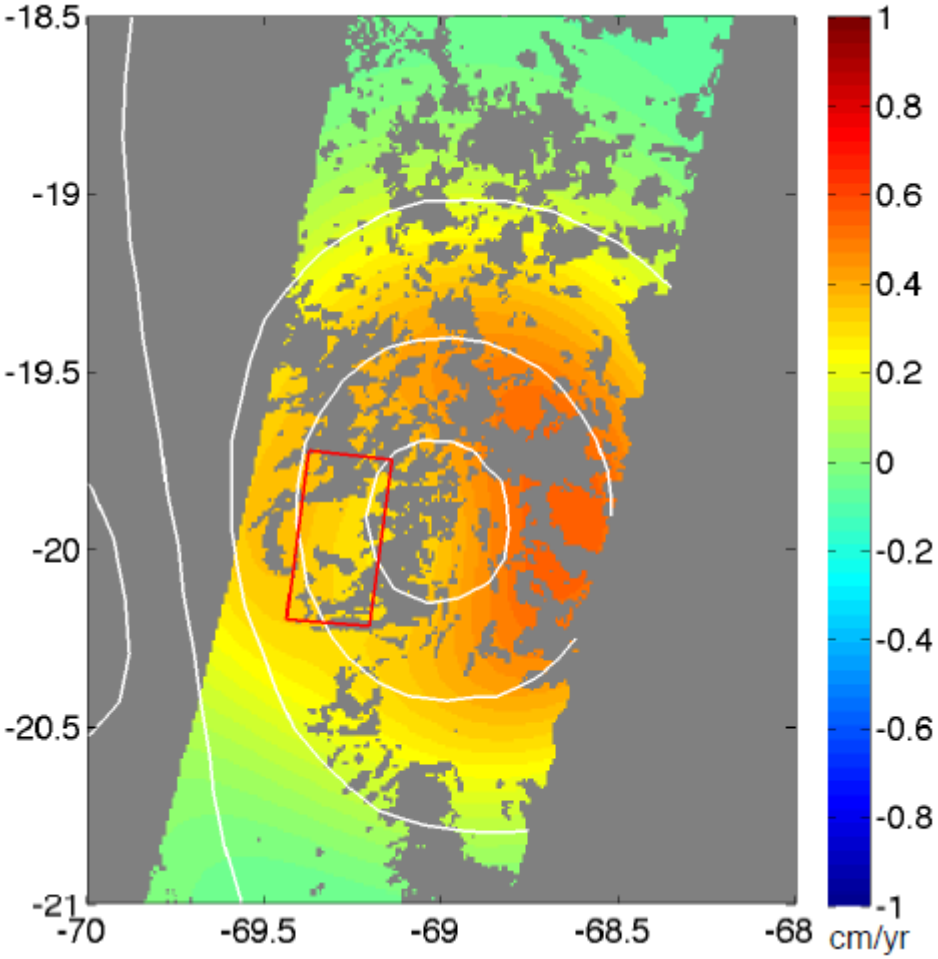

Figure S5.3. Forward modeled LOS displacement with a viscoelastic zone A, sharing same viscosity as zone B and C (4×10^{18} Pa s).

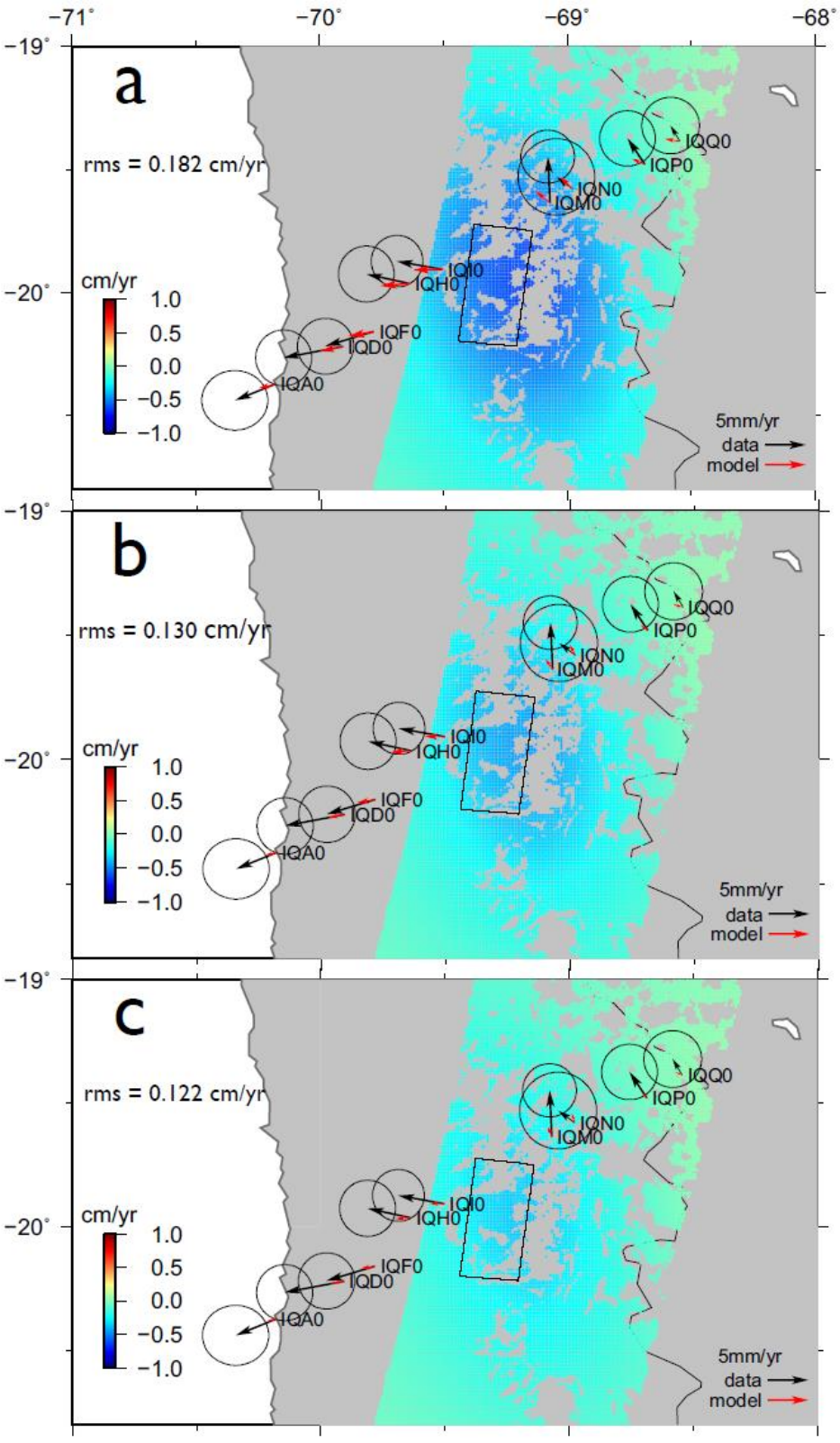

Figure S5.4. Modelled rate map of InSAR LOS displacement and GPS horizontal displacements (red arrows) with zone C viscosity of: (a) 3.2×10^{18} Pa s; (b) 5×10^{18} Pa s; (c) 6.4×10^{18} Pa s. Other parameters are: $H_A = H_B = 45$ km, $\eta_B = 5 \times 10^{19}$ Pa s. Black arrows are the same as shown in Fig. 5.3(b). RMS misfit between model and data is given with unit cm/yr.

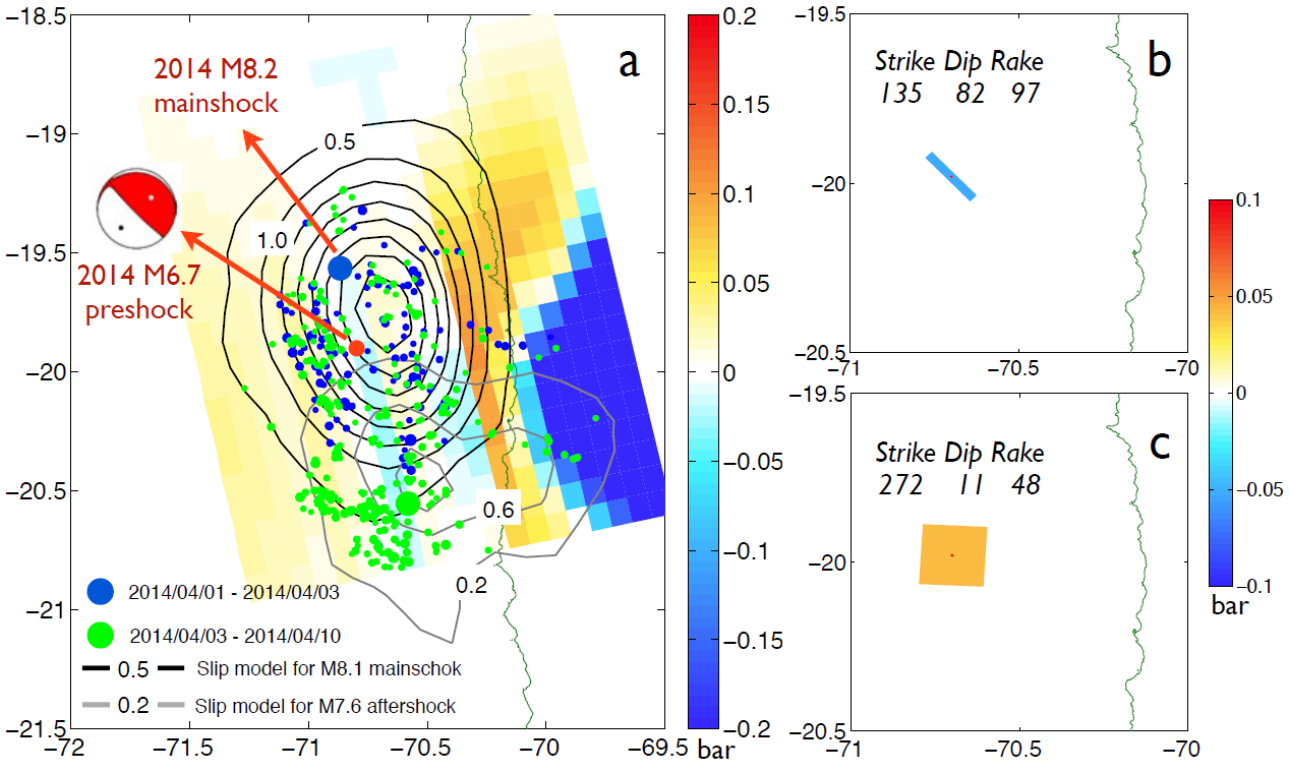

Figure S5.5. Coulomb stress changes induced by the coseismic rupture of the Tarapaca earthquake only. (a) Stress change on the subduction interface. Aftershock distribution, and slip models for *M* 8.2 Iquique earthquake and its *M* 7.6 aftershock, are from Schurr et al. (2014). (b) and (c) Stress change resolved on the nodal planes of the *M* 6.7 preshock.

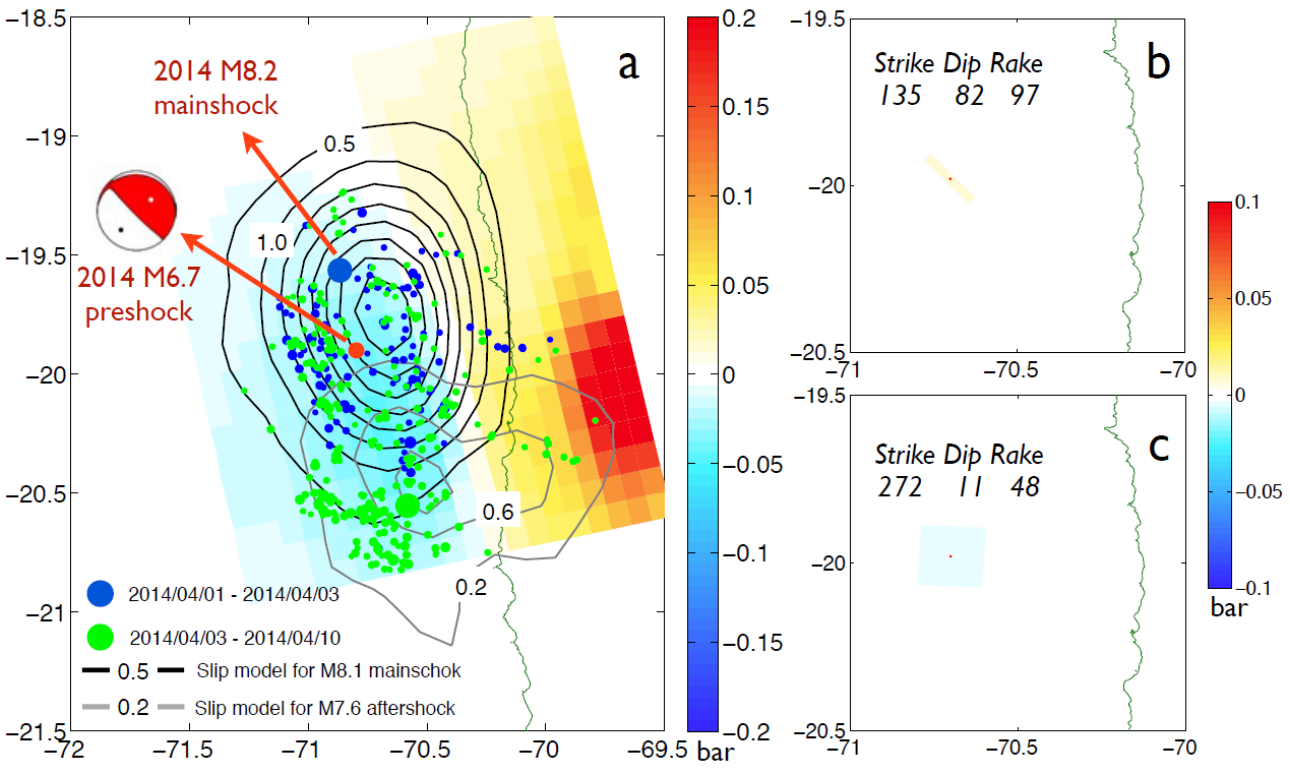

Figure S5.6. Coulomb stress changes induced by the postseismic VER after the Tarapaca earthquake only. (a) Stress change on the subduction interface. Aftershock distribution, and slip models for *M* 8.2 Iquique earthquake and its *M* 7.6 aftershock, are from Schurr et al. (2014). (b) and (c) Stress change resolved on the nodal planes of the *M* 6.7 preshock.

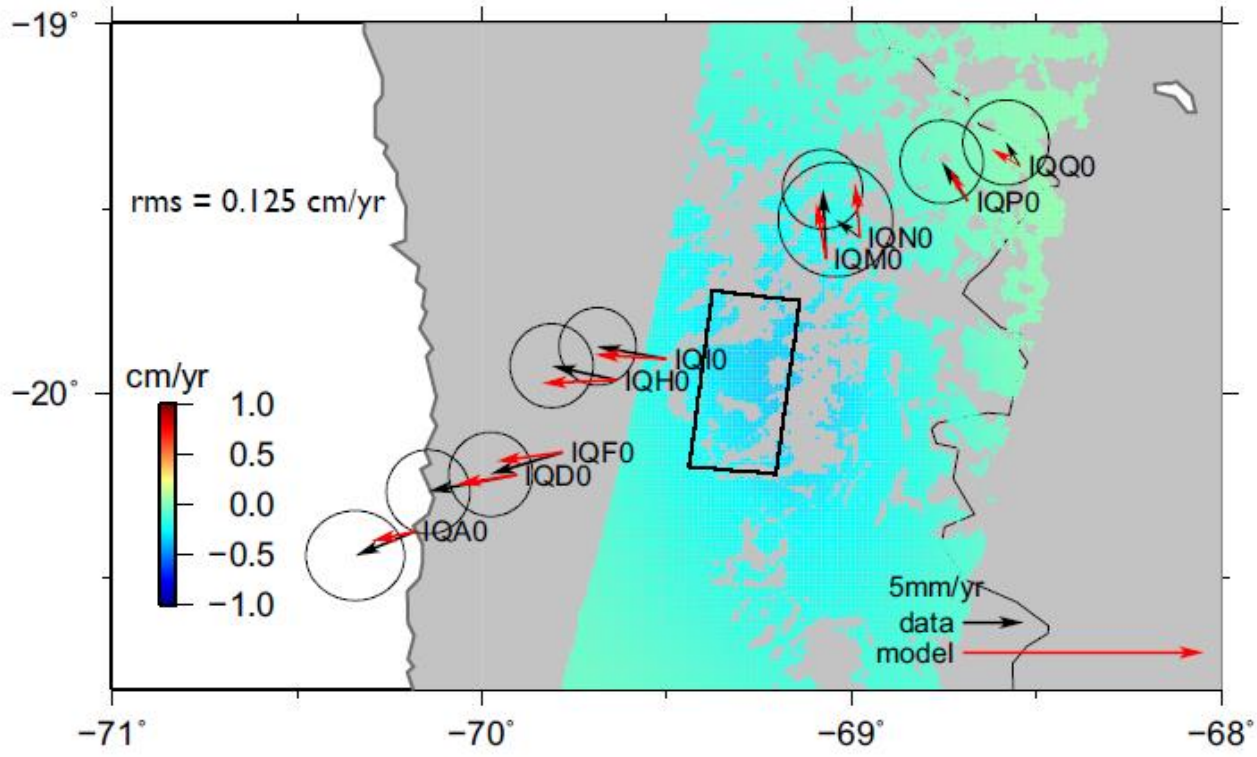

Figure S5.7. A reproduction of Fig. 5.6. Modelled rate map of InSAR LOS displacement and GPS horizontal displacements (red arrows) with zone C viscosity of 8×10^{18} Pa s. In comparison to Fig. 5.6(a), modelled GPS horizontal displacements in Fig. S5.7 are scaled up by 4 times, in order to clearly show the agreement with data in azimuth.